

# Self-Assembly and Evaporation of Superparamagnetic Colloids

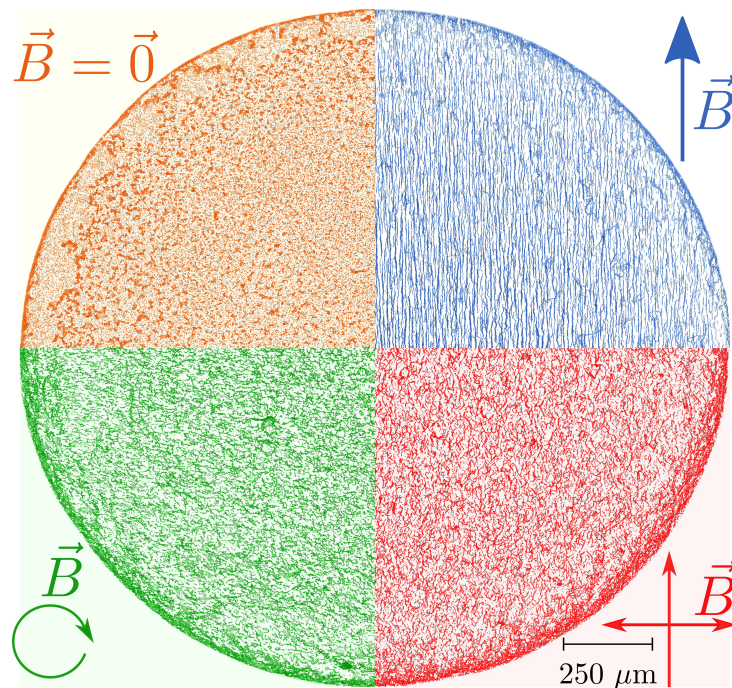
---

Dissertation  
zur Erlangung des Grades  
des Doktors der Naturwissenschaften  
der Naturwissenschaftlich-Technischen Fakultät  
der Universität des Saarlandes  
als Cotutelle de Thèse mit  
der Universität Liège

von  
**Alexis Darras**  
Saarbrücken  
2019



# Self-Assembly and Evaporation of Superparamagnetic Colloids



PhD Thesis defended by  
**Alexis Darras**  
to obtain the title of PhD of Science  
Academic Year 2018-2019



## Acknowledgements

*"All things are connected, like the blood that unites us. We did not weave the web of life, we are merely a strand in it."*

Chief Seattle

Science would not make any sense if its results weren't built and shared with other people. Therefore, before presenting the research performed during my thesis, I would like to thank the many people without whom this work could not have been performed, or at least not in such enjoyable conditions. The following paragraphs are written in the most suitable language for each recipient.

Je tiens tout d'abord à remercier mon promoteur, Geoffroy Lumay, qui m'a ouvert les portes de son laboratoire et proposé la thématique de recherche qui m'a passionné ces dernières années. Son soutien jovial et son optimisme dynamique n'ont d'égal que la grande liberté qu'il m'a laissée pour explorer à ma guise les idées et questions soulevées lors de mes recherches. Merci de m'avoir offert l'occasion de faire ces premiers pas sur le chemin de la recherche académique.

I also want to thank my co-promoter, Christian Wagner, who welcomed me in his laboratory with a complete trust. I've been impressed by his care for the comfort and wellness of his PhD candidates. I'm grateful for his proposition of joint supervision and all the technical knowledge I learned during my stay in his research group. More anecdotally, I also need to thank him for giving me the opportunity to discover Paris.

Je tiens également à remercier Nicolas Vandewalle, directeur du GRASP, dont les conseils avisés et les questions pertinentes ont souvent fait avancer à grands bonds mes réflexions et la démarche scientifique de ce travail. Merci pour le temps consacré aux relectures attentives des divers articles que j'ai eu le plaisir d'écrire au cours de ce séjour de recherche.

Besides these main mentors, I would like to thank the great researchers, John Martin, Stéphane Dorbolo, Jorge Fiscina, Alvaro Marin and Benoit Scheid, who accepted to be members of my thesis jury. Particular (and many) thanks are due to Stéphane Dorbolo for his early reading and report giving me the right to defend this thesis, as well as for his role of secretary of the jury. I am grateful for the time all of you spent reading in details this manuscript and the attention you brought to my work.

Je dois également des remerciements particuliers à Éric Opsomer, qui fut pour moi un guide sur les voies numériques, germaniques et cartographiques. Il fut pendant plusieurs années un camarade de bureau exemplaire, aux côtés de Marti, Vincent et Salvatore, dont les humours, bien caractéristiques de leurs régions, ont donné lieu à des interactions mémorables... Merci aussi au reste du labo pour les échanges d'idées, les débats passionnés lors des temps libres et le solide team building si caractéristique du GRASP. Je ne peux d'ailleurs pas passer à côté de l'occasion de laisser un mot à chaque membre de la team des p'tits loups dont la compagnie me laissera un souvenir impérissable: l'amical Galien, ce presque beau-frère qui a un don pour les montages expérimentaux; Maman Floflo, dont l'honnêteté, l'organisation toute germanique et le sens de l'esthétique n'ont d'égal que sa générosité à mettre son savoir administratif au service du plus grand nombre; le chouette Martin, à l'imagination débordante, dont personne n'a jamais imaginé relever l'heure de départ; Sébastien RG, loup blond à l'oreille attentive, chaleureux et enthousiaste qui aura organisé tant de nos rencontres; Bobo, le métalleux au cœur tendre qui nous aura fait voir de si charmantes photos et paysages; les trois louves : Joséphine, petite filleule qui a bien grandi, engagée, humble et luxuriante à la fois; Florence, dont la charmante jovialité et la passion partagée pour la Chimay bleue illuminent nos réunions et la cafet'; Ylona, la plus festive des trois, jeune louve imaginative et créative qui sait si bien décrire et prendre soin des étudiants; Jean, porte-étandard à mi-temps de nos élans

créatifs, dont le calme olympien a plusieurs fois permis de poser le décor; enfin, merci à Adrien, dont le caractère angelin aura su bien nous faire rire en diverses occasions. Merci également à Stéphane, mentor occasionnel mais efficace, avec qui j'aurai eu le plaisir de découvrir la haute technologie de Noordwijk. Merci à Hervé, qui m'aura donné la chance de participer à diverses activités de vulgarisation dont l'inoubliable initiative du micro-musée. Je remercie également Christophe, digne représentant, coordinateur, organisateur de tant de cours, réunions, détails pratiques, jeux mathématiques et festivités qu'il est un exemple de dévouement pour nous tous. Merci à Charlotte pour ses relectures attentives et consciencieuses de mes productions anglophones, dont celle-ci. Je pense également aux doctorants que j'ai côtoyés moins longtemps, mais qui ont laissé une empreinte indélébile au labo, par leur personnalité comme leur travail scientifique : Sofiene, sympathique et courageux collègue qui n'a pas hésité à traverser la frontière agronomique pour nous rejoindre; Maxime, qui m'a bien aidé pour expliquer l'effet de serre; Julien, dont l'amour du couscous et de la zumba sont légendaires; Laurent, dit le Mac, dont les standards culinaires font référence dans nos couloirs, aujourd'hui encore; Martin BdB, dont l'usage expérimental des chaussures et des balais reste gravé dans ma mémoire. Merci également aux différents techniciens de l'atelier d'électromécanique, Med, Sam, Olivier et Manon, pour les menus mais nombreux services et réalisations effectués en soutien à mes recherches, ainsi que pour les discussions détendues lors des temps de midi et barbecues du labo.

A particular thanks also goes to the postdocs I had the opportunity to collaborate with during this thesis. In particular, I would like to thank Jorge Fiscina, with whom I was lucky to first work in Liège and then share the office in Saarbrücken. He has been a relentless co-worker and mentor at the same time. Maryam Pakpour also deserves my recognition for the help she gave me at the beginning of my work with colloids, her delicacy was the key to develop the initial successful protocol. I also thank Nicolas Rojas with whom we made theoretical developments on magnetic assemblies.

If I spent a lot of time in Liège, I also had the great chance to meet a great team of motivated researchers in Saarbrücken. I'd like to thank Thomas John for his help and advice during my stay, both for scientific and administrative processes. Thanks a lot to Manu and his precious advice in microfluidics, those were amongst the most useful I received during my stay. I would also thank Alexander, Revaz and Daniel, with whom I can say I truly shared some blood and nice time. Thanks also to Greta, Asena and Vivi, whose smiling company and kindness made this stay more pleasant to live (even though it was the first time somebody doubted my pastry skills). I probably forgot some names but, guys, I'd like you all to know that you all rock and I had a very good time with you, even far from family and (other) friends.

Au cours de cette thèse, j'ai aussi eu l'occasion de participer à plusieurs activités de vulgarisation, à chaque fois entouré de super collaborateurs passionnés et passionnants. Merci à Stéphanie, Audrey, Bernard et tout l'équipe de Science et Culture pour les bons moments passés à préparer et présenter leurs super expos, merci à la team MT180, dont Evelyne Favart et son service. Merci au Réseau des Doctorants pour le soutien apporté à cette occasion et à travers ses diverses activités annuelles. Le soutien du statut des doctorants et le réseautage que vous mettez en place a réellement contribué à faire de cette thèse une expérience humaine enrichissante.

Merci également à l'équipe de la toute jeune cellule Young Minds Liège. Particulièrement à Peter Schlagheck pour l'impulsion initiale et le soutien académique, ainsi qu'à Joseph, Sylvain et Émile d'avoir accepté de démarrer cette aventure un peu folle à mes côtés. Je suis aussi extrêmement reconnaissant envers les nombreux motivés qui nous ont rejoint en cours de route. Je suis persuadé que ce réseau de l'EPS a beaucoup à apporter aux jeunes physiciens liégeois et que cette initiative permettra de partager notre passion de la physique au grand public, tout

en resserrant les liens qui nous unissent. Puisse cette épopée durer longtemps !

Enfin, ces remerciements ne seraient pas complets sans mentionner ma famille et mes amis proches, qui m'ont soutenu au quotidien et m'ont permis de m'épanouir aussi dans ma vie privée. Une mention particulière va à mes parents, mon frère et ma belle-soeur, cette cellule familiale solide, positive et joviale sur laquelle j'ai pu compter en toute occasion. De plus, je ne peux m'empêcher de rajouter une pensée pour Isa, la tendre moitié qui m'a continuellement soutenu et supporté lors de cette intense dernière année de thèse. Merci à vous cinq, vous êtes les joyaux de mes relations.





---

## Self-assembly and evaporation of superparamagnetic colloids

### Abstract

The evaporation of colloidal droplets is an area of intensive research. From paint coating to blood analysis on crime scene, applications of patterning from evaporation of colloids are numerous and various. In our work, we aimed to bring highlight on how interactions between colloidal particles influence the eventual deposit's pattern. To do this we used superparamagnetic colloids as a way to have a tunable interaction with these particles.

We first studied the influence of dipolar interactions on the suspension of particles. We performed systematic experiments to characterize the thermodynamic equilibrium reached by the suspensions. We showed that tuning the viscosity parameter could be used to speed-up numerical simulations. We used this process in sped-up simulations in order to study a new range of volume fraction. We showed that high volume fraction conditions led to higher chains' length than expected. We proposed a modification of current models.

We then focused on evaporating droplets. We began by reviewing the liquid flows in our suspensions. We showed there was a competition between coffee-ring flow and Marangoni instability. We then characterized the deposits left after evaporating suspensions under magnetic fields, and showed the influence of both this parameter and the Marangoni instability on the eventual deposits. We evidenced a transition in the deposit's behaviour when the DLVO interaction between the particles and the substrate becomes attractive.

---



---

# Selbstorganisation und Verdampfung superparamagnetischer Kolloide

## Zusammenfassung

Die Verdampfung kolloidaler Tropfen ist ein Gebiet intensiver Forschung. In unserer Arbeit wollen wir hervorheben, wie die Interaktionen zwischen superparamagnetischen kolloidalen Partikeln die Muster in den Ablagerungen beeinflussen.

Wir untersuchen zunächst den Einfluss dipolarer Wechselwirkungen auf die Suspension von Partikeln. Wir haben systematische Experimente durchgeführt, um das thermodynamische Gleichgewicht der Suspensionen zu charakterisieren. Wir haben gezeigt, dass eine Verringerung dieser Viskosität numerische Simulationen beschleunigen kann. Wir haben dieses Verfahren dann in beschleunigten Simulationen verwendet, um höhere Volumenfraktionen als üblich zu untersuchen. Wir haben gezeigt, dass die Kettenlängen für hohe Volumenfraktionen größer sind als erwartet und eine Modifikation aktueller Modelle vorgeschlagen.

Wir dann auf die Verdampfung Tropfen konzentriert. Wir haben mit der Überprüfung der Flüssigkeitsströme unserer Suspensionen begonnen und gezeigt, dass es einen Wettkampf zwischen dem Kaffeeeringeffekt und der Marangoni-Instabilität gibt. Dann haben wir die unter den Magnetfeldern entstandenen Ablagerungen charakterisiert und den Einfluss dieses Parameters sowie der Marangoni-Instabilität auf die Endablagerungen gezeigt. Wir haben einen Übergang im Ablagerungsverhalten hervorgehoben, wenn die Wechselwirkung zwischen den Partikeln und dem Substrat attraktiv wird.

---



---

## Auto-assemblage et évaporation de colloïdes superparamagnétiques

### Résumé

L'évaporation de gouttes colloïdales est actuellement un sujet d'intenses recherches. Dans notre travail, nous avons voulu mettre en évidence comment les interactions entre les particules colloïdales influencent le dépôt, à l'aide de colloïdes superparamagnétiques.

Nous avons d'abord étudié l'influence des interactions dipolaires sur la suspension de particules. Nous avons caractérisé l'état d'équilibre thermodynamique atteint par les suspensions avec des mesures expérimentales systématiques. Nous avons montré que diminuer la viscosité pouvait être un moyen d'accélérer des simulations numériques. Nous avons utilisé ce processus pour accélérer des simulations et étudier une gamme de fractions volumiques jusqu'alors inexplorée. Nous avons montré que des fractions volumiques élevées conduisaient à des chaînes plus longues que prédit. Nous avons alors proposé une modification des modèles actuels.

Nous nous sommes alors concentrés sur les gouttes en évaporation. Nous avons examiné les flux dans nos suspensions et montré qu'il existait une concurrence entre l'effet "coffee-ring" et l'instabilité de Marangoni. Nous avons alors caractérisé les dépôts obtenus sous un champ magnétique constant, et montré l'influence de ce paramètre et de l'instabilité de Marangoni sur ces dépôts. Nous avons mis en évidence une transition dans le comportement des dépôts lorsque l'interaction entre les particules et le substrat devient attractive.

---



## Preamble

Self-assembly of superparamagnetic colloids and evaporation of colloidal droplets are two areas of intensive research. However, no previous work, to our knowledge, has been studying how those two topics mix together. The main objective of our work is then to study how self-assembly of superparamagnetic colloids influences the evaporative deposit of a droplet containing those colloids. In order to efficiently introduce and describe our work, the first part of this manuscript gives a general introduction to the physics and properties of colloidal systems, as well as the thermodynamics of evaporating droplets and magnetic assemblies. Each of this topic is described in a separate chapter since the literature on both topic is independent.

After this state of the art, this manuscript gathers a selection of scientific articles written in the scope of my PhD thesis. Those articles are divided in two sections, classifying our research as self-assembly or evaporation themed. However, the last evaporation papers actually describe evaporation of droplets containing self-assembled superparamagnetic colloids. For each article, we briefly describe the motivations of the study along with the setup used, and the main results are briefly discussed. Each of those summaries are followed by the original and complete paper. Eventually, conclusion and perspectives from our whole work are described at the end of this manuscript.





# Complete list of publications

- *Remote control of self-assembled microswimmers*: G. Grosjean, G. Lagubeau, A. Darras *et al.*, Scientific Reports, **5**, 16035 (2015)
- *Ribbons of superparamagnetic colloids in magnetic field*: A. Darras, J. Fiscina, M. Pakpour *et al.*, Eur. Phys. J.-E, **39**(4), 47 (2016)
- *Statics and dynamics of magnetocapillary bonds*: G. Lagubeau, G. Grosjean, A. Darras, *et al.*, Phys. Rev. E. **93**(5), 053117 (2016)
- *Relating Brownian motion to diffusion with superparamagnetic colloids*: A. Darras, J. Fiscina, N. Vandewalle and G. Lumay, Am. J. of Phys. **85**(4), 265 (2017)
- *Self-assembly processes of superparamagnetic colloids in a quasi-two-dimensional system*: N. Rojas, A. Darras and G. Lumay, Phys. Rev. E. **96**(1), 012608 (2017)
- *Superparamagnetic colloids in viscous fluids*: A. Darras, E. Opsomer, N. Vandewalle and G. Lumay, Scientific Reports **7**(1), 7778 (2017)
- *Threshold of gas-like to clustering transition in driven granular media in low-gravity environment*: M. Noirhomme, A. Cazaubiel, A. Darras *et al.*, Eur. Phys. Lett. **123**(1), 14003 (2018)
- *Remote-controlled deposit of superparamagnetic colloidal droplets*: A. Darras, F. Mignolet, N. Vandewalle and G. Lumay, Phys. Rev. E **98**(6), 062608 (2018)
- *Transitional bulk-solutal Marangoni instability in sessile drops*: A. Darras, N. Vandewalle and G. Lumay, Phys. Rev. E. **98**(6), 062609 (2018)
- *Effect of volume fraction on chains of superparamagnetic colloids at equilibrium*: A. Darras, E. Opsomer, N. Vandewalle and G. Lumay, Eur. Phys. J.-E, submitted (2019)
- *Combined effects of Marangoni, sedimentation and coffee-ring flows on evaporative deposits of superparamagnetic colloids*: A. Darras, N. Vandewalle, G. Lumay, in preparation



GRASP-CESAM/AG Wagner  
Departments of physics  
University of Liege, Saarland University  
Belgium

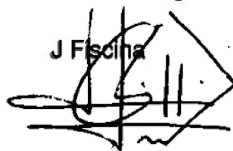
March 20, 2019

Hereby, we, co-authors of the below-mentioned articles, attest that Alexis Darras took a prominent part in the scientific design and implementation of the technical measures and protocols, as well as in the analysis and interpretation of the results obtained in the scientific research of every and each of those articles. Detailed contributions of each author for each article are presented in the next page.

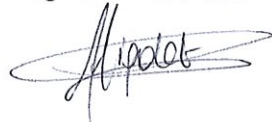
In addition, Alexis Darras wrote the first version of these articles, collected our remarks and ensured the correspondence with the editors and referees. Therefore, we support his use of these articles as substantial parts of his PhD thesis.


- *Ribbons of superparamagnetic colloids in magnetic field*: A. Darras, J. Fiscina, M. Pakpour *et al.*, Eur. Phys. J.-E, **39**(4), 47 (2016)
- *Superparamagnetic colloids in viscous fluids*: A. Darras, E. Opsomer, N. Vandewalle and G. Lumay, Scientific Reports **7**(1), 7778 (2017)
- *Remote-controlled deposit of superparamagnetic colloidal droplets*: A. Darras, F. Mignolet, N. Vandewalle and G. Lumay, Phys. Rev. E **98**(6), 062608 (2018)
- *Transitional bulk-solutal Marangoni instability in sessile drops*, A. Darras, N. Vandewalle and G. Lumay, Phys. Rev. E. **98**(6), 062609 (2018)
- *Effect of volume fraction on chains of superparamagnetic colloids at equilibrium*: A. Darras, E. Opsomer, N. Vandewalle and G. Lumay, Eur. Phys. J.-E, submitted (2019)
- *Combined effects of Marangoni, sedimentation and coffee-ring flows on evaporative deposits of superparamagnetic colloids*: A. Darras, N. Vandewalle, G. Lumay, in preparation

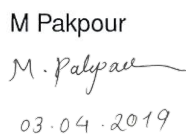
Date and signature :

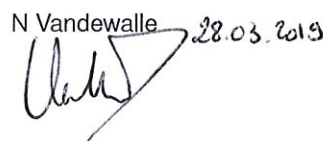
J Fiscina  
  
28.03.2019

G Lumay 27/03/19  


F Mignolet 27.03.2019  


E Opsomer  
27/03/19  


M Pakpour  
M. Pakpour  
03-04-2019  


N Vandewalle 28.03.2019  


GRASP, Department of physics, University of Liege, allée du 6 Aout, 17, B-4000 LIEGE (Belgium)  
AG Wagner, Department of physics, Saarland University, Postfach 151150, D-66041 Saarbrücken (Germany)

## Detailed contributions of authors for each publication

- *Ribbons of superparamagnetic colloids in magnetic field*: A. Darras, J. Fiscina, M. Pakpour *et al.*, Eur. Phys. J.-E, **39**(4), 47 (2016)

AD, JF, GL and NV conceived the experiments, AD, JF and MP conducted the experiments, AD conceived and performed the numerical computations, AD wrote the manuscript. All authors analysed the results and reviewed the manuscript.

- *Superparamagnetic colloids in viscous fluids*: A. Darras, E. Opsomer, N. Vandewalle and G. Lumay, Scientific Reports **7**(1), 7778 (2017)

GL and AD conceived the experiments, AD conducted the experiments, EO and AD conceived the simulation code, EO wrote the simulation code, AD managed the simulations, EO and AD wrote the manuscript. AD, EO, GL and NV analysed the results and reviewed the manuscript.

- *Remote-controlled deposit of superparamagnetic colloidal droplets*: A. Darras, F. Mignolet, N. Vandewalle and G. Lumay, Phys. Rev. E **98**(6), 062608 (2018)

AD, GL and NV conceived the experiments, AD and FM built the experimental setup and conducted the experiments, AD conceived the image analysis algorithm, AD and FM developed and managed the code, AD wrote the manuscript. All authors analysed the results and reviewed the manuscript.

- *Transitional bulk-solutal Marangoni instability in sessile drops*: A. Darras, N. Vandewalle and G. Lumay, Phys. Rev. E. **98**(6), 062609 (2018)

AD, GL and NV conceived the experiments, AD conducted the experiments and wrote the manuscript. All authors analysed the results and reviewed the manuscript.

- *Effect of volume fraction on chains of superparamagnetic colloids at equilibrium*: A. Darras, E. Opsomer, N. Vandewalle and G. Lumay, Eur. Phys. J.-E, submitted (2019)

GL and AD conceived the experiments, AD conducted the experiments, EO and AD conceived the simulation code, EO wrote the simulation code, AD managed the simulations, EO and AD wrote the manuscript. AD and NV built the theoretical model. AD, EO, GL and NV analyzed the results and reviewed the manuscript.

- *Combined effects of Marangoni, sedimentation and coffee-ring flows on evaporative deposits of superparamagnetic colloids*: A. Darras, N. Vandewalle, G. Lumay, in preparation

AD, GL and NV conceived the experiments, AD conducted the experiments and wrote the manuscript. All authors analysed the results and reviewed the manuscript.

# Contents

<b>I</b>	<b>Introduction</b>	<b>1</b>
<b>1</b>	<b>Superparamagnetic colloids</b>	<b>3</b>
1.1	Colloids . . . . .	3
1.2	Magnetic interactions . . . . .	8
1.3	Self-assembly dynamics . . . . .	13
1.4	Self-assembly equilibrium . . . . .	15
1.5	General motivations and open questions . . . . .	16
1.6	Personal contribution . . . . .	16
<b>2</b>	<b>Evaporative deposits</b>	<b>17</b>
2.1	Coffee-Ring . . . . .	17
2.2	Marangoni . . . . .	20
2.3	Substrate . . . . .	22
2.4	General motivations and open questions . . . . .	24
2.5	Personal contribution . . . . .	24
<b>3</b>	<b>Objectives and plan</b>	<b>25</b>
<b>II</b>	<b>Self-Assembly up to thermodynamic equilibrium</b>	<b>27</b>
<b>4</b>	<b>Existence of ribbons</b>	<b>29</b>
4.1	Motivations . . . . .	29
4.2	Setup and methods . . . . .	29
4.3	Main results . . . . .	29
4.4	Conclusion . . . . .	30
4.5	Credits . . . . .	30
4.6	Paper as published in EPJE . . . . .	31
4.7	Additional remarks . . . . .	37
<b>5</b>	<b>Influence of viscosity</b>	<b>39</b>
5.1	Motivations . . . . .	39
5.2	Setup and methods . . . . .	39
5.3	Main results . . . . .	39
5.4	Conclusion . . . . .	41
5.5	Credits . . . . .	41
5.6	Paper as published in Scientific Reports . . . . .	42
<b>6</b>	<b>Effect of volume fraction</b>	<b>51</b>
6.1	Motivations . . . . .	51
6.2	Setup and methods . . . . .	51
6.3	Main results . . . . .	51
6.4	Conclusion . . . . .	52
6.5	Credits . . . . .	52
6.6	Paper as submitted in EPJE . . . . .	53

<b>III</b>	<b>Self-Assembly in evaporating droplets</b>	<b>63</b>
<b>7</b>	<b>Transitional Marangoni instability</b>	<b>65</b>
7.1	Motivations . . . . .	65
7.2	Setup and methods . . . . .	65
7.3	Main results . . . . .	65
7.4	Conclusion . . . . .	67
7.5	Paper as published in PRE . . . . .	68
7.6	Additional Comments . . . . .	75
<b>8</b>	<b>Remote-controlled deposits</b>	<b>77</b>
8.1	Motivations . . . . .	77
8.2	Setup and methods . . . . .	77
8.3	Main results . . . . .	77
8.4	Conclusion . . . . .	78
8.5	Paper as published in PRE . . . . .	80
<b>9</b>	<b>Combined effects</b>	<b>85</b>
9.1	Motivations . . . . .	85
9.2	Setup and methods . . . . .	85
9.3	Main results . . . . .	85
9.4	Conclusion . . . . .	86
9.5	Paper as submitted in Colloid and Interface Science Communication . . . . .	87
<b>IV</b>	<b>Conclusion and perspectives</b>	<b>97</b>
<b>10</b>	<b>Conclusion and perspectives</b>	<b>99</b>
10.1	Conclusion . . . . .	99
10.2	Perspectives . . . . .	101
<b>A</b>	<b>Self-assembly equilibrium : detailed calculations</b>	<b>103</b>

## Part I

# Introduction





# Chapter 1

## Superparamagnetic colloids

If you ask anyone on the street what is the common point between ink, paint, fog, blood, milk and coffee, they will probably have a hard time to find a convincing answer... However, if it turns out that this person has a scientific background in multiphase systems, he should answer pretty fast that they are colloidal systems. In other words, they consist of tiny particles (from a few nanometres to a few tens of micrometres) suspended in a continuous phase. This common aspect of their constitution gives them some common physical properties. Therefore, understanding and mastering colloidal behaviours leads to applications in various fields such as printing, food handling or crime scene analyses. This first chapter offers a glimpse of the general properties and topics concerning colloidal suspensions and gives the required background in order to understand the main results of our research.

### 1.1 Colloids









Continuous phase \ Dispersed phase	gas	liquid	solid
gas (bubbles)		foam 	solid foam 
liquid (droplets)	liquid aerosol 	liquid emulsion 	solid emulsion 
solid (particles)	solid aerosol 	sol 	solid sol 

Figure 1.1: Various types of colloids depending on the thermodynamic state of dispersed and continuous phase. Pictures represents, from left to right, then from top to bottom : whipped cream, shaving foam, marshmallow, suitcase foam, clouds, liquid spray, mayonnaise, milk, butter, cheese, smoke, suspended dust, coffee, paint, zircon gemstone and selenium ruby (a type of coloured glass).

There is no rigorous definition of colloids which is accepted by the whole scientific community. [1] The most cautious authors define them as a dispersion of small particles (with varying size limitations, but comprised between the nanometre and a few hundreds of micrometre) in a continuous media [2–4]. Depending on the thermodynamic state of each phase, this gives various types of colloids which all have their own specific name, as illustrated in Figure 1.1, along with a few common examples. Typical structure of colloids, on a microscopic scale, is shown in Figure 1.2.

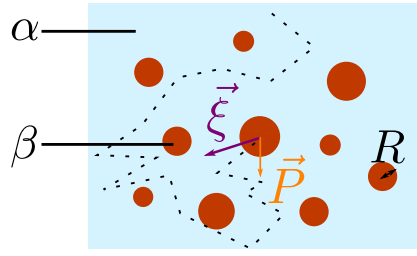


Figure 1.2: Typical structure of a colloidal suspension. The colloid is constituted by a continuous (or dispersing) phase, noted  $\alpha$ , and a dispersed phase, noted  $\beta$ . The radius (or typical size)  $R$  of the suspended particles ranges from between the nanometre and a few hundreds of micrometre. A typical example of Brownian motion is represented in dotted lines for the central particle. The Péclet number, sometimes used in the definition of colloids, explicitly depends on the diffusion coefficient of this motion. The Brownian motion results from the interaction between the resulting force from the weight and the buoyancy of the particles  $\vec{P}$  and the random thermodynamic force  $\vec{\xi}$  due to collisions with molecules of the continuous phase, according to Langevin theory. [5]

However, some other authors prefer to define the colloidal suspensions as suspensions where the dispersed particles present a Brownian motion, due to  $\vec{\xi}$ , the random thermodynamic force arising from the collisions with surrounding molecules of the continuous phase [5]. According to this, a suspension is colloidal if the displacement due to the Brownian motion is significant when compared with the displacement due to other motion mechanisms. Usually, the sedimentation (or flotation) due to  $\vec{P}$ , the resulting force from the weight and the buoyancy of the particles, is used as the reference for this comparison [6, 7]. This definition is often more restrictive than the previous one. Indeed, it excludes every case where the continuous phase is solid, unless you consider that zero is significant in comparison with zero, which can be kind of tricky... Nonetheless, it has the advantage to highlight one common property of almost all sols and aerosols. In the case of sols, it is easy to demonstrate that, in usual conditions, small particles have a Brownian motion significantly higher than their sedimentation. The comparison between those two motions is usually made through the Péclet number

$$Pe = \frac{D}{vL}, \quad (1.1)$$

where  $D$  is the diffusion coefficient of the particles,  $v$  is the characteristic sedimentation speed and  $L$  is a characteristic length of motion. If we approximate the particles as spheres of radius  $R$ , the Stokes-Einstein relation gives

$$D = \frac{k_B T}{6\pi R \eta}, \quad (1.2)$$

with  $k_B$  the Boltzmann constant,  $T$  the temperature, and  $\eta$  the viscosity of the fluid. Furthermore, the sedimentation speed can be obtained by equaling the Stokes force to the weight of a particle, minus the buoyancy

$$6\pi R \eta v = \frac{4}{3}\pi R^3 \Delta \rho g \Leftrightarrow v = \frac{2 \Delta \rho R^2 g}{9\eta}, \quad (1.3)$$

with  $g$  the gravitational acceleration and  $\Delta \rho$  the difference between the density of the particle and those of the fluid. We then have  $Pe = \frac{D}{vR} = \frac{3k_B T}{4\pi R^4 \Delta \rho g}$ . By considering  $\Delta \rho \approx 10^3$  close to

the water density, usual room temperature  $T \approx 300$  K and  $g = 9.81 \text{ ms}^{-2}$ , we obtain

$$Pe \approx \frac{10^{-25}}{R^4}. \quad (1.4)$$

Assuming that Brownian motion is significant if  $Pe > 0,1$ , this leads to a condition on the particles radius  $R < 1 \text{ }\mu\text{m}$ . This is then in agreement with the micron limit for the size of particles. Moreover, it is often considered that a colloidal particle should be much bigger than the molecules of the dispersed phase in order to differ from usual solutions, i.e.  $R > 10 \text{ nm}$  [8]. This somehow gives concrete grounds for the aforementioned size limitation of colloidal particles, and is particularly relevant for colloids with a fluid continuous phase as the ones on which we will focus in this thesis.

Another topic which concerns every colloid, particularly when the continuous phase is fluid, is their stability. Actually, from a thermodynamic point of view, all colloids are in a metastable state. [7] Indeed, (at constant temperature) the presence of interface between dispersed and continuous phases either increases the (free) energy of the system or decreases it. If it increases the energy, then the global minimum of energy is when there is the least possible interface. Which is achieved with a macroscopic segregation of both phases. If the presence of interface decreases the energy, then the minimal energy is achieved with a homogeneous mixture of the components, i.e. with a dissolution of the dispersed phase. Therefore, colloidal dispersion is never the state with the absolute minimal energy. However, they might still be stable, i.e. the dispersed phase can stay dispersed on arbitrarily long times. When the continuous phase is fluid, this is nevertheless not obvious and requires a stabilization of their interface. Indeed, at such small scales, the particles are subjected to significant Van der Waals interactions, creating an attractive force between them. When two solid particles, much bigger than a molecule of their constituent material, are close enough to each other (i.e. the distance between their surface is much smaller than their diameter), this force scales as  $F_{VdW} = A R / (12 z^2)$ , where  $A$  is the Hamaker constant ( $A = 2.43 \cdot 10^{-20} \text{ J}$  for water) and  $z$  the distance between the surfaces of the particles [9]. This attractive force tends to agglomerate all particles, thus creating a macroscopic separation of both phases. Any stabilization process has to overcome this attraction by creating a repulsion between the particles.

While various repulsive forces may occur between micrometric particles, the most abundant is the electrical double layer repulsion [10]. This interaction describes the repulsion between two charged particles (with the same electrical charge) immersed in an fluid containing free ions. Actually, there are several ways a colloidal particle can get a net electric charge when immersed in a polar solvent like water. Ranging from ion adsorption to ionisation via ion dissolution, all those phenomena give a similar net charge to similar particles [3, 4]. For the experiments in this thesis, we used particles covered with carboxyl groups ( $-\text{COOH}$ ). In water, those tend to ionize into ( $-\text{COO}^- + \text{H}^+$ ), then giving a negative charge to the particles. The dissociation rate of those groups is then obviously highly dependent on the pH of the solution, from Le Chatelier's principle. Adding electrolytes which modifies the pH is then a way to control the charge of the particles. Besides, when a particle having a net charge is immersed in a liquid containing free ions, these ions do not stay evenly distributed in the vicinity of the particles. Indeed, they are attracting ions with opposite charges (unless specific adsorption of surface-active ions), which is then creating a screening layer of electrical interactions. In more details, the Stern-Gouy-Chapman model describes this layer as having two parts : an inner layer (or Helmholtz layer) and a diffuse layer, as illustrated in Figure 1.3. The inner layer goes from the surface of the charged particles (and contains possible adsorbed ions) upto the closest distance where fully solvated ions can approach the surface of the particles. The outer, diffuse layer contains ions in the solvent experiencing Brownian motion. Their concentration

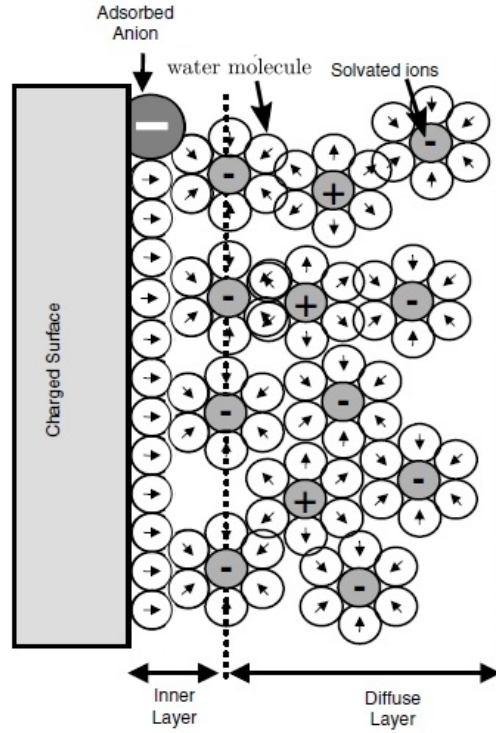


Figure 1.3: Illustration of the ionic double layer around a charged colloidal particle. Picture modified from [3].

decreases exponentially with a typical length of decay called the Debye length  $\lambda$ ,

$$\lambda = \sqrt{\frac{\epsilon_r \epsilon_0 k_B T}{2 N_A e^2 I}}, \quad (1.5)$$

where  $\epsilon_r \epsilon_0$  is the effective electric permittivity of water,  $k_B$  is the Boltzmann constant,  $T$  the temperature,  $N_A$  is the Avogadro number,  $e$  the fundamental charge of the electron and  $I = \frac{1}{2} \sum_i z_i^2 C_i$  the ionic strength of the continuous phase containing the various species of ions with valence  $z_i$  and concentration  $C_i$ . [9, 11] This length is often considered to be the thickness of the diffuse layer, or even of the whole screening layer. The decay of both these layers strongly depends on the concentration of ions in the solvent, then making the electric interactions between the particles highly dependent on this parameter. This creates a complex electric potential around the particles, depending on many parameters of the continuous phase and the particles [1–4, 6, 7, 10].

However, when particles repel each other efficiently, this interaction can be approximated by the electrostatic repulsion created beyond the Debye length  $\lambda$  [9]. The electrostatic repulsion  $F_e$  between particles is then

$$F_e = \lambda^{-1} \frac{R_1 R_2}{R_1 + R_2} Z \exp(D/\lambda) \quad (1.6)$$

where  $R_1, R_2$  are the radii of the two interacting particles,  $D$  is the distance between the surfaces of the particles and  $Z$  is a so-called "interaction constant"

$$Z = 64\pi\epsilon_0\epsilon \left( \frac{k_B T}{e} \right)^2 \tanh^2 \left( \frac{e\psi_0}{4k_B T} \right), \quad (1.7)$$

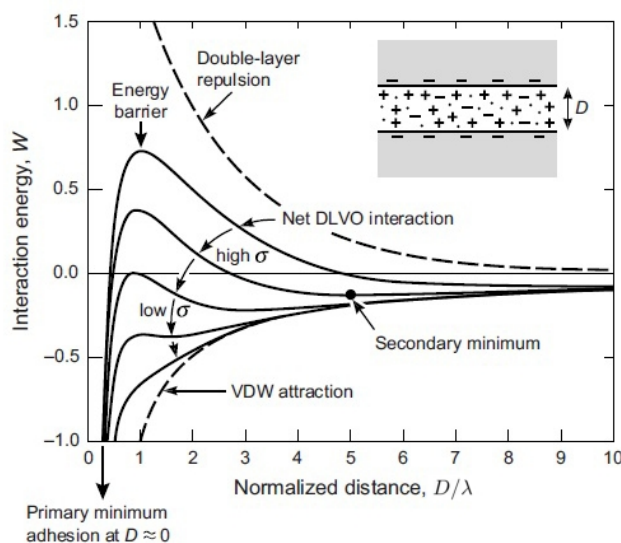


Figure 1.4: Interaction energy given by DLVO theory for various surface charge  $\sigma$  (and then for various surface potential  $\psi_0$ ). Figure modified from [9].

with  $\psi_0$  the surface potential. Regarding particles charged by ionisation corresponding to the release or adsorption of a  $\text{H}^+$  (or  $\text{OH}^-$ ) ion, the potential  $\psi_0$  is fixed by the pH of the solution through the Nernst equation [3, 10]. (Then the  $\text{H}^+$  or  $\text{OH}^-$  ions are then said to be Potential-determining ions) An appropriate buffer solution can then fix it. However, it is clear that the concentration of the buffer has an influence on the Debye length and the effective electrostatic interaction between the particles.

The theory describing the combined effect of these two interactions, van der Waals force and double layer interaction, is called the DLVO theory, in reference to B. Derjaguin, L. Landau, E. Verwey and T. Overbeek. The resulting potential is pictured in Figure 1.4 for various possible situations. As can be seen in this graph, various qualitatively different behaviours can occur. When the double layer repulsion is strong enough, it creates a potential barrier which is typically much higher than the thermal energy  $k_B T$ , preventing the particles to stick together. In this case, the colloidal suspension is said to be stable. When the double layer repulsion decreases, e.g. because of a change of ions concentration, a secondary minimum appears. In some conditions, this minimum can have a sharp shape with a few  $k_B T$  depth, while the barrier still prevents particles to reach the primary minimum. In this case, the particles can form loose agglomerates, or flocs which can be easily broken by mechanical agitation. This process of reversible agglomeration is often referred to as flocculation. Depending the size of the agglomerates and whether or not an equilibrium can be achieved between the flocs and the initial particles, a suspension where flocculation occurs can be considered as stable or not... Eventually, if the energy barrier decreases below a few  $k_B T$ , the particles then reach the primary minimum and begin to form permanent aggregates which will eventually sediment (or float depending on their relative density). When this kind of aggregation occurs, the suspension is unstable. While many authors make distinction between flocculation, aggregation and/or agglomeration, there is no consensus on which case each word should be used [12–14].

Of course, additional forces may appear between colloidal particles and modify their interaction energy. In some cases, the particles are even manufactured in order to present some properties such as electric dipole, magnetic susceptibility, complex surfaces (Janus particles),... Those properties often offer some possible manipulation of the particles, possibly leading to

reversible or irreversible self-assembly of an initially stable suspension. In the frame of this thesis, we used superparamagnetic colloids. In order to understand their specific interactions, the next section presents some notions of magnetism.

## 1.2 Magnetic interactions

Magnetic materials are often used in applications to move objects without contact, like in motors or actuators. At the scale of colloidal materials, this is possible too. For micrometric particles, classical magnetic behaviors (i.e. ferro- para- and diamagnetism), can still be observed [15–17]. Furthermore, a class of extensively used colloids are superparamagnetic colloids [18]. Those composite particles are combining a quasi-zero remanent magnetization, typical from paramagnetic materials, and a high magnetic response, typical from ferromagnetic materials [19–21]. In applications, the superparamagnetic colloids are functionalized to capture specific targets, which can then be manipulated through magnetic fields. This leads to several applications such as protein isolation, cell separation, waste capture, bacteria processing, chromatography, etc [18, 19, 22–30]. An example of such interactions is illustrated in Figure 1.5, where superparamagnetic colloids are used to separate RNA molecules from cells sample. In such application, the outer layer of the particles is functionalized in order to bind to the RNA, which can then be isolated and manipulated through external magnetic fields.

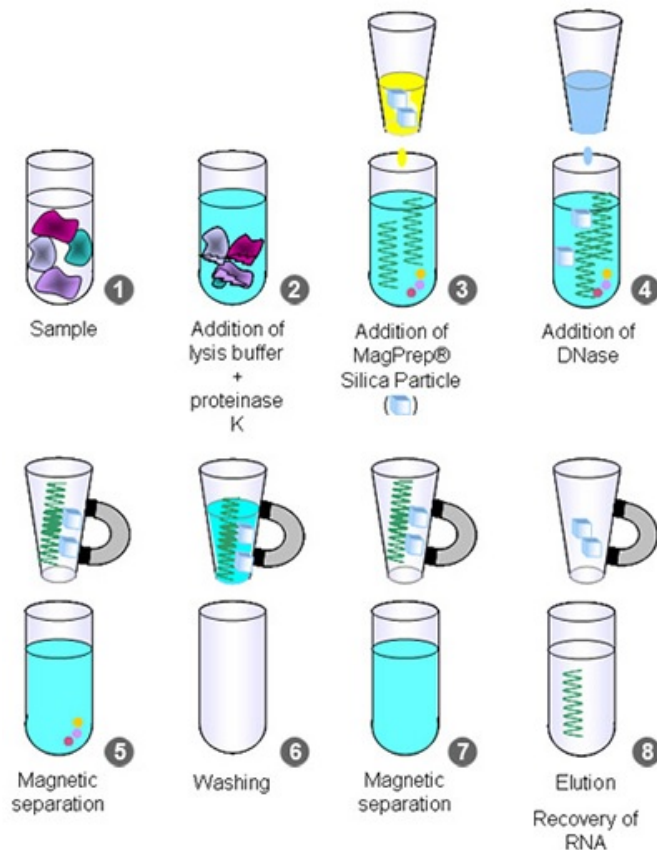


Figure 1.5: Picture from [31]. Illustration of an application of superparamagnetic colloids. The surface of the colloids is functionalized in order for them to bind to RNA. They are then removed with the RNA from the rest of the sample thanks to magnetic fields.

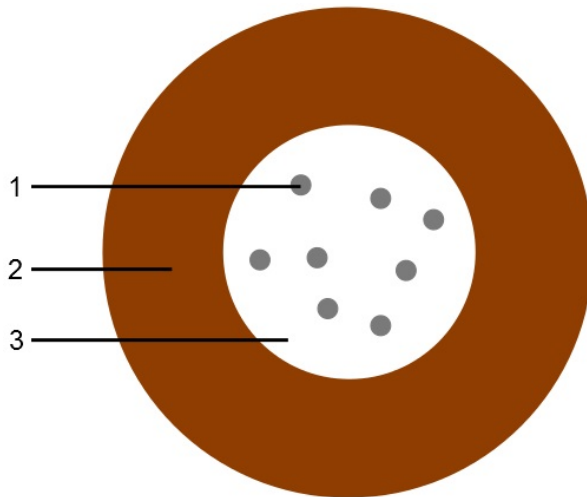


Figure 1.6: Characteristic structure of a superparamagnetic colloidal particle. 1: Inclusion of ferromagnetic nanoparticle 2: Diamagnetic shell. 3: Superparamagnetic core, containing the ferromagnetic nano-inclusions in a diamagnetic matrix. Practically, the diamagnetic matrix and the shell can be made of the same diamagnetic material, depending on the manufacturing process. The surface of the shell can be covered with functional groups, for specific applications or in order to stabilize the suspension [20].

Superparamagnetic colloids are magnetic nanoparticles (being a magnetic monodomain) inserted in a matrix of non-magnetic material (polystyrene or silica) to obtain particles with diameter  $d$  ranging from 100nm to a few micrometers [32]. This core is then surrounded by a diamagnetic shell. This shell makes that the particles can be assimilated as magnetic dipoles, without taking into account the details of the core structure, even when two particles are touching each other [20]. Such a structure is illustrated in Figure 1.6. The paramagnetic properties of the whole particle comes from the fact that there is no long-range order between the ferromagnetic inclusions. Such inclusions, due to their small size implying a low magnetic cohesion energy, are actually already superparamagnetic, since thermal agitation can reverse their magnetic orientation on a time scale much smaller than the observation time. The time required to reverse this orientation is called the Néel time and highly depends on the materials and the size of the sample [33]. Without external magnetic field, the colloidal particle has thus no remanent magnetic moment, which is characteristic of paramagnetic materials. When immersed in a magnetic field, it gets a reversible induced magnetization because the orientation of the magnetic moment of each nano-inclusion acquires a preferential direction along the field. Their magnetization process is illustrated in Figure 1.7. Moreover, inclusions are often embedded in the diamagnetic center of the particle, creating a superparamagnetic core.

A wide range of experimental situations have shown the efficiency to approximate superparamagnetic colloidal particles as spherical dipoles for modelling purposes [19,20,25–28,30,32,34–38]. This means the magnetic dipole  $\vec{\mu}$  is a sufficient parameter to describe every other magnetic property of a given particle. Indeed, spherical dipoles are equivalent to point dipoles [39] and create a magnetic field

$$\vec{B}_\mu = \frac{\mu_0}{4\pi} \frac{3(\vec{\mu} \cdot \vec{e}_r) \vec{e}_r - \vec{\mu}}{r^3}, \quad (1.8)$$

at any point  $\vec{r}$  if the dipole is at the origin  $\vec{r} = \vec{0}$ , with  $\mu_0$  the magnetic permeability of vacuum and  $\vec{e}_r = \vec{r}/|r|$ . It is worth noting that if the dipole is not surrounded by vacuum, this relation remains true if  $\mu_0$  is replaced by the magnetic permeability of the surrounding medium.

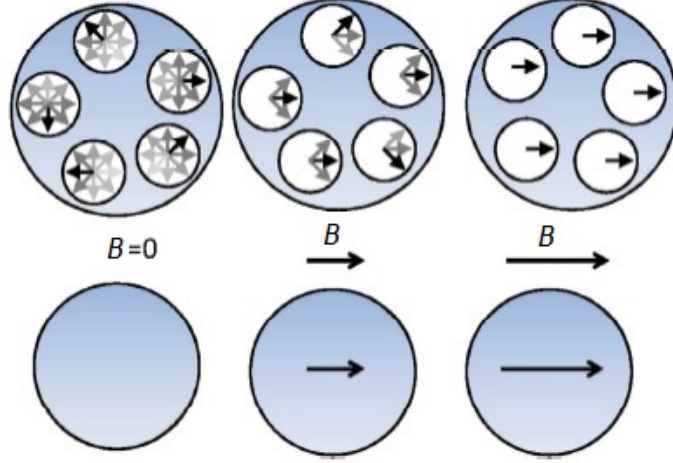


Figure 1.7: Picture modified from [33]. Illustration of the magnetization process of a superparamagnetic particle. The fluctuating magnetic moment of the nanoinclusions are pictured in the above pictures, depending on the external magnetic field  $B$ . The global magnetic moment of the particle is represented by an arrow on the bottom line.

However, common diamagnetic media, such as water and air, have a magnetic permeability close to  $\mu_0$ . It is thus a good approximation to use  $\mu_0$  to compute the field in these media. Any dipole immersed in an external field  $\vec{B}(\vec{r})$  and at position  $\vec{r}$  also has a magnetic energy  $U(\vec{r}, \vec{\mu}) = -\vec{\mu} \cdot \vec{B}(\vec{r})$ . The potential energy of magnetic interaction between two dipoles  $\vec{\mu}_1$  and  $\vec{\mu}_2$  is then given by

$$U(\vec{r}, \vec{\mu}_1, \vec{\mu}_2) = \frac{\mu_0}{4\pi} \frac{\vec{\mu}_1 \cdot \vec{\mu}_2 - 3(\vec{\mu}_1 \cdot \vec{e}_r)(\vec{\mu}_2 \cdot \vec{e}_r)}{r^3}, \quad (1.9)$$

where  $\vec{r}$  is then the vector going from the position of the first dipole to the position of the other one.

By definition, in case of (super-)paramagnetic materials, as long as the amplitude of the external magnetic field  $\vec{B} = B\vec{e}_z$ ,  $\vec{e}_z$  being a unit vector pointing in the direction of  $\vec{B}$ , is under some saturation value, the dipolar moment of a given particle of radius  $R$  can be expressed as

$$\vec{\mu} = \frac{\chi 4\pi R^3 \vec{B}}{3\mu_0}, \quad (1.10)$$

with  $\chi$  the particle susceptibility and  $\mu_0$  the magnetic permeability of vacuum. If the magnetic field  $\vec{B}$  is over that saturation value, the magnetic susceptibility  $\chi$  cannot be considered to be a constant any more. From Eq. (1.10), we can infer that these particles have a magnetic energy  $U_m \equiv -\vec{\mu} \cdot \vec{B} = -\chi 4\pi R^3 / (3\mu_0) \vec{B} \cdot \vec{B}$ , and that they all have a magnetic moment in the direction of the field (unless they have a susceptibility  $\chi \approx 10$ , the field created by the neighbouring dipoles has a negligible amplitude in comparison with the external field). Moreover, from Eqs. (1.10) and (1.8), the potential energy of the magnetic interaction between two particles can be expressed as

$$U(r, \theta) = \frac{\chi^2 4\pi R^6 B^2}{9\mu_0} \left( \frac{1 - 3 \cos^2 \theta}{r^3} \right), \quad (1.11)$$

if  $\theta = \cos^{-1}(\vec{e}_z \cdot \vec{e}_r)$ . Two particles thus tend to attract each other and to create a pair of particles aligned with the external magnetic field  $\vec{B}$ , since the minimum value of their



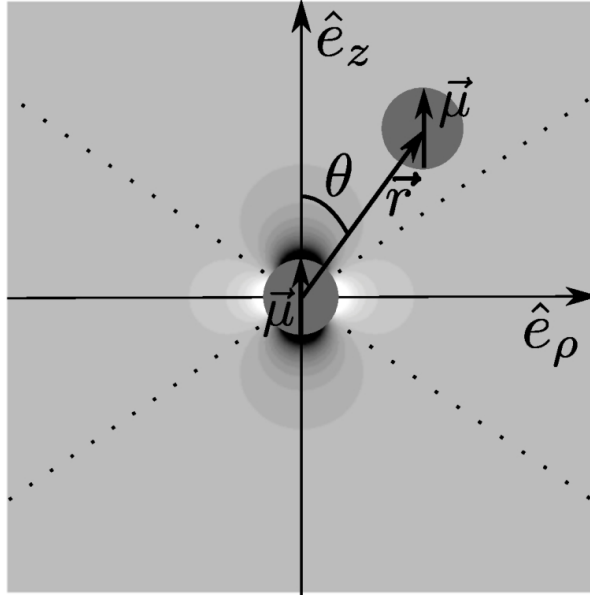


Figure 1.8: Diagram of the magnetic interaction potential. The different parameters of  $U(r, \theta)$  are illustrated in this diagram, and the attractive and repulsive zones of  $\vec{F}_r$  are bounded by the dotted lines. The background shading indicates the value of  $U$  at each point, from black (very negative) to white (very positive). The main gray color denotes a negligible magnetic energy.

interaction energy is reached when  $\theta = 0$  or  $\pi$ , and  $r$  is minimal (i.e.  $r = R$  for solid particles). It is worth noting that the radial part of the magnetic force

$$\vec{F}_r = -\frac{\partial U}{\partial r} \vec{e}_r = \frac{\chi^2 4\pi R^6 B^2}{3\mu_0} \left( \frac{1 - 3 \cos^2 \theta}{r^4} \right) \vec{e}_r \quad (1.12)$$

vanishes if  $\theta = \cos^{-1} 1/\sqrt{3} \approx 55^\circ$  or  $\theta = \cos^{-1}(-1/\sqrt{3}) \approx 125^\circ$  and is repulsive if  $55^\circ < \theta < 125^\circ$ . It is attractive in all other cases. The magnetic interaction potential as well as the attractive and repulsive zones of  $\vec{F}_r$  are illustrated in Figure 1.8.

This interaction notably implies that when two particles are immersed in a constant and uniform magnetic field  $\vec{B}$ , they reach a stable configuration when they touch each other and are aligned with this external field  $\vec{B}$ . This might lead the particles to self-organize into chains aligned with the field [19, 25, 26, 32, 34–37].

When it comes to describing the behaviour of colloidal particles, which are highly sensitive to the thermal agitation, it is convenient to introduce the parameter  $\Gamma$ , which compares the maximal absolute value of magnetic interaction energy with the thermal energy :

$$\Gamma \equiv \frac{-U_m}{k_B T} = \frac{\chi^2 \pi R^3 B^2}{9\mu_0 k_B T} \quad (1.13)$$

where  $U_m = U(2R, 0)$  is the minimum of the magnetic interaction energy, reached when two particles are in contact ( $r = 2R$  in Eq. (1.11)) and they are aligned with the external field ( $\theta = 0$  or  $\pi$ ). Given this definition of  $\Gamma$ , the magnetic interaction energy can be written, from Eq. (1.11),

$$U = -k_B T \Gamma \frac{8R^3}{r^3} \left( 1 - \frac{3}{2} \sin^2 \theta \right)$$

or, when particles are in contact,

$$U = -k_B T \Gamma \left(1 - \frac{3}{2} \sin^2 \theta\right). \quad (1.14)$$

This parameter  $\Gamma$  then gives a quick idea to determine if the magnetic interaction has a significant influence on the system, given its thermal agitation.

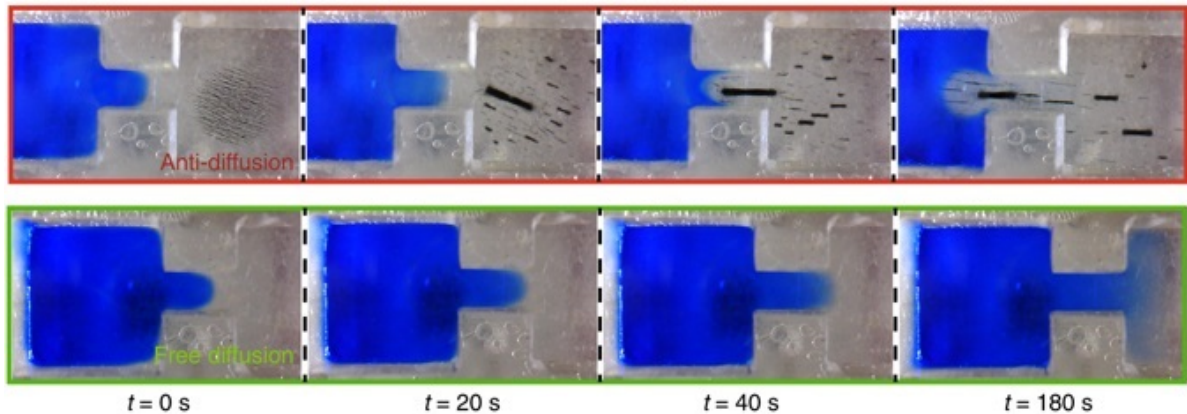


Figure 1.9: Figure from [40]. A magnetically assembled swarm of colloidal particles can be used as a mean to prevent diffusion in a microchannel.

Currently, some research is still performed on the stable assemblies of magnetic dipoles [41–47]. More complex structures of superparamagnetic colloids can also be obtained by using rotating fields, even possibly leading to microswimmers or tracers of local dynamics [38, 48–57]. Those complex structures open ways to new kind of applications as they have unique optical properties and offer tunable structures able to adapt to their environment and execute functional tasks [38, 40, 50, 53]. An example of such flexible self-assembled structure is presented in Figure 1.9. The next section describes the basic notion of self-assembly dynamics for the simplest configuration, i.e. when superparamagnetic colloidal particles are immersed in a constant and homogeneous magnetic field.

### 1.3 Self-assembly dynamics

As explained in the previous section, when paramagnetic colloids are immersed in an external magnetic field  $B$ , they form chains aligned with this external field. This process is illustrated in Figure 1.10. Moreover, this aggregation is reversible meaning that the chains break up if the magnetic field  $\vec{B}$  is suppressed, due to their almost zero remanence [26,54,58]. Experimentally, chains of several particles are typically observed [32,34,36] and the growth is successfully described on short time (typically up to 300s) by a Smoluchowsky equation, predicting a power law behavior of the mean size of the chains  $\langle s \rangle \propto t^z$  after a transient behavior [32,34–37]. Such chains can be useful in applications since they enhance the magnetophoresis of the particles, as illustrated in Figure 1.11 [19,20].

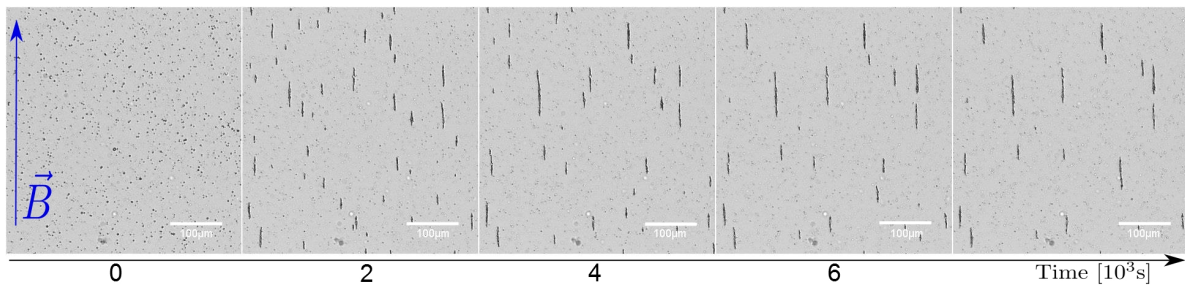


Figure 1.10: Pictures of the formation and growth of chains of superparamagnetic colloids immersed in a magnetic field. Images were obtained with a reversed optical microscope with transmitted light and a 10X lens.

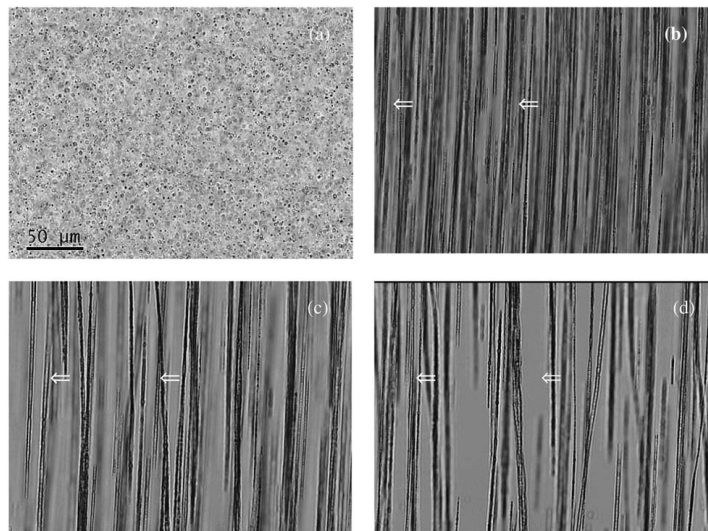


Figure 1.11: Pictures from [19]. Magnetophoresis of chains of colloids in an inhomogeneous field from a permanent magnet. The chains are aligned with the local direction of the field, but drift in the direction of the field gradient. The time between each picture is 120 s, the first picture being taken when the magnet is placed close to the suspension. A video of the process is available at <http://www.youtube.com/watch?v=MyTXFOSPWTU> [19].

The usual Smoluchowsky equation is written by assuming that particles are irreversibly

aggregating [26,32,34,36]. It is then obtained

$$\frac{dA_s}{dt} = \frac{1}{2} \sum_{i+j=s} K_{ij} A_i A_j - A_s \sum_{j=1}^{+\infty} K_{sj} A_j, \quad (1.15)$$

where  $A_s$  is the number of chains with length  $s$  and  $K_{ij}$  is the aggregation rate of a  $i$ -length chain with a  $j$ -length chain. This parameter  $K_{ij}$  is also called the reaction kernel. The first term in the above equation represents the aggregation of two smaller chains into a chain with length  $s$ . The second is related to the aggregation of such chains with others. This equation only takes into account binary aggregation and is therefore only valid for low concentration of particles. In order to solve this equation, one has first to find the expression of the  $K_{ij}$  as a function of  $i$  and  $j$ . It has been solved for spherical particles with radii  $r_i$  and  $r_j$  which are freely diffusing and aggregate when they come into contact. In this case, the reaction kernel is written

$$K_{ij} = 4\pi(r_i + r_j)(D_i + D_j),$$

where  $D_i$  is the diffusion coefficient of a sphere with radius  $r_i$  [36]. That kernel is called the Brownian kernel. It is the usual starting point for theoretical development aiming to determine  $K_{ij}$  in the case of superparamagnetic colloids [26,32,37], which are not spherical any more when  $s > 1$  and have an anisotropic interaction along diffusion. It is commonly assumed in theoretical models that particles and chains can only aggregate from tip-to-tip, since the magnetic interaction is only attractive if particles are more or less aligned with the magnetic field, as expressed in Equation (1.12). Then, the chains keep the same cross-section as the particles regarding aggregation. From there, the kernel dependency regarding the length of the chains is only related to their diffusion coefficient. If one assumes this dependency has the form  $D_i \propto i^\gamma$ , it implies  $K_{ij} \propto i^\gamma + j^\gamma$ . In this case, at long time scale, the mean length of the chains  $\langle s \rangle$  evolves as

$$\langle s \rangle \propto (t/t_B)^z, \quad (1.16)$$

with the time  $t$ ,  $t_B$  a characteristic time scale and  $z = \frac{1}{1-\gamma}$  [35]. Such a behaviour has been observed both numerically [37] and experimentally [26,32,36]. Experimentally, values of  $z$  are obtained between  $z = 0.4$  and  $z = 0.8$ . Those values vary with the system's dimension (2D or 3D). It seems that it also depends on the volume fraction of the particles  $\phi$  and the parameter  $\Gamma$  [32,36]. The most recent and efficient scaling for the characteristic time  $t_B$ , in the case of diffusion-limited aggregation, is given by [32,33]

$$t_B = \frac{6\pi\eta R^3}{24 [(1/3)^{1/2} - (1/3)^{3/2}] U_m \phi}. \quad (1.17)$$

The previous developments successfully model a wide range of situations on a time scale of several minutes. However, those chains do not grow forever and become arbitrarily long. Indeed, after some time, due to the competition between magnetic attraction and the mixing entropy of the system, which tends to maximize the number of various chains, the suspension should reach a thermodynamic equilibrium characterized by a minimum of the free energy of the system. [33] The next section introduces the notions required to model this equilibrium.

## 1.4 Self-assembly equilibrium

While the previous studies have explored the kinetics of the formation of chains of superparamagnetic colloids, only a few works have been performed on their thermodynamics. This is although particularly relevant, since it has been predicted that self-assembled chains of superparamagnetic colloids should reach a state of thermodynamic equilibrium [19,25]. Indeed, it has been shown numerically that the mean size of the chains  $\langle s \rangle$  saturate after some time, as illustrated in Figure 1.12. The equilibrium value of this parameter  $\langle s \rangle$  depends on various parameters that Faraudo *et al.* modeled based on some thermodynamic considerations. This section describes the basic notions and equations to understand their model and its limitations. More detailed demonstrations can be found in Appendix A.

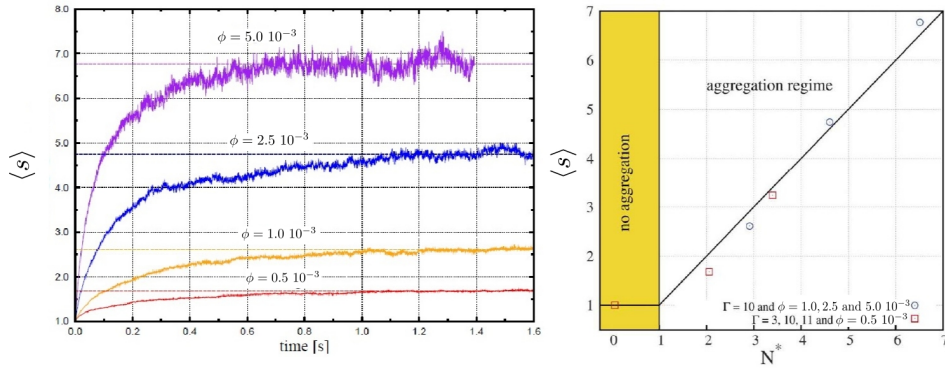


Figure 1.12: Pictures modified from [25] and [19]. Left: illustration of the saturation of the mean length of the particles  $\langle s \rangle$  along time. Right : evolution of the mean length of the chains at equilibrium as a function of the predicted length  $N^* = \sqrt{\phi_0 \exp(\Gamma - 1)}$ .

When particles are mixed in a fluid and can form linear agglomerates, the chemical potential  $\mu_s$  of a particle in a chain of size  $s$  can be written as [9,25]

$$\mu_s = \frac{1}{s} \left[ k_B T \ln \left( \frac{\phi_s}{s} \right) - (s-1)\epsilon_m \right] + \mu^0, \quad (1.18)$$

where the first term comes from the mixing entropy, and the second is due to the binding energy between two particles. Each bond between the constituting particles is considered to be  $-\epsilon_m$ , and it is assumed the particles only interact with their first neighbour. The term  $\mu^0$  represents the other possible contributions and is often considered as not depending on  $s$  (see Appendix A for more details). The thermodynamic equilibrium is characterized by the equality of all the chemical potential, then  $\mu_1 = \mu_s, \forall s \in \mathbb{N}_0$ . Moreover, the total volume fraction of the particles  $\phi_0$  being constant (i.e. the volume fraction of single particles before agglomeration arises), if one defines  $\phi_s$  as the volume fraction of the chains of length  $s$ , we can write this constraint as  $\phi_0 = \sum_{s=1}^{\infty} \phi_s$ . These two constraints, with a few approximations, lead to a value of

$$\langle s \rangle \approx \sqrt{\phi_0 \exp(\Gamma - 1)}. \quad (1.19)$$

To write this, it has been assumed that the binding energy  $\epsilon_m$  is the mean magnetic energy of two particles in contact which can be averaged as  $\beta\epsilon_m \equiv \Gamma - 1$ , where  $\beta = (k_B T)^{-1}$ . This model has been tested by Faraudo *et al.* on various conditions [19,25,33]. Their main results are illustrated in Figure 1.12.

## 1.5 General motivations and open questions

As we described it previously, complex structures of superparamagnetic colloids can lead to various applications such as microswimmers or tracers of local dynamics [38, 48–57]. The originality of those applications arises from the unique optical properties and tunability of the structures which are able to adapt to their environment and execute functional tasks [38, 50, 53]. However, the previous studies about those complex structures focused on their properties, without having a deep understanding of their formation process. The only system for which some model of growth has been published in the literature is the colloidal chains formed under constant magnetic fields.

Regarding this particular system, on one hand, the early self-assembly dynamics of superparamagnetic colloids under constant magnetic field has been extensively studied, with both experimental measurements and numerical simulations [26, 32, 34–37]. On the other hand, when we began this thesis, the thermodynamic equilibrium reached by this system had been tested numerically extensively by their authors [25]. No experimental measurements had systematically tested it. Since this model predicts a completely different behaviour than the previous studies, a complete and systematic experimental characterization of this equilibrium seemed necessary in order to confirm the model and the simulations results. This statement was even more critical since the situations with high total volume fraction  $\phi_0$  were still problematic to explore numerically [33]. Indeed, the high number of particles involved made the computing time extremely long... The only way to circumvent this difficulty was to consider that the agglomeration of a particle with chain is irreversible, then decreasing the number of objects to simulate along time. However, this is fundamentally incompatible with the definition of a dynamic equilibrium, where links between particles are supposed to be created and destroyed at the same rate. The previous hypothesis would then only allow zero rates of creation and destruction. Those rates corresponds only to the case where a high magnetic field (implying a quasi-zero destruction rate) is applied on a very dilute suspension (implying a quasi-zero creation rate), which is limiting.

There was then a call for more complete description and an experimental characterization of colloidal chains formed under constant magnetic fields. Indeed, we needed to consolidate our knowledge about this model system, and this could lead to some unexpected discoveries. Moreover, it was a first step into achieving a deep understanding of the more complex systems used in applications.

## 1.6 Personal contribution

The first part of our work, presented in this manuscript, focuses on an experimental study of this thermodynamic equilibrium. We first present and discuss some systematic experimental measurements in Chapter 4 [59], and report some deviations of experimental measurements with the current model. We then introduce a viscosity scaling of the dynamics of the system, and show how it can be used to accelerate high volume fraction simulations in Chapter 5 [60]. We then present some numerical and experimental measurements on the equilibrium reached in this condition. We show that it is interesting to consider interactions between the formed aggregates to have a more accurate model, and we proposed a modification of the analytical model in Chapter 6 [61].

## Chapter 2

# Evaporative deposits

The evaporation of colloidal droplets is an omnipresent phenomenon around us. From the stain of spilled coffee on our kitchen tables to the painting of our offices walls, via blood stains on a crime scene, there are numerous cases where droplets of colloids fall around and dry, leaving their solid content on a substrate once all the liquid is evaporated. Sometimes, we consider the left pattern as pollution or waste, as for the example of the coffee stain on the kitchen table. On other situations, it is used in application as when it comes to painting, possibly on micro- or nano-scales [62,63]. In the case of blood droplets, it is a source of information on crime scenes [64,65], and is foreseen as a possible diagnostic tool [66,67]. For these reasons, and many others, the evaporation of sessile colloidal droplets is currently a topic of intense research [68–75]. This chapter introduces some generic phenomena which occur in evaporating colloidal droplets.

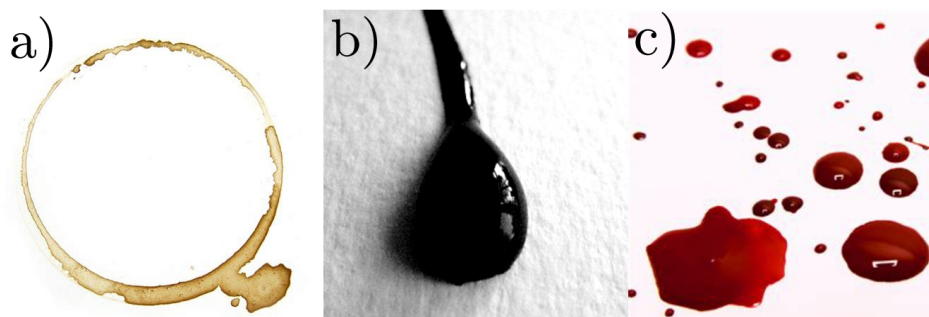


Figure 2.1: Example of evaporating colloid droplets/deposits. a) A coffee stain made by a mug has dried out and left a characteristic stain on the substrate. One can see that the borders of the stain are darker than its centre. b) A drop of Chinese ink is drying on a paper surface. c) Droplets of blood have been spilled out on a flat surface and are evaporating.

### 2.1 Coffee-Ring

One of the most abundant phenomena in evaporating droplets of colloids is the so-called "coffee-ring" effect [76]. This nickname emphasizes the fact that particles tend to migrate to the edge of an evaporating droplet, leading to a ring-like deposit, which is typically observed in everyday coffee stains, as illustrated in Figure 2.2. The first model of this phenomenon is usually attributed to Deegan *et al.* [77, 78]. Their model states that a global current exists in the droplet, from the centre to the edge. This current results from the combination of three main phenomena. Firstly, the evaporation rate at the surface of the droplet is not homogeneous. If it is determined by the diffusion of water vapor from the droplet to a distance far from its surface, the evaporation rate is indeed higher at the edge of the droplet due to its geometry. Secondly, the contact line tends to be pinned on the substrate at the beginning of the evaporation. This is even reinforced by the colloidal particles deposited at that location. Thirdly, the shape is fixed by the surface tension, i.e. a spherical cap for small droplets (smaller than the capillary length). The uneven distribution of the evaporation rate, if the liquid was not moving, would

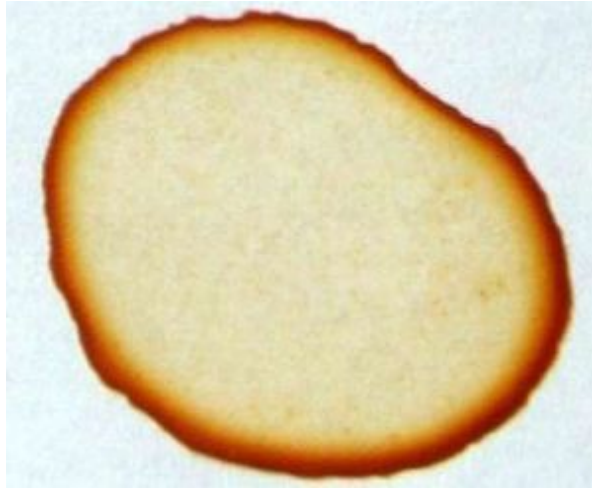


Figure 2.2: Illustration of the typical deposit left by an evaporated droplet of coffee. As can be seen, the edge of the droplet is darker than the centre, showing that most of the colloidal particles are located in the border of the droplet.

create a kind of a bell shape. The surface tension then induces outward flows in order to keep a spherical cap shape, with a fixed edge. This process is illustrated in Figure 2.3. This flow then pushes the particles to the edge of the droplet, where they are deposited.

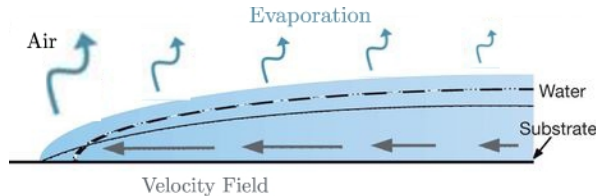


Figure 2.3: Illustration of the mechanism leading to the coffee ring. The evaporation rate at the surface of the droplet is represented by blue arrows. After a while, the resulting shape of the droplet, if the liquid was not moving, is given by the dashed line. The solid line gives the actual new surface of the droplet, as the liquid moves accordingly to the grey horizontal arrows. Figure modified from [79].

Deegan *et al.* also performed a series of original experiments with droplets confined in various geometries of boxes. [78] Those boxes were designed to modify the spatial dependency of the evaporation rate at the surface of the droplet. They then showed that the deposit depends on the evaporation rate's profile and intensity. In order to study systematically the evaporation of droplet, one has then necessarily to design an evaporative chamber. Such a chamber not only determines the spatial dependency of the evaporation rate, but also ensures that no air stream is modifying the transport of the water vapour. Indeed, such air stream would also modify the evaporation rate. Moreover, the concentration of water vapour in the air surrounding the droplet also determines the evaporation rate and then the velocity of the fluid and the suspended particles. The air humidity is then another crucial parameter of the system.

While the pioneer work of Deegan *et al.* modelled the mean outward flows in an evaporating sessile droplet, an analytical equation describing the entire velocity field has been developed by Hu and Larson [80]. Namely, they describe the radial component of the velocity field



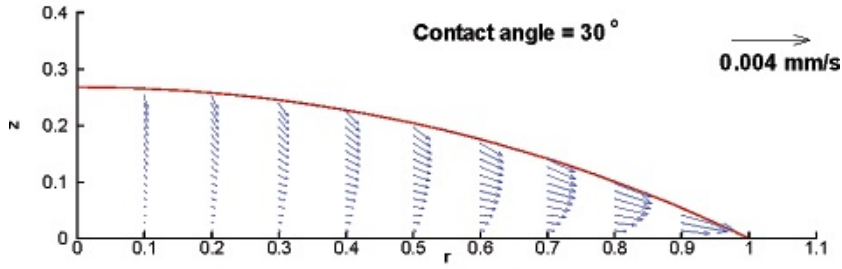


Figure 2.4: Picture modified from [80]. Velocity field inside an evaporating sessile droplet, as computed by Hu and Larson, in agreement with their analytical solution. [80] The outward flow is responsible for the coffee-ring effect by advecting the colloidal particles to the edge of the droplet.

$u_r = \tilde{u}_R R_d / t_f$  as

$$\tilde{u}_r = \frac{3}{8} \frac{1}{1 - \tilde{t}} \frac{1}{\tilde{r}} \left[ (1 - \tilde{r}^2) - (1 - \tilde{r}^2)^{-\lambda(\theta)} \right] \left( \frac{\tilde{z}^2}{\tilde{h}^2} - 2 \frac{\tilde{z}}{\tilde{h}} \right) + \frac{\tilde{r} h_0^2 \tilde{h}}{R_d^2} \left( 1 + \tilde{J}(0, t) \lambda(\theta) (1 - \tilde{r}^2)^{-\lambda(\theta)-1} \right) \left( \frac{\tilde{z}}{\tilde{h}} - \frac{3\tilde{z}^2}{2\tilde{h}^2} \right), \quad (2.1)$$

where  $\tilde{t} = t/t_f$  is the dimensionless time  $t$  divided by the total time of evaporation  $t_f$ ,  $\tilde{r} = r/R_d$  is the dimensionless radial coordinate  $r$  divided by the contact radius of the droplet  $R_d$ . The dimensionless vertical coordinate  $\tilde{z} = z/h_0$  is the ratio between the vertical coordinate  $z$  and the initial height of the droplet and the centre  $h_0$ , while the parameter  $\lambda(\theta) = 0.5 - \theta/\pi$  is a function of the contact angle  $\theta$ . The dimensionless evaporation rate  $\tilde{J} = J(0, \theta)/(\rho h(0, t))$  is the evaporation rate at the centre of the droplet  $J(0, \theta)$  over the current height at the centre of the droplet  $h(0, t)$  and the fluid density  $\rho$ . The evaporation rate  $J(0, \theta)$  can be approximated as of function of the contact angle as

$$J(0, \theta) = \frac{D c_v (1 - H)}{R_d} (0.27\theta^2 + 1.30) (0.6381 - 0.2239(\theta - \pi/4)^2), \quad (2.2)$$

where  $D$  is the water vapour diffusivity,  $H$  the humidity of the evaporation chamber and  $c_v$  the saturation value of the vapor concentration (so that the vapour concentration far the droplet is  $H c_v$ ). It is interesting to notice that, when the height  $h(0, t) \equiv h$  of the droplet tends to zero, one can determine a scaling of this radial velocity. Indeed, for any fixed coordinate  $\tilde{r}$  and  $\tilde{z}$ , and assuming we are in a linear regime for the decrease of the volume (with  $R_d \gg h$ ), which is often the case [72, 80] (i.e.  $1 - \tilde{t} = \tilde{h}$ ), the dominating term (the first one) in Eq. (2.1) goes like  $\tilde{h}^{-3}$ . This gives a scaling of  $u_r \propto \frac{h_0^3 R_d}{h^3 t_f}$ .

However, even if this coffee-ring effect is omnipresent, various other phenomena can occur in an evaporating droplet and modify its eventual deposit. The next section describes what happens when a gradient of surface tension creates some Marangoni recirculation.

## 2.2 Marangoni

When a droplet of pure liquid is evaporating, the evaporation process consumes some energy. Actually, a heat flux  $J_h$  is associated to the mass flux  $J$  through the latent heat of evaporation  $H_W$  :  $J_h = H_W J$ . This heat flux  $J_h = -k\vec{\nabla}T$ , from Fourier's law, then induces a variation of the surface temperature of the droplet. In turn, this change of temperature can induce a variation of surface tension, then leading to a surface stress along the interface of the droplet, creating so-called Marangoni flows.

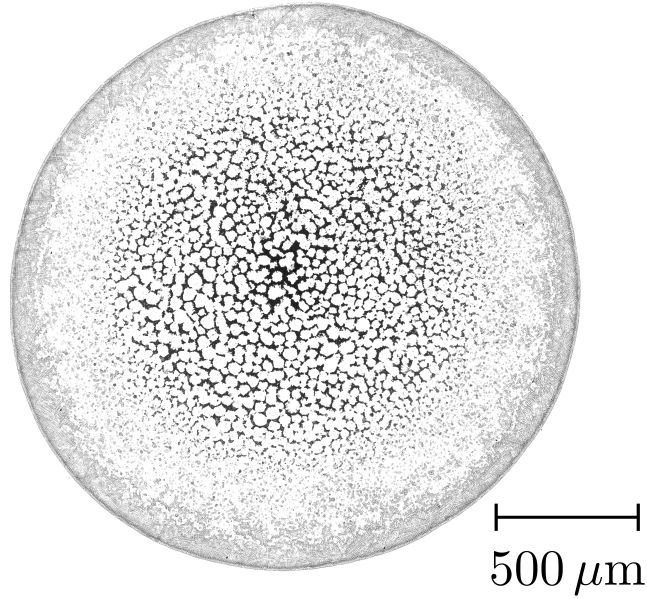


Figure 2.5: Deposit obtained from reversed sessile drop (i.e. a droplet suspended on the bottom side of a glass plate). The honey-comb like pattern is generated by the recirculation cells of a Marangoni instability. Particles trapped at the interface (due to gravity) are located at the location where the velocity of the fluid goes up, inward the droplet. The initial suspension was PBS diluted to volume fraction  $5 \cdot 10^{-2}$  with volume fraction  $5 \cdot 10^{-4}$  of M1-070/60 particles from Estapor.

The importance of the surface tension stress compared to the viscous dissipation leads to the dimensionless Marangoni number  $Ma$ , which is written in our case [81, 82]

$$Ma = -\frac{d\sigma}{dT} \frac{\Delta T_0 t_f}{\eta R_d}, \quad (2.3)$$

where  $\sigma$  is the surface tension of the fluid,  $\Delta T_0$  is the difference between the temperature at the edge  $T_e$  and at the top center  $T_c$  of the droplet (the top is usually colder since the substrate heats the edge), and  $\eta$  is the viscosity of the fluid. Taking into account this additional stress at the surface of the droplet, Hu and Larson derived an additional term in the velocity field of Eq. (2.1) [81, 82]

$$\tilde{u}_{r, Ma} = \frac{Ma h_0 \tilde{h}}{4R_d} \frac{d\tilde{T}}{d\tilde{r}} \left( 2 \frac{\tilde{z}}{\tilde{h}} - 3 \frac{\tilde{z}^2}{\tilde{h}^2} \right), \quad (2.4)$$

where  $\tilde{T}$  is the dimensionless temperature defined as the ratio  $\tilde{T} = (T - T_c)/(T_e - T_c)$ . When  $h$  tends to zero, at fixed  $\tilde{z}$ ,  $\tilde{r}$  and  $\frac{d\tilde{T}}{d\tilde{r}}$ , the last term is dominating and the radial velocity due to Marangoni stress scales as  $u_{r, Ma} \propto Mah_0^2/(ht_f)$ .

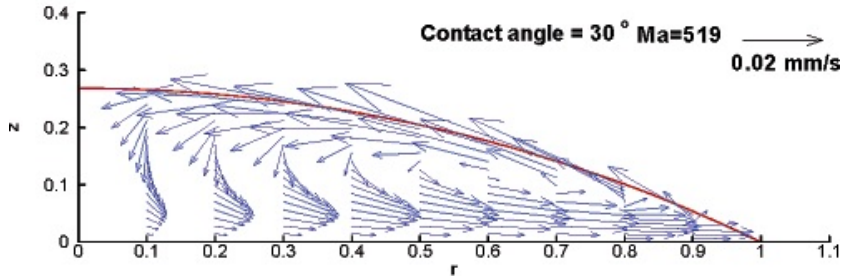


Figure 2.6: Picture modified from [81]. Velocity field inside an evaporating sessile droplet, as computed by Hu and Larson, in agreement with their analytical solution taking into account the thermal Marangoni stress. [81] A strong recirculation flow is observed near the surface. This recirculation can prevent the apparition of the coffee-ring deposit [82].

Besides the temperature, any tensioactive agent in the droplet can create a Marangoni stress. The first publication of Hu and Larson showed that such surfactant could counter-balance the thermal Marangoni stress. [81] However, several studies have also shown that those tensioactive Marangoni stress could also create a Marangoni stress leading to a recirculation or even a Marangoni *instability*, where several recirculation cells appear on the radius length. [83–86] Typical patterns obtained in these conditions are shown in Figures 2.7 and 2.5, and are typically observed for Marangoni numbers of at least  $10^2$  of magnitude order.

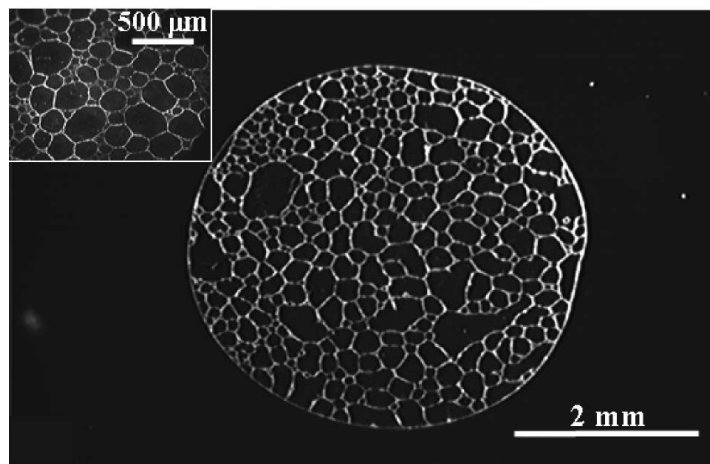


Figure 2.7: Picture modified from [86]. Deposit left after evaporation of a droplet of HCl suspensions containing 0.01% solid w/v of microspheres, covered by an insoluble monolayer of pentadecanoic acid. The hexagonal pattern comes from Marangoni(-Bénard) instability flows due to Marangoni stresses.

Another feature which can be created by Marangoni recirculation is the so-called Marangoni eddy, previously described by Still *et al.* [84]. Actually, the Marangoni recirculation near the edge of the droplet and can rearrange a part of the particles from the coffee-ring. This creates a secondary peak of density in the deposit, a bit further from the edge. That secondary peak is called the Marangoni eddy. This pattern and its creation process are illustrated in Figure

2.8.

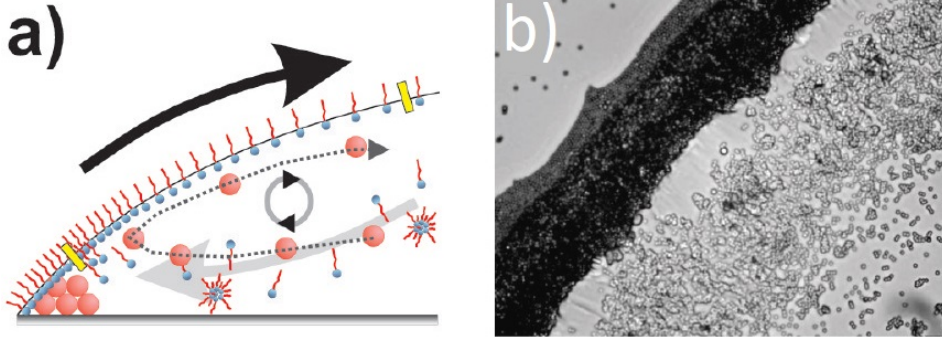


Figure 2.8: Picture modified from [84]. Picture *a* : Scheme of the mechanism creating the Marangoni eddy. In this set-up, the surface tension gradient is due to accumulation of surfactant at the interface. Picture *b* : actual deposit left after evaporation. A less dense ring of colloids is observed below the coffee-ring.

The coffee-ring mechanism and the Marangoni stress allow to understand the fluid flow inside most of the evaporative droplets. However, the deposition of solid colloidal particles on a substrate highly depends on the interaction between these particles and this substrate. The next section describes the basic notions about how DLVO interactions between a substrate and the suspended particles influence the eventual deposit.

### 2.3 Substrate

The interactions between the particles and the substrate also play a key role in the final deposit. [11, 87, 88] Those interactions are usually dominated by the DLVO interaction we introduced in Section 1.1. Given the geometry, the electrostatic interaction  $F_e$  can be written as [9, 11]

$$F_e = -64\pi \tanh\left(\frac{e\psi_0}{4k_B T}\right) \tanh\left(\frac{e\psi_S}{4k_B T}\right) dnk_B T \lambda \exp(z/\lambda) \quad (2.5)$$

with previously defined notations, and  $\psi_S$  is the surface potential of the substrate,  $n$  is the number of counterions (molecules by  $\text{m}^3$ ),  $z$  is the interdistance between the substrate and the particle,  $k_B$  is the Boltzmann constant,  $T$  the temperature and  $d$  is the particle's diameter. It is then highly depending on the global ions concentration (through  $n$  and  $\lambda$ ). For particles covered by carboxyl termination (or other  $H^+/OH^-$  releasing or adsorbing groups), the pH also modifies this force, through  $\lambda$  and the surface potential of the particles.

Several authors have shown that modifying this interaction, through salt concentration or modification of the pH, could lead to some transition from coffee-ring deposit to uniform deposit. [11, 87, 88] Intermediate results where a coffee-ring is observed with some particles sticking in the centre of the deposit have been observed too. [87, 88] The detailed morphological properties of those deposits can also be influenced by both of those parameters, creating a way to obtain amorphous or highly ordered hexagonal networks in the deposit. [88]

Bhardwaj *et al.* introduced the idea that the eventual deposit properties should rely on the competition of the three mechanisms we have introduced so far. They summed up their conclusion through a phase diagram (Fig.2.9). However, they were only able to test this diagram on the axes, meaning that the intermediate states and transition between the various deposit structures have not been completely described yet.

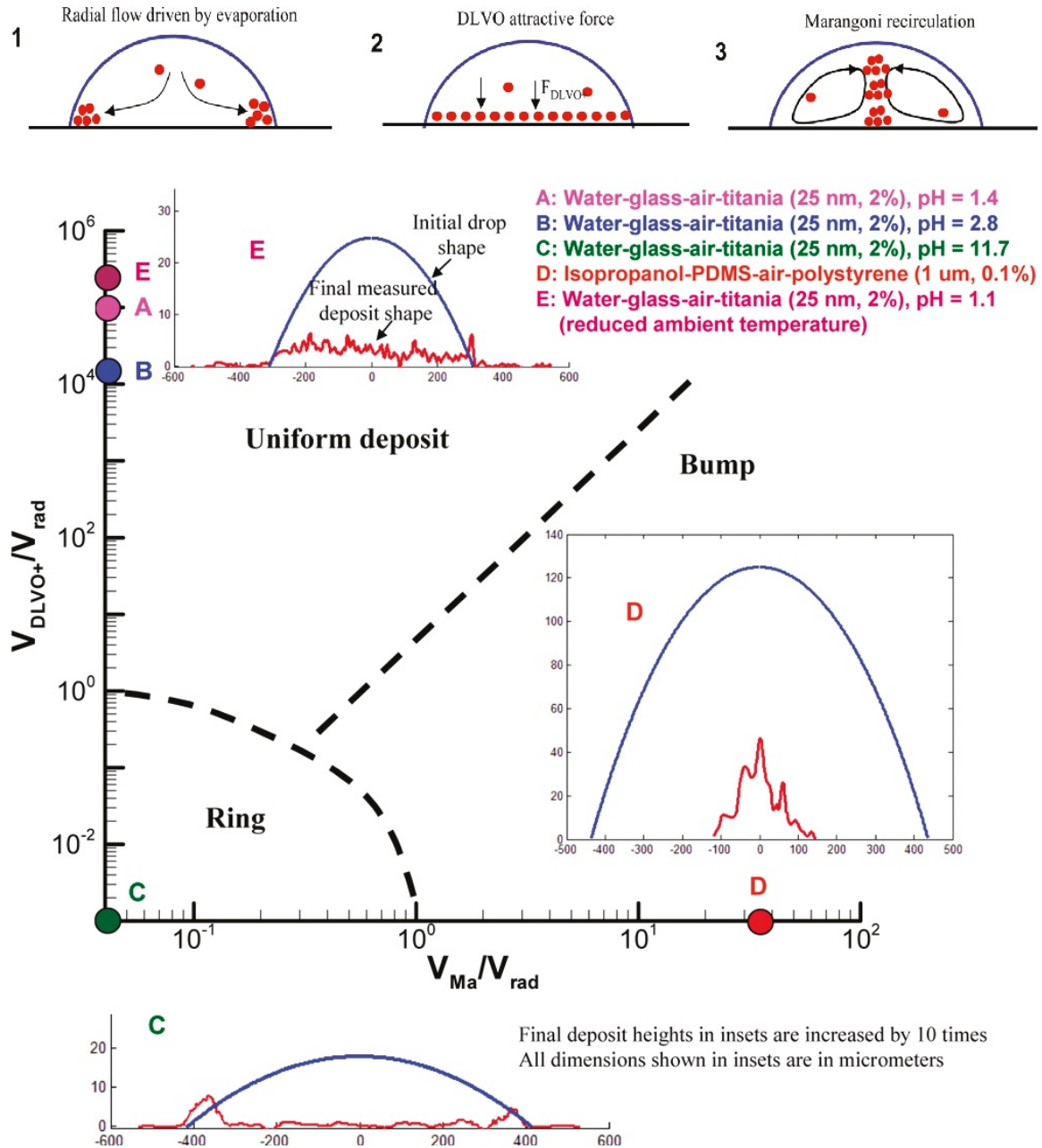


Figure 2.9: Picture modified from [11]. On top : mechanisms highlighted by Bhardwaj *et al.* and their associated final deposits. Below : phase diagram proposed by Bhardwaj *et al.* to explain the various final deposits shapes. With our notations, the scaling they proposed of the various velocities are written  $V_{rad} \propto J/\rho$ , where  $J$  is an average of the evaporation rate,  $V_{DLVO} \propto F_e/(6\pi R\eta)$  and  $V_{Ma} \propto (1/32) \left( \frac{d\sigma}{dT} \theta^2 \Delta T/\eta \right)$ .

## 2.4 General motivations and open questions

As we stated at the beginning of this Chapter 2, the range of applications and use of colloidal deposits is really broad [62–75]. But up to now, research on the evaporative deposits of colloidal droplets has tended to comprehend or control their properties through the composition of the suspension. This composition has indeed a lot of implications regarding the Marangoni stress and the DLVO interactions. While this is already very interesting, it might also be a bit limiting. Indeed, that would mean that each given application requires a specific suspension.

A way to circumvent this limitation is to use a remote control which could change the properties of the suspension. The main objective of our work is then to understand what influence the self-assembly of superparamagnetic colloids can have on the final deposit. Indeed, a significant influence of magnetic self-assembly would mean that the magnetic field could be used as a remote control of the evaporative deposit.

Moreover, this gives us a simple probe to characterize the influence of interactions between the particles on the substrate, without modifying any other parameter. This then enables us to describe systematically and in more details how the previous mechanisms, coffee-ring effect, Marangoni stress and substrate interactions, interact with each other to create the deposit structure.

## 2.5 Personal contribution

In this manuscript, the part dedicated to evaporation begins by studying more in detail the dynamics of the competition between Marangoni and coffee-ring mechanisms in Chapter 7 [89]. We show that an evaporating droplet actually contain various regimes transitions and that these regime have an determining leverage on the deposit. We then introduce how self-assembly can influence the deposit properties, in appropriate conditions for effective DLVO interactions in Chapter 8 [90]. We show that self-assembled structures can be deposited almost as is in on the substrate, which opens new ways to manufacture micro-texturing. We then conclude by proposing a model for the shape of the deposit density depending on the strength of the three mechanisms with Chapter 9 [91]. In this model, the external magnetic field appears as a remote control which can enhance the homogeneous deposition caused by DLVO interactions.

# Chapter 3

## Objectives and plan

As we described in the previous chapters, self-assembly of superparamagnetic colloids and evaporation of colloidal droplets are two areas of intensive research. However, no previous work, to our knowledge, has been studying how those two topics mix together. The main objective of our work is to study how self-assembly of superparamagnetic colloids influences the evaporative deposit of a droplet containing those colloids. In order to do this, one has to describe as accurately as possible the self-assembly of the particles as well as the phenomena occurring during the evaporation of a droplet. Therefore, we also performed experiments describing only the self-assembly or the evaporation of superparamagnetic colloids.

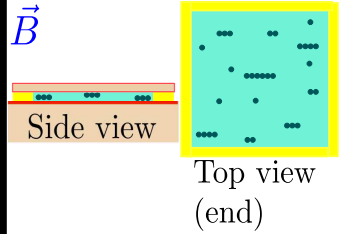
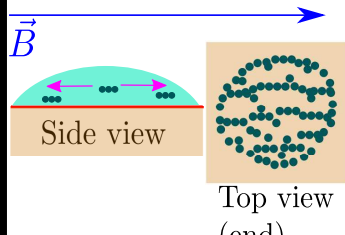
<b>Part II</b>		Chapter 4 Influence of $\vec{B}$
	Chapter 5 Influence of $\eta$	
	Chapter 6 Influence of $\phi$	
<b>Part III</b>		Chapter 7 Influence of flows
	Chapter 8 Influence of $\vec{B}$	
	Chapter 9 Influence of $\vec{B} + \text{PBS}$	

Figure 3.1: Summarized plan of the results Parts of the manuscript. Part II regroups articles describing the influence of various parameters on the airtight suspension, while Part III presents articles about evaporating droplets. Chapters 8 and 9 actually describe the evaporation of droplets containing self-organizing superparamagnetic particles.

For the sake of clarity, the original work of this thesis is then divided in two parts. In the first part, Part II of the manuscript, we describe the experiments performed with an original setup in order to observe experimental realizations of the thermodynamic equilibrium predicted by Faraudo *et al.* in airtight systems. We managed to produce an almost 2D system in order to perform easier and more efficient observations. In this part, we describe the influence of three parameters on the self-assembly and the thermodynamic equilibrium of the superparamagnetic colloids: magnetic field  $\vec{B}$ , viscosity  $\eta$  and volume fraction  $\phi$ . While all Chapters 4,5 and 6 describe the effect of the magnetic field, Chapter 4 describe the widest range of this parameter and how it can leads to unexpected ribbons configurations. Chapter 5

describes how the particles self-organize in suspensions with various viscosities. Experimentally, we prepared suspensions with various glycerol-water mixtures. We also performed numerical simulations with decreased viscosities. Chapter 6 describes how the volume fraction of the particles influences the thermodynamic equilibrium, both through experiments and numerical simulations.

In the second part, Part III of the manuscript, we describe experiments performed within an evaporation chamber where the liquid phase of the suspension evaporates along time. The experiments end with the creation of a static dried deposit. Chapter 7 describes the temporal evolution of the flows in the system thanks to PIV measurements. It also describes the subsequent dried deposit. The next Chapters discuss how interaction between these flows and self-organization leads to various dried deposits. More accurately, Chapter 8 describes the influence of the magnetic field on the final deposit. Finally, Chapter 9 describes the 2D configuration space of the final deposit produced by the interplay of magnetic field and Phosphate Buffered Saline (PBS) concentration. This structure is summarized in Figure 3.1.



## Part II

# Self-Assembly up to thermodynamic equilibrium



# Chapter 4

## Existence of ribbons

### 4.1 Motivations

When we began this thesis, no systematic experiment had been published to confirm the model of Faraudo *et al.*, predicting the mean size  $\langle s \rangle$  of the chains at equilibrium [19, 25, 33]. Since we were going to work under conditions where this equilibrium could potentially be observed, it seemed natural to start our research work by an experimental characterization of this equilibrium.

### 4.2 Setup and methods

We used an inverted microscope to observe a suspension of superparamagnetic colloids. A droplet of the suspension is placed on a glass plate, covered by an epoxy layer except for a central circular region. Some oil is added on the epoxy, to ensure airtightness, before the whole sample is covered with another thin glass plate. An homogeneous and constant magnetic field is then applied on the suspension through a controlled current in a surrounding pair of coils. The whole growth of the chains is recorded with a camera during 5h. The size of the chains along time is determined through image analysis. The average size of the chains at equilibrium is computed through the average value of this mean length during the last thousand seconds.

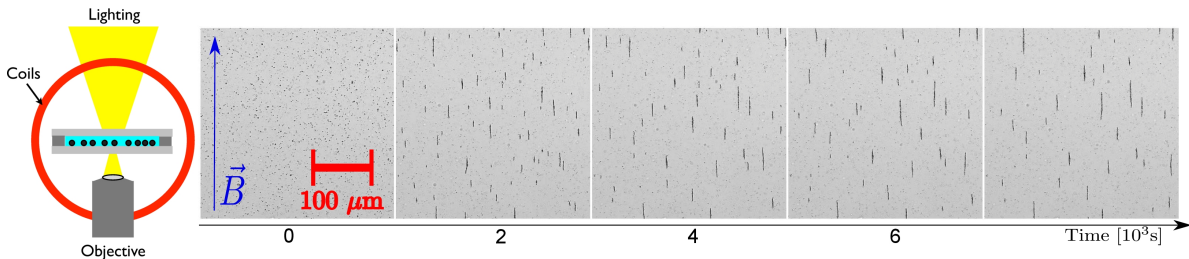


Figure 4.1: Illustration of the experimental set-up, along with some characteristic pictures of the suspension along time. Picture from [59].

### 4.3 Main results

We observed that the previous model was efficient to describe the evolution of the mean length of the chains  $\langle s \rangle$  at equilibrium. However, above a certain threshold value the system reaches lower values than expected. We assume this is due to the existence of ribbons, appearing by lateral aggregation of the chains. In order to support this claim, we computed the energy of several configurations and showed that ribbons were more energetically favourable than chains for aggregates of 30 particles, which gives a consistent critical size of deviation between the model and data, as illustrated in Figure 4.2. Indeed, the model, represented by the black continuous line, systematically overestimates the mean length of the chains once this parameter  $\langle s \rangle$  becomes greater than approximately  $\langle s \rangle = 23$ . This limit value is represented by the horizontal dashed line, and can be understood by comparing the energy of chains and the

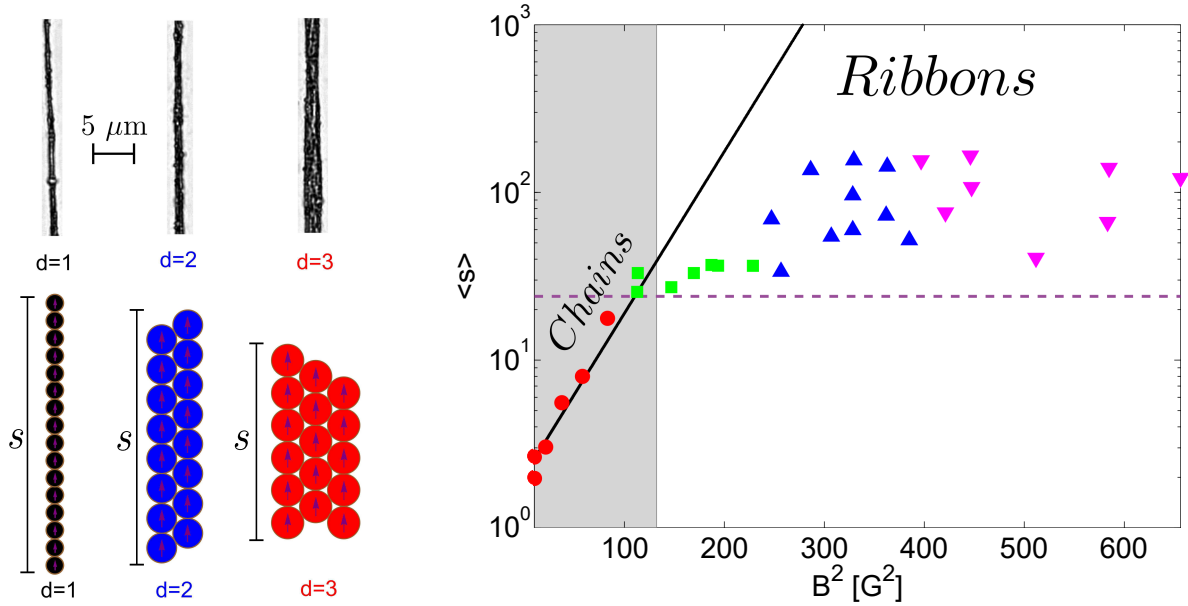


Figure 4.2: Illustration of the main results : the existence of ribbons limits the validity of the theoretical model for the mean length of agglomerates at equilibrium. Picture modified from [59]

energy of ribbons with width  $d = 2$ . Our computations showed that the energy of a ribbons is smaller than a chain for aggregates of 30 particles. Then, when aggregates contain on average 30 particles, there is a mixture of linear chains of 30 particles and ribbons composed of two linear chains of 15 particles. The mean size of those aggregates is then about 23 particles. The Figure 4.2 then summarizes the experimental data we collected and show how it diverges from previously established models.

## 4.4 Conclusion

This first experiment was in agreement with the previous model under a critical value of the magnetic field. However, it also highlighted the importance of the apparition of more complex structures on the system's global properties.

## 4.5 Credits

The paper in the next pages is included in this thesis with kind permission of The European Physical Journal (EPJ). Reference of the original paper is [59].

# Ribbons of superparamagnetic colloids in magnetic field

A. Darras<sup>1,2,a</sup>, J. Fiscina<sup>3</sup>, M. Pakpour<sup>1</sup>, N. Vandewalle<sup>1</sup>, and G. Lumay<sup>1</sup>

<sup>1</sup> GRASP - Physics Department, University of Liège, B-4000 Liège, Belgium

<sup>2</sup> F.R.S.-FRNS, B-1000 Bruxelles, Belgium

<sup>3</sup> Experimental Physics, Saarland University, D-66123 Saarbrücken, Germany

Received 21 December 2015 and Received in final form 26 February 2016

Published online: 27 April 2016 – © EDP Sciences / Società Italiana di Fisica / Springer-Verlag 2016

**Abstract.** While the aggregation process of superparamagnetic colloids in strong magnetic field is well known on short time since a few decades, recent theoretical works predicted an equilibrium state reached after a long time. In the present paper, we present experimental observations of this equilibrium state with a two-dimensional system and we compare our data with the predictions of a pre-existing model. Above a critical aggregation size, a deviation between the model and the experimental data is observed. This deviation is explained by the formation of ribbon-shaped aggregates. The ribbons are formed due to lateral aggregation of chains. An estimation of the magnetic energy for chains and ribbons shows that ribbons are stable structures when the number of magnetic grains is higher than  $N = 30$ .

## 1 Introduction

Superparamagnetic colloids are magnetic nanoparticles inserted in a matrix of non-magnetic material (polystyrene or silica) to obtain particles with diameter  $d$  ranging from 100 nm to a few micrometers. These composite particles are combining a quasi-zero remanent magnetization and a high magnetic response [1–3]. In applications, the superparamagnetic colloids are functionalized to capture specific targets. After the capture, an inhomogeneous external magnetic field is applied to separate the superparamagnetic particles by magnetophoresis [4]. Moreover, the formation of chains along the magnetic field enhances the separation process. This technique is used for protein isolation, cell separation, waste capture, bacteria processing, chromatography, etc. [1, 5–14]. More complex structures of superparamagnetic colloids can be obtained by using rotating fields, even possibly leading to microswimmers or tracers of local dynamics [15–25]. Those complex structures open ways to new kinds of applications as they have unique optical properties and offer tunable structures able to adapt to their environment and execute functional tasks [17, 18, 21]. However, the previous studies about those complex structures focus on the properties of the structures obtained, without having a deep understanding of their formation process. The only system for which some model of growth has been published in the literature is the colloidal chains formed under constant magnetic fields.

In colloidal science, it is well known that particles tend to agglomerate due to van der Waals interactions [26, 27].

In the present experiments, this agglomeration is prevented by covering the particles with carboxyl charged groups. These charged groups create a short range repulsion between the particles, typically within a range of 10 nm between the particles [2, 28]. This ensures the stability of the dispersion. In the following, this electrostatic interaction is considered to define an effective size of the particles for the contact of particles which is 10 nm wider than the natural size of the particles [1]. However, when an external magnetic field  $\mathbf{B}$  is applied on the suspension, the superparamagnetic particles acquire a magnetic dipole  $\boldsymbol{\mu} = \chi V \mathbf{B}$ , with the magnetic susceptibility  $\chi$  of the particles and their volume  $V = \frac{4}{3}\pi R^3$ , given their radius  $R$ . The particles then interact with each other through dipolar interactions. The potential energy of magnetic interaction between two identical particles at distance  $r$  is therefore given by

$$U(r, \theta) = \frac{\chi^2 4\pi R^6 B^2}{9\mu_0} \left( \frac{1 - 3 \cos^2 \theta}{r^3} \right), \quad (1)$$

with  $\theta$  being the angle between the magnetic field  $\mathbf{B}$  and the line joining the center of the particles. Two particles then attract when they are aligned with the field  $\mathbf{B}$ , while they repel each other if they are side-by-side. This interaction implies that two particles tend to aggregate in a chain aligned with the magnetic field  $\mathbf{B}$ . Several studies, both experimental and theoretical, have shown that superparamagnetic colloids self-organize into chains under those conditions [10, 29–33]. Moreover, this aggregation is reversible meaning that the chains break up if the magnetic field  $\mathbf{B}$  is suppressed. Experimentally, chains of several particles are typically observed [29, 30, 32] and the

<sup>a</sup> e-mail: alexis.darras@ulg.ac.be

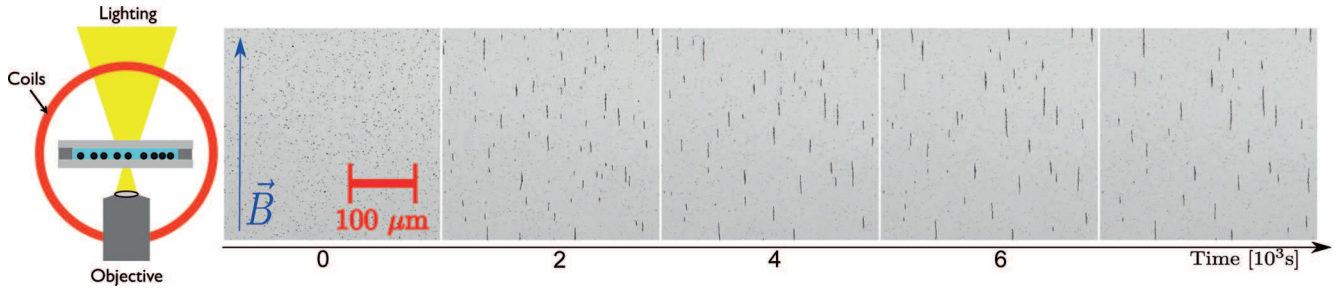


**Fig. 1.** Left: Sketch of the experimental set-up. A transparent chamber containing the colloidal suspension is placed between two coils generating a constant and homogenous magnetic field  $\vec{B}$ . The sample is enlightened from the top and observed from the bottom thanks to an inverted microscope. Right: Evolution of the chains formation along time as observed from one of our experiments. The pictures are part of images obtained with a magnetic field  $B = 6$  G. One can observe the formation of chains aligned with the external magnetic field.

growth is successfully described on short time (typically up to 300 s) by a Smoluchowsky equation, predicting a power law behavior of the mean size of the chains  $\langle s \rangle \propto t^z$  after a transient behavior [29–33].

Recently, Andreu *et al.* [9] have predicted that such a system, in three dimensions, should reach a thermodynamic equilibrium on long-time experiments. The installation of this equilibrium implies a saturation of the mean size  $\langle s \rangle$  of the chains, expressed as a number of particles. This saturation has been predicted by Andreu *et al.* both by numerical simulations and a thermodynamic analysis [1, 9]. The equilibrium results from a competition between the magnetic energy of the particles, which is minimal when all the particles are aggregated, and the entropy of mixing, which is maximized for a mixture of different chains. For three dimensional systems, this competition leads to the expression

$$\langle s \rangle^{(3D)} = \sqrt{\phi_0 \exp(\Gamma - 1)}, \quad (2)$$

where  $\Gamma = \frac{\chi^2 \pi R^3 B^2}{9 \mu_0 k_B T}$  is a dimensionless parameter comparing the magnetic energy with the thermal energy and  $\phi_0$  being the total volume fraction of particles. The particles are assumed to form only linear chains, without taking into account the existence of other stable structures such as ribbons or rings [2, 34, 35]. Moreover, a clear experimental observation of the equilibrium state is still lacking.

In the present paper, we provide both a two-dimensional experimental observation of this equilibrium and a suitable adaptation of the model obtained by Andreu *et al.* [9]. We show that this model is in good agreement with experimental data under a critical mean chains size and we evidence the existence of this critical value. Above this critical value, the formation of stable ribbon-shaped aggregates is observed.

## 2 Experimental set-up

A sketch of the experimental set-up is presented in fig. 1. The experiments were performed with superparamagnetic microspheres dispersed in water (Estapor<sup>®</sup> M1-070/60), with a volumic fraction of  $\phi = 2 \cdot 10^{-3}$ . We measured,

by image analysis, a radius of particles  $r = 0.6 \pm 0.3 \mu\text{m}$  while the mean susceptibility, measured by magnetophoresis [2, 36–38], is  $\chi = 0.09 \pm 0.03$ . Those values are consistent with previous characterization of that sample found in the literature [22, 23]. The suspension is placed inside a cylindrical chamber of diameter  $D = 5$  mm and thickness  $h = 50 \mu\text{m}$ . The chamber is formed by two parallel glass plates. The first glass plate is covered with a  $50 \mu\text{m}$  layer of epoxy at the exemption of a circular region. A suspension droplet of  $1 \mu\text{l}$  is placed inside this region. Afterward, the second glass plate is placed on the first one. A small quantity of low viscosity silicon oil is placed on the epoxy to asses the watertightness of the chamber. A constant and homogeneous magnetic field  $B$  is applied by sending a constant current in surrounding coils at the beginning of each experiment. The magnetic field produced by those coils has been characterized with a Hall probe and is homogeneous within the precision range of the probe of 2% around the cell. The current is sent in the coils with a constant intensity by a programmable DC power supply GenH-750W from TDK Lambda, with a precision of 0.01 A. The suspension is observed from the bottom with a  $10\times$  magnification. The microscope used is a inverted microscope Olympus IX73, connected to a 4070M-CL Thorlabs Camera with 2048 by 2048 pixels of 16 Bits depth. The images are recorded with a frame rate of 1 fps.

## 3 Results

The time evolution of the system is shown in fig. 1. We measured, as a function of time, the normalized mean size  $\langle s \rangle$  of the chains formed by the colloidal particles when the magnetic field is applied. This parameter is obtained through image analysis, by averaging the major axis of ellipses fitted on each chain in the image (at least 2000). For short time experiments, after a transient behavior, we obtained a power law growth, as observed in previous studies [29, 30, 32] (see fig. 2).

For long-time experiments, a saturation of the mean size  $\langle s \rangle$  is observed as expected from the theoretical development of Andreu *et al.* (see fig. 2). When the saturation is reached, we observed some typical behaviors from dynamical equilibria. For example, some parts of the

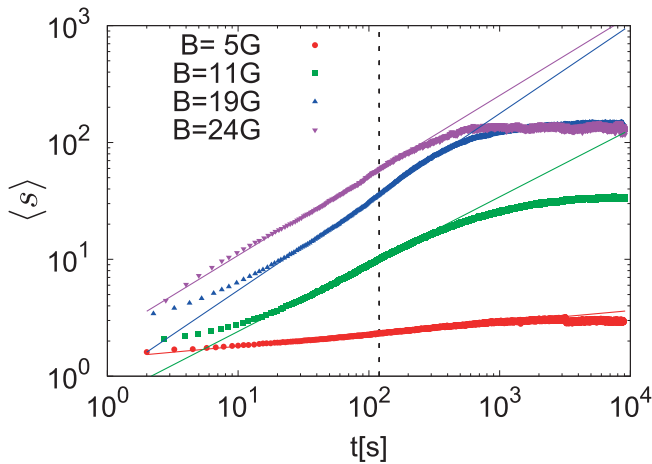


**Fig. 2.** Log-log plot of the evolution of the mean size of the chains  $\langle s \rangle$  during experiments. The mean chains length is expressed in mean diameter of particles. On short time, before the dashed line, a power law growth of the mean size of the chains is obtained after a transient behavior, as observed previously [29,30,32]. The solid lines are the fit of a power law on the data before the dashed line (the values of the corresponding exponents are respectively 0.1, 0.57, 0.75 and 0.68 with a statistical error of 0.01). However, a saturation of this length is systematically observed on long time, for all the experimental conditions we used. The mean length of the chains at the saturation depends on the magnetic field amplitude. The error is given by the size of the points.

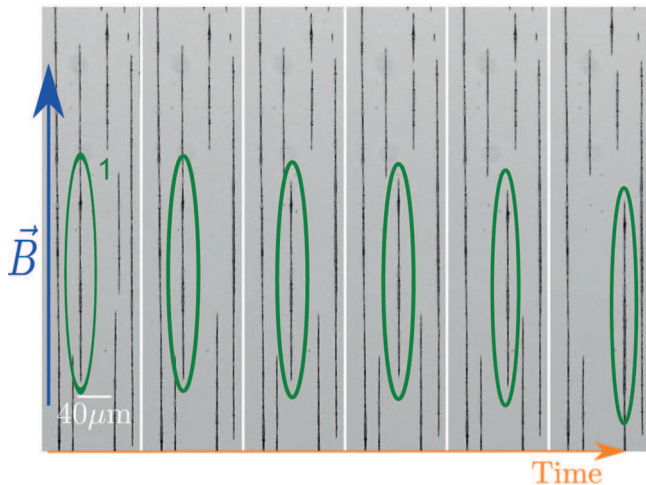


**Fig. 3.** Images from experiment performed with a magnetic field  $B = 24\text{G}$ . A part of a chain exhibits a typical behavior from dynamical equilibrium. The part of chain numbered 1, and circled in every image, leaves the chains where it was first before merging with another one. The time interval between each image is 45 minutes.

longest chains spontaneously leave those chains to merge with some other ones a few minutes later as illustrated in fig. 3. The observation of such behavior confirms that some thermodynamical equilibrium has been reached by the system and indicates that it is not useful to wait a longer time. Such phenomena also implies that the aggrega-

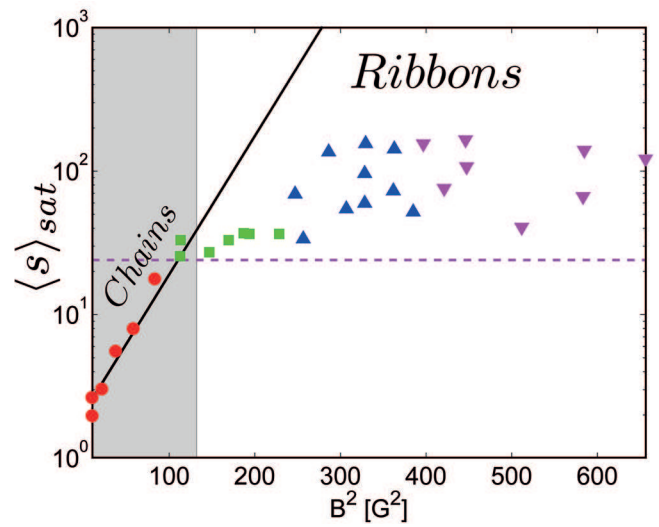


**Fig. 4.** Mean size of the chains at the saturation  $\langle s \rangle_{\text{sat}}$  for different values of the magnetic field. Those measurements have been obtained by considering the lengths of the chains at the plateau in fig. 2 for different experiments where the magnetic field is constant. The measurements are represented by the circles, the squares, the upward and downward triangles, according to the range of the magnetic field. The measurements represented in fig. 2 are then typical behaviors of curves whose saturation lengths are given here with the same symbol. Error bars are smaller than the points. The scaling has been chosen such that the fit of the model  $\langle s \rangle = C_2 \sqrt{\exp(C_1 B^2)}$  (line) (see sect. 4), calculated with the data in the gray area, draws a straight line. The model predicts higher values than observed ones for strong magnetic fields. We can conclude that the grey area is the range of magnetic field for which the behavior of the chains is sufficient to explain the global mean length of the aggregates, while the white area requires to take into account the existence of the ribbons. The horizontal dashed line is the line  $\langle s \rangle = 23$ , which is an approximation of the limit above which magnetic ribbons wider than one particle have significant influence on the mean size of the aggregates as explained in the text (see sect. 4).

tion of the particles is not completely irreversible, as assumed to establish the Smoluchowsky equation [29–33].

The mean chains size at the saturation  $\langle s \rangle_{\text{sat}}$  has been measured for different values of the magnetic field by considering the lengths of the chains at the plateau in fig. 2 for different experiments where the magnetic field is constant (see fig. 4). This maximum size  $\langle s \rangle_{\text{sat}}$  first increases with the magnetic field and can be adjusted with an adaptation of the model obtained by Andreu *et al.* only under a critical value (see sect. 4). After that critical value, the maximum size  $\langle s \rangle_{\text{sat}}$  is very sensitive to external noise but is systematically smaller than predicted by such a model.

## 4 Discussion

When the particles are restricted to a two-dimensional plane (as considered for some previous experiments [30]), the model proposed by Andreu *et al.* for the three dimensional cases should be adapted. Indeed, we have to

consider the thermal average of the magnetic energy  $U(R, \theta)$  of two particles in contact in the range  $\theta \in [0, \theta_0]$  implying an attraction between those particles, with  $\theta_0 = \arccos \frac{1}{\sqrt{3}}$ . This average involves Jacobians which are different for two dimensional systems. In two dimensions, by using the same approximation as Andreu *et al.* [9], we obtained a thermal average of  $\langle \sin^2 \theta \rangle \approx \frac{1}{3\Gamma}$  instead of  $\frac{2}{3\Gamma}$  for three-dimensional calculations. In case of a two-dimensional situation, the surface fraction  $\phi_0^S$  also replace the volume fraction  $\phi_0$  and the mean size of the chains at the equilibrium is therefore given by

$$\langle s \rangle^{(2D)} = \sqrt{\phi_0^S \exp\left(\Gamma - \frac{1}{2}\right)}. \quad (3)$$

With our experimental setup, the situation is more complex than the ideal case presented hereinbefore. Firstly, we measured a dispersion of both radius and susceptibility of the colloidal particles, as described in sect. 2. Therefore, the estimation of the parameter  $\Gamma$  is not straightforward and a fitting parameter  $C_1$  is used, with  $\Gamma = C_1 B^2$ . This fitting parameter  $C_1$  is an effective value of  $\frac{\pi R^3 \chi^2}{\mu_0 9 k_B T}$ .

Secondly, our system is not perfectly two dimensional. The particles are confined in a quasi-2D system due to sedimentation induced by gravity. By changing slightly the focal plane height, we observed that the chains and the single particles are not rigorously confined in a plane. The typical height of the confinement region corresponds to twice the particles diameter. This observation is consistent with theoretical comparison of the thermal energy  $U_{th} = k_B T$ , where  $k_B$  is the Boltzmann constant and  $T$  is the temperature, with the gravitational energy of the particles (taking the buoyancy into account)  $U_g = \Delta \rho g \frac{4}{3} \pi R^3 H$ , where  $H$  is the height of the particles from the bottom of the cell,  $R \approx 0.6 \mu\text{m}$  their radius,  $g = 9.81 \text{ m/s}^2$  the gravitational acceleration and  $\Delta \rho \approx 200 \text{ kg/m}^3$  the difference of density between the beads (mainly in polystyrene) and water. Both energy are equals when  $H \approx 2.3 \mu\text{m}$ , which is then the typical height reached by the particles at the equilibrium and is approximately two diameters of the beads, as observed experimentally.

Then we should have a situation between ideal 2D and 3D cases:  $\langle \sin^2 \theta \rangle = \frac{d}{3\Gamma}$ , with  $1 \leq d \leq 2$ . It is therefore more relevant to express the mean size of the chains as

$$\langle s \rangle = C_2 \sqrt{\exp(C_1 B^2)}, \quad (4)$$

where  $C_2$  is a second fitting parameter being the effective value of  $\sqrt{\phi_0 \exp(-d)}$ . This expression is used to fit the evolution of the mean chain size at the saturation as a function of the magnetic field (see fig. 4). The experimental data can not be fitted with a determination coefficient higher than 0.9 unless the fit is restricted to the points below the critical value  $B = 12 \text{ G}$  giving  $\langle s \rangle = 24 \pm 3$ . Above that value, the measurements give shorter chains than predicted by this fit. The coefficients obtained from

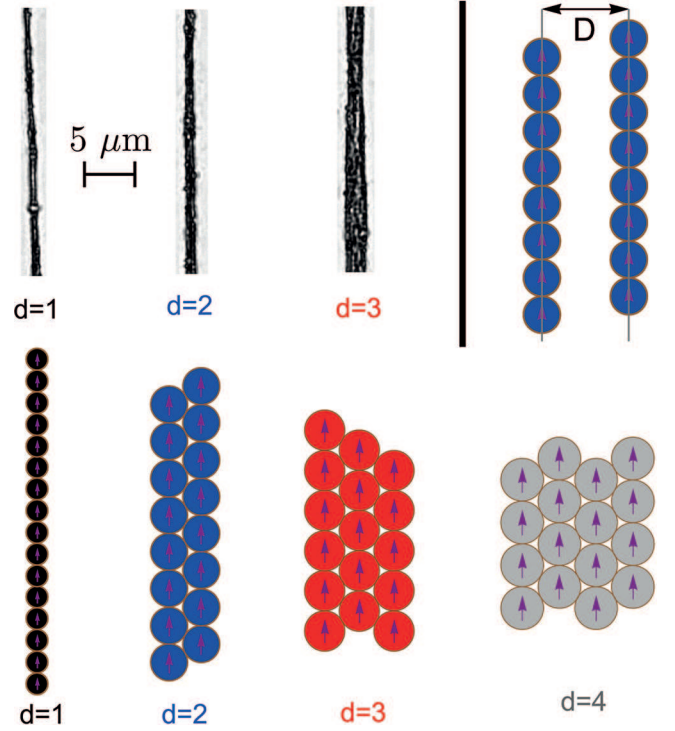


**Fig. 5.** Structures wider than one particle (magnetic ribbons). Top left: Experimental observations of magnetic ribbons with different widths. Bottom: Structures whose magnetic energy has been numerically computed, from the sum of all the dipole-dipole interaction energy. The different structures with 16 particles have been depicted. The small arrow in each circle gives the orientation of the magnetic dipoles. Top right: The distance  $D$  used to compute the energy barrier to the formation of the structures is pictured.

the fit presented in fig. 4 are  $C_1 = 4.4 \cdot 10^6 \pm 1.3 \cdot 10^6 \text{ T}^{-2}$  and  $C_2 = 2.1 \pm 1.4$ .

The fact that chains shorter than predicted by the model are observed is not incompatible with the numerical simulations of Andreu *et al.* because these simulations implied situations where the mean length of the chains was equal to or below 7 particles [9]. For such situations, the model provides a relevant fit with our data. However, that model assumes that particles always agglomerate in linear chains. This is not always true. Experimentally, we observed lateral aggregation of long chains, leading to structures with more than one particle of width, which are magnetic ribbons, as illustrated in fig. 5. We then calculated the magnetic energy of different structures, chains and ribbons, illustrated in fig. 5, and assessed the energy barrier to the formation of ribbons by lateral aggregation. To do this we considered a dimensionless mean energy given by

$$u_N(N, d, z) = \frac{1}{NU_0} \sum_{i=0}^{N-1} \sum_{j=i+1}^N U(|\mathbf{r}_i - \mathbf{r}_j|, \theta_{ij}), \quad (5)$$

where  $U(r, \theta)$  is defined in eq. (1),  $U_0 = \frac{\chi^2 \pi R^3 B^2}{18 \mu_0}$  is a reference magnetic energy,  $\mathbf{r}_i$  is the position of the particle  $i$  of the structure containing  $N$  particles,  $\theta_{ij}$  is the



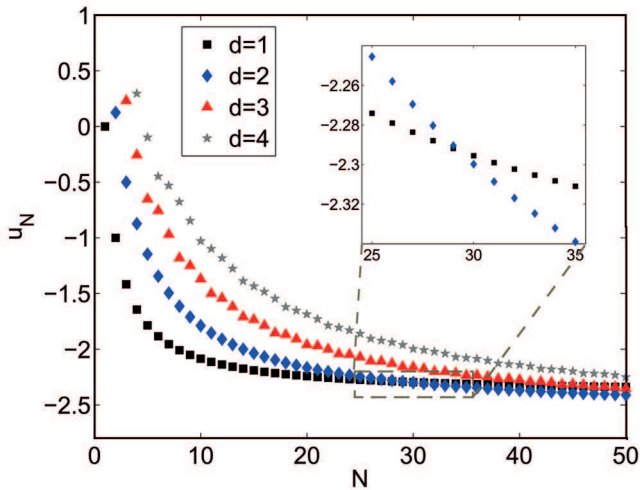


**Fig. 6.** Mean dimensionless energy of a particle  $u_N = \frac{1}{NU_0} \sum_{i=0}^{N-1} \sum_{j=i+1}^N U(|\mathbf{r}_i - \mathbf{r}_j|, \theta_{ij})$ , with  $U_0 = \frac{\chi^2 \pi R^3 B^2}{18\mu_0}$ , in the different structures as a function of the number of the particles  $N$ , for  $z = 0$ . The most stable structure with 30 particles is the ribbon with two particles of width. When  $N$  increases further, the most stable structure becomes successively the structure with 3 particles ( $N \approx 113$ ) then 4 particles ( $N \approx 263$ ).

angle between the direction of the field  $\mathbf{B}$  and the vector  $\mathbf{r}_i - \mathbf{r}_j$ ,  $d$  denotes the type of structure as on fig. 5 and  $z \equiv \frac{D - 2R \cos(\frac{\pi}{6})}{2R}$  is a dimensionless distance used to compute the barrier energy to the formation of the ribbons by lateral aggregation. This reasoning is similar to analyses from previous studies published in recent articles [34, 35], and the asymptotic value we obtained for  $\lim_{N \rightarrow \infty} u_N$  in the case of linear chains approaches  $-2\zeta(3) \approx -2.404$  as expected from the results of those studies.

This estimation shows that ribbons composed of two linear chains side by side are the most stable structures for aggregates of 30 particles (see fig. 6). When aggregates contain on average 30 particles, there is a mixture of linear chains of 30 particles and ribbons composed of two linear chains of 15 particles. The mean size of those aggregates is then about 23 particles. This is approximately the size from which the model diverges from our experimental data (see fig. 4).

We also noticed that above the critical value of the field, which seems actually to be determined by a critical size of chains, our measurements were very sensitive to external noise such as residual flows from the fluid. We believe this sensitivity to be due to the energy barrier preventing the appearance of the most stable structures. Indeed, fig. 7 clearly shows there is a barrier of potential to the formation of the structure by lateral aggregation. This implies a complex configuration space with metastable states for the chains. It is worthwhile to notice that the  $U_0$  reference energy can be expressed as  $k_B T \frac{C_1 B^2}{2}$ , and ribbons have been observed in our cases for  $B^2$  ranging from  $2 \cdot 10^{-6} \text{ T}^2$  to  $6 \cdot 10^{-6} \text{ T}^2$ . In such cases,  $U_0$  ranges from  $4.4 k_B T$  to  $13.2 k_B T$ . The potential barriers we have computed were ranging from  $0.5U_0$  to  $2U_0$ , depending on the

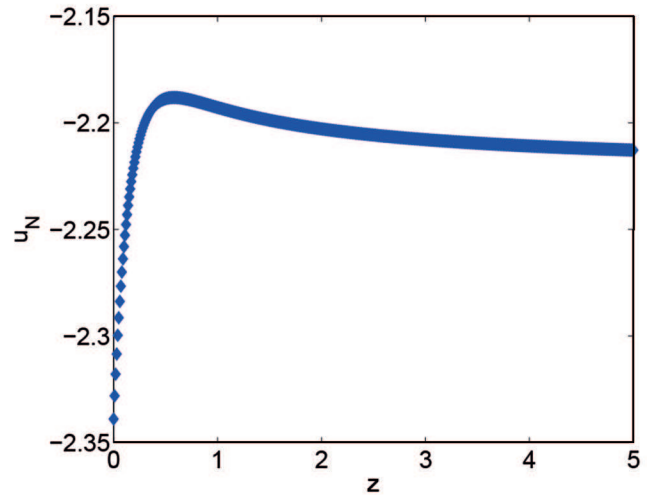


**Fig. 7.** Dimensionless mean magnetic energy  $u_N$  for a ribbon with two particles of width and  $N = 35$  particles. The variable  $z \equiv \frac{D - 2R \cos(\frac{\pi}{6})}{2R}$  is a dimensionless distance separating the two chains forming the ribbon, as pictured in the fig. 5. One can distinguish an energy barrier.

number of particles in the considered structures and the width  $d$  of the ribbons. Then, as weakest barriers are of the order of  $2k_B T$ , thermal agitation of the particles itself is likely to trigger some ribbons formation, but not as much as observed in our experiments. Actually, some external noise can move one or several chains from a metastable state to another one and then changing the mean length of the chains. In our experimental setup, such noise can be produced, for instance, by the flow around a small moving air or oil bubble accidentally trapped in the chamber with the colloidal suspension. During our experiments, which can last up to 5 hours, such perturbations are likely to occur, but not systematically.

## 5 Conclusion

In the present paper, we reported the first experimental observation of the saturation predicted by the model of Andreu *et al.* [9]. We experimentally validated this model on a range of experimental parameters such that  $\langle s \rangle < 23$ , but we showed that this model diverges with experimental data above a critical value for which we proposed an explanation, by highlighting the existence of magnetic ribbons. In the future, the model could be improved by considering the existence of these ribbons, in order to predict the mean size of the chains above the critical size. Our observations also highlighted that the hypothesis of irreversible aggregation assumed by the usual Smoluchowsky equation is not verified for long-time experiments. A more accurate equation taking into account some terms expressing the reversibility of this aggregation could be developed. The physical mechanisms we highlighted here could also be a starting point to develop protocols of controlled ribbons generation.

A.D. is financially supported by FNRS as research fellow. J.F. thanks the FNRS and Alexander Von Humboldt Foundation. This work was financially supported by the FNRS (Grant PDR T.0043.14) and by the University of Liège (Starting Grant C-13/88).

## References

- J. Faraudo, J.S. Andreu, J. Camacho, *Soft Matter* **9**, 6654 (2013).
- J. Faraudo, J. Camacho, *Colloid Polym. Sci.* **288**, 207 (2010).
- J.W. Tavacoli, P. Bauër, M. Fermigier, D. Bartolo, J. Heuvingh, O. du Roure, *Soft Matter* **9**, 9103 (2013).
- C.T. Yavuz, A. Prakash, J. Mayo, V.L. Colvin, *Chem. Eng. Sci.* **64**, 2510 (2009).
- C.T. Yavuz, J. Mayo, W.Y. William, A. Prakash, J.C. Falkner, S. Yean, L. Cong, H.J. Shipley, A. Kan, M. Tomson *et al.*, *Science* **314**, 964 (2006).
- K.M. Krishnan, *IEEE Trans. Magn.* **46**, 2523 (2010).
- J.L. Corchero, A. Villaverde, *Trends Biotechnol.* **27**, 468 (2009).
- U. Jeong, X. Teng, Y. Wang, H. Yang, Y. Xia, *Adv. Mater.* **19**, 33 (2007).
- J.S. Andreu, J. Camacho, J. Faraudo, *Soft Matter* **7**, 2336 (2011).
- G.P. Gajula, M.T. Neves-Petersen, S.B. Petersen, *Appl. Phys. Lett.* **97**, 103103 (2010).
- K.S. Khalil, A. Sagastegui, Y. Li, M.A. Tahir, J.E. Socolar, B.J. Wiley, B.B. Yellen, *Nat. Commun.* **3**, 794 (2012).
- Y. Gurevich, Y. Mankov, R. Khlebopros, *Dokl. Phys.* **11**, 478 (2013).
- F. Martinez-Pedrero, P. Tierno, *Phys. Rev. Appl.* **3**, 051003 (2015) DOI: 10.1103/PhysRevApplied.3.051003.
- H. Carstensen, V. Kapaklis, M. Wolff, *Phys. Rev. E* **92**, 012303 (2015) DOI: 10.1103/PhysRevE.92.012303.
- K. Muller, N. Osterman, D. Babic, C.N. Likos, J. Dobnikar, A. Nikoubashman, *Langmuir* **30**, 5088 (2014).
- M. Llera, J. Codnia, G.A. Jorge, *J. Magn. & Magn. Mater* **384**, 93 (2015).
- R.M. Erb, H.S. Son, B. Samanta, V.M. Rotello, B.B. Yellen, *Nature* **457**, 999 (2009).
- F. Martinez-Pedrero, P. Tierno, *Phys. Rev. Appl.* **3**, 051003 (2015).
- F. Martinez-Pedrero, A. Ortiz-Ambriz, I. Pagonabarraga, P. Tierno, *Phys. Rev. Lett.* **115**, 138301 (2015).
- H. Carstensen, V. Kapaklis, M. Wolff, *Phys. Rev. E* **92**, 012303 (2015).
- P. Liu, J.W. De Folter, A.V. Petukhov, A.P. Philipse, *Soft matter* **11**, 6201 (2015).
- P. Domínguez-García, J. Pastor, M. Rubio, *Eur. Phys. J. E* **34**, 1 (2011).
- P. Domínguez-García, S. Melle, J. Pastor, M. Rubio, *Phys. Rev. E* **76**, 051403 (2007).
- K.V. Edmond, H. Park, M.T. Elsesser, G.L. Hunter, D.J. Pine, E.R. Weeks, *Chaos-Woodbury* **21**, 041103 (2011).
- R. Dreyfus, J. Baudry, M.L. Roper, M. Fermigier, H.A. Stone, J. Bibette, *Nature* **437**, 862 (2005).
- D.H. Everett, *Basic Principles of Colloid Science* (Royal Society of Chemistry, 1988).
- J.N. Israelachvili, *Intermolecular and Surface Forces*, revised third edition (Academic Press, 2011).
- C.P. Royall, W.C. Poon, E.R. Weeks, *Soft Matter* **9**, 17 (2013).
- J.H. Promislow, A.P. Gast, M. Fermigier, *J. Chem. Phys.* **102**, 5492 (1995).
- S. Fraden, A.J. Hurd, R.B. Meyer, *Phys. Rev. Lett.* **63**, 2373 (1989).
- M. Kolb, *Phys. Rev. Lett.* **53**, 1653 (1984).
- F. Martínez-Pedrero, M. Tirado-Miranda, A. Schmitt, J. Callejas-Fernández, *Phys. Rev. E* **76**, 011405 (2007).
- S. Miyazima, P. Meakin, F. Family, *Phys. Rev. A* **36**, 1421 (1987).
- R. Messina, L.A. Khalil, I. Stanković, *Phys. Rev. E* **89**, 011202 (2014).
- N. Vandewalle, S. Dorbolo, *New J. Phys.* **16**, 013050 (2014).
- M. Suwa, H. Watarai, *Anal. Chim. Acta* **690**, 137 (2011).
- G. De Las Cuevas, J. Faraudo, J. Camacho, *J. Phys. Chem. C* **112**, 945 (2008).
- J. Ally, A. Amirfazli, *Colloids Surf. A* **360**, 120 (2010).

## 4.7 Additional remarks

It is interesting to notice that when  $N < 23$ , the ribbons are stable structures, but they are not observed because the linear chains are more stable and there is no potential barrier to the formation of those chains. When  $N$  decreases below 30 (which is the value for which the ribbons become more stable than the chains), the local minimum when the two chains are in contact ( $z = 0$ ) is higher than the value obtained when chains are infinitely far away from each other. The potential barrier is also more pronounced. The ribbons are then only metastable and are not observed. However, while lateral aggregation is the main formation process we have observed for ribbons, it is not the only one. A complete discussion of the formation process of the ribbons would still be an interesting research by itself, and could probably be based on recent theoretical developments. [45] The graphics of dimensionless energy corresponding to short ribbons are represented in Figure 4.3.

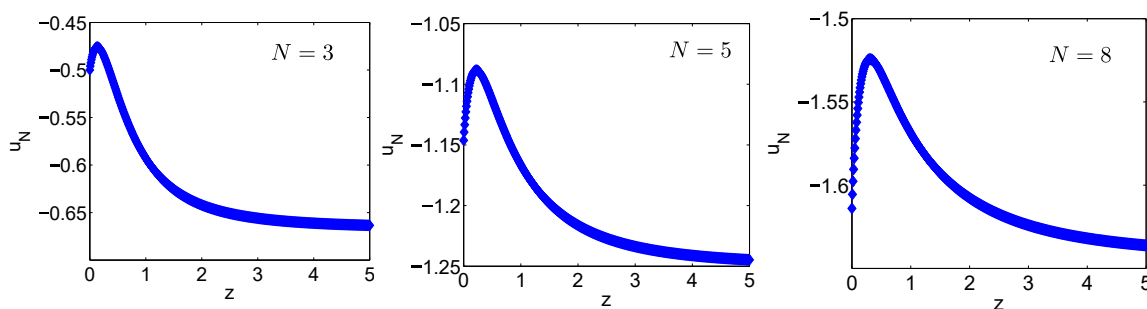


Figure 4.3: Representation of the potential barrier for various particles number for short ribbons. Dimensionless mean magnetic energy  $u_N$  for ribbons with  $N = 3, 5$  and  $8$  particles are successively considered. The variable  $z \equiv \frac{D - 2R \cos(\frac{\pi}{6})}{2R}$  is a dimensionless distance separating the two chains forming the ribbon, where  $D$  is the lateral distance between the chains, as illustrated in the paper.

This highlights that the aggregation process actually determines the structures which can be observed in the system. If other aggregation processes were occurring in the system, one might expect to see those structure earlier, or even observe other structures, such as cubic or triangular assemblies. The assembling process of the agglomerates is then a crucial point to determine the properties of the suspension.



# Chapter 5

## Influence of viscosity

### 5.1 Motivations

Since the aggregation process of the colloids plays a crucial role in their equilibrium properties, one can wonder how the dynamic parameters of the system influence the equilibrium state. Since the characteristic time of aggregation is given by  $t_B = \frac{6\pi\eta R^3}{48[(1/3)^{1/2} - (1/3)^{3/2}]U_0\phi}$ , a way to modify the dynamics of the system is by modifying the viscosity  $\eta$  of the surrounding fluid. Actually, this is the only parameter on which  $t_B$  relies and which does not intervene in the theoretical value of the mean size of agglomerates at saturation.

Moreover, being able to modify the characteristic time of aggregation without changing its saturation state would lead to a new method to reduce the numerical simulation time from several orders of magnitude, without modifying the intrinsic physical behaviour of the particles. This result should facilitate further numerical investigation about colloidal assemblies, which is still a crucial problem. Indeed, current techniques of numerical simulations would require several years of computing time to reach equilibrium state under some conditions: actual experiments last for hours and one second of simulation currently takes from 300 to 1100 hours of computer time. The most challenging situations are the ones leading to long chains, for which our previous experiments and analytical models disagree. [25,33]

### 5.2 Setup and methods

We performed both experiments and simulations in order to determine the effect of viscosity in a wide range of this parameter. The experimental set-up is the same as for the previous paper ([59], Chapter 4) : we used an inverted microscope to observe suspensions of colloids in airtight cells. However, we mixed glycerol with water in order to obtain suspending liquids with higher viscosities (from 1 mPa s to 100 mPa s). We applied magnetic fields through a pair of coils surrounding the sample.

The numerical simulations were performed using a Soft Sphere Discrete Element Method [92–94] taking into account the dipole-dipole interactions between the colloidal particles as well as the Brownian agitation in the system. The algorithm progresses with a constant time step  $\Delta t$  and solves Newton's equations of motion at each iteration. We computed the evolution of systems viscosities ranging from  $0.5 \mu\text{Pa s}$  to  $50 \mu\text{Pa s}$ . We did not use higher viscosities in numerical simulations, because the longest we used already took more than one month to compute.

We then focused on the evolution of the mean length of the chains  $\langle s \rangle(t)$  in both experiments and simulations. This parameter has been obtained through image analysis for the experiments while the analysis of the simulations is directly relying on the positions of the particles given by the simulation.

### 5.3 Main results

The time evolution of the system is shown in Figure 5.1(a) for the experiments and 5.1(b) for the simulations. We measured, as a function of time, the normalised mean size  $\langle s \rangle$  of the

chains, expressed in particles diameter, formed by the colloidal particles when the magnetic field is applied with an intensity of about 12 G. When applying a time scaling proportional to the typical aggregation time  $t_B \propto \eta^{-1}$ , the various curves collapse if the viscosity  $\eta$  is higher than a critical value  $\eta_c$  (see panels (c) and (d) of Fig. 5.1). However, we observed in the simulations that the evolution diverge from other curves if the viscosity is higher than this value  $\eta > \eta_c$ . This Figure 5.1 then illustrates the main influence of viscosity on the system and the possible divergence between the expected behaviour and actual data.

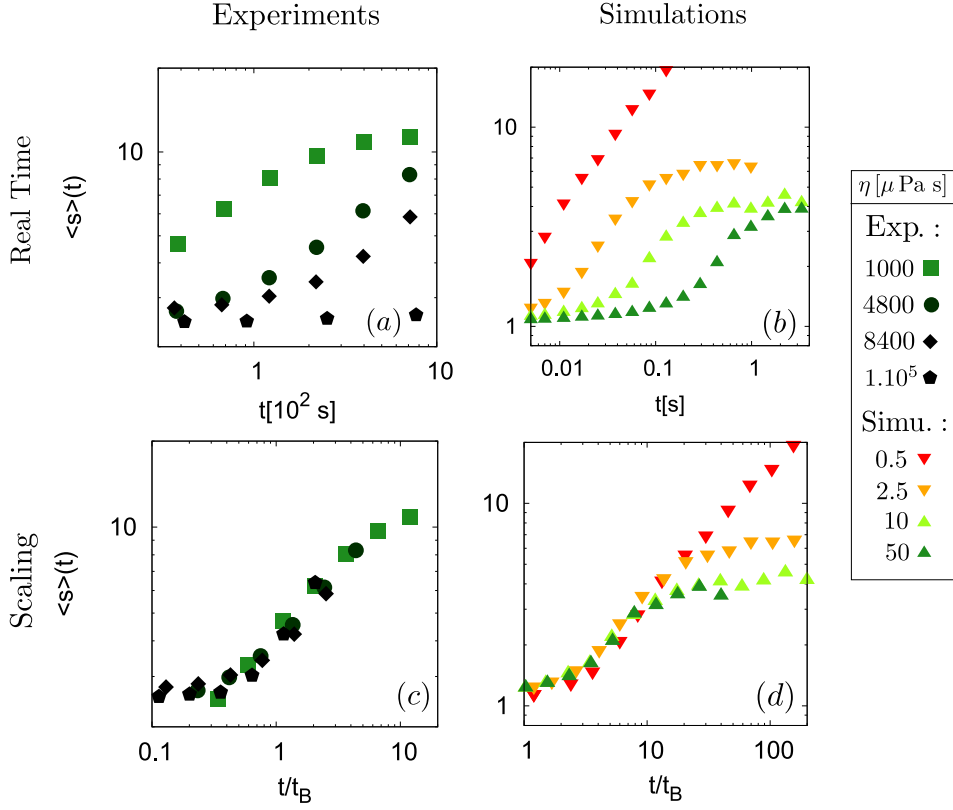


Figure 5.1: Picture from [60]. Log-log plots of the evolution of the mean size of the chains  $\langle s \rangle$  during experiments ((a) and (c)) and simulations ((b) and (d)). The mean chains length is expressed in mean diameter of particles. After a transient behaviour whose duration depends on the viscosity, a power law growth is obtained with an exponent close to 0.5. In (a) and (b), a clear trend can be seen on that graph: the higher the viscosity, the slower the growth. In (c) and (d), the mean size of the chains is plotted as a function of the parameter  $t/t_B$ , where the characteristic time is defined in equation (1.17). All experimental curves then collapse. In simulations, if the magnetic field  $B = 12$  G, curves collapse only for  $\eta > \eta_c$ , with  $\eta_c \in ]2.5 \mu\text{Pa s}; 5 \mu\text{Pa s}[$ . Colours and points shapes correspondence are described in the box on the right side.

This divergence is explained by a change of regime in the balance of two types of motions. More accurately, a Peclet number comparing the drift transport due to magnetic interaction to the stochastic transport due to the Brownian motion can be defined as

$$Pe = \frac{R\chi^2}{36\mu_0} \sqrt{\frac{m}{3k_B T}} \frac{B^2}{\eta}, \quad (5.1)$$

with  $m$  the mass of the particles. We found a critical value of the Peclet number  $Pe_C \approx 0.825$  above which the curves diverge from the others performed with the same particles and magnetic

field. This defines a phase diagram represented in Figure 5.2, which summarizes the transition between collapsing and divergent curves.

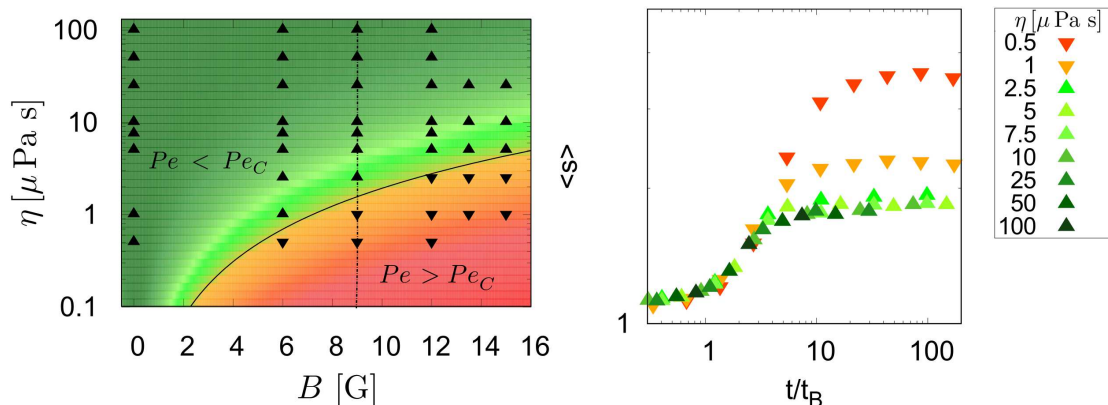


Figure 5.2: Picture from [60]. Left: global efficiency of the time scaling for all simulations. Upward triangles are the simulations whose curves collapse with others with the same magnetic field. Downward triangles are the simulations which don't collapse. The black curve represents the transition  $Pe = Pe_C$ , and the colour gradient is related to the difference of local Péclet number and its critical value  $Pe - Pe_C$ . Right: a graphic showing the curves obtained for the simulations performed with a magnetic field  $B = 9$  G. Those curves then correspond to the points on the dot-dashed line in the left graphic. The red and orange curves are not collapsing with the others and correspond to cases  $Pe > Pe_C$ .

## 5.4 Conclusion

This work shows that modifying the viscosity of the fluid only rescales the characteristic time of the agglomeration process, without modifying the properties of the system. Numerical simulations also showed that another aggregation regime occurs for low viscosities or high magnetic field. This indicates that granular gases could have a very different behaviour from colloidal liquids. Moreover, we identified the limit between those two regimes thanks to a Péclet number.

These results also imply that numerical simulations can be performed on systems with lower viscosities and still quantitatively model experimental situations. The benefit of using lower viscosities is that the computer time of the simulations can be reduced from several months to a few days. This then opens a new way to efficiently simulate complex colloidal systems in previously challenging situations.

## 5.5 Credits

The paper in the next pages [60] is included in this thesis according to the Creative Commons Attribution 4.0 International License. To view a copy of the Creative Commons license, please visit <http://creativecommons.org/licenses/by/4.0/>.

# SCIENTIFIC REPORTS

OPEN

## Superparamagnetic colloids in viscous fluids

A. Darras<sup>1,2,3</sup>, E. Opsomer<sup>1,4</sup>, N. Vandewalle<sup>1</sup> & G. Lumay<sup>1</sup>

The influence of a magnetic field on the aggregation process of superparamagnetic colloids has been well known on short time for a few decades. However, the influence of important parameters, such as viscosity of the liquid, has received only little attention. Moreover, the equilibrium state reached after a long time is still challenging on some aspects. Indeed, recent experimental measurements show deviations from pure analytical models in extreme conditions. Furthermore, current simulations would require several years of computing time to reach equilibrium state under those conditions. In the present paper, we show how viscosity influences the characteristic time of the aggregation process, with experimental measurements in agreement with previous theories on transient behaviour. Afterwards, we performed numerical simulations on equivalent systems with lower viscosities. Below a critical value of viscosity, a transition to a new aggregation regime is observed and analysed. We noticed this result can be used to reduce the numerical simulation time from several orders of magnitude, without modifying the intrinsic physical behaviour of the particles. However, it also implies that, for high magnetic fields, granular gases could have a very different behaviour from colloidal liquids.

Superparamagnetic colloids are magnetic nanoparticles inserted in a matrix of non-magnetic material (polystyrene or silica) to obtain particles with diameter  $d$  ranging from 100 nm to a few micrometres. These composite particles are combining a quasi-zero remanent magnetisation and a high magnetic response<sup>1–3</sup>. In applications, the superparamagnetic colloids are functionalised to capture specific targets such as protein, cell or bacteria<sup>4–7</sup>. After the capture, an inhomogeneous external magnetic field is applied to separate the superparamagnetic particles by magnetophoresis<sup>8</sup>. Moreover, the formation of chains along the magnetic field enhances the separation process. This technique is used for protein isolation, cell separation, waste capture, bacteria processing, chromatography, etc.<sup>1, 4–7, 9–17</sup>. More complex structures of superparamagnetic colloids can be obtained by using rotating fields, even possibly leading to microswimmers or tracers of local dynamics<sup>18–32</sup>. Those complex structures open ways to new kinds of applications as they have unique optical properties and offer tunable structures able to adapt to their environment and execute functional tasks<sup>20, 23, 26</sup>. However, the previous studies about those complex structures focus on the properties of the structures obtained, without having a deep understanding of their formation process. To our knowledge, the only system for which some model of growth has been published in the literature up to now is the colloidal chains formed under constant magnetic fields.

In colloidal science, it is well known that particles tend to agglomerate due to van der Waals interactions<sup>33, 34</sup>. In the present experiments, this agglomeration is prevented by covering the particles with carboxyl charged groups. These charged groups create a short range repulsion between the particles, typically within a range of 10 nm between the particles<sup>2, 35</sup>. This ensures the stability of the dispersion. In the following, this electrostatic interaction is considered to define an effective size of the particles for the contact of particles which is 10 nm wider than the natural size of the particles<sup>1</sup>. However, when an external magnetic field  $\vec{B}$  is applied on the suspension, the superparamagnetic particles acquire a magnetic dipole  $\vec{\mu} = \chi V \vec{B}$ , with the magnetic susceptibility  $\chi$  of the particles and their volume  $V = \frac{4}{3}\pi R^3$ , given their radius  $R$ . The particles then interact with each other through dipolar interactions. The potential energy of magnetic interaction between two identical particles at distance  $r$  is therefore given by

<sup>1</sup>GRASP, CESAM - Physics Department, University of Liège, B-4000, Liège, Belgium. <sup>2</sup>F.R.S.-FRNS, B-1000, Bruxelles, Belgium. <sup>3</sup>Experimental Physics, Saarland University, D-66123, Saarbrücken, Germany. <sup>4</sup>Université Paris Diderot, Sorbonne Paris Cité, MSC, CNRS (UMR 7057), F-75013, Paris, France. Correspondence and requests for materials should be addressed to A.D. (email: alexis.darras@ulg.ac.be)



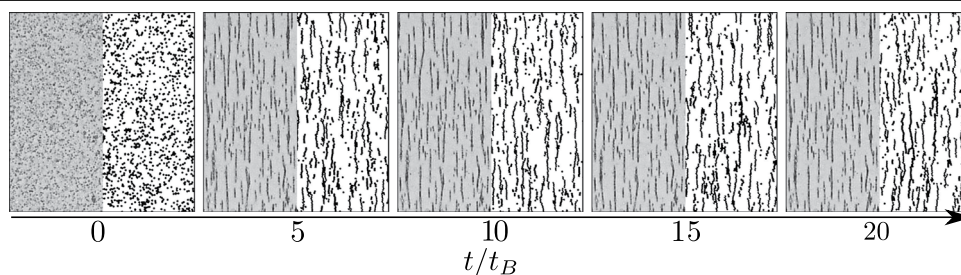


**Figure 1.** Evolution of the chain formation along scaled time as observed from one of our experiments (left side of each picture) and one of our simulations (right side of each picture). The pictures are part of images obtained with a magnetic field  $B = 12$  G. One can observe the formation of chains aligned with the external magnetic field and a qualitative similarity between experiments and simulations. The characteristic time  $t_B$  is defined in equation (3).

$$U(r, \theta) = \frac{\chi^2 4\pi R^6 B^2}{9\mu_0} \left( \frac{1 - 3 \cos^2 \theta}{r^3} \right), \quad (1)$$

with  $\theta$  being the angle between the magnetic field  $\vec{B}$  and the line joining the centre of the particles. The force associated with this interaction is then

$$\vec{F}_m = -\vec{\nabla} U(r, \theta) = \frac{3\mu_0 \mu^2}{4\pi r^4} ((1 - 3 \cos^2 \theta) \vec{e}_r - \sin 2\theta \vec{e}_\theta), \quad (2)$$

with  $\vec{e}_r = \frac{\vec{r}}{r}$  and  $\vec{e}_\theta = \vec{e}_z \times \vec{e}_r$  if  $\vec{e}_z$  is the unitary vector perpendicular to the plan containing  $\vec{e}_r$  and  $\vec{B}$  (if  $\vec{B}$  and  $\vec{e}_r$  are parallel, the orientation of  $\vec{e}_\theta$  is meaningless since  $\theta = 0$ ). Two particles then attract each other when they are aligned with the field  $\vec{B}$ , while they repel each other if they are side-by-side. This interaction implies that two particles tend to aggregate in a chain aligned with the magnetic field  $\vec{B}$ . Several studies, both experimental and theoretical, have shown that superparamagnetic colloids self-organise into chains under those conditions, through diffusion-limited aggregation<sup>13, 36–41</sup>. Moreover, this aggregation is reversible, meaning that the chains break up if the magnetic field  $\vec{B}$  is suppressed<sup>28, 42</sup>. Experimentally, chains of several particles are typically observed<sup>36, 37, 39</sup> and the growth is successfully described on short time (typically up to 300 s) by a Smoluchowski equation, predicting a power law behaviour of the mean size of the chains  $\langle s \rangle \propto t^z$  after a transient behaviour<sup>36–40</sup>. Current research usually focuses on more complex structures that have recently been observed under those conditions<sup>43, 44</sup> and new theoretical models are currently studied in order to take them into account and describe their properties<sup>41, 45, 46</sup>.

However, only little attention has been given to the influence of the viscosity of the surrounding fluid. Yet since the aggregation is diffusion-limited, the viscosity of the fluid could modify the aggregation mechanism through its influence on the diffusion coefficient. Moreover, the equilibrium state reached after a long time is still challenging on some aspects. Indeed, recent experimental measurements show deviations from pure analytical models in extreme conditions<sup>12, 43, 44</sup>. Current techniques of numerical simulations would require several years of computing time to reach equilibrium state under some conditions: actual experiments last for hours and one second of simulation currently takes from 300 to 1100 hours of computer time. The most challenging situations are the ones leading to long chains, for which experiments and analytical models disagree<sup>12, 43</sup>.

In the present work, we first provide experimental observation of the influence of viscosity on the formation of such chains, and compare our results with previous theoretical models. Then, a modification of this viscosity is tested in simulations, in order to explore a wider range of viscosity. This allows to test conditions which are closer to dust suspensions in the air, where we observe another aggregation regime. Moreover, a nice application would be to use it to speed up the simulation time of colloidal system.

## Experimental Setup

A sketch of the experimental pictures is presented in Fig. 1. The experiments were performed with superparamagnetic microspheres dispersed in glycerol-water mixtures (Estapor<sup>®</sup> M1-070/60), with a volumic fraction of  $\phi = 2 \cdot 10^{-3}$ . The viscosity of each liquid phase was measured before adding the particles to the suspension with a Haake-MARS rheometre. The measurements were consistent with the available tables<sup>47</sup>. The range of viscosity we used goes from 1 mPa s to 100 mPa s. We measured, by image analysis, a radius of particles  $r = 0.6 \pm 0.3 \mu\text{m}$  while the mean susceptibility, obtained by magnetophoresis<sup>2, 48–50</sup>, was  $\chi = 0.09 \pm 0.03$ . Those values are consistent with previous characterisation of that sample found in the literature<sup>28, 29</sup>. The suspension was placed inside a cylindrical chamber of diameter  $D = 5$  mm and thickness  $h = 50 \mu\text{m}$ . The chamber was formed by two parallel glass plates. The first glass plate was covered with a  $50 \mu\text{m}$  layer of epoxy with the exemption of a circular region. A suspension droplet of  $1 \mu\text{l}$  was placed inside this region. Afterwards, the second glass plate was placed on the first one. A small quantity of low-viscosity silicon oil was placed on the epoxy to assess the watertightness of the chamber. A constant and homogeneous magnetic field  $B$  was generated by a constant current in surrounding coils at the

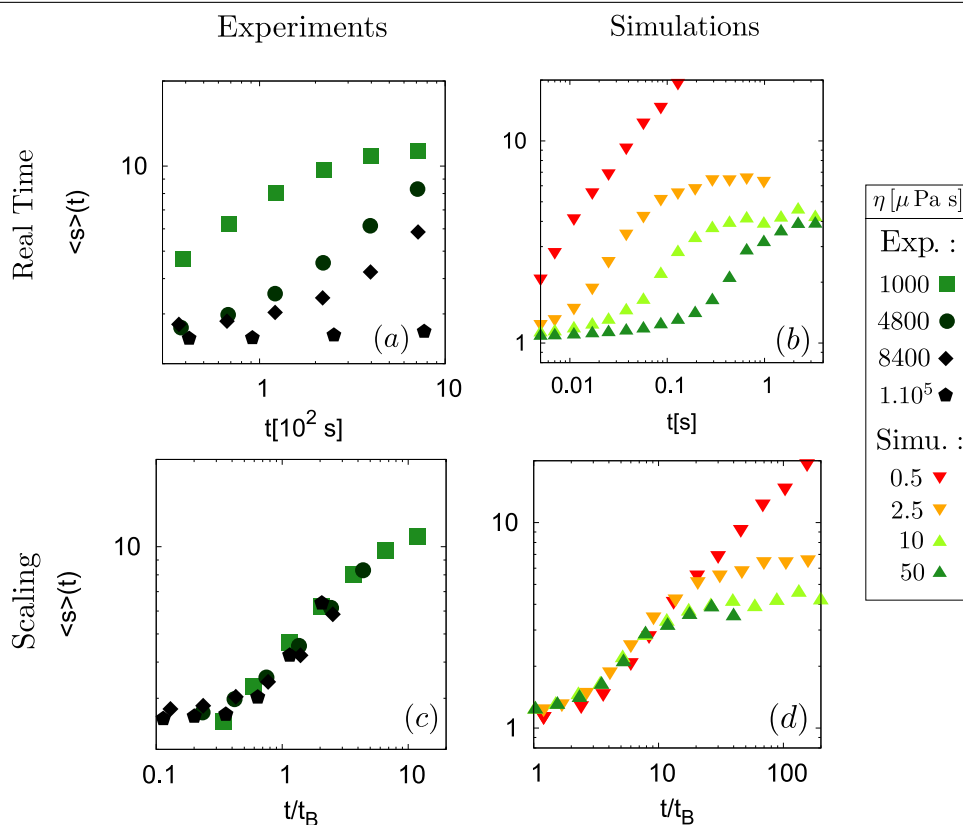


**Figure 2.** Log-log plots of the evolution of the mean size of the chains  $\langle s \rangle$  during experiments ((a) and (c)) and simulations ((b) and (d)). The mean chains length is expressed in mean diameter of particles. After a transient behaviour whose duration depends on the viscosity, a power law growth is obtained with an exponent close to 0.5. In (a) and (b), a clear trend can be seen on that graph: the higher the viscosity, the slower the growth. In (c) and (d), the mean size of the chains is plotted as a function of the parameter  $t/t_B$ , where the characteristic time is defined in equation (3). All experimental curves then collapse. In simulations, if the magnetic field  $B = 12$  G, curves collapse only for  $\eta > \eta_c$ , with  $\eta_c \in ]2.5 \mu\text{Pa s}; 5 \mu\text{Pa s}[$ . Colours and points shapes correspondence are described in the box on the right side.

beginning of each experiment. The magnetic field produced by those coils was characterised with a Hall probe and was homogeneous within the precision range of the probe of 2% around the cell. The current in the coils had a constant intensity controlled by a programmable DC power supply GenH-750W from TDK Lambda, with a precision of 0.01 A. The suspension was observed from the bottom with a 10x magnification. The microscope used was an inverted microscope Olympus IX73, connected to a 4070M-CL Thorlabs Camera with 2048 by 2048 pixels of 16 Bits depth. The images were recorded with a frame rate of 1fps.

## Experimental Results

The time evolution of the system is shown in Fig. 2(a). We measured, as a function of time, the normalised mean size  $\langle s \rangle$  of the chains, expressed in particles diameter, formed by the colloidal particles when the magnetic field is applied with an intensity of about 12 G. This size is obtained through image analysis, by averaging the major axis of ellipses fitted on each chain in the image (at least 2000 chains). For short time experiments, after a transient behaviour, we obtained a power law growth, with an exponent  $z$  close to 0.5, as observed in previous studies<sup>36,37,39</sup>. In Fig. 2(a), a clear trend can be seen on that graph: the higher the viscosity, the slower the growth.

For long times and low viscosity experiments, a saturation of the mean size  $\langle s \rangle$  is observed as expected from the theoretical development of Andreu *et al.*<sup>12</sup> and observed in some of our previous experiments (see Fig. 2(a))<sup>44</sup>.

Those differences of behaviour can be explained on the basis of the Smoluchowsky equation and the mechanism of diffusion-limited aggregation. Indeed, a diffusion-limited aggregation, taking into account an effective capture volume as suggested by Fermigier *et al.*, has a characteristic time scale  $t_B = \frac{R^2}{24[(1/3)^{1/2} - (1/3)^{3/2}]D\Gamma\phi}$ <sup>36</sup>, where  $R$  is the radius of the particles,  $D$  is the diffusion coefficient of a single particle,  $\Gamma = \frac{\chi \pi R^3 B^2}{9\mu_0 k_B T} \equiv \frac{2U_0}{k_B T}$  is a dimensionless parameter comparing the magnetic energy with the thermal energy  $k_B T$  ( $\chi$  is the magnetic susceptibility of the particles and  $B$  is the magnetic field amplitude) and  $\phi$  is the volume fraction of the particles. By using the Stokes-Einstein relation  $D = \frac{k_B T}{6\pi R\eta}$ , where  $\eta$  is the viscosity of the fluid, we can then write this characteristic time as

$$t_B = \frac{6\pi\eta R^3}{48[(1/3)^{1/2} - (1/3)^{3/2}]U_0\phi}. \quad (3)$$

When the data are expressed as a function of this dimensionless time  $\frac{t}{t_B}$ , we obtain the plot in Fig. 2(c), where all the curves collapse. Since the only difference between our experiments is the viscosity  $\eta$  of the fluid, this collapse highlights that, in the range of our experiments, the viscosity simply slows down the aggregation process, without modifying further the intrinsic physical mechanism of aggregation.

But one can wonder: if increasing the viscosity simply slows down the growth process of the chains, would reducing the viscosity speed up this growth? This is what we tried to achieve in some numerical simulations, since fluids with lower viscosity than water are not abundant. Actually, the range of viscosity we explored is closer to the viscosity of the air. This means that experiments corresponding to those conditions should be performed with micrometric superparamagnetic dust or powder suspended in a gas, which is not easily available.

### Numerical Simulations: Methods

Numerical simulations are useful tools to compare ideal experiments with, on the one hand, actual experiments or, on the other hand, theoretical expectations. Comparing with actual experiments can indicate if all the key physical ingredients are taken into account in the models. It can also be used to test some models in range of parameters which are not accessible experimentally. In the case of the analytical models for the mean chains length at saturation<sup>12,51</sup>, such simulations can (dis)confirm the mathematical approximations. However, each second of numerical simulation can require between 300 and 1100 hours of computer time, the most challenging situations being the ones leading to long chains<sup>12,43</sup>. Speeding up the simulations is then critical to study the cases corresponding to experiments which can last up to five hours.

In our study, simulations are realised using a Soft Sphere Discrete Element Method<sup>52–54</sup> taking into account the dipole-dipole interactions between the colloidal particles as well as the Brownian agitation in the system. The algorithm progresses with a constant time step  $\Delta t$  and solves Newton's equations of motion at each iteration. The different force models we considered are described here below.

The normal contact force acting on two impacting particles is modelled using a linear spring-dashpot. The repulsive component is proportional to the overlap  $\delta$  between particles while the energy dissipation during the collision is taken into consideration via an additional damping force. Altogether one obtains,

$$\vec{F}_n = -k_n\delta\vec{n} - \gamma\frac{d\delta}{dt}\vec{n}, \quad (4)$$

where  $k_n$  is the spring stiffness,  $\vec{n}$  the normal unit vector and  $\gamma$  a complex function of  $k_n$  and the restitution coefficient  $\varepsilon$ . The tangential contact force is proportional to the relative slipping velocities  $v_s$  of the particles. Moreover, it is bounded by Coulomb's criterion which yields in,

$$\vec{F}_t = -k_t v_s \vec{t}, \quad |F_t| \leq \mu_d |F_n|, \quad (5)$$

where  $k_t$  is a large positive constant,  $\vec{t}$  the tangential unit vector and  $\mu_d$  is the dynamic friction coefficient.

When exposed to an external magnetic field, the colloidal particles acquire a magnetic dipole inducing long-range interactions between them. The associated force  $\vec{F}_m$ , given in equation (2), can directly be used in the simulations for each pair of particles. However, in order to gain some computational time, we introduced a cut-off distance of about  $12r$  by using a linked-cell method<sup>55</sup>.

The random motion of a particle due to its interaction with surrounding fluid molecules in the heat bath can be described by using a Langevin equation<sup>56</sup>. The drag force is considered to be  $\vec{F}_d = -6\pi R\eta\vec{v}$ , where  $\vec{v}$  is the velocity of the particle. The Brownian force  $\vec{F}_b$  is modelled as a Gaussian white noise process<sup>57,58</sup>. One has,

$$\vec{F}_b = \vec{\xi} \sqrt{6\pi R\eta} \sqrt{\frac{2D}{\Delta t}} \quad (6)$$

where  $\Delta t$  is the time step in the simulation and  $\vec{\xi}$  is a vector of three random gaussian variables with zero mean and unit variance.

Since sedimentation plays an important role in the dynamics of our system, gravity and buoyancy, noted respectively  $\vec{F}_g$  and  $\vec{F}_a$ , have to be included.

It is worthwhile to notice that changing the viscosity parameter  $\eta$  then modifies both the drag force  $\vec{F}_d$  and the Brownian force  $\vec{F}_b$  in the simulations (indeed,  $F_d \propto \eta$  and  $F_b \propto \eta\sqrt{D} \propto \sqrt{\eta}$ ). Besides this, all the other parameters remain constant since they depend only on temperature and particles' properties.

### Numerical Simulations: Results

Simulations allow to test the scaling resulting from the former relation in equation (3) relating the characteristic time of the system  $t_B \propto \eta$  to the viscosity  $\eta$  for low viscosities. If this scaling is valid for every value of viscosity, it can be used to speed up the simulations related to our experiments. Indeed, to some extent, it would mean simulations performed with a fluid viscosity which is lower than the ones available experimentally are faster but the colloidal assemblies retain the same geometrical properties and aggregation mechanisms. We then performed simulations for viscosities varying from  $\eta = 5 \cdot 10^{-7}$  Pa s to  $10^{-4}$  Pa s. As illustrated in curve Fig. 2b, the same trend as in experimental is observed: the higher the viscosity, the slower the growth. In curve and Fig. 2d, the curves

efficiently collapse with the scaling  $t/t_B$ , except if the viscosity  $\eta$  is smaller than a critical value  $\eta_c$ , with  $\eta_c \in ]2.5 \mu\text{Pa}; 5 \mu\text{Pa} [$  in the case of Fig. 2.

One might wonder if this viscosity threshold arises from a numerical bias. But in our numerical model, the main approximation depending on viscosity is the use of the Brownian force  $\vec{F}_b$  to create the diffusive motion of the particles, according to the Langevin model<sup>56</sup>. This model is valid as long as the characteristic autocorrelation time of the Brownian force, which is determined by the time step  $\Delta t \approx 10^{-7}$  s in our simulations, is negligible compared to the characteristic viscous time  $\frac{2\rho R^2}{9\eta} \approx \frac{10^{-10}\text{Pa s}^2}{\eta}$ , with  $\rho = 1200 \frac{\text{kg}}{\text{m}^3}$  the density of the particles. This viscous time is defined as the characteristic speed relaxation time of a particle with a non-zero initial speed, if only the drag force is acting on it. We then have to respect  $10^{-7} \text{ s} \ll \frac{10^{-10}\text{Pa s}^2}{\eta} \Leftrightarrow \eta \ll 10^{-3} \text{ Pa s}$ , which is always the case in our simulations since the maximum value of the viscosity we used is  $\eta = 10^{-4} \text{ Pa s}$ . Actually, we chose it accordingly to the time step fixed by the contact dynamics  $\Delta t \ll 2\pi \sqrt{\frac{m}{k_n}}$ <sup>52-54</sup>. To be certain of the validity of this assumption, we also performed some simulations with a reduced time step of  $\Delta t \approx 10^{-8}$  s but no modification of the simulations' results was then observed, for any of the viscosity we used. Eventually, this shows that the Langevin model is only better when the viscosity decreases, and the Langevin model can not be responsible for an artificial onset of the behaviour transition we observed in the simulations.

This means that no numerical effect is responsible for this behaviour transition. Actually, we believe that a new physical aggregation mechanism appears when the viscosity is below a critical threshold. Our hypothesis is that this threshold comes from the rise of a non-negligible drift due to the magnetic interactions of the grains. Indeed, every particle close to another one has a drift velocity due to the magnetic force exerted by this neighbour. On long times  $t \gg t_\eta$  greater than the viscous time  $t_\eta = \frac{m}{6\pi R\eta}$ , since the particles are in a viscous fluid, the motion equation for average values of a single particle can be written  $\langle \vec{F}_m \rangle = 6\pi R\eta \langle \vec{v}_D \rangle$ , where  $\langle \vec{v}_D \rangle$  is then the mean drift velocity of the particles. The mean magnetic force  $\langle \vec{F}_m \rangle$  depends on the actual particles density in the neighbourhood of the considered sphere, as well as its distance from the closest neighbour. However, a characteristic value is the maximum of this force  $F_{m,M} = \frac{\pi\chi^2 R^2 B^2}{6\mu_0}$ , which is then related with the maximum drift velocity as

$$\langle v_{D,m} \rangle = \frac{F_{m,M}}{6\pi R\eta} = \frac{R\chi^2 B^2}{36\mu_0\eta}. \quad (7)$$

The impact of the magnetic interaction in the motion of the particles can then be assessed by the ratio of this maximum drift speed  $\langle v_{D,m} \rangle$  and the characteristic root mean square speed due to Brownian agitation  $\tilde{v}_{th} = \sqrt{\frac{3k_B T}{m}}$ . This defines a kind of Peclet number, comparing the drift transport due to magnetic interaction to the stochastic transport due to the Brownian motion

$$Pe \equiv \frac{\langle v_{D,m} \rangle}{\tilde{v}_{th}} = \frac{F_{m,M}}{6\pi R\eta\tilde{v}_{th}} = \frac{F_{m,M}}{F_{\eta,\tilde{v}_{th}}} = \frac{R\chi^2}{36\mu_0} \sqrt{\frac{m}{3k_B T}} \frac{B^2}{\eta}, \quad (8)$$

where  $F_{\eta,\tilde{v}_{th}}$  is the modulus of drag force applied to a particle whose velocity is  $\tilde{v}_{th}$ . The third expression above then expresses that this Peclet number  $Pe$  is also the ratio between the maximum magnetic force and the characteristic drag force during the Brownian motion. Actually, it is easy to show that this is the only force competition which is able to explain the breakdown of scaling depending on both magnetic field and viscosity. Indeed, the only forces concerned by (at least) one of those quantities are the drag force  $\vec{F}_d$ , the Brownian force  $\vec{F}_b$  (both depending only on viscosity) and the magnetic force  $\vec{F}_m$  (depending only on magnetic field). In our simulations, the ratio  $\frac{F_m}{F_b}$  is ranging from 0 to approximately  $10^{-2}$ , which indicates that the magnetic force is always negligible compared to the thermal agitation. Then this competition is not likely to give rise to any transition. However, in our simulations, the ratio  $\frac{F_m}{F_d}$  ranges from 0 to approximately 4, indicating that the magnetic force becomes, in some experiments only, greater than the characteristic viscous force. Any comparison between two forces including any another force would fail to completely explain our observations by missing at least one of this parameter. This is then enough to conclude that the competition between drag and magnetic interaction is the only one relevant to explain the scaling breakdown.

The last side of the equalities in equation (8) shows that, if the transition occurs for a critical value of  $Pe_c$ , there is a value of viscosity  $\eta$  under which the mechanism of aggregation is intrinsically different from usual experimental observations. This minimal viscosity  $\eta_{lim} = \frac{R\chi^2}{36\mu_0} \sqrt{\frac{m}{3k_B T}} \frac{B^2}{Pe_c}$  depends on  $B^2$  for a given set of particles. Through all the simulations we performed, with magnetic fields ranging from 0 G to 15 G, the range of viscosity for which the scaling efficiently collapses the curves is consistent with a critical value of the Peclet number  $Pe_c = 0.825 \pm 0.025$ , see Fig. 3.

Another argument supporting this assumption is given by the analysis of the Mean Square Displacement (MSD) of the particles along time (see Fig. 4). Indeed, for a given magnetic field, the MSDs of the particles in that plane are similar for all viscosities were  $Pe < Pe_c$ , while it is not if  $Pe > Pe_c$ . This clearly means that when  $Pe > Pe_c$  another kinematic process, acting against the diffusion, occurs. The existence of such threshold also determines the limit of how the simulations related to a given experiment can be artificially sped up by decreasing the viscosity.

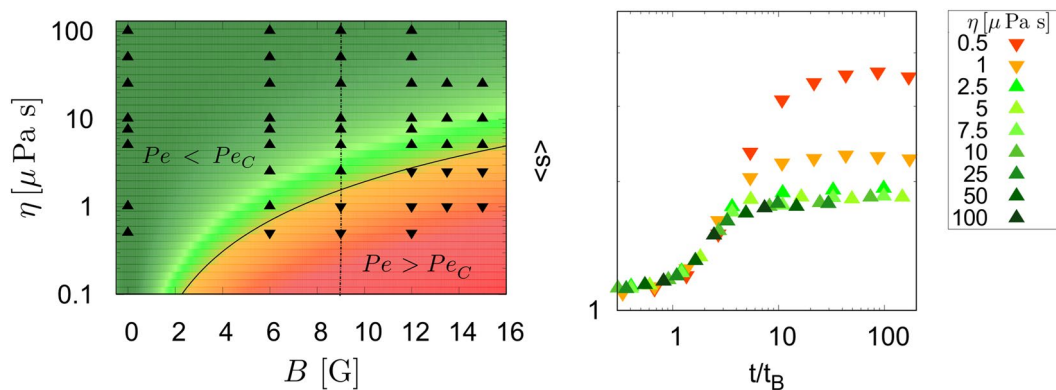


**Figure 3.** Left: global efficiency of the time scaling for all simulations. Upwards triangles are the simulations whose curves collapse with others with the same magnetic field. Downwards triangles are the simulations which don't collapse. The black curve represents the transition  $Pe = Pe_C$ , and the colour gradient is related to the difference of local Peclet number and its critical value  $Pe - Pe_C$ . Right: a graphic showing the curves obtained for the simulations performed with a magnetic field  $B = 9$  G. Those curves then correspond to the points on the dot-dashed line in the left graphic. The red and orange curves are not collapsing with the others and correspond to cases  $Pe > Pe_C$ .

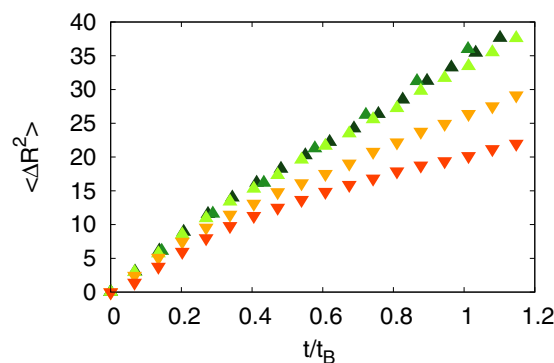


**Figure 4.** Mean Square displacement of the particles in the horizontal plane as a function of dimensionless time. The mean square displacement is expressed in particles diameter and the time has been scaled by the aggregation characteristic time  $t_B$  (equation (3)) to compare curves from various simulations under a magnetic field of 9 G. All the curves corresponding to points in the region  $Pe < Pe_C$  collapse, while curves in the region  $Pe > Pe_C$  have a different behaviour.

## Conclusions

Our experiments show that modifying the viscosity of the fluid only rescales the characteristic time of the agglomeration process, without modifying the underlying physical mechanisms. Then, numerical simulations showed that another aggregation regime occurs for low viscosities or high magnetic field. This indicates that, for high magnetic fields, the granular gases could have a very different behaviour from colloidal liquids. This also implies that numerical simulations can be performed on systems with lower viscosities and still be an efficient model for the experiments. The benefit of using lower viscosities is that the computer time of the simulations can be reduced from several months to a few days. This then also opens new prospects to efficiently simulate complex colloidal systems.

## References

1. Farauto, J., Andreu, J. S. & Camacho, J. Understanding diluted dispersions of superparamagnetic particles under strong magnetic fields: a review of concepts, theory and simulations. *Soft Matter* **9**, 6654–6664 (2013).
2. Farauto, J. & Camacho, J. Cooperative magnetophoresis of superparamagnetic colloids: theoretical aspects. *Colloid Polym. Sci.* **288**, 207–215 (2010).
3. Tavaoli, J. W. *et al.* The fabrication and directed self-assembly of micron-sized superparamagnetic non-spherical particles. *Soft Matter* **9**, 9103–9110 (2013).
4. Corchero, J. L. & Villaverde, A. Biomedical applications of distally controlled magnetic nanoparticles. *Trends Biotechnol.* **27**, 468–476 (2009).
5. Kozissnik, B., Bohorquez, A. C., Dobson, J. & Rinaldi, C. Magnetic fluid hyperthermia: advances, challenges, and opportunity. *International Journal of Hyperthermia* **29**, 706–714 (2013).
6. Pankhurst, Q., Thanh, N., Jones, S. & Dobson, J. Progress in applications of magnetic nanoparticles in biomedicine. *Journal of Physics D: Applied Physics* **42**, 224001 (2009).

7. Colombo, M. *et al.* Biological applications of magnetic nanoparticles. *Chemical Society Reviews* **41**, 4306–4334 (2012).
8. Yavuz, C. T., Prakash, A., Mayo, J. & Colvin, V. L. Magnetic separations: from steel plants to biotechnology. *Chem. Eng. Sci.* **64**, 2510–2521 (2009).
9. Yavuz, C. T. *et al.* Low-field magnetic separation of monodisperse Fe<sub>3</sub>O<sub>4</sub> nanocrystals. *Science* **314**, 964–967 (2006).
10. Krishnan, K. M. Biomedical nanomagnetism: a spin through possibilities in imaging, diagnostics, and therapy. *IEEE Trans. Magn.* **46**, 2523–2558 (2010).
11. Jeong, U., Teng, X., Wang, Y., Yang, H. & Xia, Y. Superparamagnetic colloids: controlled synthesis and niche applications. *Adv. Mater.* **19**, 33 (2007).
12. Andreu, J. S., Camacho, J. & Faraudo, J. Aggregation of superparamagnetic colloids in magnetic fields: the quest for the equilibrium state. *Soft Matter* **7**, 2336–2339 (2011).
13. Gajula, G. P., Neves-Petersen, M. T. & Petersen, S. B. Visualization and quantification of four steps in magnetic field induced two-dimensional ordering of superparamagnetic submicron particles. *Appl. Phys. Lett.* **97**, 103103 (2010).
14. Khalil, K. S. *et al.* Binary colloidal structures assembled through Ising interactions. *Nat. Commun.* **3**, 794 (2012).
15. Gurevich, Y., Mankov, Y. & Khlebopros, R. Self-assembly of superparamagnetic ferrihydrite nanoparticles. *Dokl. Phys.* **11**, 478–481 (2013).
16. Martínez-Pedrero, F. & Tierno, P. Magnetic propulsion of self-assembled colloidal carpets: Efficient cargo transport via a conveyor-belt effect. *Phys. Rev. Applied* **3**, 051003, doi:10.1103/PhysRevApplied.3.051003 (2015).
17. Carstensen, H., Kapaklis, V. & Wolff, M. Phase formation in colloidal systems with tunable interaction. *Phys. Rev. E* **92**, 012303, doi:10.1103/PhysRevE.92.012303 (2015).
18. Müller, K. *et al.* Pattern formation and coarse-graining in two-dimensional colloids driven by multiaxial magnetic fields. *Langmuir* **30**, 5088–5096 (2014).
19. Llera, M., Codnia, J. & Jorge, G. A. Aggregation dynamics and magnetic properties of magnetic micrometer-sized particles dispersed in a fluid under the action of rotating magnetic fields. *J. Magn. Magn. Matter* **384**, 93–100 (2015).
20. Erb, R. M., Son, H. S., Samanta, B., Rotello, V. M. & Yellen, B. B. Magnetic assembly of colloidal superstructures with multipole symmetry. *Nature* **457**, 999–1002 (2009).
21. Löwen, H. Colloidal dispersions in external fields: recent developments. *Journal of Physics: Condensed Matter* **20**, 404201 (2008).
22. Froltsov, V., Blaak, R., Likos, C. & Löwen, H. Crystal structures of two-dimensional magnetic colloids in tilted external magnetic fields. *Physical Review E* **68**, 061406 (2003).
23. Martínez-Pedrero, F. & Tierno, P. Magnetic propulsion of self-assembled colloidal carpets: Efficient cargo transport via a conveyor-belt effect. *Phys. Rev. Applied* **3**, 051003 (2015).
24. Martínez-Pedrero, F., Ortiz-Ambriz, A., Pagonabarraga, I. & Tierno, P. Colloidal microworms propelling via a cooperative hydrodynamic conveyor belt. *Phys. Rev. Lett.* **115**, 138301 (2015).
25. Carstensen, H., Kapaklis, V. & Wolff, M. Phase formation in colloidal systems with tunable interaction. *Phys. Rev. E* **92**, 012303 (2015).
26. Liu, P., De Folter, J. W., Petukhov, A. V. & Philipse, A. P. Reconfigurable assembly of superparamagnetic colloids confined in thermoreversible microtubes. *Soft Matter* **11**, 6201–6211 (2015).
27. Blair, D. L. & Kudrolli, A. Clustering transitions in vibrofluidized magnetized granular materials. *Physical Review E* **67**, 021302 (2003).
28. Domínguez-García, P., Pastor, J. & Rubio, M. Aggregation and disaggregation dynamics of sedimented and charged superparamagnetic micro-particles in water suspension. *Eur. Phys. J. E* **34**, 1–7 (2011).
29. Domínguez-García, P., Melle, S., Pastor, J. & Rubio, M. Scaling in the aggregation dynamics of a magnetorheological fluid. *Phys. Rev. E* **76**, 051403 (2007).
30. Merminod, S., Jamin, T., Falcon, E. & Berhanu, M. Transition to a labyrinthine phase in a driven granular medium. *Physical Review E* **92**, 062205 (2015).
31. Edmond, K. V. *et al.* Tracking the brownian diffusion of a colloidal tetrahedral cluster. *Chaos-Woodbury* **21**, 041103 (2011).
32. Dreyfus, R. *et al.* Microscopic artificial swimmers. *Nature* **437**, 862–865 (2005).
33. Everett, D. H. *Basic principles of colloid science* (Royal Society of Chemistry, 1988).
34. Israelachvili, J. N. *Intermolecular and surface forces: revised third edition* (Academic press, 2011).
35. Royall, C. P., Poon, W. C. & Weeks, E. R. In search of colloidal hard spheres. *Soft Matter* **9**, 17–27 (2013).
36. Promislow, J. H., Gast, A. P. & Fermigier, M. Aggregation kinetics of paramagnetic colloidal particles. *J. Chem. Phys.* **102**, 5492–5498 (1995).
37. Fraden, S., Hurd, A. J. & Meyer, R. B. Electric-field-induced association of colloidal particles. *Phys. Rev. Lett.* **63**, 2373 (1989).
38. Kolb, M. Unified description of static and dynamic scaling for kinetic cluster formation. *Phys. Rev. Lett.* **53**, 1653 (1984).
39. Martínez-Pedrero, F., Tirado-Miranda, M., Schmitt, A. & Callejas-Fernández, J. Formation of magnetic filaments: A kinetic study. *Phys. Rev. E* **76**, 011405 (2007).
40. Miyazima, S., Meakin, P. & Family, F. Aggregation of oriented anisotropic particles. *Phys. Rev. A* **36**, 1421 (1987).
41. Ezzaier, H. *et al.* Two-stage kinetics of field-induced aggregation of medium-sized magnetic nanoparticles. *The Journal of Chemical Physics* **146**, 114902 (2017).
42. Darras, A., Fiscina, J., Vandewalle, N. & Lumay, G. Relating brownian motion to diffusion with superparamagnetic colloids. *American Journal of Physics* **85**, 265–270 (2017).
43. Faraudo, J., Andreu, J. S., Calero, C. & Camacho, J. Predicting the self-assembly of superparamagnetic colloids under magnetic fields. *Advanced Functional Materials* **3837** (2016).
44. Darras, A., Fiscina, J., Pakpour, M., Vandewalle, N. & Lumay, G. Ribbons of superparamagnetic colloids in magnetic field. *The European Physical Journal E* **39**, 1–6 (2016).
45. Messina, R., Khalil, L. A. & Stanković, I. Self-assembly of magnetic balls: From chains to tubes. *Physical Review E* **89**, 011202 (2014).
46. Vandewalle, N. & Dorbolo, S. Magnetic ghosts and monopoles. *New Journal of Physics* **16**, 013050 (2014).
47. Cheng, N.-S. Formula for the viscosity of a glycerol-water mixture. *Industrial & engineering chemistry research* **47**, 3285–3288 (2008).
48. Suwa, M. & Watarai, H. Magnetoanalysis of micro/nanoparticles: a review. *Anal. Chim. Acta* **690**, 137–147 (2011).
49. De Las Cuevas, G., Faraudo, J. & Camacho, J. Low-gradient magnetophoresis through field-induced reversible aggregation. *J. Phys. Chem. C* **112**, 945–950 (2008).
50. Ally, J. & Amirfazli, A. Magnetophoretic measurement of the drag force on partially immersed microparticles at air-liquid interfaces. *Colloids Surf., A* **360**, 120–128 (2010).
51. Rojas, N., Darras, A. & Lumay, G. Self-assembly processes of superparamagnetic colloids. *to be published* (2017).
52. Pöschel, T. & Schwager, T. *Computational granular dynamics: models and algorithms* (Springer Science & Business Media, 2005).
53. Radjai, F. & Dubois, F. *Discrete-element modeling of granular materials* (Wiley-Iste, 2011).
54. Ooi, J. Y., Magnanimo, V., Sun, J. & Luding, S. Particle modelling with the discrete element method: A success story of pardem. *Powder technology* **293**, 1–2 (2016).
55. Welling, U. & Germano, G. Efficiency of linked cell algorithms. *Computer Physics Communications* **182**, 611–615 (2011).
56. Pottier, N. *Physique statistique hors d'équilibre: processus irréversibles linéaires* (EDP Sciences, 2007).

57. Peng, Z., Doroodchi, E. & Evans, G. Dem simulation of aggregation of suspended nanoparticles. *Powder Technology* **204**, 91–102 (2010).
58. Li, A. & Ahmadi, G. Dispersion and deposition of spherical particles from point sources in a turbulent channel flow. *Aerosol science and technology* **16**, 209–226 (1992).

### Acknowledgements

A.D. is financially supported by FNRS as research fellow. This work was financially supported by the FNRS (Grant PDR T.0043.14) and by the University of Liège (Starting Grant C-13/88). E.O. acknowledges financial support by the European Space Agency and Belspo (Prodex) via the VipGran Project. Authors thank their colleague Dr. Jorge Fiscina for useful advice about preparing and characterising glycerol-water mixtures. Authors also thank Charlotte Marique for spell-checking the manuscript.

### Author Contributions

G.L. and A.D. conceived the experiments, A.D. conducted the experiment(s), E.O. and A.D. conceived the simulation code, E.O. wrote the simulation code, A.D. managed the simulations, E.O. and A.D. wrote the manuscript. A.D., E.O., G.L. and N.V. analysed the results and reviewed the manuscript.

### Additional Information

**Competing Interests:** The authors declare that they have no competing interests.

**Publisher's note:** Springer Nature remains neutral with regard to jurisdictional claims in published maps and institutional affiliations.



**Open Access** This article is licensed under a Creative Commons Attribution 4.0 International License, which permits use, sharing, adaptation, distribution and reproduction in any medium or format, as long as you give appropriate credit to the original author(s) and the source, provide a link to the Creative Commons license, and indicate if changes were made. The images or other third party material in this article are included in the article's Creative Commons license, unless indicated otherwise in a credit line to the material. If material is not included in the article's Creative Commons license and your intended use is not permitted by statutory regulation or exceeds the permitted use, you will need to obtain permission directly from the copyright holder. To view a copy of this license, visit <http://creativecommons.org/licenses/by/4.0/>.

© The Author(s) 2017





# Chapter 6

## Effect of volume fraction

### 6.1 Motivations

While the model of Faraudo *et al.* was developed and efficient for volume fractions of  $\phi \sim 10^{-3}$ , one can wonder if this model is still actually efficient for higher volume fraction from  $\phi \sim 10^{-2}$  to  $10^{-1}$ ... Experimentally, the parameter  $\Gamma$  is pretty hard to assess due to possible variations on the features of the particles. Indeed, a dispersion  $\sigma_r$  of 10% on the radius  $R$  distribution along a distribution with 10% of dispersion  $\sigma_\chi$  of the magnetic susceptibility  $\chi$  leads to a dispersion  $\sigma_\Gamma$  of 46% of  $\Gamma$ , meaning a factor  $\approx 2.73$  between  $\Gamma - \sigma_\Gamma$  and  $\Gamma + \sigma_\Gamma$ . Moreover this range of volume fraction was previously very time-consuming to compute in numerical simulations, due to the high number of particles involved. However, our previous results on the influence of viscosity now open a faster way to simulate this range of volume fraction and allow us to compare this model with an idealized system where the value of  $\Gamma$  is perfectly known.

### 6.2 Setup and methods

We fixed the viscosity of the fluid in our simulations to  $\eta = 25 \cdot 10^{-6}$ . We performed numerical simulations of systems with effective volume fraction between  $\phi_E = 8.8 \cdot 10^{-3}$  and  $\phi_E = 88 \cdot 10^{-3}$  at  $\Gamma = 8$ . The effective volume fraction  $\phi_E = \phi_0 \frac{h}{2R}$  is the volume fraction of the system after sedimentation (i.e. the volume fraction in the vicinity of the particles once the thermodynamic equilibrium is reached). We also made simulations with  $\Gamma$  varying from 0 to 19 for the extremal values of  $\phi_E$ .

In order to confirm experimentally the trend we observed and modeled from the numerical results, we also performed systematic measurement with effective volume fraction varying from  $5 \cdot 10^{-3}$  to  $115 \cdot 10^{-3}$ , at  $\Gamma = 8$ . The experimental set-up is otherwise the same as in the previous experiments.

### 6.3 Main results

We showed that Faraudo's model is efficient to model systems with volume fraction upto  $\phi_E = 25 \cdot 10^{-3}$ . However, from  $\phi_E = 40 \cdot 10^{-3}$  and beyond, the model underestimates the mean size of the chains at equilibrium. It means that the dependency of Faraudo's model regarding the volume fraction has to be adapted for high values of this parameter. We showed that such an adaptation could be done by taking into account the magnetic repulsion between long chains. This consideration leads to a model of the mean chains' size at equilibrium

$$\langle s \rangle = \sqrt{\phi_E \exp(\Gamma - 1 + K\Gamma\phi_E)}, \quad (6.1)$$

where  $K$  is a geometric factor that geometric idealization estimates as  $K = 6/\pi$ . Fitting the numerical data gives the value of  $K = 2.2$ . The various curves and the numerical data are shown in Figure 6.1. On the left graph of this Figure, one can clearly see that Faraudo's model (black line) diverges from our numerical for high volume fractions. Meanwhile, the model we proposed, represented by the magenta curve (with  $K = 2.2$ , obtained as a fitted value) and

the cyan curve (with  $K = 1.9$ , obtained as an approximation for extreme cases), is in good agreement with all the data on the range of volume fraction we explored.

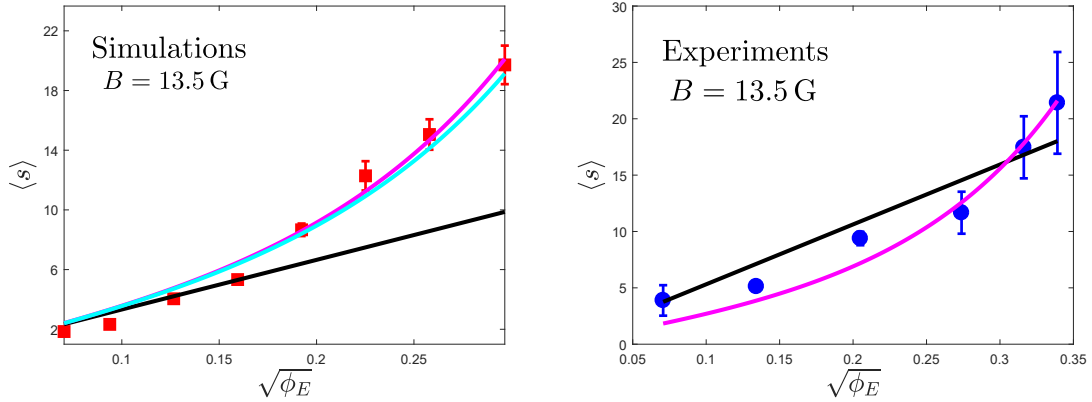


Figure 6.1: Picture from [61], with kind permission of The European Physical Journal (EPJ). Left : Average lengths of the chains at saturation for various volume fraction with a magnetic field  $B = 13.5$  G ( $\Gamma = 8$ ). Red points are data obtained from several numerical simulations. The black line is Faraudo's model, while the blue (mid-high) curve is our new model (eq. (6.1)), with the approximate value  $K = 6/\pi$ . The magenta (higher) curve is a fit of this latter, with  $K$  as a fitting parameter, giving  $K = 2.2$ . Right : Equilibrium mean size of the particles as a function of effective volume fraction  $\phi_E$ . The circles are experimental measurements while the curves are the fitted models, with  $\Gamma$  as a fit parameter and  $K = 2.2$ . The black line is the fit from Faraudo's model, while the magenta curve is a fit from our model (eq.(6.1)). One can see that eq.(6.1) gives a trend consistent with the experimental data.

As can be seen on the left panel of Figure 6.1, experimental measurements also show a better agreement with our model (eq. (6.1), magenta curve), when both models are fitted with  $\Gamma$  as a fit parameter. Moreover, the values of  $\Gamma$  we obtained in the fits are  $\Gamma = 7$  for eq.(6.1) and  $\Gamma = 9$  for Faraudo's model. The range of plausible  $\Gamma = \frac{\pi R^3 \chi^2 B^2}{\mu_0 9 k_B T}$ , computed from the distributions of radius  $R$  and susceptibility  $\chi$  in our sample of colloids, is  $\Gamma \in [2.2; 8.3]$ . This further supports that our model is more relevant than the previous one.

## 6.4 Conclusion

Thanks to the method we developed previously to speed up numerical simulations of superparamagnetic colloids, we were able to simulate systems with higher volume fraction than previously. We showed that these situations are challenging for existent models and we proposed a successful modification taking into account the interaction between separate chains.

## 6.5 Credits

The paper in the next pages is included in this thesis with kind permission of The European Physical Journal (EPJ). Reference of the original paper is [61].

# Effect of volume fraction on chains of superparamagnetic colloids at equilibrium

A. Darras<sup>1,2,3,a</sup>, E. Opsomer<sup>1</sup>, N. Vandewalle<sup>1</sup>, and G. Lumay<sup>1</sup>

<sup>1</sup> GRASP - Physics Department, University of Liège,  
B-4000 Liège, Belgium

<http://www.grasp-lab.org>

<sup>2</sup> F.R.S.-FRNS,

B-1000 Bruxelles, Belgium

<http://www.fnr.be>

<sup>3</sup> Experimental Physics, Saarland University,

D-66123 Saarbrücken, Germany

<http://agwagner.physik.uni-saarland.de>

Received: date / Revised version: date

**Abstract.** For a few decades, the influence of a magnetic field on the aggregation process of superparamagnetic colloids has been well known on short time scale. However, the accurate study of the equilibrium state is still challenging on some aspects. On the numerical aspect, current simulations have only access to a restricted set of experimental conditions due to the computational cost of long range interactions in many body systems. In the present paper, we numerically explore a new range of parameters thanks to sped up numerical simulations validated by a recent experimental and numerical study. We first show that our simulations reproduce results from previous study in well-established conditions. Then we show that unexpectedly long chains are observed for higher volume fractions and intermediate fields. We also present theoretical developments taking into account the interaction between the chains which are able to reproduce the data that we obtained with our simulations. We finally confirm this model thanks to experimental data.

**PACS.** 81.16.Dn Self-assembly – 47.57.J- Colloidal systems – 82.60.Lf Thermodynamics of solutions

## 1 Introduction

Self-assembly of superparamagnetic colloids is a topic of intense research since a few decades [1–18]. Indeed, resulting structures can form microswarms or microswimmers useful for mixing in low Reynolds number or manipulate specific targets such as proteins, cells or bacteria, which leads to applications in waste capture, protein isolation, chromatography, bacteria processing, cell separation, etc.[4,7,10,18–32]. However, the previous studies often focus on the properties of such complex assemblies. The detailed formation process and the origin of those properties is still an open question. To our knowledge, the only system for which some model of growth has been published in the literature up to now is the colloidal chains formed under constant magnetic fields [12, 23,33–39]. The assembling mechanisms rely on the characteristic high magnetic response and quasi-zero residual magnetization of the building particles consisting of mag-

netic nanoparticles inserted in a matrix of non-magnetic material (polystyrene or silica).[17,18,23,35]

Given those properties, the particles interact magnetically as if they were perfect dipoles. Formally, let us consider the effective magnetic susceptibility  $\chi$  of the particles and their volume  $V = \frac{4}{3}\pi R^3$ , given their radius  $R$ . Then, when an external magnetic field  $\mathbf{B}$  is applied on the suspension, the particles acquire a magnetic dipole moment  $\boldsymbol{\mu} = \chi V \mathbf{B} / \mu_0$ . Actually, this equation is only valid for values far under the so-called magnetic saturation. With the paramagnetic materials we used, the magnetic field where this saturation is reached is of the order of 250 G.[40,33,12] Since we will consider only magnetic field of the order of 10 G, we will always stay in this linear regime for the considerations of this work. The interaction force, between two identical particles separated by a distance  $r$ , is therefore given by

$$\mathbf{F}_m = \frac{3\mu_0\mu^2}{4\pi r^4} ((1 - 3\cos^2\theta)\mathbf{e}_r - \sin 2\theta\mathbf{e}_\theta), \quad (1)$$

where  $\theta$  is the angle between the line joining the centre of the particles and the magnetic field  $\mathbf{B}$ ,  $\mathbf{e}_r = \frac{\mathbf{r}}{r}$  and

Send offprint requests to: Alexis Darras

<sup>a</sup> Corresponding author: alexis.darras@uliege.be

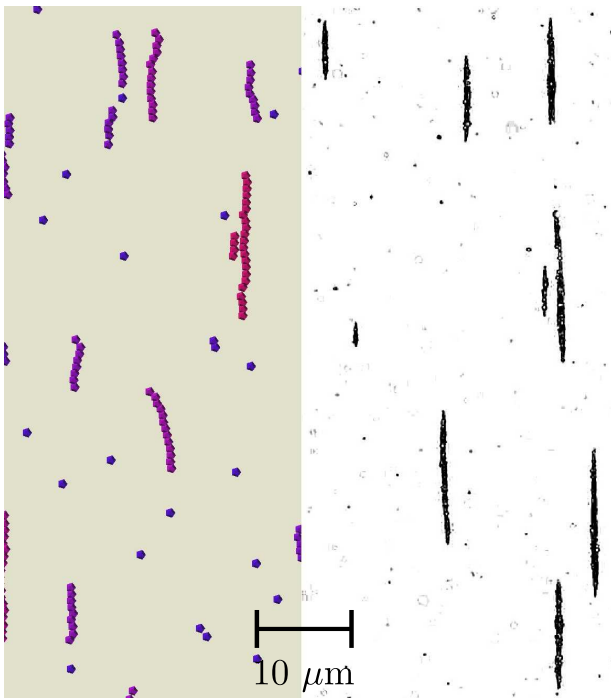


**Fig. 1.** Typical chains from numerical simulations (left) and experiments (right). Effective volume fraction of approximately  $\phi_E = 0.015$ .

$\mathbf{e}_\theta = \mathbf{e}_z \times \mathbf{e}_r$  if  $\mathbf{e}_z$  is the unitary vector perpendicular to the plan containing  $\mathbf{e}_r$  and  $\mathbf{B}$ . If  $\mathbf{e}_r$  and  $\mathbf{B}$  are parallel,  $\theta = 0$  and the orientation of  $\mathbf{e}_\theta$  is meaningless. The subsequent magnetic interaction energy between those particles ( $\mathbf{F}_m = -\nabla U(r, \theta)$ ) is then

$$U(r, \theta) = \frac{\chi^2 4\pi R^6 B^2}{9\mu_0} \left( \frac{1 - 3 \cos^2 \theta}{r^3} \right), \quad (2)$$

Two particles then repel each other if they are side-by-side, while they attract each other when they are aligned with the field  $\mathbf{B}$ . This interaction implies that two particles tend to aggregate aligned with the magnetic field  $\mathbf{B}$ . As shown by several studies, both experimental and theoretical, superparamagnetic colloids self-organize into chains under those conditions, through diffusion-limited aggregation, as illustrated in fig.1 [34,41–44,27,45]. The characteristic dimensionless parameters governing this self-assembly are the volume fraction  $\phi_0$  and the ratio between the maximum of the magnetic energy and the thermal energy

$$\Gamma = \frac{\mu_0}{4\pi} \frac{\mu^2}{4R^3 k_B T} = \frac{\pi R^3 \chi^2 B^2}{\mu_0 9 k_B T}. \quad (3)$$

Moreover, this aggregation is reversible, meaning that the chains break up if the magnetic field  $\mathbf{B}$  is suppressed [12, 38]. Experimentally, chains of several particles are typically observed [34,43,41] and, after a transient behaviour, the growth is successfully described on short timescale (typically a few hundreds of seconds) by a Smoluchowsky equation, predicting a power law behaviour of the mean size of the chains  $\langle s \rangle \propto t^z$  [34,41–44]. It has also been

shown that the magnetic field produced by each particle influences the magnetic moments of their neighbours, through mutual induction [46]. However, this effect is significant only if the magnetic susceptibility is of the order of ferromagnetic materials. In this paper we used particles with magnetic susceptibility of  $\chi \approx 0.09$ , with SI units convention. In this situation, the mutual induction only modifies the magnetic moment of approximately one percent, while the value of  $\Gamma$  is modified by less than two percent. We can then neglect this effect. Current research usually focuses on more complex structures, looking like ribbons or bundles, that have been observed under those conditions [47,36] and new theoretical models are studied in order to take them into account and describe their properties [45,48,49]. On longer time scales, though, it has been shown that the system reaches a thermal equilibrium [23,35,47,36,39]. The saturation time varies between the instantness and tenths of years, depending on the volume fraction and the value of  $\Gamma$  [23]. For values of mean length at saturation  $\langle s \rangle$  varying from unity to  $\approx 10^2$ , we previously observed experimental saturation time in the range of a few minutes to a few hours [36,39]. Up to now, the most convenient and efficient model for the mean length  $\langle s \rangle$  of the agglomerates at thermal equilibrium has been established by Faraudo *et al.* [47]

$$\langle s \rangle = \sqrt{\phi_0 \exp(\Gamma - 1)}. \quad (4)$$

Numerical simulations can be seen as useful tools to compare ideal experiments with actual experiments or theoretical expectations. Comparing with actual experiments can indicate if all the key physical ingredients are taken into account in the models. It can also be used to test some models in range of parameters which are not accessible experimentally. In the case of the analytical models for the mean chains length at saturation, [26,37] such simulations can (dis)confirm the mathematical approximations and the dependencies in the various parameters. However, classical techniques of numerical simulations (Langevin Dynamics, soft sphere discrete element methods, molecular dynamics, ...) would require several years of computing time to reach equilibrium state under some conditions: actual experiments last for hours and one second of simulation currently takes from 300 to 1100 hours of computing time. The most challenging situations are the ones leading to long chains, for which experiments and analytical models disagree [26,36,47]. Some researchers have developed alternative simulation techniques, where they consider the aggregation of the particles as irreversible and use a simplified magnetic interaction. This allows them to dynamically redefine the objects in the system and shorten the simulations by decreasing the numbers of objects to simulate [47]. However, those hypothesis are only valid when the magnetic interactions are really high and the system is diluted.

In the present work, we performed simulations with a modification of the viscosity of the surrounding fluid. We considered a fluid with a viscosity of  $\eta = 2.5 \cdot 10^{-5} \text{ Pa s}$ . As we showed in a previous work, above a certain threshold value, this doesn't fundamentally change the prop-

erties of the equilibrium of the system. [39] To validate our approach, we first begin to show that we indeed obtain the same results as with water ( $\eta = 1 \cdot 10^{-3} \text{ Pa s}$ ) in well-known conditions. Afterwards, we numerically explore the equilibrium of high volume fractions systems, which could not be reached previously. We obtain unexpected high average lengths of the chains. We then demonstrate that interaction between chains can explain those results through a statistical approach. Eventually, we confirm the improvement of those theoretical considerations with actual experimental data.

## 2 Numerical simulations methods

In our study, simulations are realised using a Soft Sphere Discrete Element Method [50–52]. The code is the same as the one we developed for previous studies. [39] The algorithm progresses with a constant time step and solves Newton’s equations of motion at each iteration. Regarding the involved forces, it takes into account the dipole-dipole interactions between the colloidal particles as well as the Brownian agitation in the system. In order to limit the computational cost, we introduced a cut-off distance for the magnetic dipole-dipole interaction, of about  $12R$ , by using a linked-cell method [53]. The random motion of a particle due to its interaction with surrounding fluid molecules in the heat bath can be described by using a Langevin equation [54]. To reproduce the effects of these interactions with the fluid, we then considered a drag force as  $\mathbf{F}_d = -6\pi R\eta\mathbf{v}$ , where  $\mathbf{v}$  is the velocity of the particle. The Brownian force  $\mathbf{F}_b$  is modeled as a Gaussian white noise process [55,56]. Regarding the collisions between particles, as well as collisions between a wall and a sphere, we model the normal contact force acting on two impacting objects as a linear spring-dashpot. We also take into account a tangential contact force, proportional to the relative slipping velocities of the particles and bounded by Coulomb’s criterion. Furthermore, since sedimentation plays an important role in the dynamics of our system, gravity and buoyancy have to be included. Detailed equations for each force can be found in a previous publication [39].

It is worthwhile to notice that changing the viscosity parameter  $\eta$  modifies both the drag force  $\mathbf{F}_d$  and the Brownian force  $\mathbf{F}_b$  in the simulations (indeed,  $F_d \propto \eta$  and  $F_b \propto \eta\sqrt{D} \propto \sqrt{\eta}$ ). Besides this, all the other parameters remain constant since they depend only on temperature and particle properties. In our simulations, we fixed the viscosity at  $\eta = 25 \mu\text{Pa.s}$ , in order to speed up the simulations. [39] This value of the viscosity is fixing the Peclet number  $Pe = \frac{R\chi^2}{36\mu_0} \sqrt{\frac{m}{3k_B T}} \frac{B^2}{\eta} \approx 0.11$  in a value largely below the critical Peclet number  $Pe_C = 0.825$  we determined in an earlier work. [39] This should then guarantee that the equilibrium behaviour of the suspension is not modified by the change of viscosity, but represents a gain of a factor 40 on the simulation time. This gain would not be possible by simply reducing the time step of the simulations. Indeed, the time step intervals are fixed according

to numerical stability of the collisions between particles. A safe value, not slowing down excessively the computation time, is given by  $t_{step} = \frac{2\pi}{40} \sqrt{\frac{m}{k}}$ , where  $m$  is the mass of the particles and  $k$  is the stiffness in the Hooke model for the particles collisions [50–52]. While decreasing this time step by a factor 40 would lead to numerical instability of the collisions, increasing the viscosity by this factor does not modify the evolution of the mean size if the system, as demonstrated in our previous work [39].

## 3 Numerical simulations results

We simulated systems within boxes with height  $Z = 10 \mu\text{m}$ , width  $X = 100 \mu\text{m}$  and length  $Y = 400 \mu\text{m}$ . The magnetic field has a component only in the direction  $y$  of the length of the box  $\mathbf{B} = B\mathbf{e}_y$ , where  $\mathbf{e}_y$  is the unitary horizontal vector parallel to the length  $Y$  of the box (the gravity being defined as  $\mathbf{g} = -g\mathbf{e}_z$ ). While there is a periodic boundary condition on the vertical walls of the boxes (in order to limit the effect of the system size), the particles interact with the horizontal walls with the same contact forces as between two spheres. The fact that no further interaction is required to model real colloidal systems is supported by our previous experimental studies, where particles experience free diffusion near the wall. [38]

Typical growth of the mean size of the chains along time  $\langle s \rangle(t)$  is represented in Fig. 2. The time has been adimensionalized by the characteristic time of aggregation of the particles  $t_B = \frac{6\pi\eta R^3}{48[(1/3)^{1/2} - (1/3)^{3/2}]U_0\phi}$  [34,39]. As one can see, the equilibrium state is reached after a characteristic time depending on the conditions of the simulations, as expected from previous works [26,39,36,23]. The rest of this section focus on the mean size of the chains at equilibrium, noted  $\langle s \rangle$

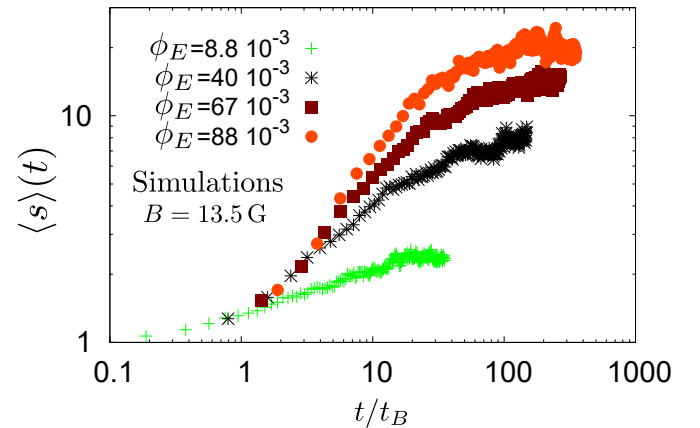


**Fig. 2.** Log-log plots of the evolution of the mean size of the chains  $\langle s \rangle(t)$  during simulations, for a magnetic field  $B \approx 13.5 \text{ G}$  ( $I = 8$ ), and various effective volume fractions  $\phi_E$ . The mean chains length is expressed in mean diameter of particles. The mean size of the chains is plotted as a function of the parameter  $t/t_B$ , where the characteristic time  $t_B$ .

We first performed simulations in a range of volume fraction  $\phi_0 = 1.15 \cdot 10^{-3}$  and magnetic field  $B \in [0; 21 \text{ G}]$  (i.e.  $\Gamma \in [0; 19]$ ) well characterized by previous studies. [26,23,47] In our system, we have to take into account the sedimentation. We then consider an effective sediment volume fraction of  $\phi_E = \phi_0 \frac{h}{2R} = 8.8 \cdot 10^{-3}$ , computed by assuming the height available for the particles is their diameter  $2R$ , and where  $h$  is the height of the cell. When this value of volume fraction is injected in eq.(4), we obtain the expected saturation value for the mean length of the chains  $\langle s \rangle$ , as illustrated in fig. 3. This confirms the thermal equilibrium in our simulations is equivalent to the observed equilibrium in systems with higher viscosities.

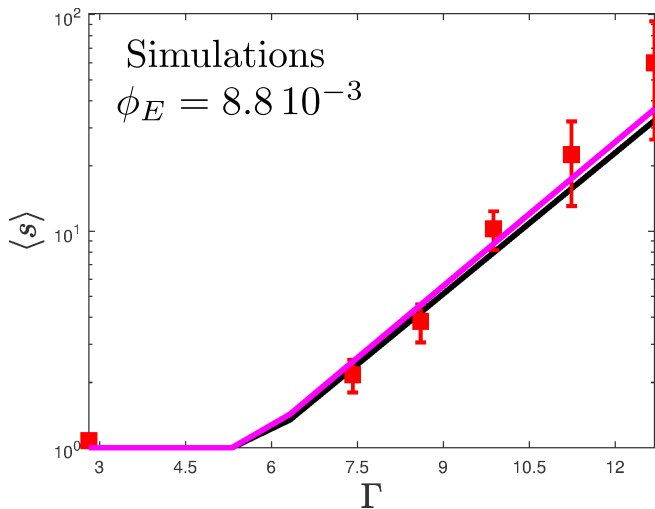


**Fig. 3.** Average lengths of the chains at saturation for various magnetic field with an effective sediment volume fraction  $\phi_E = 8.8 \cdot 10^{-3}$ . Red points are data obtained from several numerical simulations. The black (lower) curve is the model of eq. (4) and the magenta (higher) curve is the model from eq.(9), with  $K = 2.2$ .

We also performed simulations for the same magnetic fields  $B$  and parameters  $\Gamma$ , but with a ten times higher volume fraction  $\phi_0 = 11.5 \cdot 10^{-3}$ , or  $\phi_E = 88 \cdot 10^{-3}$ . The results for those conditions are illustrated in fig. 4. As one can see, the model from eq.(4) systematically underestimates the mean length of the chains  $\langle s \rangle$  in that particular situation. This highlights that a high volume fraction influences the mean length  $\langle s \rangle$  in some way which has still to be understood.

In order to understand the role of the volume fraction, we then performed simulations with a fixed magnetic field  $B = 13.5 \text{ G}$  and parameter  $\Gamma = 8$ , but various volume fraction  $\phi_0$  (and  $\phi_E$ ). The data from those simulations are represented in fig. 5. From these, we can see that the model from eq.(4) is accurate for sediment volume fractions up to  $\phi_E = 2.6 \cdot 10^{-2}$ . However, for higher volume fractions, the mean length at equilibrium  $\langle s \rangle$  is higher than predicted by this law. Then, there must be some mechanism through which the volume fraction modifies this length. We discuss in the next section how the interaction between existing chains can be this mechanism.

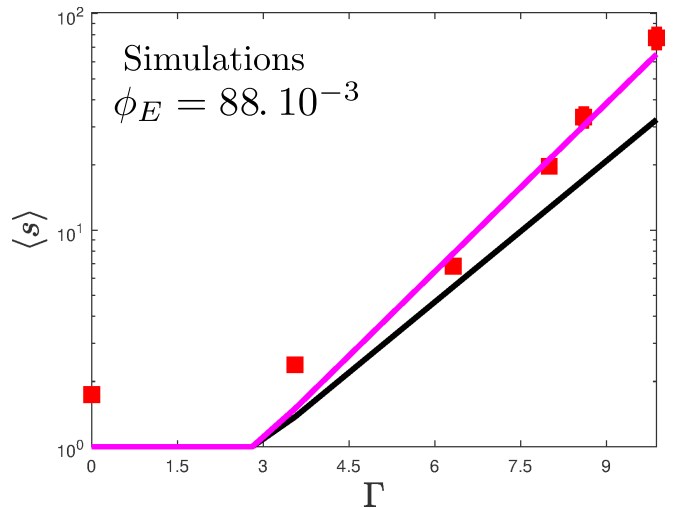


**Fig. 4.** Average lengths of the chains at saturation for various magnetic field with an effective sediment volume fraction  $\phi_E = 88 \cdot 10^{-3}$ . Red points are data obtained from several numerical simulations. The black (lower) curve is the model of eq. (4) and the magenta (higher) curve is the model from eq.(9), with  $K = 2.2$ .

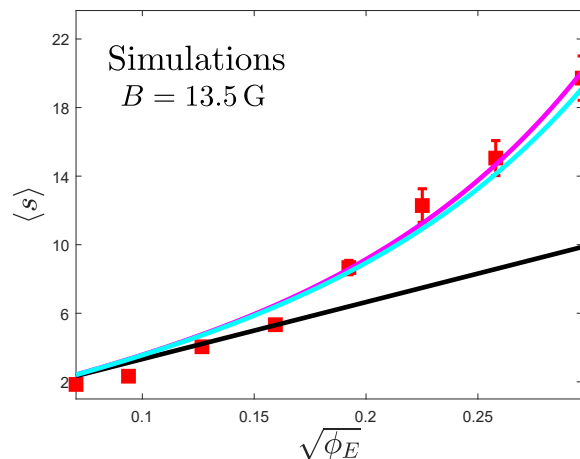


**Fig. 5.** Average lengths of the chains at saturation for various volume fraction with a magnetic field  $B = 13.5 \text{ G}$  ( $\Gamma = 8$ ). Red points are data obtained from several numerical simulations. The black line is the previous model (eq.(4), while the blue (mid-high) curve is our new model (eq. (9)), with the approximate value  $K = 6/\pi$ . The magenta (higher) curve is a fit of this latter, with  $K$  as a fitting parameter, giving  $K = 2.2$ .

We also measured the distribution of the chains' size obtained in our last set of simulations. As one can see in Fig. 6, these distributions can be scaled thanks to predictions of the thermodynamic model (see section 4).

## 4 Thermodynamic model

The previous model (eq. (4)) is based on thermodynamics development where the thermal equilibrium determines

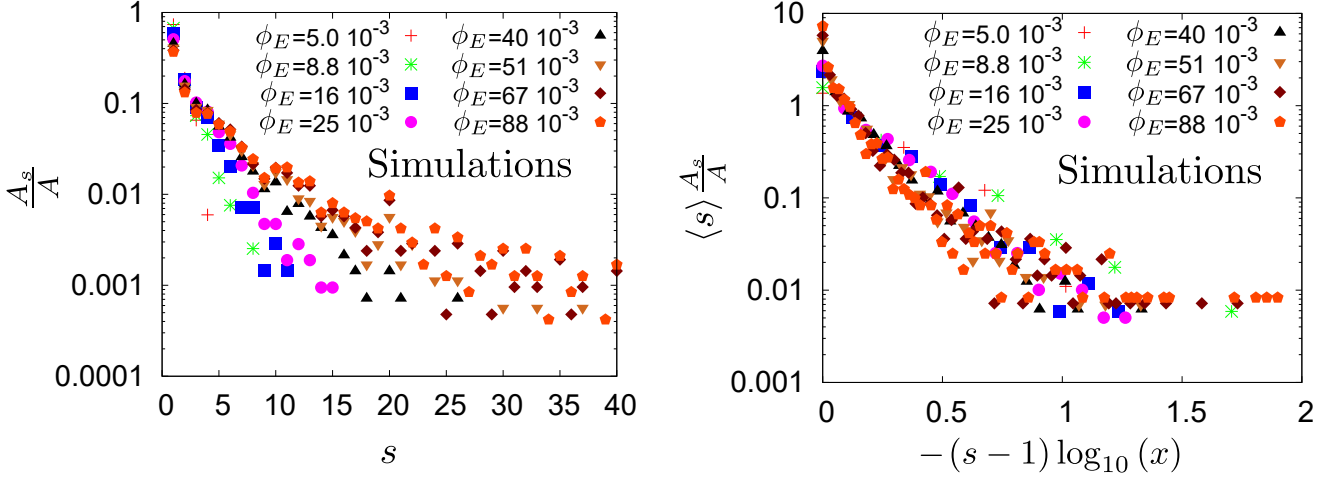


**Fig. 6.** Distribution of the chains' size  $s$  obtained with simulations, for various volume fraction and  $\Gamma = 8$ . Left: Normalized distribution of the number of chains  $A_s$  on the total number of chains  $A$ , for various effective volume fraction. Right: Scaling predicted by the models, with  $\langle s \rangle$  being the actual mean size of the agglomerates at equilibrium and  $x = (1 - 1/\langle s \rangle)$ . With this scaling, predicted by both models, all the data collapse on the same curve.

the homogeneity of the chemical potential of every particles. This model can then be easily modified if one finds a dependency of the chemical potential as a function of the volume fraction. For this purpose, we consider the expression of the chemical potential  $\mu_s$  for a chain of  $s$  colloidal particles

$$\mu_s = \mu_s^0 + \frac{1}{s} \left[ k_B T \ln \frac{\phi_s}{s} \right] \quad (5)$$

where  $\mu_s^0$  is the mean free-energy per particle and the second term comes from the entropy, with  $\phi_s$  being the volume fraction of the chains of lengths  $s$  (see Eqs. (19.1) and (19.6) in Ref. [57], and development in Ref. [47]). The model leading to eq.(4) has been established by considering that the energy of a chain of  $s$  colloids with a magnetic bond energy  $-\epsilon$  is  $-(s-1)\epsilon$ . This gives  $\mu_s^0 = \mu^0 - (s-1)\epsilon/s$ . [47,57]. In 3D, the bond can be assessed as  $\beta\epsilon \approx \Gamma - 1$ , where  $\beta = 1/(k_B T)$ , from a mean-field hypothesis. We discuss in Appendix 7 the difference between 2D and 3D models and show that the 3D model has to be used in our case.

In order to have a further effect of the volume fraction, we suggest considering the interaction between the chains of colloids. We will here introduce a reasoning to apply another mean-field theory to this interaction. Let us consider the case of long chains created in a high volume fraction suspension. We can idealize the system as a succession of parallel chains separated by a mean distance  $d$ . If we assume that the chains are long compared to their distance  $d$ , we can assimilate these chains to magnetic needles whose interacting energy  $U_{CC}$  behaves like

$$U_{CC} = \frac{\mu_0}{4\pi} \frac{\mu^2}{4R^2} \frac{2}{d}, \quad (6)$$

see eq.(16) in Ref. [58]. By considering the sedimentation, the available volume for each particle goes like  $\tilde{V} \approx d4R^2$ , while their own volume is  $V_p = 4\pi R^3/3$ . The total sediment volume fraction is then  $\phi_E = V_p/\tilde{V} = (\pi R)/(3d)$ .

This leads the average distance  $d$  between the chains to be  $d = (\pi R)/(3\phi_E)$ . Then, each chain has a repulsive interaction with its two neighbours, creating an interaction energy per chain

$$U_{CC} = \frac{\mu_0}{4\pi} \frac{\mu^2}{4R^2} \frac{6\phi_E}{\pi R} = \frac{6}{\pi} \Gamma k_B T \phi_E \equiv K k_B T \Gamma \phi_E, \quad (7)$$

where  $K = \frac{2R}{d\phi_E}$  is a geometric constant that our idealization approximates as  $K \approx 6/\pi$ . The chemical potential of the particles can then eventually be expressed as

$$\mu_s = \mu^0 + \frac{1}{s} \left[ k_B T \ln \left( \frac{\phi_s}{s} \right) - (s-1)\epsilon + K k_B T \Gamma \phi_E \right]. \quad (8)$$

Then, a reasoning perfectly analogous to the one of Faraudo *et al.* [26], based on the equilibrium of the chemical potential  $\mu_1 = \mu_s$  and the constraint  $\phi_E = \sum_s \phi_s$ , leads to

$$\langle s \rangle = \sqrt{\phi_E \exp(\Gamma - 1 + K\Gamma\phi_E)}. \quad (9)$$

This model has been represented in fig. 5. The value of  $K = 6/\pi$  gives the blue curve. As can be seen in the graph, this curve has the right trend and is in good agreement with the numerical data. Moreover, if one would like to determine a more accurate value for  $K$ , one can fit this eq. (9) with the data from Fig. 5. Fitting eq. 9 with  $K$  as a fitting parameter gives a value of  $K \approx 2.2$  (magenta curve on fig. 5). Since we really simplified the system to obtain the value of  $K = 6/\pi \approx 1.9$ , and given the good agreement with all the data (for the fit  $R^2 = 0.95$ ), it seems reasonable to accept that actual geometrical constraints lead to this value. Furthermore, the fact that the actual value of  $K$  is higher than the ideal value we computed can be justified by the fact that all the chains are not separated exactly by the mean distance  $d$ . For instance, let us consider that all the chains are not separated by exactly the same lateral distance  $D$ , but that this distance has a homogeneous distribution between  $(1-a)d$  and  $(1+a)d$ . This kind of

distribution is somehow realistic because, due to the fixed volume of the suspension, if one chain approaches one of its neighbour it moves away from another one. (Strictly, this implies that real distributions have to be symmetric around  $d$ .) The mean value of  $1/D$  is then found to be

$$\left\langle \frac{1}{D} \right\rangle = \frac{1}{2ad} \int_{(1-a)d}^{(1+a)d} \frac{1}{D} dD = \frac{\ln\left(\frac{1+a}{1-a}\right)}{2a} \frac{1}{d}. \quad (10)$$

The effective value of the energy between the chains should then consider this mean value of  $1/D$  instead of  $1/d$ :  $U_{CC} = \frac{\mu_0 \mu^2}{4\pi 4R^2} 2 \left\langle \frac{1}{D} \right\rangle \dots$  And we then obtain  $K = \frac{2R}{\phi_E} \left\langle \frac{1}{D} \right\rangle$ . A value of  $K = 2.2$  is then given by a width of distribution  $a = 0.604$ , which would mean that the distribution of the distance  $D$  has a width of 64% of its mean value, given it was uniform.

Moreover, the curve corresponding to eq.(9) with  $K = 2.2$  has been represented on the Figs. 3 and 4. Indeed, eq.(9) also shows a different dependency on  $\Gamma$  than eq.(4). For the case of low volume fraction (fig. 3), both models give pretty similar results, in good agreement with the numerical data. In the case of high volume fraction (fig. 4), both models fail to explain the low  $\Gamma$  data, but eq. (9) is in good agreement with the numerical data for higher  $\Gamma$ . Actually, such a deviation in the beginning of the data is due to an increased probability of random collisions between particles which create temporary aggregates. Those agglomerates are formed by particles whose contact time is directly controlled by the collision of the particles and are not sticking together due to magnetic interactions. Of course, this can only occur in low  $\Gamma$  configuration, and they are not taken into account in the equilibrium ensemble of the models, because it is not the competition between their magnetic and thermal energy which creates the agglomerate, but rather geometrical constraints (i.e. the space available for each particle during their free diffusion). For instance, some of these agglomerates can be oriented perpendicularly to the magnetic field, which is not considered in the equilibrium model, given their repulsive magnetic interaction. Actually, the model computing  $\beta\epsilon \approx \Gamma - 1$  considers only chains constituted of particles whose angles between their magnetic moment (in the direction of the external field) and the direction pointing to the centre of their closest neighbours is comprised between  $-\theta_0$  and  $\theta_0$ , where  $\theta_0 = \arcsin \sqrt{2/3}$ , so that the radial component of the magnetic interaction is attractive. Moreover, the analytical expression of both models have been obtained with approximations assuming that  $\Gamma$  and the predicted value of the average chains length are large in front of 1. (see eqs. (6) and (7) in Ref. [26]). Furthermore, the configuration of parallel long chains leading to eq. (9), which can happen only with an important magnetic field, or  $\Gamma$ , is not suitable to describe a system composed of small agglomerates. The expression of  $U_{CC}$  in eq. (7) has explicitly be obtained by assuming that the length of the chains is longer than their distance (see Ref. [58]) which means  $d > \langle s \rangle R \Leftrightarrow \phi_E \langle s \rangle > \pi/3$ . Since the effective volume fraction we used is of the order of  $\phi \approx 0.1$ , this is another reason why our model becomes accurate for values

of  $\langle s \rangle \gtrsim 10$ . The agreement with only the high  $\Gamma$  points is then not surprising. For lower volume fraction, however, the term  $K\Gamma k_B T \phi_E$  is often negligible to  $\Gamma - 1$  and does not modify too much the predicted value (as illustrated in Fig. 3).

The distribution of the chains size obtained in our simulations is represented in the Fig. 6. To compare with the models, one can note that both model imply that the number  $A_s$  of chain with length  $s$  is proportional to  $A_s \propto \phi_s/s \propto x^s$ , where  $x = \phi_1 \exp(\Gamma - 1 + K\Gamma\phi_E)$  in our case and  $x = \phi_1 \exp(\Gamma - 1)$  in the previous model. From this, it comes that the normalized distribution of the chains  $A_s/A$ , with  $A = \sum_{s=1}^{+\infty} A_s$  behaves like  $A_s/A = (1-x)x^{s-1}$ .

In the limit  $\langle s \rangle \gg 1 \Rightarrow x \approx (1 - 1/\langle s \rangle)$ , leading to eqs. (4) and (9), we can then write  $\log_{10}(\langle s \rangle A_s/A) = (s-1) \log_{10} x$ . The mean size of particles at equilibrium is then the only relevant parameter in the system, since it determines the distribution of the particles. While the finite size of the systems we simulated prevent the data to exactly follow this relation, it can still be used as an efficient scaling law to collapse all the data on a same master curve, as illustrated in Fig. 6

In order to confirm those theoretical considerations, we also performed actual experiments described in the next section.

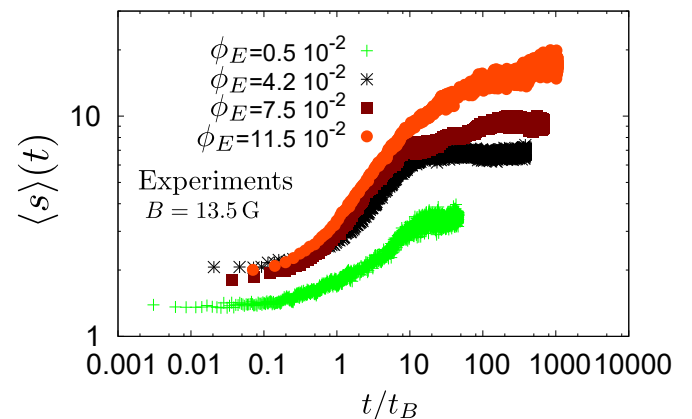


**Fig. 7.** Log-log plots of the evolution of the mean size of the chains  $\langle s \rangle(t)$  during experiments, for a magnetic field  $B \approx 13.5$  G, and various effective volume fraction  $\phi_E$ . The mean chains length is expressed in mean diameter of particles. The mean size of the chains is plotted as a function of the parameter  $t/t_B$ , where the characteristic time  $t_B$ .

## 5 Experimental setup

A part of a typical experimental picture is presented in fig. 1. The experiments were performed with superparamagnetic microspheres dispersed in water (Estapor<sup>®</sup> M1-070/60), with a volumic fraction varying from  $\phi_0 = 1 \cdot 10^{-4}$  to  $\phi_0 = 23 \cdot 10^{-4}$  ( $\phi_E = 5 \cdot 10^{-3}$  to  $\phi_E = 115 \cdot 10^{-3}$ ). The suspension was placed inside a cylindrical chamber



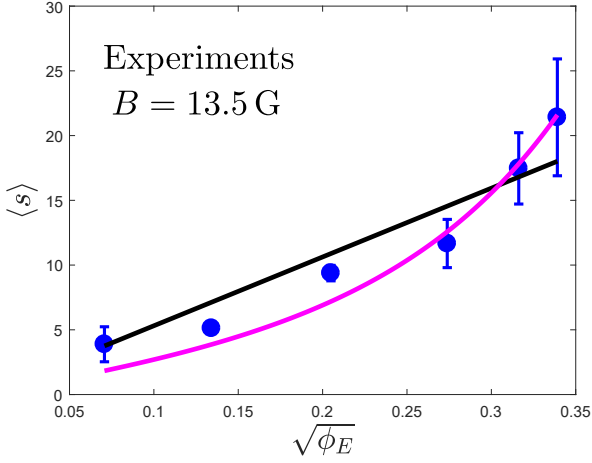


**Fig. 8.** Equilibrium mean size of the particles as a function of effective volume fraction  $\phi_E$ . The circles are experimental measurements while the curves are the fitted models. The black line is the fit from eq.(4), while the magenta curve is a fit from our model (eq.(9)). One can see that eq.(9) gives a trend consistent with the experimental data.

of diameter  $D = 5$   $\mu\text{m}$  and thickness approximately  $h = 50$   $\mu\text{m}$ . The chamber was formed by two parallel glass plates. The first glass plate was covered with an approximately 50  $\mu\text{m}$  layer of epoxy with the exemption of a circular region. A suspension droplet of 1  $\mu\text{l}$  was placed inside this region. Afterwards, the second glass plate was placed on the first one. A small quantity of low-viscosity silicon oil was placed on the epoxy to assess the watertightness of the chamber. A constant and homogeneous magnetic field  $B \approx 13.5$  G was generated by a constant current in surrounding coils at the beginning of each experiment. The magnetic field produced by those coils was characterized with a Hall probe and was homogeneous within the precision range of the probe of 2% around the cell. The current in the coils had a constant intensity controlled by a programmable DC power supply GenH-750W from TDK Lambda, with a precision of 0.01 A. The suspension was observed from the bottom with a 40x magnification. The microscope used was an inverted microscope Olympus IX73, connected to a 4070M-CL Thorlabs Camera with 2048 by 2048 pixels of 16 Bits depth. The images were recorded with a frame rate of 1fps during ten minutes, then a frame rate of 0.1 fps is applied. Each experiment lasted between five and eight hours. Experiments were performed at least three times for each condition in order to assess reproducibility of the results.

## 6 Experimental validation

Experimental growth of the mean size of the chains along time  $\langle s \rangle(t)$  is represented in Fig. 7. As for the simulations, the time has been adimensionalized by the characteristic time of aggregation of the particles  $t_B$ . As one can see, the equilibrium state is again reached after a characteristic

time depending on the conditions of the simulations. The rest of this section focus on the mean size of the chains at equilibrium, noted  $\langle s \rangle$

The measured equilibrium mean size of the particles as a function of effective volume fraction is shown in fig. 8. The dispersion of the properties of the particles making the efficient  $\Gamma$  value hard to estimate, we performed a fit on its value. Actually, one can estimate the range of plausible  $\Gamma = \frac{\pi R^3 \chi^2 B^2}{\mu_0 9 k_B T}$  from the distributions of radius  $R$  and susceptibility  $\chi$  in our sample of colloids. Since the distribution of  $R$  has a width of approximately 15% around its mean and the distribution of susceptibility  $\chi$  has a width of 10% around its mean value, we obtain a range of plausible  $\Gamma \in [2.2; 8.3]$ . This range being actually pretty large, is why it seems more suitable to determine the actual effective value of  $\Gamma$  through a fit.

One can see that eq.(9), considering  $K = 2.2$ , gives a trend consistent with the experimental data. Moreover, our model (eq.(9)) gives a higher coefficient of determination ( $R^2 \approx 0.95$ ) than the previous model (eq.(4),  $R^2 \approx 0.89$ ), and the fitted value of the  $\Gamma$  parameter is also closer from the value computed from mean properties of the particles. Indeed, the value of  $\Gamma$  computed from mean square susceptibility and cube radius is around  $\Gamma = 4.5$  while the fittings gives  $\Gamma = 7$  for eq.(9) and  $\Gamma = 9$  for eq.(4).

The experimental distribution of chains size is illustrated in Fig. 9. These distribution contain more noise (mainly due to image analysis) and are as clearly separated than the ones obtained with the simulations. However, the previous scaling  $\log_{10}(\langle s \rangle A_s / A) = (s - 1) \log_{10} x$  still collapse all the data on the same curve.

## 7 Conclusions

Our simulations and experiments demonstrated that the current model (eq. (4)) regarding the equilibrium length of superparamagnetic colloids under magnetic field does not reproduces the adequate volume fraction dependency. Indeed, we identified the ignored interactions between the chains as a cause of divergence between this model and both numerical and experimental data. Moreover, we showed that idealizing assumptions could lead to a consistent model. We showed this modification is not only important when only the volume fraction is varying, but also when considering a high volume fraction system and varying the characteristic interaction energy of the particles (i.e. by varying  $\Gamma$  by any means). Accordingly, this work opens new perspectives to model and understand such high volume fraction systems.

## Acknowledgements

A.D. is financially supported by FNRS as research fellow. This work was financially supported by the FNRS (Grant PDR T.0043.14) and by the University of Liège (Starting Grant C-13/88). E.O. acknowledges financial support by the European Space Agency and Belpo (Prodex) via the

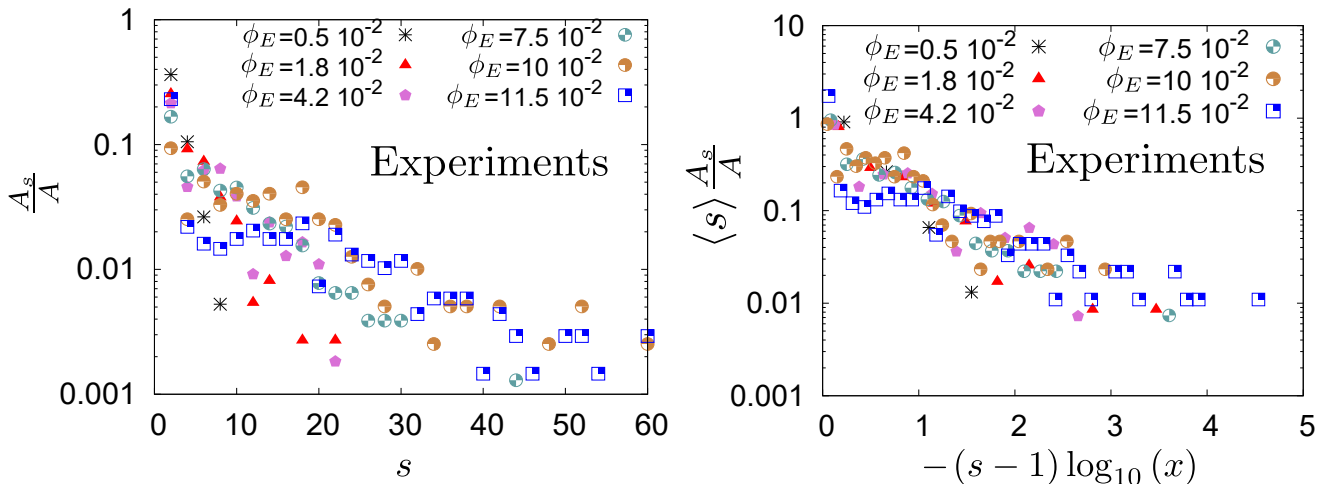


**Fig. 9.** Distribution of the chains of size  $s$  obtained in experiments, for various volume fraction and a constant magnetic field  $B \approx 13.5$  G. Left: Normalized distribution of the number of chains  $A_s$  on the total number of chains  $A$ , for various effective volume fraction. Right: Scaling predicted by the models, with  $\langle s \rangle$  being the actual mean size of the agglomerates at equilibrium and  $x = (1 - 1/\langle s \rangle)$ . With this scaling, predicted by both models, all the data collapse on the same curve.

VipGran Project. Authors thank Charlotte Marique for spell-checking the manuscript.

Faraudo *et al.*[26] leads to  $\beta\epsilon^{2D} = \Gamma - 1/2$  [36]. We then have a final model  $\langle s \rangle = \sqrt{\phi_S^{2D} \exp(\Gamma - 1/2)}$ .

### Author contributions statement

GL and AD conceived the experiments, AD conducted the experiments, EO and AD conceived the simulation code, EO wrote the simulation code, AD managed the simulations, EO and AD wrote the manuscript. AD and NV built the theoretical model. AD, EO, GL and NV analyzed the results and reviewed the manuscript.

### Additional information

The datasets generated during and/or analysed during the current study are available from the corresponding author on reasonable request.

### Appendix A. Dimensionality of the models

We used a 3D model for the aggregation instead of a 2D model, even if the particles sediment in our simulations and experiments. Indeed, as we demonstrated in a previous work [36], there are two ways Faraudo's model should be modified to take a change of dimension into account. The first one is that the surface fraction  $\phi_S^{2D} \equiv \frac{N\pi R^2}{A}$ , where  $N$  is the number of particles,  $R$  their radius and  $A = XY$  the area of the bottom plate, should be used instead of the volume fraction. The second way the model should be modified is through the effective mean bond energy  $\epsilon$ . This parameter is related to  $\Gamma$  through a thermodynamic mean value of the magnetic interaction energy, and makes use of a Jacobian depending on the dimensionality. Introducing the right 2D configuration space in the computations of

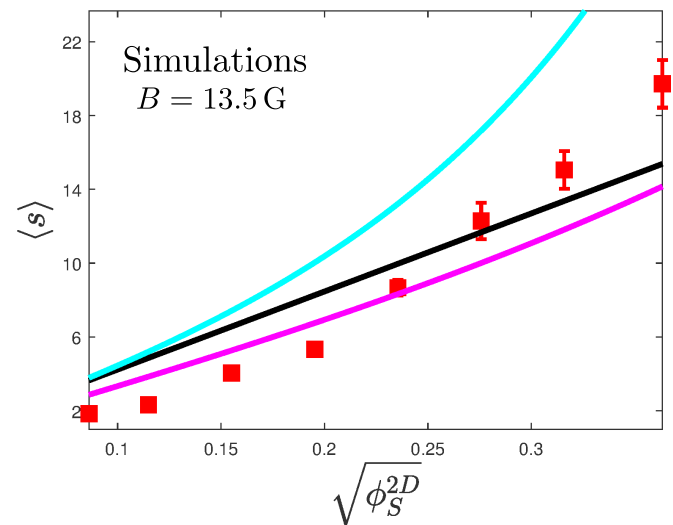


**Fig. 10.** Average lengths of the chains at saturation for various surface fraction with a magnetic field  $B = 13.5$  G ( $\Gamma = 8$ ). Red points are data obtained from several numerical simulations. The black line is the 2D version of Faraudo's model, while the blue (mid-high) curve is the 2D version of our new model, with the approximate value  $K = 4/\pi$ . The magenta (higher) curve is a fit of this latter, with  $K$  as a fitting parameter, giving  $K = 0.32$ .

However, as illustrated in Fig.10 when we compared this model with our data, it does not catch their trend at all... While the 3D version of Faraudo's model actually predicts efficiently the saturation values, once we used the effective volume fraction  $\phi_E$  in the vicinity of the sedimented particles (which differs from the 2D surface frac-

tion by a factor  $2/3$   $\phi_E = \frac{N4\pi R^3}{3XY2R} = \frac{2}{3}\phi_S^{2D}$ , as it does for the case of data in Fig. 3 (which has been obtained in conditions similar to those for which the model has been developed).

Similarly, our proposition and the computation of  $d$  and  $K$  would depend on the dimensionality. In 2D, the available surface for each particle would go like  $\tilde{A} \approx 2Rd$  while their own surface is  $\pi R^2$ . The mean distance  $d$  would then be obtained through  $\phi_S^{2D} = \frac{\pi R}{2d} \Rightarrow d = \frac{\pi R}{2\phi_S^{2D}}$  leading to  $K = \frac{4}{\pi}$  to write  $U_{CC} = K k_B T \Gamma \phi_S^{2D}$ .

As can be seen from Fig.10, none of the 2D curves match any part of the data's trend. One should not be surprised that the 2D models do not efficiently predicts what happens in our simulations, which are as close as possible from our experiments. Indeed, the particles are not strictly restricted to a 2D plane : the thermal energy of the system is approximately equal to  $mg2R$ , with  $m$  the mass of the particles, allowing single particles to elevate their centre of mass over another particle. This means that collisions between particles are actually 3D. Since the volume fraction influences the mean size of the chains through their probability of collisions, this explains why one has to take into account the volume fraction of the particles in the sedimented layer and not their surface fraction. Moreover, this thermal agitation makes that no solid constraint restricts the elevation between two neighbouring particles. Then, the same configuration space is available for the particles as in 3D (contact between two particles is still defined through a surface, not through a curve). Since this configuration space determines the properties of the systems at equilibrium, it is then not surprising that it is the same as predicted by a 3D model. While the kinetics leading to this equilibrium might differ (since approximately one half of the path leading to aggregation are missing compared to pure 3D cases), there are no reasons why the equilibrium state should be considered to be 2D.

## References

- J. Yu, B. Wang, X. Du, Q. Wang, L. Zhang, Nature communications **9**, 3260 (2018)
- K. Müller, N. Osterman, D. Babič, C.N. Likos, J. Dobnikar, A. Nikoubashman, Langmuir **30**, 5088 (2014)
- M. Llera, J. Codnia, G.A. Jorge, J. Magn. Magn. Matter **384**, 93 (2015)
- R.M. Erb, H.S. Son, B. Samanta, V.M. Rotello, B.B. Yellen, Nature **457**, 999 (2009)
- H. Löwen, Journal of Physics: Condensed Matter **20**, 404201 (2008)
- V. Froltsov, R. Blaak, C. Likos, H. Löwen, Physical Review E **68**, 061406 (2003)
- F. Martinez-Pedrero, P. Tierno, Phys. Rev. Applied **3**, 051003 (2015)
- F. Martinez-Pedrero, A. Ortiz-Ambriz, I. Pagonabarraga, P. Tierno, Phys. Rev. Lett. **115**, 138301 (2015)
- H. Carstensen, V. Kapaklis, M. Wolff, Phys. Rev. E **92**, 012303 (2015)
- P. Liu, J.W. De Folter, A.V. Petukhov, A.P. Philipse, Soft Matter **11**, 6201 (2015)
- D.L. Blair, A. Kudrolli, Physical Review E **67**, 021302 (2003)
- P. Domínguez-García, J. Pastor, M. Rubio, Eur. Phys. J. E **34**, 1 (2011)
- P. Domínguez-García, S. Melle, J. Pastor, M. Rubio, Phys. Rev. E **76**, 051403 (2007)
- S. Merminod, T. Jamin, E. Falcon, M. Berhanu, Physical Review E **92**, 062205 (2015)
- K.V. Edmond, H. Park, M.T. Elsesser, G.L. Hunter, D.J. Pine, E.R. Weeks, Chaos-Woodbury **21**, 041103 (2011)
- R. Dreyfus, J. Baudry, M.L. Roper, M. Fermigier, H.A. Stone, J. Bibette, Nature **437**, 862 (2005)
- J.W. Tavacoli, P. Bauër, M. Fermigier, D. Bartolo, J. Heuvingh, O. du Roure, Soft Matter **9**, 9103 (2013)
- U. Jeong, X. Teng, Y. Wang, H. Yang, Y. Xia, Adv. Mater. **19**, 33 (2007)
- J.L. Corchero, A. Villaverde, Trends Biotechnol. **27**, 468 (2009)
- B. Kozissnik, A.C. Bohorquez, J. Dobson, C. Rinaldi, International Journal of Hyperthermia **29**, 706 (2013)
- Q. Pankhurst, N. Thanh, S. Jones, J. Dobson, Journal of Physics D: Applied Physics **42**, 224001 (2009)
- M. Colombo, S. Carregal-Romero, M.F. Casula, L. Gutiérrez, M.P. Morales, I.B. Böhm, J.T. Heverhagen, D. Prosperi, W.J. Parak, Chemical Society Reviews **41**, 4306 (2012)
- J. Faraudo, J.S. Andreu, J. Camacho, Soft Matter **9**, 6654 (2013)
- C.T. Yavuz, J. Mayo, W.Y. William, A. Prakash, J.C. Falkner, S. Yean, L. Cong, H.J. Shipley, A. Kan, M. Tomson et al., Science **314**, 964 (2006)
- K.M. Krishnan, IEEE Trans. Magn. **46**, 2523 (2010)
- J.S. Andreu, J. Camacho, J. Faraudo, Soft Matter **7**, 2336 (2011)
- G.P. Gajula, M.T. Neves-Petersen, S.B. Petersen, Appl. Phys. Lett. **97**, 103103 (2010)
- K.S. Khalil, A. Sagastegui, Y. Li, M.A. Tahir, J.E. Socolar, B.J. Wiley, B.B. Yellen, Nat. Commun. **3**, 794 (2012)
- Y. Gurevich, Y. Mankov, R. Khlebopros, Dokl. Phys. **11**, 478 (2013)
- F. Martinez-Pedrero, P. Tierno, Phys. Rev. Applied **3**, 051003 (2015)
- H. Carstensen, V. Kapaklis, M. Wolff, Phys. Rev. E **92**, 012303 (2015)
- C.T. Yavuz, A. Prakash, J. Mayo, V.L. Colvin, Chem. Eng. Sci. **64**, 2510 (2009)
- P. Domínguez-García, S. Melle, J. Pastor, M. Rubio, Physical Review E **76**, 051403 (2007)
- J.H. Promislow, A.P. Gast, M. Fermigier, J. Chem. Phys. **102**, 5492 (1995)
- J. Faraudo, J. Camacho, Colloid Polym. Sci. **288**, 207 (2010)
- A. Darras, J. Fiscina, M. Pakpour, N. Vandewalle, G. Lumay, The European Physical Journal E **39**, 1 (2016)
- N. Rojas, A. Darras, G. Lumay, Physical Review E **96**, 012608 (2017)
- A. Darras, J. Fiscina, N. Vandewalle, G. Lumay, American Journal of Physics **85**, 265 (2017)
- A. Darras, E. Opsomer, N. Vandewalle, G. Lumay, Scientific reports **7**, 7778 (2017)
- M. Fermigier, A.P. Gast, Journal of colloid and interface science **154**, 522 (1992)

41. S. Fraden, A.J. Hurd, R.B. Meyer, *Phys. Rev. Lett.* **63**, 2373 (1989)
42. M. Kolb, *Phys. Rev. Lett.* **53**, 1653 (1984)
43. F. Martínez-Pedrero, M. Tirado-Miranda, A. Schmitt, J. Callejas-Fernández, *Phys. Rev. E* **76**, 011405 (2007)
44. S. Miyazima, P. Meakin, F. Family, *Phys. Rev. A* **36**, 1421 (1987)
45. H. Ezzaier, J. Alves Marins, I. Razvin, M. Abbas, A. Ben Haj Amara, A. Zubarev, P. Kuzhir, *The Journal of Chemical Physics* **146**, 114902 (2017)
46. H. Zhang, M. Widom, *Physical Review E* **51**, 2099 (1995)
47. J. Faraudo, J.S. Andreu, C. Calero, J. Camacho, *Advanced Functional Materials* p. 3837 (2016)
48. R. Messina, L.A. Khalil, I. Stanković, *Physical Review E* **89**, 011202 (2014)
49. N. Vandewalle, S. Dorbolo, *New Journal of Physics* **16**, 013050 (2014)
50. T. Pöschel, T. Schwager, *Computational granular dynamics: models and algorithms* (Springer Science & Business Media, 2005)
51. F. Radjaï, F. Dubois, *Discrete-element modeling of granular materials* (Wiley-Iste, 2011)
52. J.Y. Ooi, V. Magnanimo, J. Sun, S. Luding, *Powder technology* **293**, 1 (2016)
53. U. Welling, G. Germano, *Computer Physics Communications* **182**, 611 (2011)
54. N. Pottier, *Physique statistique hors d'équilibre: processus irréversibles linéaires* (EDP Sciences, 2007)
55. Z. Peng, E. Doroodchi, G. Evans, *Powder Technology* **204**, 91 (2010)
56. A. Li, G. Ahmadi, *Aerosol science and technology* **16**, 209 (1992)
57. J.N. Israelachvili, *Intermolecular and surface forces: revised third edition* (Academic press, 2011)
58. R. Messina, L. Spiteri, *The European Physical Journal E* **39**, 81 (2016)

## Part III

# Self-Assembly in evaporating droplets



# Chapter 7

## Transitional Marangoni instability

### 7.1 Motivations

When performing preliminary tests with evaporating droplets of superparamagnetic colloids under magnetic field, we observed qualitatively different stages during the lifetime of a droplet. At first, it seemed that chains were forming as if evaporation had no influence on their growth... But at the end of the evaporation, chains were destroyed by the inner flows. Moreover, some patterns looking like the ones produced by Marangoni instabilities were observed superimposed to the remaining chains... We then decided to characterize the fluid flows inside the droplet in order to better understand what phenomena were occurring and how they compete with each other along time.

### 7.2 Setup and methods

We evaporated a series a colloid droplets containing some fluorescent particles, in order to measure the inner flows through PIV. The microspheres were dispersed in water with diluted phosphate buffered saline (PBS). The PBS has been chosen since it is a commercially available pH buffer involving only non-organic molecules. Indeed, pH and ions concentration are often used as parameters to control electrostatic stabilization, and organic molecules could potentially feed bacteria who could reach the suspension as it ages (which was a main trouble during the exploratory part of this work).

We used an inverted microscope to film the droplet from below, and performed experiments with various focal planes in order to have an idea of the 3D flows. A custom airtight evaporative chamber is placed upon the droplet, in order to prevent air flow around it and to ensure the reproducibility of the measurements.

### 7.3 Main results

We identified four stages during the evaporation of the droplets. The first one (*I*) is characterized by an overall diverging flow characteristic from the coffee ring effect. This stage is followed by a transition to a Marangoni instability (*II*), where several recirculation cells are observed along one radius of length. During this stage, a honeycomb-like pattern is formed at the surface of the droplet. The stage *III* is a short time during which the structures at the surface collapse towards the top center. At the end, a stage *IV* with a strong diverging flow is observed again. This behaviour is illustrated in Figure 7.1. The top row *a*) of this Figure 7.1 shows images obtained by fluorescence microscopy, showing the structure formed by the particles at various time. The row *b*) shows the velocity field and its divergence, highlighting the various flow regimes. The bottom row *c*) shows 3D schemes of the velocity field, built accordingly to the observations we performed in various focus planes and summarizing the various flow regimes.

The transition from stage *I* to stage *II* can be explained through a solutal Marangoni number  $Ma = (\frac{\partial\sigma}{\partial\kappa} \Delta \kappa t_f)/(\eta R_d)$ , with the notations defined in the Introduction and  $\kappa \equiv C_i/C_i(PBS)$  is a dimensionless volumic concentration defined as the ratio between the

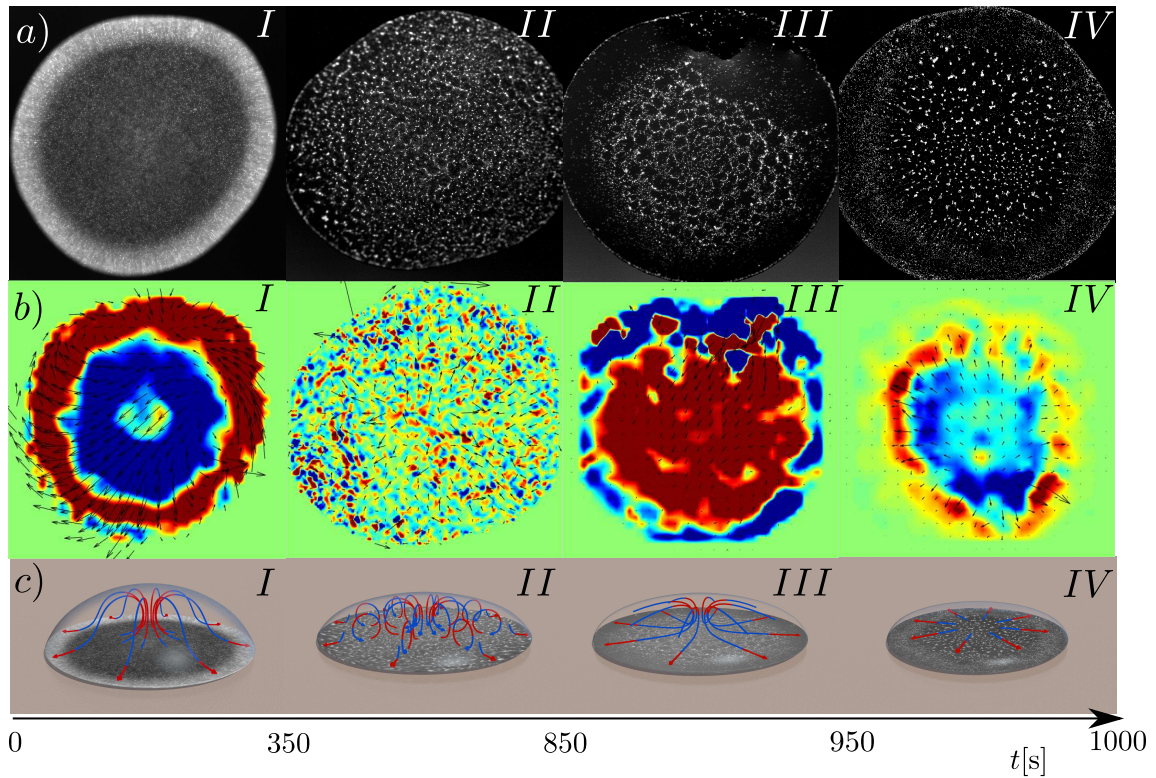


Figure 7.1: Picture from [89]. Main results from PIV measurements. The pictures in row *a*) are obtained experimentally with focus near the top of the droplet. The pictures for different times are then taken from different focus height. Row *b*) shows the computed 2D velocity field  $\vec{v}(\vec{r})$  corresponding to the upper pictures. The colours correspond to the velocity's 2D divergence  $\vec{\nabla} \cdot \vec{v}(\vec{r})$ , with blue being the positive values corresponding to areas from where the particles diverge and red being the negative values corresponding to areas of convergence. The green areas correspond to a zero divergence. Row *c*) depicts a 3D scheme of the streamlines based on the cumulative observations of the different heights, the colours of the arrows qualitatively matching the colours of the computed divergence. The approximate time of the transition between the different stages is indicated below in seconds with a typical precision of 20 s.



concentration  $C_i$  of any ionic component of the PBS over the concentration  $C_i(PBS)$  of the same component in the stock solution of PBS. Actually, the surface tension of the liquid increases with the concentration of PBS. We then showed that accumulation of PBS along the edge of the droplet during stage *I* creates a surface tension gradient large enough to trigger the Marangoni instability.

Moreover, the ratio between the Marangoni and the coffee-ring velocities can be expressed as  $u_r/u_{r,Ma} \sim (R_d h_0)/(Mah^2)$  when  $h$  tends to zero (see Sections 2.1 and 2.2). This ratio can then go up to  $10^4$  at the end of the evaporation (given  $h \sim 10^{-6}$  for the particles being able to move). This then explains the two main transitions in our observations.

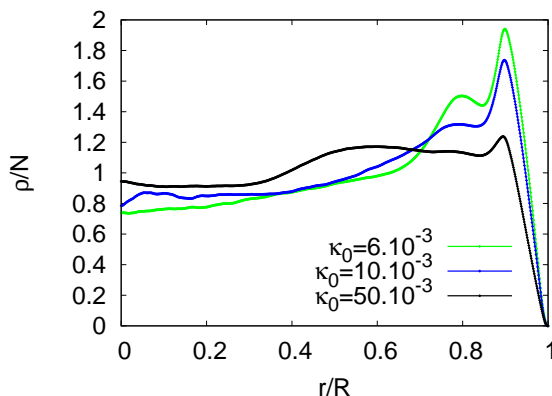


Figure 7.2: Picture from [89]. Normalized mean surface density of the dried agglomerates as a function of the radial distance, for the various PBS concentration. For high PBS concentration the coffee ring effect is significantly reduced.

We were also able to extract the surface density of particles in the eventual deposits, as illustrated in Figure 7.2. This surface density is highly depending on the concentration of PBS in the suspending liquid. This concentration modifies two parameters. The first parameter is the amplitude of the peak of density near the edge of the droplet. This edge significantly decreases when the concentration of PBS increases. The second parameter is the size of the cells in the honeycomb-like pattern due to Marangoni recirculation. The size of those cells decreases when the concentration of PBS increases, leading to a more homogeneous pattern.

## 7.4 Conclusion

We evidenced the competition between Marangoni and coffee-ring flow in our system and characterized its evolution along time. This competition by itself is responsible for features of the final deposit : the intensity of the surface density peak near the edge of the droplet (due to coffee-ring effect) and the honeycomb-like pattern in the deposit, homogenizing surface density. This knowledge will then allow us to determine the specific effect of magnetic interactions between colloids in further studies.

## Transitional bulk-solutal Marangoni instability in sessile drops

Alexis Darras,<sup>1,2,3,\*</sup> Nicolas Vandewalle,<sup>1</sup> and Geoffroy Lumay<sup>1</sup>

<sup>1</sup>GRASP, CESAM, Physics Department, University of Liège, B-4000 Liège, Belgium<sup>†</sup>

<sup>2</sup>F.R.S.-FNRS, B-1000 Bruxelles, Belgium

<sup>3</sup>Experimental Physics, Saarland University, D-66123 Saarbrücken, Germany



(Received 24 August 2018; revised manuscript received 29 October 2018; published 14 December 2018)

Evaporation of sessile droplets is a method to organize suspended particles on solid substrates. Many studies have demonstrated that Marangoni flows caused by surface-adsorbed molecules or temperature gradients can strongly affect the dried deposit. In the present paper, we show how transitional Marangoni instability can be triggered by bulk-diluted tensioactive ions. Thanks to particle image velocimetry analysis, we identify four different flow stages. The transition between them can be understood by considering the competition between the Marangoni flow and the mass conservation flow, usually responsible for the coffee-ring pattern. We also demonstrate that the initial ionic concentration can select a coffee-ring pattern or a more homogeneous dried deposit.

DOI: [10.1103/PhysRevE.98.062609](https://doi.org/10.1103/PhysRevE.98.062609)

### I. INTRODUCTION

The self-assembly of colloids is currently a topic of intensive research, both on fundamental [1–11] and applied aspects [12–20]. Amongst the self-assembly processes, the evaporation of colloidal droplets has attracted much interest due to its wide range of potential applications, extending from blood analysis [21–24] via inkjet printing, paint, and polymers [25–27] up to and including nanotechnology [28]. The main feature of colloidal droplet evaporation is the so-called coffee-ring effect [29–32]. This effect implies that particles tend to be deposited at the edge of the final dried pattern. However, several studies have shown various mechanisms preventing this effect [27,33]. Notably, it has been shown that Marangoni flows, driven by surface tension gradients, can be created from temperature gradients and surface tensioactive agents or in binary mixtures [34–37]. Those flows can strongly modify the deposits' pattern and lead to patterns such as homogeneous deposits or polygonal networks [38–40]. Moreover, some researchers have shown that more complex deposits' structures can be achieved thanks to various concentrations of proteins or liquid crystals [41,42]. However, solutal Marangoni flows have been thoroughly described only when surface tension gradients have been caused by temperature gradients or by tensioactive agents adsorbed at the surface of the droplets.

In the present paper, we show Marangoni instability can be triggered as a transitional flow by bulk-diluted tensioactive ions. Indeed, we evidence the flows which appear when a colloidal droplet containing bulk-diluted phosphate-buffered saline (PBS) is evaporating. We then show those flows can be understood by considering a competition between the mass conservation flow inducing the coffee ring [29–32] and the

solutal Marangoni flows [38,43]. This comes from the fact that the bulk concentration of PBS has a slight influence on the surface tension, like other salts [44] (see Supplemental Material which contains data of surface tension as a function of PBS concentration [45]). We computed a few dimensionless numbers to understand the competition's mechanisms. We eventually show how the PBS concentration consequently influences the final dried deposit of colloids and can possibly suppress the coffee-ring effect. We show that the PBS concentration can be used as a parameter to progressively change the dried deposit pattern after the evaporation.

### II. METHODS

#### A. Suspension preparation

The experiments are performed with microspheres dispersed in water (Estapor M1-070/60 and F1-100XC), with a volume fraction of  $\phi = 50 \times 10^{-5}$  for M1-070 and  $\phi = 2 \times 10^{-5}$  for F1-100XC. Those 1.2- $\mu\text{m}$ -diameter particles are made of polystyrene and covered with carboxyl-charged groups to enable electrostatic stabilization of the suspension. The F1-100XC particles are also fluorescent and allow us to perform particle image velocimetry (PIV) analyses, while the M1-070/60 particles contain ferrite inclusions which make them dark and allow us to get high-contrast direct images to study the dried pattern. In order to ensure the purity of the dispersing phase, the commercial suspensions are first deposited in the bottom of their container with a centrifuge. The supernatant is then removed and the same quantity of distilled water is then poured back in the container. The particles are then dispersed again in the liquid thanks to an ultrasonic bath and mechanical agitation. This process is repeated three times. Then the particles are deposited once again and the supernatant is replaced with the adequate solution, i.e., water with diluted phosphate-buffered saline (PBS) (supplier: VWR; composition: 137 mM NaCl, 2.7 mM KCl, and 12 mM phosphate buffer). The PBS has been chosen

\*alexis.darras@uliege.be

<sup>†</sup><https://www.grasp-lab.org/>

since it is a commercially available pH buffer involving only nonorganic molecules. Indeed, pH and ion concentration are often used as parameters to control electrostatic stabilization [46], and organic molecules could potentially feed bacteria that could reach the suspension as it ages (which was a main trouble during the exploratory part of this work). At the final stage, particles are dispersed again thanks to an ultrasonic cell disruptor, SONICS Vibra-Cell VC505.

### B. Microscopy observations

To perform the observations, a  $2\text{-}\mu\text{l}$  droplet of the suspension is placed on a microscope cover glass. A custom airtight evaporative chamber is placed upon it. The chamber is made of plexiglass and is T shaped. The ends of the upper branches of the T are filled with silica gel to ensure reproducible humidity conditions in the chamber. The central trunk is kept empty in order to keep a clear path for the light. Petroleum jelly is applied on the bottom of the chamber's base to assess airtightness between the plexiglass and the cover glass. The suspension is observed from the bottom with a  $6.4\times$  magnification (or  $20\times$  to get details of the eventually dried deposits from several pictures). The microscope used is an inverted microscope Olympus IX73, connected to a 4070M-CL Thorlabs camera with 2048 by 2048 pixels of 16-bit depth.

The PIV pictures are obtained by enlightening the sample with a blue LED source, a 470-nm centered coolLED pE-100, and then filtering the re-emitted green light, centered around 525 nm from the Estapor datasheet, thanks to an Olympus filter cube U-FBWA. The PIV images are recorded with a frame rate of 1 fps, and the velocity field is computed with a MATLAB code, with embedded image filtering to decrease the focus depth and based on the open-source PIVLAB tool [47,48]. Typical videos of evaporating drops are available in the Supplemental Material [45].

### III. RESULTS

We prepared three different suspensions, each of them with various concentrations of PBS but with the same colloidal volume fraction of  $\phi = 50 \times 10^{-5}$  for the M1-070 and  $\phi = 2 \times 10^{-5}$  for the F1-100XC. The PBS was diluted in volume fraction as  $6 \times 10^{-3}$ ,  $10 \times 10^{-3}$ , and  $50 \times 10^{-3}$  of the respective final suspensions. For each of these suspensions, we observed the evaporation with 5 different focus heights above the glass substrate. For each of the specific conditions, we observed at least 3 different droplets' evaporation in order to assess the reproducibility of the results. In total, we then performed 15 measurements for each PBS concentration, leading to a total of 45 exploited videos. Typical videos for the

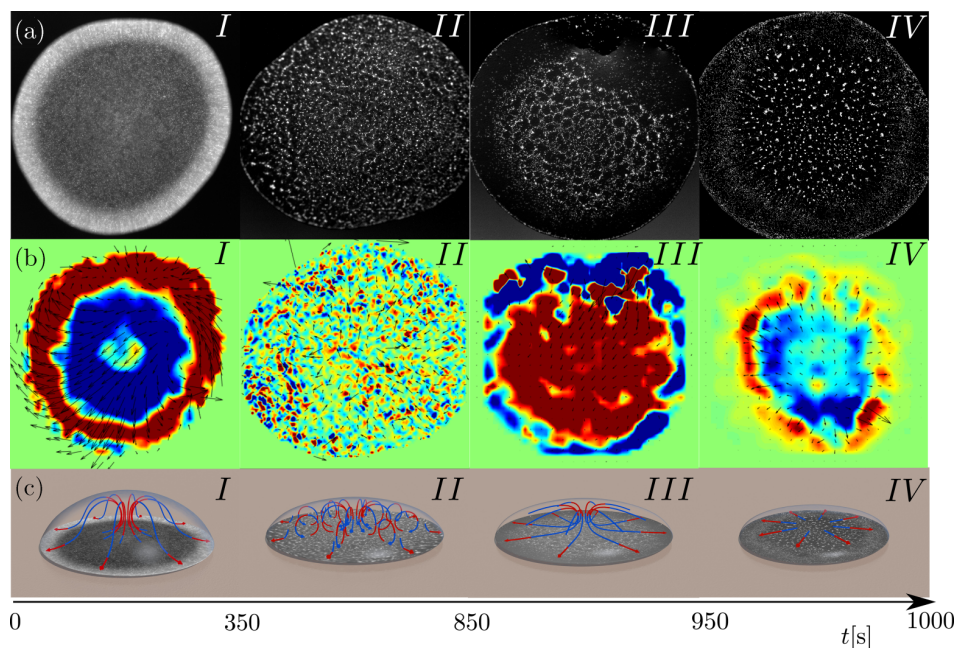


FIG. 1. Main results from PIV measurements. The pictures in row (a) are obtained experimentally with focus near the top of the droplet. The pictures for different times are then taken from different focus heights. Row (b) shows the computed two-dimensional (2D) velocity field  $\vec{v}(\vec{r})$  corresponding to the upper pictures. The colors correspond to the velocity's 2D divergence  $\vec{\nabla} \cdot \vec{v}(\vec{r})$ , with blue being the positive values corresponding to areas from where the particles diverge and red being the negative values corresponding to areas of convergence. The green areas correspond to a zero divergence. Row (c) depicts a 3D scheme of the streamlines based on the cumulative observations of the different heights, the colors of the arrows qualitatively matching the colors of the computed divergence. The approximate time of the transition between the different stages is indicated below in seconds with a typical precision of 20 s. Stage I corresponds to an outward flow. During stage II, a honeycomblike pattern is observed near the surface of the droplet due to Marangoni instability. This pattern is then somehow collapsing on itself near the center of the drop during stage III. An outward flow, which tends to destabilize the previous structure, is observed during the final stage IV.

chosen focus height are available as Supplemental Material [45]. From those videos, we were able to determine four different stages during the evaporation process, observed for every tested concentration of PBS and illustrated in Fig. 1. An initial outward flow is observed during stage I. During stage II, Marangoni recirculation cells create a surface pattern of particles. This pattern collapses toward the center in stage III, while an outward flow occurs near the substrate. During the last stage, stage IV, a global outward flow dominates the fluid motion while the particles are eventually deposited on the substrate. A quantitative approach to experimentally describe those transitions is to measure the mean 2D divergence of the flow field in a plane near the bottom plate, as described in Fig. 2. As we will show, the transition between the different stages can be understood mainly by considering a competition between the mass conservation flow, usually responsible for the coffee-ring effect [36], and a solutal Marangoni instability [38,43].

### A. Stage I: Initial outward flow

During stage I, an outward flow mainly corresponding to the usual mass conservation flow is observed. A small recirculation is observed at the center of the drop near the substrate, which is unusual. However, this might be understood by the fact that the outward flow increases the concentration of PBS near the edge of the droplet, which increases the surface outward flow. The mass leaving the center top of the droplet

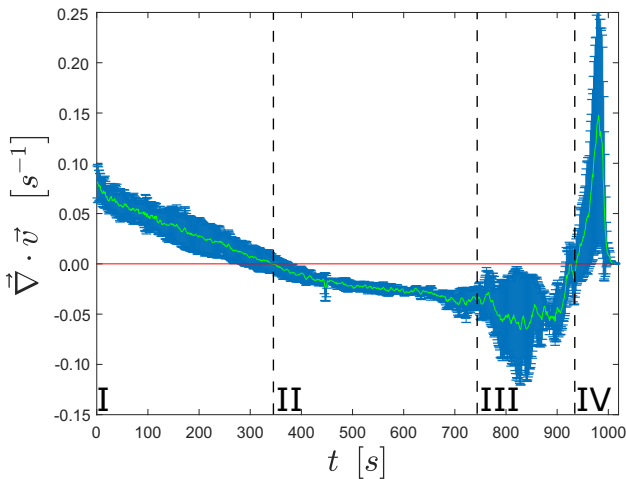


FIG. 2. Evolution of the mean 2D divergence of the flow field in a horizontal plane of the droplet, near the bottom plate. Stage I, characterized by a divergent flow of mass conservation, has a positive mean divergence. This mean divergence decreases as the Marangoni number  $Ma$  increases (see main text). When stage II occurs, along with Marangoni instability, this mean divergence crosses the 0 value and becomes negative. When the Cheerios collapse, characterizing stage III, occurs, the divergence encounters some negative peak. Stage IV, seeing the resurgence of a strong outward flow before final deposition, is characterized by an important peak of divergence. Error bars are obtained from standard deviations between measurements. Differences are mainly due to the difficulty in accurately defining the starting time of the experiments, as well as slight variations of the initial conditions for each droplet.

must then be replenished by an upward recirculation in the center of the drop. The mean divergence of the flow field near the bottom plate is then positive, since the fluid mainly leaves the center of the drop to reach the edge, as illustrated in Fig. 2. During this first stage, the whole recirculation keeps increasing the concentration gradient of the PBS and then the surface tension gradient. Recent study has shown that such a gradient can also be caused by an active capture of the moving surface [49]. This surface tension gradient also slowly decreases the outward flow and then decreases the mean divergence (Fig. 2).

### B. Stage II: Marangoni recirculation cells

After approximately 300 s, a flow pattern corresponding to Marangoni instability cells is observed. Actually, Rayleigh-Bénard instabilities could also lead to similar convection cells. However, since our drops are smaller than the capillary length, this gravity-driven flow is not plausible in our system. This implies that we observe a Marangoni recirculation, driven by a gradient of surface tension. This flow creates a honeycomblike structure with the particles which are trapped at the surface, in all probability due to some partial unwetting as observed previously in other systems [40]. The detailed analysis of the 2D velocity's divergence [row (b) in Fig. 1] allows one to clearly see those structures, with the alternation of regions where particles strongly converge with areas where particles strongly diverge. The mean 2D divergence, observed near the bottom plate, is then almost constant, but slightly negative (Fig. 2). Indeed, when observed near the bottom plate, the velocity field still converges towards the edge of the droplet near its boundaries, creating a bias in the mean value.

Such a surface tension gradient is often produced by a temperature gradient, but temperature gradients along the surface of evaporating droplets appear almost instantly and only decrease with time [34,38]. It is then not plausible that the observed delayed instability is driven by the temperature gradient. Moreover, we noticed that modifying the PBS concentration modifies the size of the cells, which can also not be explained by temperature gradients. In our case, the most probable explanation is then that the gradient of the PBS concentration creates the surface tension gradient responsible for such instability.

The time at which this transition occurs is consistent with a magnitude order analysis, as we demonstrate here. Let us first consider a Marangoni number  $Ma = (\frac{\partial \gamma}{\partial \kappa} \Delta \kappa t_f) / (\eta R)$  adapted from thermal Marangoni number [34,38], where  $\gamma$  is the surface tension of the fluid,  $\kappa \equiv C_i / C_i(\text{PBS})$  is a dimensionless volumic concentration defined as the ratio between the concentration  $C_i$  of any ionic component of the PBS over the concentration  $C_i(\text{PBS})$  of the same component in the stock solution of PBS,  $t_f \approx 1600$  s is the drying time,  $\eta \approx 10^{-3}$  Pa s is the viscosity of the fluid and  $R \approx 10^{-3}$  m is the radius of the droplet's contact line (often identified as the droplet's radius). The typical Marangoni number  $Ma$  at which Marangoni instability occurs is of the order of  $Ma_c \approx 10^2$  [34,38,40]. We measured that  $\frac{\partial \gamma}{\partial \kappa} \approx 10^{-4}$  N/m from the pending drop method measurements performed with a CAM 200 apparatus from KSV instruments LTD (Supplemental Material contains the

data [45]). The difference of concentration  $\Delta\kappa$  can be assessed from several hypotheses. First of all, we assume that every ionic component of the PBS has the same distribution profile along the droplet radius, when normalized by its total amount. This ensures the definition of  $\kappa$  does not change when another component of the PBS is used to define its value. Then, since during stage I the fluid in the center of the droplet globally flows to the edge of the drop, we assume that the concentration of the ions near the center of the droplet is close to the initial concentration  $\kappa_0 \approx 10^{-2}$  before the droplet begins to evaporate. Eventually, we estimate that the concentration of ions near the droplet of the edge is of the order of magnitude of the average concentration  $\kappa_m = \kappa_0 V_0/V$ , where  $V_0$  is the initial volume and  $V$  is the current volume of the drop. Since the volume of the droplet decreases linearly with time  $t$ , in the pinned contact line regime we observed, we can write  $V \approx V_0(t_f - t)/t_f$  [28,50]. The difference of concentration can then be assessed as  $\Delta\kappa \approx \kappa_0 t/(t_f - t)$ . After  $t = 350$  s of evaporation, we then obtain a Marangoni number of

$$\text{Ma} \approx \frac{\frac{\partial\gamma}{\partial\kappa}\kappa_0 t_f t}{\eta R(t_f - t)} \approx 10^2, \quad (1)$$

which is then the order of usual critical Marangoni numbers  $\text{Ma}_c$  above which Marangoni instability occurs.

### C. Stage III: Cheerios collapse

At the end of the second stage, the honeycomblike structure collapses near the center of the surface, decreasing the size of the pattern's cells. During this stage III, there is an inward surface flow while the flow near the substrate is an outward flow corresponding to the usual mass conservation flow creating the coffee ring. In Fig. 2, however, one can still see a negative peak corresponding to the convergence of the particles of the surface structures. Indeed, the chosen focal

plane is slightly above the bottom plate (in order to avoid noise from wall interaction), and the drop is then thin enough for the surface to be seen in the focal plane. Moreover, the detailed motion of the structure during this stage is highly dependent on the geometry of the droplet and the resulting honeycomb structure. Regarding quantitative data, it is then the stage with the highest noise amongst the four stages we identified.

We believe the inward surface flow is due to the Cheerios attraction between the particles forming the honeycomb-like pattern. This is pretty hard to assess theoretically since we do not have any accurate idea on the contact angle between the spheres or their actual wetting and also because interaction of capillary charged particles is still challenging to model, especially for short distances, even on flat surfaces [51–53]. However, it has already been shown that Cheerios interactions can lead to structures of colloids and can even prevent the coffee-ring effect, leading to flows similar to this collapse [54,55]. The method used in those previous studies to verify that the Cheerios effect is responsible for structures or motion is adding surfactants in the suspension to modify those interactions. Nonetheless, such an addition of surfactants in our system would prevent or modify the Marangoni flow mechanism as well as the resulting pattern and then cannot be used to check this hypothesis in our case. This will then be the focus of future studies. On the other hand, the fact that an outward flow occurs again in the system near the substrate can be understood from the dependence of velocities on the geometry of the droplet. Indeed, Hu and Larson [38] have shown that the velocity field from the Marangoni flow and the mass conservation flow linearly superimpose. From their equations, we can also identify that the radial velocity depends on the geometry of the droplet as  $v_{\text{CR}} \sim 2h_0R/(ht_f)$  for the mass conservation flow and  $v_{\text{Ma}} \sim \text{Ma}h_0/(Rt_f)$  for the Marangoni flow, where  $h_0$  is the initial height of the droplet and  $h$  is the current height. The ratio of these two flows

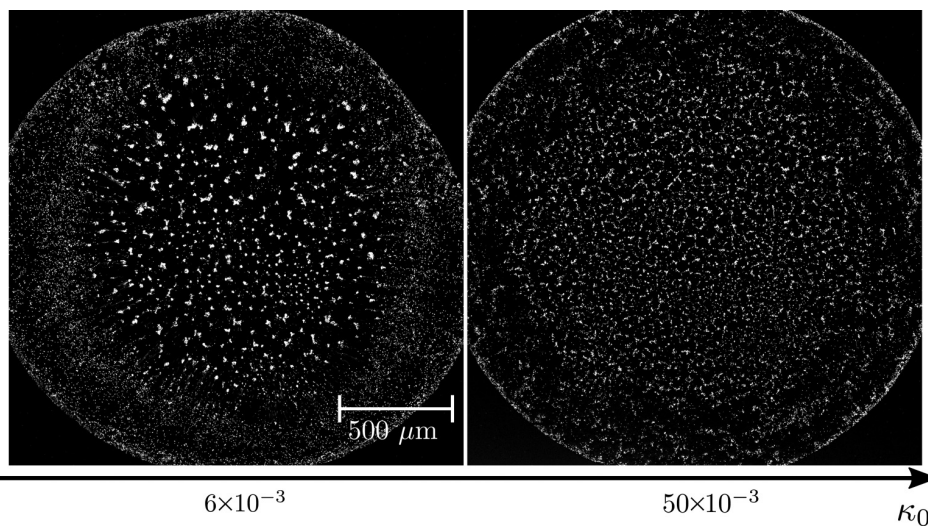


FIG. 3. Comparison of two droplets containing different concentrations of PBS. When the PBS concentration increases, the size of the Marangoni recirculation cells decreases. The resulting pattern then better resists the outward flow of stage IV. The two pictures in this figure, obtained by fluorescence microscopy, were taken after approximately 1000 s of evaporation.

then behaves as

$$\frac{v_{\text{CR}}}{v_{\text{Ma}}} \sim \frac{R^2}{Ma h^2}.$$

If we assume the Marangoni number does not change too much after the apparition of the Marangoni instability and we take into account the fact that the particles can still move for a height as small as  $h \approx 10^{-6}$  m, since the radius is pinned at  $R = 10^{-3}$  m, it is easy to understand there is a time where the outward flow will destabilize the Marangoni instability since this ratio can reach values as high as  $\frac{v_{\text{CR}}}{v_{\text{Ma}}} \approx 10^4$  at the end of the evaporation process.

#### D. Stage IV: Outward flow and deposition

During stage IV, the bottom outward flow observed previously is the only flow remaining in the droplet. In Fig. 2, a corresponding peak in the divergence is observed, in agreement with values of stage I. The outward flow can be so strong that it eventually breaks down the honeycomblike structure formed by the Marangoni recirculation cells. However, this latter observation strongly depends on the initial concentration of PBS in the droplet  $\kappa_0$ , as illustrated in Fig. 3. There are two mechanisms by which the concentration of PBS can modify the interlocking resistance and morphology of those structures. First of all, the PBS will screen electrostatic repulsion between the particles, which makes them more likely

to irretrievably aggregate, as well described in the Derjaguin-Landau-Verwey-Overbeek (DLVO) theory [56]. Moreover, we have shown in Eq. (1) that the Marangoni number  $Ma$  is proportional to the initial PBS concentration  $\kappa_0$ . Since the size of the Marangoni cells  $\lambda \propto Ma^{-\frac{1}{2}}$  is inversely proportional to the square root of the Marangoni number  $Ma$  [40,57], this then implies that an increase of the initial PBS concentration  $\kappa_0$  will give rise to smaller cells. These observations are illustrated in Fig. 3.

Those variations have a strong influence on the eventually dried deposit of the droplet. Indeed, a high initial PBS concentration  $\kappa_0$  maintains the honeycomblike structure created by the Marangoni recirculation even in the dried deposit, contrary to the low PBS concentration as illustrated in Fig. 4. The presence of this structure is then able to decrease and mainly prevent the coffee-ring effect. This can be qualitatively observed in Fig. 4. A more quantitative analysis of the deposits can be performed by computing the mean surface density  $\rho$  of the deposit. We computed this quantity as a function of the relative distance from the center  $r$  of the deposit, normalized by the radius  $R$  of the deposit. We then normalized it by its integral  $N = \int_0^1 \rho(\delta) d\delta$ , where  $\delta = \frac{r}{R}$ . This normalization enhances the relative variation values and ensures that no differences in lightening are taken into account. The resulting curves are presented in Fig. 5. As it can be concluded from those curves, the initial PBS concentration  $\kappa_0$  is a

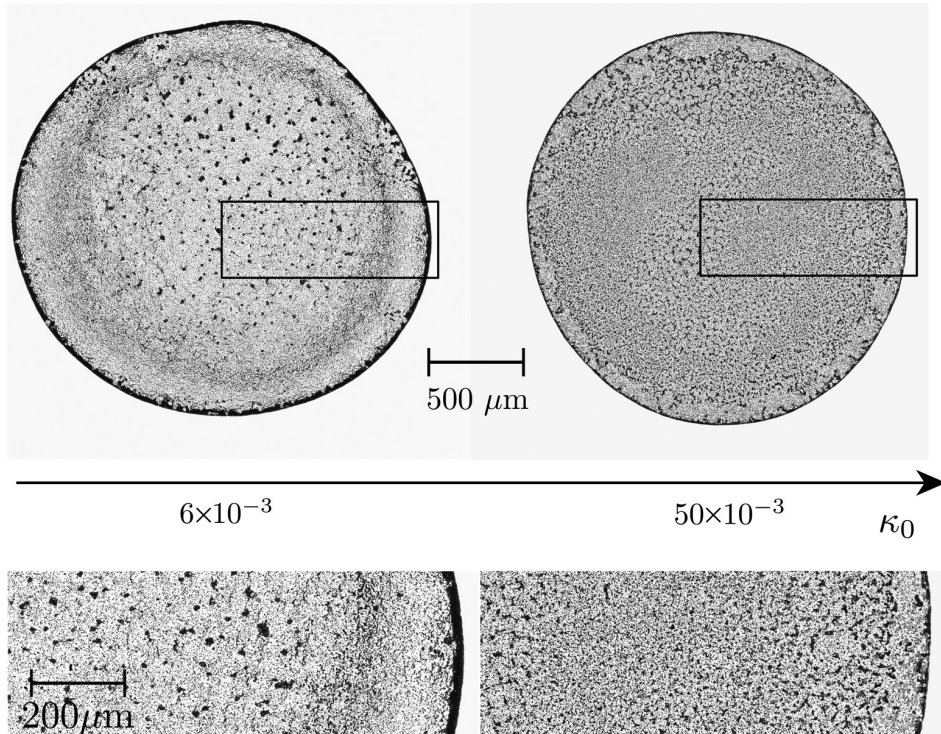


FIG. 4. Comparisons of two dried deposits from droplets containing different concentrations of PBS. The pictures are obtained from bright-field observation. When the PBS concentration increases, the particles are deposited more homogeneously all over the deposit. On a smaller scale, the pattern produced by the Marangoni instability is almost unaffected in the dried pattern. The bottom pictures are a zoom of the box in the upper pictures.

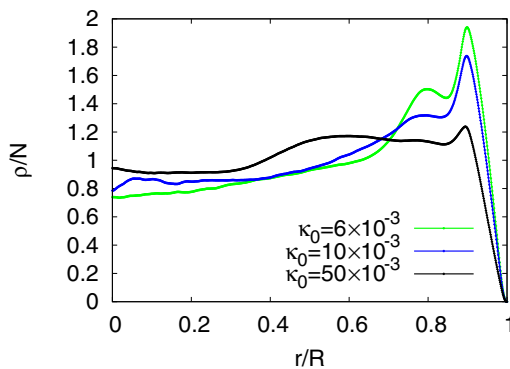


FIG. 5. Mean surface density of the dried agglomerates normalized by the number of particles (so that the integral of the curve is equal to 1) as a function of the radial distance, for the various PBS concentrations. For high PBS concentration the coffee-ring effect is mainly countered, since the averaged density of the deposited particles is mainly uniform along the droplet's radius. Error bars are not shown in order to avoid overloading of the curves; however the maximal standard deviation is below 10% of the curve value.

parameter which allows one to switch continually from a classical coffee-ring deposit (see  $\kappa_0 = 6 \times 10^{-3}$  curve in Fig. 5) to a much more homogeneous deposit where the density of

particles in the center and at the edge are comparable (see  $\kappa_0 = 50 \times 10^{-3}$  curve in Fig. 5).

#### IV. CONCLUSION

Our experiments evidenced the different flow steps induced by a solutal Marangoni flow in a sessile droplet by using PIV on various heights of the droplet. Moreover, we were able to model most of the transitions and enhance how the initial concentration of PBS influences the flow mechanisms by using simple dimension analysis. This analysis showed that the key mechanism to understand the flow behavior is the competition between solutal Marangoni flow and mass conservation flow. We also showed that this influence can be used to control the dried deposit properties. Actually, we showed that a sufficient initial PBS concentration maintains the structure formed in the previous stage of evaporation. This looks like a promising way to control the deposition of other structures, like those obtained from self-assembled magnetic or Janus colloidal particles.

#### ACKNOWLEDGMENTS

A.D. is financially supported by the FNRS as a research fellow. This work was financially supported by the FNRS (Grant No. PDR T.0043.14) and by the University of Liège (Starting Grant No. C-13/88).

- [1] J. S. Andreu, J. Camacho, and J. Faraudo, *Soft Matter* **7**, 2336 (2011).
- [2] J. H. Promislow, A. P. Gast, and M. Fermigier, *J. Chem. Phys.* **102**, 5492 (1995).
- [3] P. Domínguez-García, J. Pastor, and M. Rubio, *Eur. Phys. J. E* **34**, 1 (2011).
- [4] A. Darras, E. Opsomer, N. Vandewalle, and G. Lumay, *Sci. Rep.* **7**, 7778 (2017).
- [5] J. Faraudo, J. S. Andreu, and J. Camacho, *Soft Matter* **9**, 6654 (2013).
- [6] A. Darras, J. Fiscina, M. Pakpour, N. Vandewalle, and G. Lumay, *Eur. Phys. J. E* **39**, 1 (2016).
- [7] N. Rojas, A. Darras, and G. Lumay, *Phys. Rev. E* **96**, 012608 (2017).
- [8] A. Darras, J. Fiscina, N. Vandewalle, and G. Lumay, *Am. J. Phys.* **85**, 265 (2017).
- [9] H. Ezzaier, J. Alves Marins, I. Razvin, M. Abbas, A. Ben Haj Amara, A. Zubarev, and P. Kuzhir, *J. Chem. Phys.* **146**, 114902 (2017).
- [10] K. S. Khalil, A. Sagastegui, Y. Li, M. A. Tahir, J. E. Socolar, B. J. Wiley, and B. B. Yellen, *Nat. Commun.* **3**, 794 (2012).
- [11] Y. Gurevich, Y. Mankov, and R. Khlebopros, *Dokl. Phys.* **58**, 478 (2013).
- [12] F. Martínez-Pedrero and P. Tierno, *Phys. Rev. Appl.* **3**, 051003 (2015).
- [13] H. Carstensen, V. Kapaklis, and M. Wolff, *Phys. Rev. E* **92**, 012303 (2015).
- [14] K. Müller, N. Osterman, D. Babič, C. N. Likos, J. Dobnikar, and A. Nikoubashman, *Langmuir* **30**, 5088 (2014).
- [15] M. Llera, J. Codnia, and G. A. Jorge, *J. Magn. Magn. Matter* **384**, 93 (2015).
- [16] R. M. Erb, H. S. Son, B. Samanta, V. M. Rotello, and B. B. Yellen, *Nature (London)* **457**, 999 (2009).
- [17] F. Martínez-Pedrero, A. Ortiz-Ambriz, I. Pagonabarraga, and P. Tierno, *Phys. Rev. Lett.* **115**, 138301 (2015).
- [18] P. Liu, J. W. De Folter, A. V. Petukhov, and A. P. Philipse, *Soft Matter* **11**, 6201 (2015).
- [19] K. V. Edmond, H. Park, M. T. Elsesser, G. L. Hunter, D. J. Pine, and E. R. Weeks, *Chaos* **21**, 041103 (2011).
- [20] R. Dreyfus, J. Baudry, M. L. Roper, M. Fermigier, H. A. Stone, and J. Bibette, *Nature (London)* **437**, 862 (2005).
- [21] T. Yakhno, O. Sedova, A. Sanin, and A. Pelyushenko, *Tech. Phys.* **48**, 399 (2003).
- [22] T. A. Yakhno, V. G. Yakhno, A. G. Sanin, O. A. Sanina, A. S. Pelyushenko, N. A. Egorova, I. G. Terentiev, S. V. Smetanina, O. V. Korochkina, and E. V. Yashukova, *IEEE Eng. Med. Biol. Mag.* **24**, 96 (2005).
- [23] D. Brutin, B. Sobac, B. Loquet, and J. Sampol, *J. Fluid Mech.* **667**, 85 (2011).
- [24] L. Lanotte, D. Laux, B. Charlot, and M. Abkarian, *Phys. Rev. E* **96**, 053114 (2017).
- [25] K. Sefiane, *J. Bionic Eng.* **7**, S82 (2010).
- [26] J.-H. Kim, S.-B. Park, J. H. Kim, and W.-C. Zin, *J. Phys. Chem. C* **115**, 15375 (2011).
- [27] K. Sefiane, *Adv. Colloid Interface Sci.* **206**, 372 (2014).
- [28] H. Y. Erbil, *Adv. Colloid Interface Sci.* **170**, 67 (2012).
- [29] R. D. Deegan, O. Bakajin, T. F. Dupont, G. Huber *et al.*, *Nature (London)* **389**, 827 (1997).

- [30] R. D. Deegan, O. Bakajin, T. F. Dupont, G. Huber, S. R. Nagel, and T. A. Witten, *Phys. Rev. E* **62**, 756 (2000).
- [31] A. G. Marín, H. Gelderblom, D. Lohse, and J. H. Snoeijer, *Phys. Rev. Lett.* **107**, 085502 (2011).
- [32] Á. G. Marín, H. Gelderblom, D. Lohse, and J. H. Snoeijer, *Phys. Fluids* **23**, 091111 (2011).
- [33] R. G. Larson, *AIChE J.* **60**, 1538 (2014).
- [34] H. Hu and R. G. Larson, *Langmuir* **21**, 3972 (2005).
- [35] R. Bennacer and K. Sefiane, *J. Fluid Mech.* **749**, 649 (2014).
- [36] J. R. E. Christy, Y. Hamamoto, and K. Sefiane, *Phys. Rev. Lett.* **106**, 205701 (2011).
- [37] T. Still, P. J. Yunker, and A. G. Yodh, *Langmuir* **28**, 4984 (2012).
- [38] H. Hu and R. G. Larson, *J. Phys. Chem. B* **110**, 7090 (2006).
- [39] H. Kim, F. Boulogne, E. Um, I. Jacobi, E. Button, and H. A. Stone, *Phys. Rev. Lett.* **116**, 124501 (2016).
- [40] V. X. Nguyen and K. J. Stebe, *Phys. Rev. Lett.* **88**, 164501 (2002).
- [41] G. Chen and G. J. Mohamed, *Eur. Phys. J. E* **33**, 19 (2010).
- [42] Z. S. Davidson, Y. Huang, A. Gross, A. Martinez, T. Still, C. Zhou, P. J. Collings, R. D. Kamien, and A. Yodh, *Nat. Commun.* **8**, 15642 (2017).
- [43] X. Fanton and A. Cazabat, *Langmuir* **14**, 2554 (1998).
- [44] L. M. Pegram and M. T. Record, *J. Phys. Chem. B* **111**, 5411 (2007).
- [45] See Supplemental Material at <http://link.aps.org/supplemental/10.1103/PhysRevE.98.062609> for surface tension measurements and illustrative videos of the evaporation flows.
- [46] T. Cosgrove, *Colloid Science: Principles, Methods and Applications* (Wiley & Sons, New York, 2010).
- [47] W. Thielicke and E. J. Stamhuis, *J. Open Res. Software* **2**, e30 (2014).
- [48] W. Thielicke and E. J. Stamhuis, PIVlab – Time-Resolved Digital Particle Image Velocimetry Tool for MATLAB (version: 1.41), doi: 10.6084/m9.figshare.1092508.
- [49] S. Jafari Kang, V. Vandadi, J. D. Felske, and H. Masoud, *Phys. Rev. E* **94**, 063104 (2016).
- [50] A.-M. Cazabat and G. Guena, *Soft Matter* **6**, 2591 (2010).
- [51] M. Nicolson, in *Mathematical Proceedings of the Cambridge Philosophical Society*, Vol. 45(2) (Cambridge University, Cambridge, England, 1949), pp. 288–295.
- [52] P. A. Kralchevsky and K. Nagayama, *Adv. Colloid Interface Sci.* **85**, 145 (2000).
- [53] D. Vella, *Am. J. Phys.* **73**, 817 (2005).
- [54] P. Kralchevsky, N. Denkov, V. Paunov, O. Veleev, I. Ivanov, H. Yoshimura, and K. Nagayama, *J. Phys.: Condens. Matter* **6**, A395 (1994).
- [55] P. J. Yunker, T. Still, M. A. Lohr, and A. Yodh, *Nature (London)* **476**, 308 (2011).
- [56] J. N. Israelachvili, *Intermolecular and Surface Forces*, revised 3rd ed. (Academic, San Diego, 2011).
- [57] J. Pearson, *J. Fluid Mech.* **4**, 489 (1958).



## 7.6 Additional Comments

As attentive readers can notice, there is a difference between the ratio  $u_r/u_{r,Ma} \sim (R_d h_0)/(Mah^2)$  we wrote in this thesis and the equivalent ratio  $\frac{v_{CR}}{v_{Ma}} \sim \frac{R^2}{Ma h^2}$  we introduced in the paper. While this does not change the further conclusions and discussions, it is worth noticing the scalings described in the paper for the Marangoni and coffee-ring effects are unfortunately incorrect. The right developments can be found in our Sections 2.1 and 2.2.



# Chapter 8

## Remote-controlled deposits

### 8.1 Motivations

As we stated in Section 2.5, most of the control on evaporative deposits is currently made through the composition of the droplet. However, interactions between superparamagnetic colloids allow us to use the external magnetic field as a remote control to induce self-assembly. The goal of this work is to determine how this remote control can influence the eventual evaporative deposit.

### 8.2 Setup and methods

We prepared suspensions of superparamagnetic colloids with the same volume fraction as in the previous Chapter 7. The suspending liquid is diluted PBS with final volume fraction  $\kappa = 50 \cdot 10^{-3}$ . We observed evaporating droplets in the same conditions as previously, except we applied various magnetic fields on the evaporative droplets. The magnetic field is produced by surrounding coils where an electric current is injected, as in Chapters 4 to 6. We then characterized the eventual deposit for the various experimental conditions.

### 8.3 Main results

We observed that magnetic fields applied on evaporating droplets of superparamagnetic colloids can have a significant influence on the eventual deposit. It modifies both the average distribution of the surface density and the morphological details of the deposit. More accurately, the magnetic interactions between the particles tend to decrease the coffee-ring effect and create a more uniform deposit. It also has some drastic effect on the detailed pattern of the deposits. As illustrated in Figure 8.1, the self-assembled structures from the magnetic interactions between particles can remain in the deposits. This highlights the fact that an external magnetic field can be used as a versatile remote control for the final dried deposit.

For the case where a constant magnetic field is applied, we also linked the size of the chains in the deposits to their dynamical growth. Indeed, a simple hypothesis is that their growth is suddenly stopped when the evaporation process is complete. Their mean size at this time  $t_f$ ,  $\langle s \rangle(t) = k(t_f/t_B)^z$ , is then governed by the characteristic time of aggregation  $t_B \propto B^{-2}$ . This leads to the fact that the size of the chains in the deposits scales as  $\langle s \rangle \propto B^{-2z} \approx B^{-1.3}$ , from usual value of  $z \approx 0.65$ . We found that this scaling efficiently describes the evolution of chains length in our deposit, but only if one takes into account a non-zero mean length of agglomerates, due to the honeycomb-like patterns due to Marangoni recirculation. This result is illustrated in Figure 8.2, where the red line represents this scaling law  $\langle s \rangle \approx aB^{-1.3} + \langle L \rangle_0$ , with  $a$  a fit parameter and  $\langle L \rangle_0$  is the mean length of the agglomerates with no magnetic field. The points are experimental data obtained with various magnetic fields. This graph highlights that the properties of the final dried deposit directly depends on the self-assembly process of the particles.

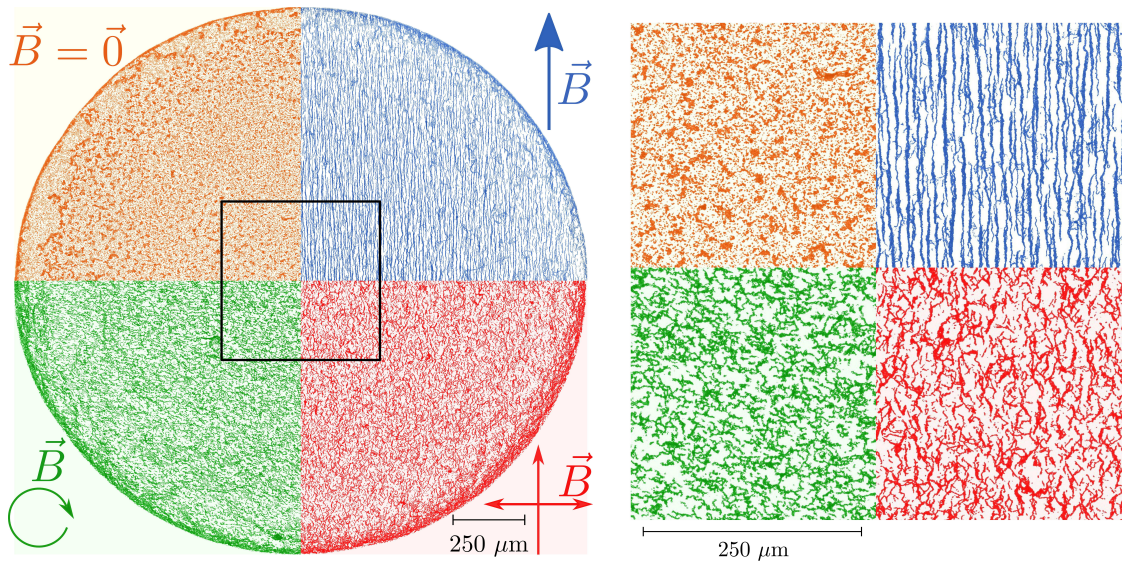


Figure 8.1: Picture modified from [90]. Parts of various deposits obtained with different magnetic fields (null, homogeneous, rotating and oscillating fields, amplitude of non-zero magnetic fields are 22.5 G). Each picture has been colourized for illustration purposes. On the right picture is a zoom on the squared area. The global surface density at the centre of the droplets does not change very much. However, one can see that the structures resulting from the magnetic self-assembly of the particles remain in the deposit.

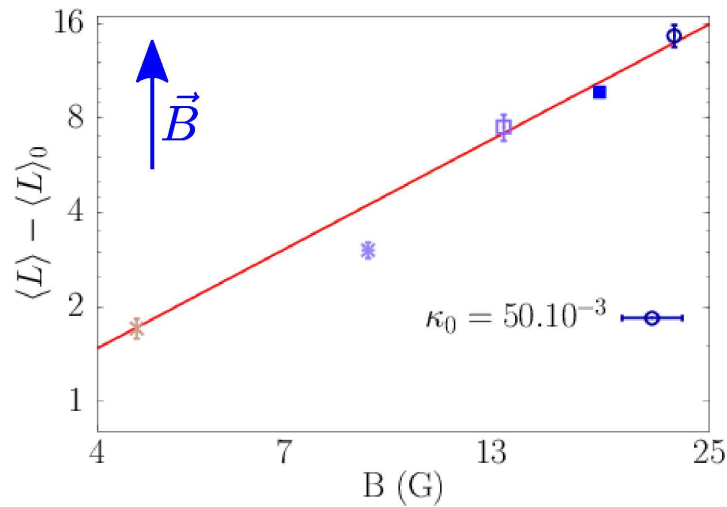


Figure 8.2: Picture from [90]. Evolution of the mean size of the agglomerates observed in the eventual deposits under constant magnetic field  $\vec{B}$ . The scaling law is obtained from the growth process of the chains. The notation  $\langle L \rangle$  is the chosen notation for  $\langle s \rangle$  in the related article, in Section 8.5.

## 8.4 Conclusion

In this study, we demonstrated that an external magnetic field can be used as a remote control to influence several features of evaporative deposits of superparamagnetic particles. We also showed that this influence is directly linked to the self-assembly process of the particles. This work should then open new perspectives in technologies using textured deposits. Moreover,

given the well-known equations governing the magnetic interactions, such a system could also be used as a model system for more complex situations.

## Remote-controlled deposit of superparamagnetic colloidal droplets

Alexis Darras,<sup>1,2,3,\*</sup> Florence Mignolet,<sup>1</sup> Nicolas Vandewalle,<sup>1</sup> and Geoffroy Lumay<sup>1</sup>

<sup>1</sup>GRASP, CESAM - Physics Department, University of Liège, B-4000 Liège, Belgium

<sup>2</sup>F.R.S.-FNRS, B-1000 Bruxelles, Belgium

<sup>3</sup>Experimental Physics, Saarland University, D-66123 Saarbrücken, Germany



(Received 2 August 2018; published 14 December 2018)

Evaporation of sessile droplets is a way to organize suspended particles and create surface coating. Many studies have demonstrated that suspensions with various compositions can give rise to qualitatively different dried patterns, often by focusing on the radial density profile of deposited particles. We demonstrate that a single suspension of superparamagnetic colloids can give rise to several dried patterns thanks to an external magnetic field applied during the evaporation process. We show the various patterns obtained with zero, constant, rotating, and oscillating magnetic fields, and evidence the continuous control given by the intensity of a constant magnetic field. We also show that this magnetic control has a substantial effect on the morphological details of the deposits.

DOI: [10.1103/PhysRevE.98.062608](https://doi.org/10.1103/PhysRevE.98.062608)

### I. INTRODUCTION

The evaporation of colloidal droplets is currently a topic of intensive research due to its wide range of potential applications, extending from blood analysis [1,2] to nanotechnology [3] via ink-jet printing, paint, and polymers [4]. The main feature of colloidal droplet evaporation is the so-called coffee-ring effect [5–9]. This effect implies that particles tend to be deposited at the edge of the finally dried pattern. However, several studies have shown various mechanisms preventing this effect. Notably, capillary interactions of ellipsoidal particles [10] and the presence of surface-adsorbed polymers [11] allow a uniform coating of the particles. Marangoni flows created by temperature gradients, tensio-active agents, or in binary mixtures can also strongly modify the deposit pattern [11–15]. More recently, some researchers have shown that more complex deposit structures can be achieved thanks to various concentrations of liquid crystals [16]. In this paper, we demonstrate that magnetic interactions between superparamagnetic colloidal particles [17–21] can be used to control the properties of colloidal droplets deposit, as illustrated in Fig. 1. This actually requires the right chemical composition of the suspension. But then, a single suspension can result in various dried patterns. The actual pattern is selected from the application of an external magnetic field during the evaporation. This induces indeed a self-assembly of the particles [22–33] which is visible in the deposit. Following a quantitative description of the pattern obtained with homogeneous and constant field, we show that different patterns are produced by rotating and oscillating fields. To our knowledge, this is the first time that such a tunable control of evaporation deposit is described in the literature.

### II. METHODS

#### A. Suspensions preparation

Our experiments were performed with superparamagnetic microspheres (diameter  $d = 1.2 \mu\text{m}$ ) dispersed in water (Estapor® M1-070/60), with a volume fraction of  $\phi = 5 \times 10^{-4}$ . Those particles are covered with carboxyl charged groups to enable electrostatic stabilization of the suspension. Further information and characterization of the particles can be found on the manufacturer's website [34]. Independent measurements were also performed and published in various scientific papers [25,26]. In order to clean the spheres of any chemical waste, the commercial suspensions are first deposited in the bottom of their container with a centrifuge. The supernatant is then removed and the same quantity of distilled water is then poured back into the container. The particles are then dispersed again in the liquid thanks to an ultrasonic bath and mechanical agitation. The whole process is repeated three times. After this cleaning process, the particles are deposited once again and the supernatant is replaced with the adequate solution, i.e., water with dilute phosphate buffered saline (PBS). The PBS has been chosen since it is a commercially available pH buffer involving only nonorganic molecules. Indeed, pH is often used as a parameter to control electrostatic stabilization, and organic molecules could potentially feed bacteria that could reach the suspension as it ages. Particles are then ultrasonicated again. After the ultrasonication, automatized size distribution measurements based on image analysis show that the particles have the same mean diameter as in the original delivered suspension ( $d = 1.2 \mu\text{m}$ ). This means that the particles are completely dispersed, as corroborated by visual control of the suspensions observed with an optical microscope.

#### B. Microscopy observations

To perform the observations, a  $2 \mu\text{l}$  droplet of the suspension is placed on a microscope cover glass. A custom airtight

\*alexis.darras@ulg.ac.be

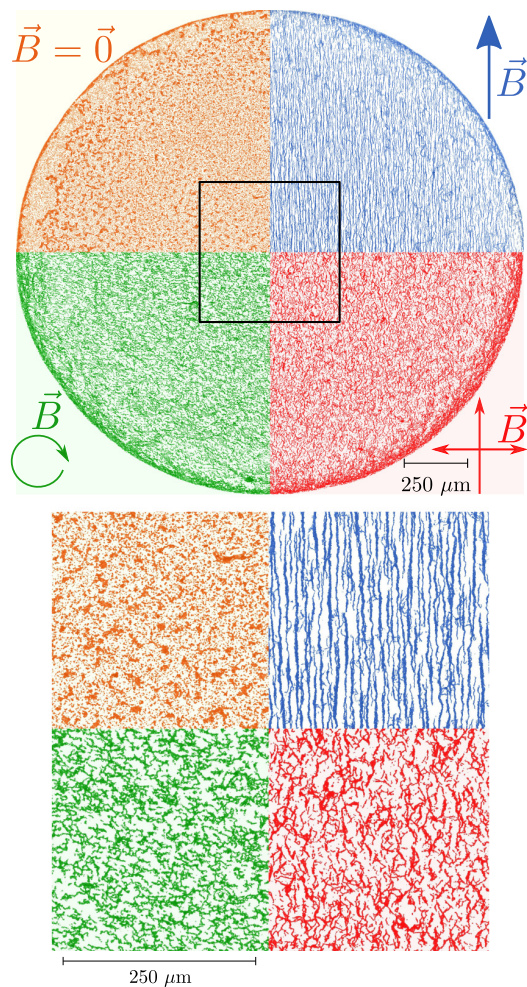


FIG. 1. Four deposits (four corners of the drop) obtained with different magnetic fields (null, homogeneous, rotating, and oscillating fields; amplitude of nonzero magnetic fields is 22.5 G). Each picture has been numerically colorized, cropped as a corner, and positioned according to the corresponding field condition. The bottom picture is a zoom on the squared area. The global surface density of particles does not change very much. However, the morphological details of the deposit are radically different from one field to the other.

evaporation chamber is placed upon it. The chamber is made of plexiglass and is T shaped. The upper branches of the T are filled with silica gel to ensure reproducible humidity condition in the chamber. The central trunk is kept empty in order to keep a clear path for the light. Petroleum jelly is applied on the bottom of the chamber's base to assess airtightness between the plexiglass and the cover glass. A magnetic field  $\vec{B}$  is applied by sending a current in surrounding coils at the beginning of each experiment. The magnetic field produced by those coils has been characterized with a Hall probe and, for a constant current, is homogeneous within the precision range of the probe of 2% around the cell. The constant current is sent in the coils with a constant intensity by a programmable dc power supply GenH-750W from TDK Lambda, with a precision of 0.01 A. The alternative currents producing rotating

and oscillating fields are produced by a dual channel arbitrary function generator AFG3022C from Tektronix and amplified by a power amplifier TOE7610 from Toellner. The suspension is observed from the bottom with a 16 $\times$  magnification. The microscope used is an inverted microscope Olympus IX73, connected to a 4070M-CL Thorlabs Camera with 2048 by 2048 pixels of 16 bits depth.

### III. RESULTS

We prepared a suspension of superparamagnetic colloids with a solid volume fraction of  $\phi = 5 \times 10^{-4}$  in diluted PBS (volume fraction of PBS  $\kappa = 50 \times 10^{-3}$ ). We then observed the evaporation of 2  $\mu$ l droplets under constant and homogeneous magnetic fields of intensity ranging from 0 to 22.5 G by steps of 4.5 G. Other magnetic fields were also tested to determine the generality of our results, namely rotating and oscillating fields. For each of the specific conditions, we observed at least five different droplets' evaporation in order to assess the reproducibility of the results.

Typical parts of eventually dried deposits are shown in Fig. 1, for the various fields we tested. When there is no magnetic field, a slight coffee-ring trend is observed, but similar surface fractions of particles are also observed in the center of the deposit. This almost homogeneous deposition of particles is actually induced by solutal Marangoni flows, due to the presence of PBS, as described in a previous study [13]. However, when a magnetic field  $|\vec{B}|$  is applied on the evaporating drop, the eventually dried deposit is radically different. The coffee-ring trend is even more reduced, as quantitatively self-assembly of the particles are observed throughout the deposit. As we will show here in detail for a constant and homogeneous magnetic field, the external field actually acts as a remote controller which can tune the morphological properties of the observed structures.

A quantitative analysis of the deposit can be performed by computing the mean surface density  $\rho$  of the drop. We computed this quantity as a function of the relative distance from the center  $r$  of the deposit, normalized by the radius  $R$  of the deposit, for various amplitudes of a constant and homogeneous magnetic field  $\vec{B}$ . We then normalized this surface density  $\rho$  by its integral  $N = \int_0^1 \rho(\delta) d\delta$ , where  $\delta = \frac{r}{R}$ . This normalization enhances the relative variation values and ensures that no difference in lightening is taken into account. Resulting curves are presented in Fig. 2. Those curves also enable one to compute the ratio between the surface fraction in the middle of the drop,  $\rho(0) \equiv \rho_m$ , and the surface fraction of the particles in the coffee ring,  $\rho_C$  (i.e., the value of the peak near the edge, see Fig. 2). This ratio  $\frac{\rho_C}{\rho_m}$  has been used previously to quantify the coffee-ring effect [10]. It is interesting to notice that, for high magnetic fields, the ratio drops below 1, implying that the coffee ring somehow does not really exist in this case (see Fig. 3). This affirmation has to be balanced by the fact that there is still a local maximum of the density near the edge of the deposit.

The mechanism through which the self-assembly influences the coffee-ring effect is by modifying the sedimentation time of the particles. Indeed, as demonstrated previously by Bhardwaj *et al.* [35], the transition from a coffee ring

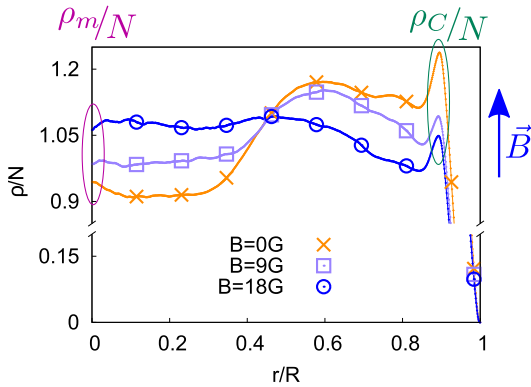


FIG. 2. Radial surface densities of the dried agglomerates normalized by the number of particles (so that the integral of the curve is equal to 1), obtained with constant and homogeneous magnetic fields of various intensities. The density of particles is mainly uniform all over the drop, but a slight coffee-ring effect is observed as a local maximum near the edge. However, the amplitude of this peak decreases when the amplitude of the external magnetic field increases. The reference density values  $\rho_m$  and  $\rho_C$  used to quantify the coffee-ring effect (see full text and Fig. 3) are highlighted in this graph.

to a homogeneous deposit can result from the competition between the sedimentation speed and the radial flow velocity. In their systems, the sedimentation speed is governed by a Derjaguin-Landau-Verwey-Overbeek (DLVO) attraction between the particles and the substrate. The presence of PBS in our system ensures that we have such attraction too. However, the sedimentation speed also depends on the size of the particles through the gravitational sedimentation. Indeed, the gravitational sedimentation time  $\tau_s$  over a typical dimension  $a$  of the particles size is proportional to  $\tau_s \propto \frac{Ca}{\rho g a^3}$ , where  $\rho$  is the difference between the particles and the fluid density,  $g$  is the acceleration of gravity, and  $C \propto \eta a$  is the drag coefficient depending on the viscosity  $\eta$ . The sedimentation time  $\tau_s$  is

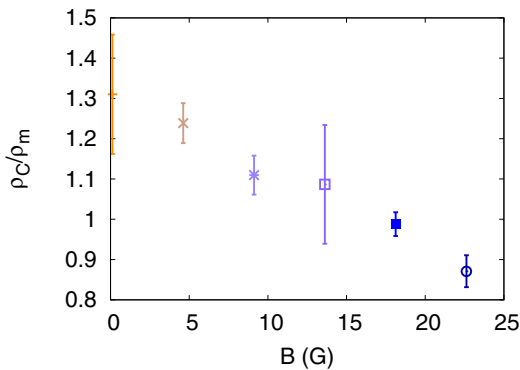


FIG. 3. Relative amplitude of the coffee rings as a function of the external magnetic field amplitude. This amplitude is computed as the ratio between the coffee-ring density  $\rho_C$  (value of the curves at the local maximum nearest from the drop's border), and the density in the center of the drop  $\rho_m$ . For high magnetic fields, this ratio drops below 1, indicating that the coffee-ring effect is mainly countered. The deposit is then almost uniform.

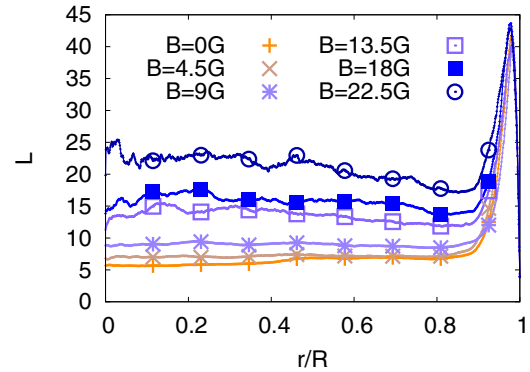


FIG. 4. Evolution of the mean major-axis length of the dried agglomerates (in particle's diameter), as a function of the normalized radial distance  $r/R$ . The main peak near the edge of the drop is actually caused by the coffee ring, which is locally seen as a very long agglomerate of particles. However, this length does not strongly depend on the position elsewhere and globally increases with the external magnetic field.

then proportional to  $\tau_s \propto a^{-1}$ . On the other hand, since the magnetic field  $\vec{B}$  induces the aggregation of the particles, this characteristic size  $a$  also depends on this field amplitude  $B$ . More accurately, for short times, the chains grow with a Smoluchowsky law  $\langle L \rangle = k(t/t_B)^z$ , where  $k$  is a geometric factor,  $t_B \propto B^{-2}$  is a characteristic time [23,36], and  $z$  is the kinetic exponent, usually measured between 0.6 and 0.7 [22–25]. If the characteristic length of the agglomerates is proportional to  $\langle L \rangle \propto B^{-1.3}$ , then the sedimentation time is proportional to  $\tau_s \propto B^{-1.3}$ . This then explains why self-assembly of particles lead to a decrease of the coffee-ring effect, depending on the magnetic field strength. The Supplemental Materials contain videos of evaporating droplet to show the self-assembly process of the particles [37]. Consistently, similar results are obtained with oscillating and rotating fields, as illustrated in the Supplemental Materials [37].

In our experiment, the magnetic field also changes morphological properties of the deposit. Namely, for a constant and homogeneous magnetic field, the chains formed by the particles during the evaporation process remain in the deposit. It is worthwhile to notice that in the case of lower Marangoni stress, as obtained with lower concentration of PBS, those structures do not necessarily deposit this way (see video in [37]). However, in the case of sufficient PBS concentration, this morphological change can be assessed by computing the local major-axis length  $L$  of the disjoint parts of the finally dried deposit (i.e., the disjoint agglomerates constituting the dried deposit). In the case of a constant field  $\vec{B}$ , the agglomerates are chains of particles aligned with the external magnetic field. The typical size of those agglomerates varies with the magnetic field intensity, but except at the edge of the deposit it does not strongly depend on the position in the deposit, as illustrated in Fig. 4 for the constant magnetic field. Those chains become longer as the magnetic field increases and the chains are observed everywhere in the finally dried deposit. The global averaged length of the chains all over the droplet increases with the amplitude of the magnetic field, as can be



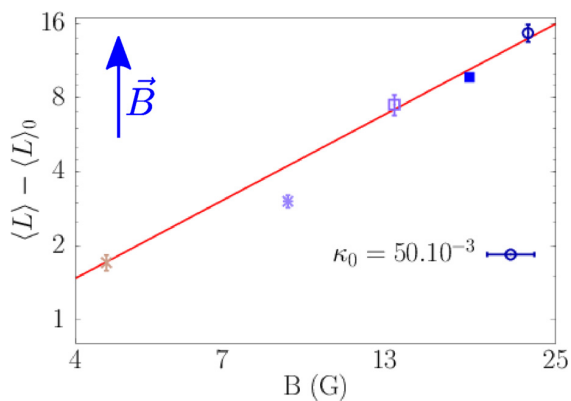


FIG. 5. Global averaged value of the major-axis length of the agglomerates in the deposit. This mean length  $\langle L \rangle$  is expressed as a function of the external magnetic field amplitude. The dots are experimental data, and the curve is a fit of the model  $\langle L \rangle = aB^{2z} + \langle L \rangle_0$  explained in the full text. The coefficient of determination  $R^2$  of the fit is  $R^2 = 0.97$ . In order to enhance the power-law behavior of the model, we subtracted the zero-field aggregate size  $\langle L \rangle_0$ .

seen in Fig. 5. The influence of the magnetic field on this parameter of the deposit can be modeled by assuming that the chains are self-organized as in an airtight chamber of liquid and then abruptly stopped after a constant time  $t_e$  which can be assimilated to the evaporation time of the droplet. Indeed, given the Smoluchowsky law  $\langle L \rangle = k(t/t_B)^z$ , at the time  $t_e$  where the evaporation of the droplet stops the assembly of the chains, the mean length of the particles should be  $\langle L \rangle = k(t_e/t_B)^z \propto B^{2z}$ . However, in our experiments, Marangoni flows can create particle agglomerates, initially at the top surface of the droplet, even without magnetic field. A first approach to take this agglomeration mechanism into account is to assume they simply shift this mean length and then consider a fit  $\langle L \rangle = aB^{2z} + \langle L \rangle_0$ , with  $a$  and  $\langle L \rangle_0$  being two fitting parameters, where  $a$  takes into account the evaporation time and the properties of both the fluid and the particles, while  $\langle L \rangle_0$  is the shift created by the Marangoni recirculation. By fixing the kinetic exponent to the typical value  $z = 0.65$ , we obtain the curve in Fig. 5, whose coefficient of determination  $R^2$  is about  $R^2 = 0.97$ . The power-law behavior of the data is enhanced in Fig. 5 by an appropriate scaling. The good agreement of this simple model with the data shows that the dominant mechanism determining the properties of the deposit in our system is indeed the magnetic self-assembly of the particles. This observation is reinforced by the various eventually dried deposits observed with different magnetic

field configurations as illustrated in Fig. 1. To obtain those deposits, we used magnetic fields of 22.5 G amplitude, and oscillating currents that have a frequency of 50 Hz. Rotating fields are generated with a sine current in the coils creating the field along the X axis, and a cosine current in the coils creating the field along the Y axis. The sign of the cosine is reversed every turn in order to avoid rotation of the particles [29]. The oscillating field is generated with a constant magnetic field along the Y axis and a sine-shape field along the X axis. While the global surface density distribution of the particles is comparable between the four conditions (zero, constant, rotating, and oscillating field), the morphological details of the deposit are radically different, as expected from the previous observations. Rotating fields create deposits with connected branches without preferential direction, as expected from previous studies [29]. Under oscillating fields, the final structures still have a preferential orientation along the average direction of the field. However, they locally acquire deviations which break the chains and connect them to their neighbors, creating a pattern in between the cases of constant and rotating fields.

#### IV. CONCLUSION

Those experiments show that, with the right strength of solutal-Marangoni instabilities, an external magnetic field can be used as a remote control of the eventually dried deposit. Indeed, due to this field, superparamagnetic colloids self-organize into structures that can be deposited almost as is on the substrate. This fine tunable control of dried deposits opens new ways to implement promising applications in microfabrication employing textured coatings (e.g., see [38–40]). Moreover, since the parameter responsible for the self-organization of the particles is the magnetic field, and given magnetic interactions can be easily written in equations, this experimental setup can be used as a model system to understand more complex systems. For instance, blood or protein deposits are known to give rise to peculiar patterns [41–43]. However, their interactions are quite complex. Tunable interactions from our setup might then be a good starting point to investigate how interactions between solid component influences their deposits.

#### ACKNOWLEDGMENTS

A.D. is financially supported by FNRS as a research fellow. This work was financially supported by the FNRS (Grant No. PDRT.0043.14) and by the University of Liège (Starting Grant No. C-13/88).

There are no conflicts to declare.

- [1] T. A. Yakhno, V. G. Yakhno, A. G. Sanin, O. A. Sanina, A. S. Pelyushenko, N. A. Egorova, I. G. Terentiev, S. V. Smetanina, O. V. Korochkina, and E. V. Yashukova, *IEEE Eng. Med. Biol. Mag.* **24**, 96 (2005).
- [2] D. Brutin, B. Sobac, B. Loquet, and J. Sampol, *J. Fluid Mech.* **667**, 85 (2011).
- [3] H. Y. Erbil, *Adv. Colloid Interface Sci.* **170**, 67 (2012).

- [4] K. Sefiane, *Adv. Colloid Interface Sci.* **206**, 372 (2014).
- [5] R. D. Deegan, O. Bakajin, T. F. Dupont, G. Huber *et al.*, *Nature (London)* **389**, 827 (1997).
- [6] R. D. Deegan, O. Bakajin, T. F. Dupont, G. Huber, S. R. Nagel, and T. A. Witten, *Phys. Rev. E* **62**, 756 (2000).
- [7] A. G. Marín, H. Gelderblom, D. Lohse, and J. H. Snoeijer, *Phys. Rev. Lett.* **107**, 085502 (2011).

- [8] Á. G. Marín, H. Gelderblom, D. Lohse, and J. H. Snoeijer, *Phys. Fluids* **23**, 091111 (2011).
- [9] Q. Xie and J. Harting, *Langmuir* **34**, 5303 (2018).
- [10] P. J. Yunker, T. Still, M. A. Lohr, and A. Yodh, *Nature (London)* **476**, 308 (2011).
- [11] H. Kim, F. Boulogne, E. Um, I. Jacobi, E. Button, and H. A. Stone, *Phys. Rev. Lett.* **116**, 124501 (2016).
- [12] H. Hu and R. G. Larson, *J. Phys. Chem. B* **110**, 7090 (2006).
- [13] A. Darras, N. Vandewalle, and G. Lumay, *Phys. Rev. E* (to be published).
- [14] R. Bennacer and K. Sefiane, *J. Fluid Mech.* **749**, 649 (2014).
- [15] J. R. E. Christy, Y. Hamamoto, and K. Sefiane, *Phys. Rev. Lett.* **106**, 205701 (2011).
- [16] Z. S. Davidson, Y. Huang, A. Gross, A. Martinez, T. Still, C. Zhou, P. J. Collings, R. D. Kamien, and A. Yodh, *Nat. Commun.* **8**, 15642 (2017).
- [17] J. Faraudo, J. S. Andreu, C. Calero, and J. Camacho, *Adv. Funct. Mater.* **26**, 3837 (2016).
- [18] J. W. Tavaicoli, P. Bauër, M. Fermigier, D. Bartolo, J. Heuvingh, and O. du Roure, *Soft Matter* **9**, 9103 (2013).
- [19] W. Wen, L. Zhang, and P. Sheng, *Phys. Rev. Lett.* **85**, 5464 (2000).
- [20] X. Xu, G. Friedman, K. D. Humfeld, S. A. Majetich, and S. A. Asher, *Adv. Mater.* **13**, 1681 (2001).
- [21] A. Snezhko and I. S. Aranson, *Nat. Mater.* **10**, 698 (2011).
- [22] J. S. Andreu, J. Camacho, and J. Faraudo, *Soft Matter* **7**, 2336 (2011).
- [23] J. H. Promislow, A. P. Gast, and M. Fermigier, *J. Chem. Phys.* **102**, 5492 (1995).
- [24] P. Domínguez-García, J. Pastor, and M. Rubio, *Eur. Phys. J. E* **34**, 36 (2011).
- [25] P. Domínguez-García, S. Melle, J. M. Pastor, and M. A. Rubio, *Phys. Rev. E* **76**, 051403 (2007).
- [26] M. Fermigier and A. P. Gast, *J. Colloid Interface Sci.* **154**, 522 (1992).
- [27] A. Darras, J. Fiscina, M. Pakpour, N. Vandewalle, and G. Lumay, *Eur. Phys. J. E* **39**, 47 (2016).
- [28] A. Darras, J. Fiscina, N. Vandewalle, and G. Lumay, *Am. J. Phys.* **85**, 265 (2017).
- [29] K. Müller, N. Osterman, D. Babič, C. N. Likos, J. Dobnikar, and A. Nikoubashman, *Langmuir* **30**, 5088 (2014).
- [30] M. Llera, J. Codnia, and G. A. Jorge, *J. Magn. Magn. Matter* **384**, 93 (2015).
- [31] R. M. Erb, H. S. Son, B. Samanta, V. M. Rotello, and B. B. Yellen, *Nature (London)* **457**, 999 (2009).
- [32] H. Carstensen, V. Kapaklis, and M. Wolff, *Phys. Rev. E* **92**, 012303 (2015).
- [33] K. V. Edmond, H. Park, M. T. Elsesser, G. L. Hunter, D. J. Pine, and E. R. Weeks, *Chaos* **21**, 041103 (2011).
- [34] S. D. Sheets and A. Finder, Polymeric microspheres and magnetic beads, <http://merckmillipore.com/>.
- [35] R. Bhardwaj, X. Fang, P. Somasundaran, and D. Attinger, *Langmuir* **26**, 7833 (2010).
- [36] A. Darras, E. Opsomer, N. Vandewalle, and G. Lumay, *Sci. Rep.* **7**, 7778 (2017).
- [37] See Supplemental Material at <http://link.aps.org/supplemental/10.1103/PhysRevE.98.062608> for rotating and oscillating magnetic field data and illustrative videos of the droplets' evaporation.
- [38] R. A. Bidkar, A. J. Kulkarni, L. S. Leblanc, and V. Bahadur, General Electric Co. Reduced fluid drag across a solid surface with a textured coating, U.S. Patent Application 14/037,790 (2015).
- [39] K. P. Gadkaree, F. M. Joos, J. R. Lim, K. P. Reddy, and J. E. Tosch, U.S. Patent No. 9,209,464 (8 December 2015).
- [40] T. Koshi and H. Kondo, U.S. Patent No. 4,761,312 (2 August 1988).
- [41] L. Lanotte, D. Laux, B. Charlot, and M. Abkarian, *Phys. Rev. E* **96**, 053114 (2017).
- [42] T. Yakhno, O. Sedova, A. Sanin, and A. Pelyushenko, *Techn. Phys.* **48**, 399 (2003).
- [43] G. Chen and G. J. Mohamed, *Eur. Phys. J. E* **33**, 19 (2010).

# Chapter 9

## Combined effects

### 9.1 Motivations

In Chapter 7, we evidenced the competition between Marangoni flows and the coffee-ring effect by using various PBS concentrations. In Chapter 8, we characterized the influence of various magnetic fields on the deposits obtained with a given PBS concentration. This work aims to complete the picture by offering the phase diagram obtained by modifying both PBS concentration and the intensity of the magnetic field.

### 9.2 Setup and methods

We used the same set-up as previously : droplets of superparamagnetic colloids suspended in diluted PBS were observed with an inverted microscope inside an airtight evaporative chamber. We prepared suspensions with three different concentrations of PBS. For each of them, we observed droplets under magnetic field from 0 G to 22.5 G. For each case, we evaporated at least five droplets in order to ensure the reproducibility of the results. We then analysed the dried deposits through image analysis.

### 9.3 Main results

We first show that three features capture the main characteristic of all our deposits. The first feature is a homogeneous background. This homogeneous trend is due to both sedimentation of the particles and the recirculation due to Marangoni instability. The second feature is the peak of density at the edge, due to the coffee-ring effect. The third and last effect is a secondary peak corresponding to a Marangoni eddy [84].

We then measured how the amplitude of these three features evolved as a function of the magnetic field and the PBS concentration. We found that the system behaves significantly differently if the DLVO forces between the substrate and the particles are repulsive or not.

In the case where they are repulsive (observed when initial volume fraction of PBS is  $\kappa_0 = 6 \cdot 10^{-3}$ ), we then have that the Marangoni effect dominates the eventual deposit. However, the coffee-ring is non negligible when the magnetic field is zero. When this magnetic field increases, it increases the influence of the sedimentation on the deposit pattern and then decreases the influence of the coffee-ring in the eventual pattern.

When the DLVO interaction between the substrate and the particles is attractive, the dominant mechanism becomes the sedimentation. The coffee-ring has then always a minimal influence. However, the exact balance between homogeneous deposit and the Marangoni eddy's amplitudes depends on the magnetic field. Indeed, this field determines the bulk sedimentation speed which is the bottleneck factor of this last phenomenon.

Examples of density profiles and evolution of amplitudes from the various features are illustrated in Figure 9.1. The panel (a) of this Figure 9.1 shows a really good agreement between the experimental data and the proposed master curve. Moreover, the evolution of the parameters  $Co$ ,  $C$  and  $Ma$  is consistent with the competition between their underlying mechanisms.

Indeed, the coefficient  $Co$  resulting from the competition between coffee-ring effect and sedimentation is immediately influenced by a change in the sedimentation induced by  $B$ . However, the competition between Marangoni recirculation and the sedimentation only appears to be balanced for high concentration of PBS, when the DLVO interaction between particles and substrate is attractive. Only at this moment can the magnetic field  $B$  influence the parameters  $C$  and  $Ma$ , describing respectively the amplitude of the homogeneous background and the Marangoni eddy, resulting from the competition between Marangoni flows and sedimentation.

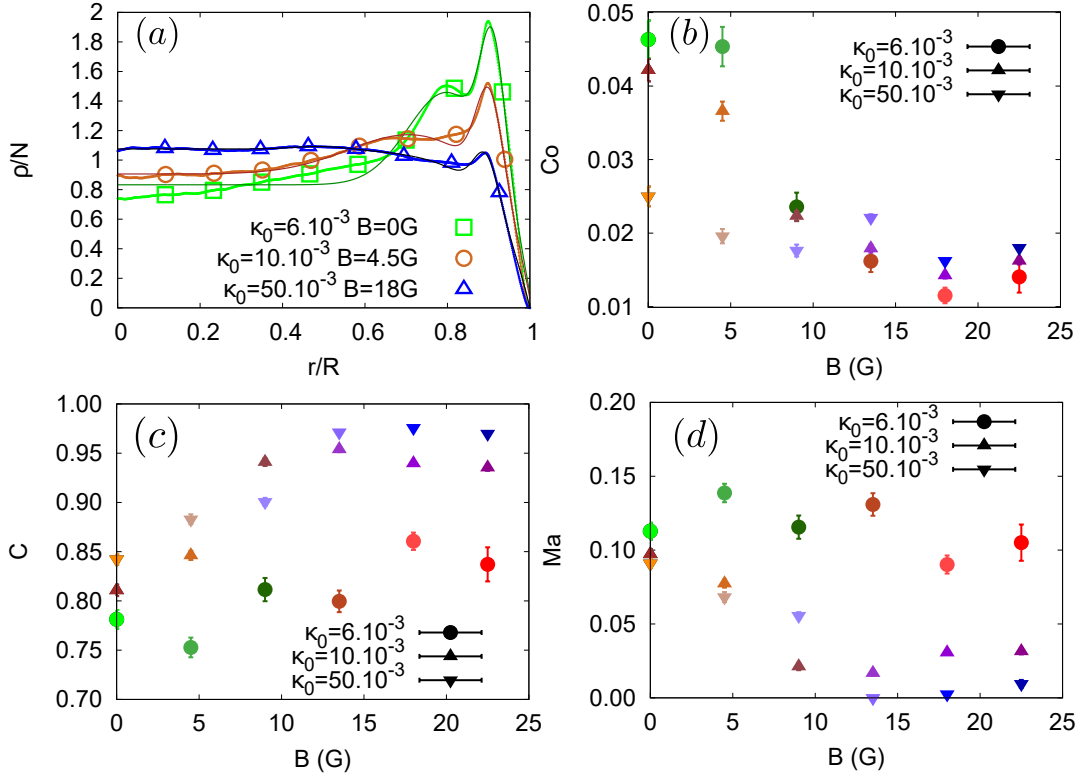


Figure 9.1: Picture from [91]. Properties of the fitted mean surface density of the agglomerates. (a) Examples of fitted profiles : the thin curves are the fits of the thick ones, which are actually a superposition of measured points. (b),(c),(d) respectively show the evolution of the fit parameters  $Co$ ,  $C$  and  $Ma$ . The  $Co$  parameter is the amplitude of the coffee-ring peak,  $C$  is the amplitude of the homogeneous background and  $Ma$  is the amplitude of the Marangoni eddy.

## 9.4 Conclusion

This paper suggests a generic curve for density of particles in evaporative deposits. We also introduced a justification of the evolution of this curve according to modifications of external parameters. These developments rationalize all our previous results on the evaporative deposits and offers insights for further theoretical modelling.

# Combined effects of Marangoni, sedimentation and coffee-ring flows on evaporative deposits of superparamagnetic colloids

Alexis Darras,<sup>1,2,3,\*</sup> Nicolas Vandewalle,<sup>1</sup> and Geoffroy Lumay<sup>1</sup>

<sup>1</sup>*GRASP, CESAM - Physics Department, University of Liège, B-4000 Liège; Belgium; <http://www.grasp-lab.org>*

<sup>2</sup>*F.R.S.-FRNS; B-1000 Bruxelles; Belgium; <http://www.frns.be>*

<sup>3</sup>*Experimental Physics, Saarland University; D-66123 Saarbrücken, Germany; <http://agwagner.physik.uni-saarland.de>*

(Dated: April 4, 2019)

Evaporation of sessile colloidal droplets is a way to organize suspended particles. It is known from long that the composition of the surrounding fluid strongly modifies the dried deposit. For the case of superparamagnetic particles, recent studies have shown that an external magnetic field can act as a remote control for those deposits. In this paper, we study the configuration space given by the interplay of this magnetic field and a modification of the fluid composition by considering various concentrations of phosphate buffered saline (PBS). We show that the magnetic field mainly modifies the morphological properties of the dried deposit, while the composition (i.e. PBS concentration) mainly modifies the density profile of the deposit. We then present an explanation of these influences by taking into account the competition between (i) sedimentation, (ii) coffee-ring and (iii) Marangoni flows. From these considerations, we propose a master curve which should be able to model the deposit densities of any system where the above three mechanisms compete with each other.

## I. INTRODUCTION

The evaporation of colloidal droplets is currently a topic of intensive research due to its wide range of potential applications, extending from blood analysis [1, 2] via inkjet printing, paint and polymers [3], up to and including nanotechnology [4]. The main feature of colloidal droplets evaporation is the so-called coffee-ring effect [5–8]. This effect implies that particles tend to be deposited at the edge of the final dried pattern. However, several studies have shown various mechanisms preventing this effect. Notably, capillary interactions of ellipsoidal particles [9, 10] or the presence of surface-adsorbed polymers [11] allows a uniform coating of the particles. Marangoni flows created by temperature gradients, tensio-active agents or in binary mixtures [12–15] can also strongly modify the deposits pattern in various ways [11, 16–18]. More recently, some researchers have shown that more complex deposit structures can be achieved thanks to various concentration of liquid crystals [19]. Regarding superparamagnetic colloids, magnetic interactions between particles can be used to control the properties of colloidal droplets' deposits [20].

Superparamagnetic colloids are magnetic nanoparticles inserted in a matrix of non-magnetic material (polystyrene or silica) to obtain particles with diameter  $d$  ranging from 100nm to a few micrometers. These composite particles are combining a quasi-zero remanent magnetization and a high magnetic response [21–23]. If immersed in a constant and homogeneous magnetic field, the particles form chains aligned with the field [21, 24–31]. This technique is used for protein isolation, cell sep-

aration, waste capture, bacteria processing, chromatography, etc [21, 24, 32–40]. More complex structures of superparamagnetic colloids can be obtained by using rotating fields, even possibly leading to microswimmers or tracers of local dynamics [26, 27, 41–49]. Those complex structures open ways to new kind of applications as they have unique optical properties and offer tunable structures able to adapt to their environment and execute functional tasks [43, 44, 47, 50]. In the context of evaporating droplets, it has been shown recently that these assemblies could be deposited in the dried deposit [20]. However, it has been highlighted that such a deposition requires the right concentration of PBS, and that this latter parameter also has an impact on the dried deposit [15].

In this paper, we focus on how those two parameters, initial PBS concentration and external magnetic field, interact with each other and describe the evolution of the various deposits resulting from their combination. We show that these parameters influence the competition between three mechanisms : (i) sedimentation, (ii) coffee-ring effect and (iii) Marangoni instabilities. While such competition between three mechanisms has already been observed previously [51], it is the first time that the resulting features are all observed at the same time in the same deposit. Bhardwaj *et al.* indeed described such a diagram where Marangoni recirculation, sedimentation and coffee ring flow compete with each other, but their actual measurements only stood on the 0-axis of their diagram, comparing only two mechanisms at a time. This work describes the evolution of their interplay through combined variations of two control parameters, namely external magnetic fields and initial PBS concentration, describing the associated configuration space.

---

\* alexis.darras@ulg.ac.be

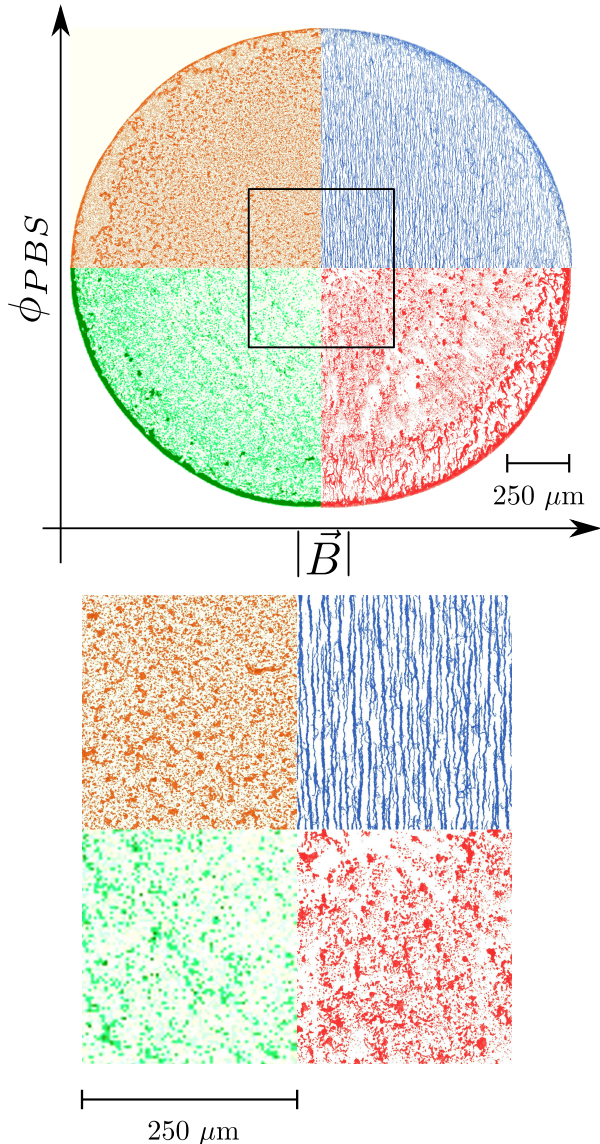


FIG. 1. Details of deposits obtained with different magnetic fields (0G and 22.5 G) and various PBS concentration ( $6 \cdot 10^{-3}$  and  $50 \cdot 10^{-3}$  initial volume fraction). Each picture has been numerically coloured according to the corresponding field condition. The bottom picture is a zoom on the squared area. Both global surface density of the particles and the morphological details of the deposits vary from one deposit to the other.

## II. METHODS

### A. Suspensions preparation

The experiments were performed with superparamagnetic microspheres dispersed in water (Estapor<sup>®</sup> M1-070/60, typical diameter  $d \approx 10^{-6}$ , and magnetic susceptibility  $\chi \approx 0.1$  in SI units [52]), with a volume fraction of  $\phi = 5 \cdot 10^{-4}$ . Those particles are covered with

carboxyl charged groups to enable electrostatic stabilization of the suspension. In order to clean the spheres from any chemical waste, the commercial suspensions are first deposited in the bottom of their container with a centrifuge. The supernatant is then removed and the same quantity of distilled water is then poured back in the container. The particles are then dispersed again in the liquid thanks to a ultrasonic bath and mechanical agitation. This process is repeated three times. Then the particles are deposited once again and the supernatant is replaced with the adequate solution, i.e. water with dilute phosphate buffered saline (PBS). The PBS has been chosen since it is a commercial available pH buffer involving only non-organic molecules. Indeed, pH is often used as a parameter to control electrostatic stabilization [53], and organic molecules could potentially feed bacteria who could reach the suspension as it ages.

### B. Microscopy observations

To perform the observations, a  $2 \mu\text{l}$  droplet of the suspension is placed on a microscope cover glass. A custom airtight evaporative chamber is placed upon it. The chamber is made of plexiglass and T-shaped. The upper branches of the T are filled with silica gel to ensure reproducible humidity condition in the chamber. The central trunk is kept empty in order to keep a clear path for the light. Petroleum jelly is applied on the bottom of the chamber's base to assess airtightness between the plexiglass and the cover glass. A magnetic field  $B$  is applied by sending a constant current in surrounding coils at the beginning of each experiment. The magnetic field produced by those coils has been characterized with a Hall probe and, for a constant current, is homogeneous within the precision range of the probe of 2% around the cell. The constant current is sent in the coils with a constant intensity by a programmable DC power supply GenH-750W from TDK Lambda, with a precision of 0.01 A. The alternative currents producing rotating and oscillating fields are produced by a dual channel arbitrary function generator AFG3022C from Tektronix and amplified by a power amplifier TOE7610 from Toellner. The suspension is observed from the bottom with a 16x magnification. The microscope used is an inverted microscope Olympus IX73, connected to a 4070M-CL Thorlabs Camera with 2048 by 2048 pixels of 16 Bits depth.

### C. Reproducibility of the results

We prepared three different suspensions, each of them with various concentration of PBS but the same colloidal volume fraction of  $\phi = 5 \cdot 10^{-4}$ . The PBS was diluted in initial volume fraction  $\kappa_0$  as  $6 \cdot 10^{-3}$ ,  $10 \cdot 10^{-3}$  and  $50 \cdot 10^{-3}$  of the respective final suspensions. For each of these suspensions, we observed the evaporation under constant and homogeneous magnetic fields of intensity

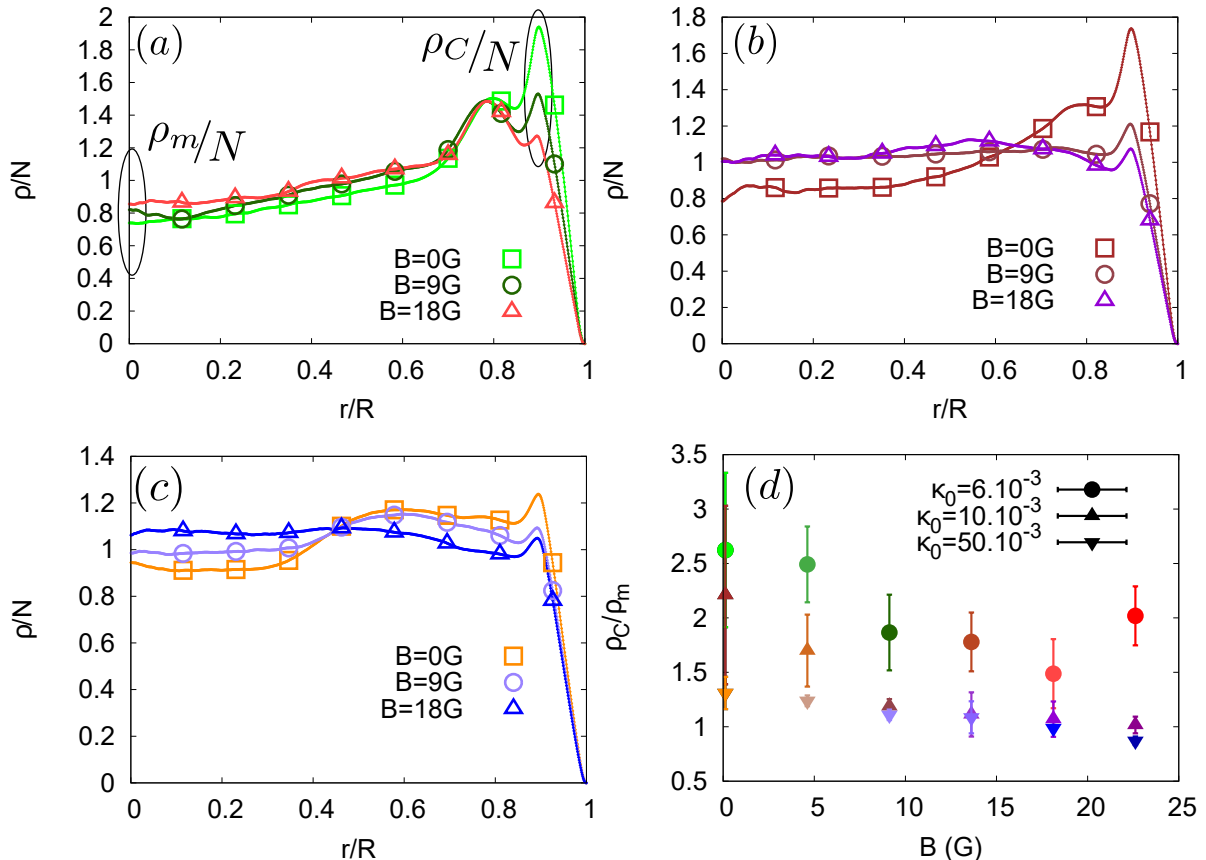


FIG. 2. Evolution of the mean surface density of the dried agglomerates normalized by the number of particles (so that the integral of the curve is equal to one), for the various PBS concentration (Initial volume fractions  $\kappa_0$  : (a)  $6 \cdot 10^{-3}$ , (b)  $10 \cdot 10^{-3}$ , (c)  $50 \cdot 10^{-3}$ ). Both curves and dots are experimental data, the dots are there to distinguish the various curves in black and white impressions. For the coloured version, those are given accordingly to the colours in Fig. 1. The relative amplitudes of the coffee rings are summarized in (d) thanks to the ratio between the coffee ring density  $\rho_c$  (value of the curves at the local maximum nearest from the drop's border) and the density in the center of the drop  $\rho_m$ . For high PBS concentration and high magnetic field, this ratio drops below one, indicating that the coffee ring effect is mainly countered. The deposit is then almost uniform. The values of  $\rho_c$  and  $\rho_m$  used to obtain (d) are highlighted in (a) for the case of  $\kappa_0 = 6 \cdot 10^{-3}$ .

ranging from 0 G to 22.5 G by steps of 4.5 G. For each of the specific conditions, we observed at least 5 different droplets evaporation in order to assess the reproducibility of the results.

### III. RESULTS

#### A. General description

Typical parts of final dried deposits are shown in Fig. 1, for the extremal conditions we tested. For low PBS concentration and no magnetic field, a clear coffee-ring effect is observed. Most of the particles are indeed deposited at the edge of the deposit. Still without field but with the highest PBS concentration, a coffee ring trend is observed again, but similar surface fractions of particles are also observed in the center of the deposit. This more homogeneous deposition of particles is actu-

ally induced by solutal Marangoni flows, as described in previous study [15]. However, when a magnetic field of intensity  $B = 22.5$  G is applied on the evaporating drop, the final deposits are radically different. For low concentration of PBS, the coffee ring effect is then strongly reduced and the deposit is characterized by a region near the edge where chains of particles aligned with the field are observed. Interestingly, the length of these chains varies with the magnetic field intensity, but does not depend significantly on the angular position in the deposit. For high PBS concentration, the coffee-ring trend is reduced as well but chains can be found even in the center of the deposit, as already described in a previous publication [20].

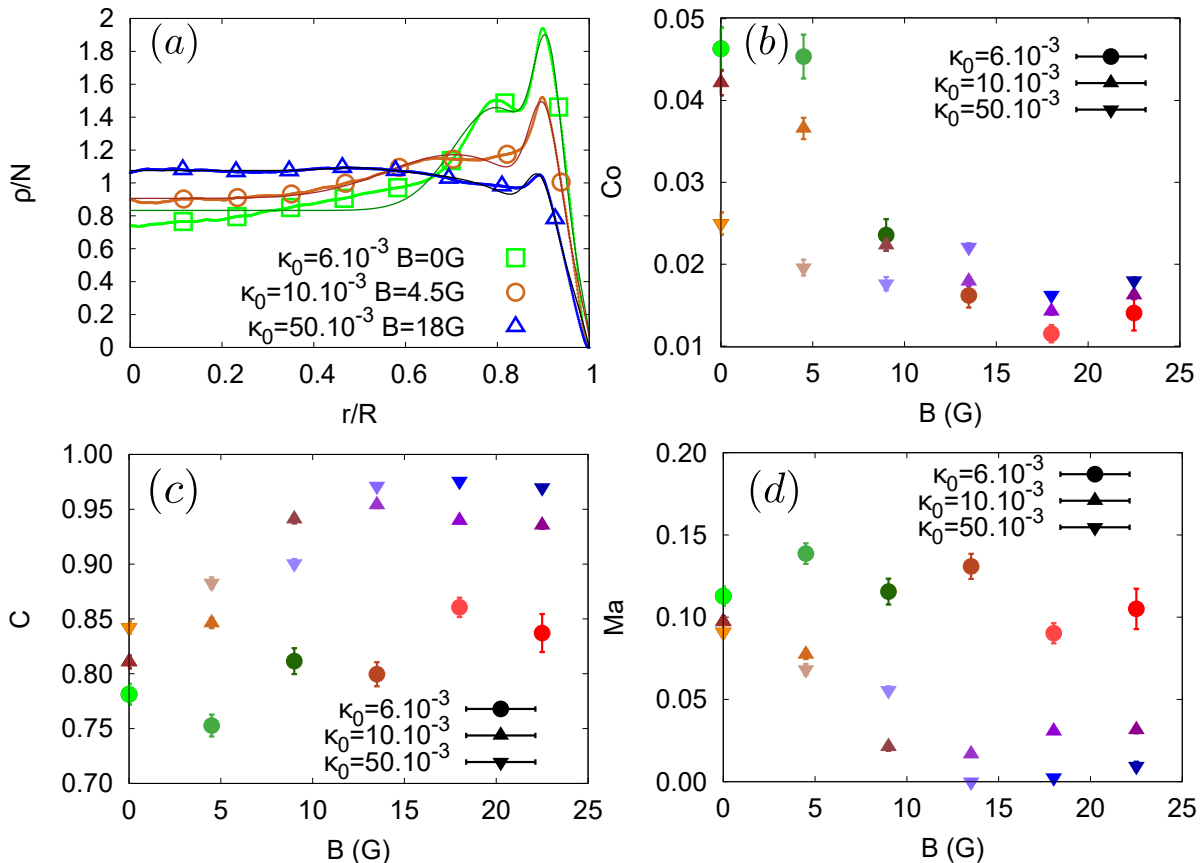


FIG. 3. Properties of the fitted mean surface density of the agglomerates. (a) Examples of fitted profiles : the thin curves are the fits of the thick ones, which are actually a superposition of measured points (containing larger points to distinguish them in black and white). For the coloured version, those are given accordingly to the colours in Fig. 1. The highest peak is characteristic from the lowest initial PBS concentration  $\kappa_0 = 6 \cdot 10^{-3}$  while the lowest peak is on the curve with the highest concentration  $\kappa_0 = 50 \cdot 10^{-3}$ . The graphs (b),(c),(d) respectively show the evolution of the fit parameters  $Co$ ,  $C$  and  $Ma$ . The  $Co$  parameter is the amplitude of the coffee-ring peak,  $C$  is the amplitude of the homogeneous background and  $Ma$  is the amplitude of the Marangoni eddy.

## B. Density profiles

### 1. Definition

A more quantitative analysis of the deposits can be performed by computing the mean surface density  $\rho$  of the drop. We computed this quantity as a function of the relative distance from the center  $r$  of the deposit, normalized by the radius  $R$  of the deposit. We then normalized it by its integral  $N = \int_0^1 \rho(\delta) d\delta$ , where  $\delta = \frac{r}{R}$ . This normalization enhances the relative variation values and ensures that no difference in lightening are taken into account. Resulting curves are presented in Fig. 2. Those curves also enable to compute the ratio between the surface fraction in the middle of the drop  $\rho(0) \equiv \rho_m$  and the surface fraction of the particles in the coffee-ring  $\rho_C$ . This ratio  $\frac{\rho_C}{\rho_m}$  has been previously used to quantify the coffee-ring effect [9]. The evolution of this ratio is summarized in Fig.2d. It is interesting to notice that for

high PBS concentration and high magnetic field, the ratio drops below 1, implying that the coffee ring is not the main phenomenon in this case.

### 2. Detailed density features

Actually, one can identify three features on our eventual density profiles, each depending on different competing mechanisms. Such competition between three mechanisms has already been observed previously [51], but it is the first time that the resulting features are all observed at the same time in the same deposit. Bhardwaj *et al.* indeed described such a diagram where Marangoni recirculation, sedimentation and coffee ring flow compete with each other, but their actual measurements only stood on the 0-axis of their diagram, comparing only two mechanisms at a time.

In our case, the first feature is the background of homogeneous density. This is induced by both sedimen-



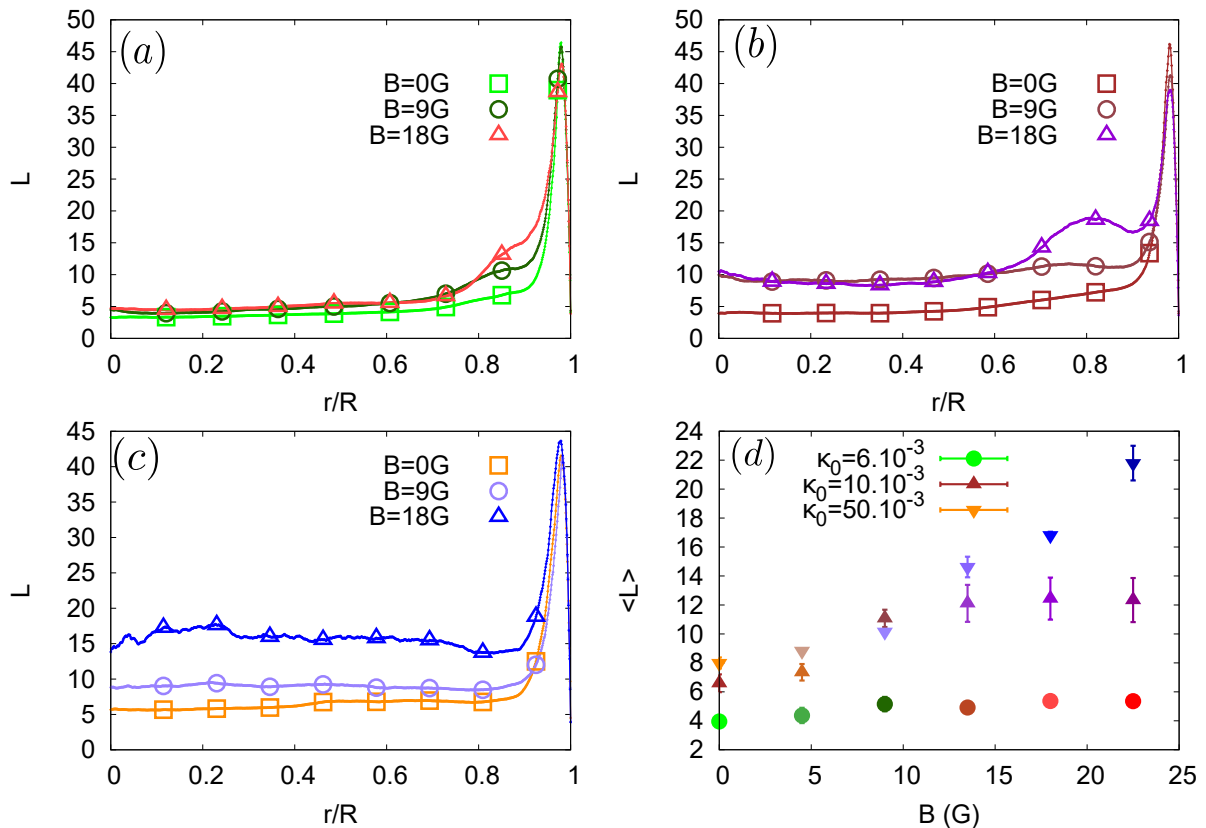


FIG. 4. Evolution of the mean major-axis length of the dried agglomerates (in particle's diameter), for the various PBS concentration (Initial volume fractions  $\kappa_0$  : (a)  $6 \cdot 10^{-3}$ , (b)  $10 \cdot 10^{-3}$ , (c)  $50 \cdot 10^{-3}$ ). The mean value of the major-axis as a function of the magnetic field amplitude length is summarized in the graph (d). For the coloured version, those are given accordingly to the colours in Fig. 1. The larger points are there to distinguish the curves in black and white version.

tation of the particles (enhanced by the DLVO interaction between particles and the substrate [51] and the self-assembly of the particles [20]) and Marangoni instability (induced by transitional Marangoni bulk instability due to PBS [15]). It is worthwhile to notice there is a difference between Marangoni instability, creating several recirculation cells on a single radius length of the droplet, and Marangoni recirculation, creating a single recirculation cell on one radius length of the droplet. The latter tends to produce a peak of density at the center of the droplet [12, 16, 51] while the former produces a more homogeneous deposit, patterned with the border of the cells [15, 17, 20]. This feature creates a density profile which can be modelled as

$$\begin{aligned} \rho/N &= (1 - e^{K(r/R-1)}) / \int_0^1 (1 - e^{K(s-1)}) ds \\ &= K(1 - e^{K(r/R-1)}) / (K - 1 + e^{-K}), \end{aligned} \quad (1)$$

where  $K > 0$  is a parameter describing the smoothness of the edge.

The second feature is the coffee-ring effect, created by the mass-conservative flow inside the droplet [5-8, 54]. This feature creates a peak of density in the eventual

deposit near the edge of the droplet, that we modelled by a normal distribution

$$\rho/N = e^{-(r/R-m_{Co})^2/(2\sigma_{Co}^2)} / (\sqrt{2\pi}\sigma_{Co}), \quad (2)$$

where  $m_{Co}$  is the position of the center of this outer peak and  $\sigma_{Co}$  is the standard deviation associated with this distribution.

The third feature is the so-called Marangoni eddies [18]. Those eddies are due to interactions between Marangoni recirculation at the edge of the deposit and the coffee-ring deposit. Indeed, the recirculation near the deposited coffee-ring tends to redistribute the particles slightly closer to the center of the droplet, which creates a secondary peak of density on a lower  $r/R$  coordinate. Such secondary peak can clearly be seen on Fig. 2(a). We modelled this peak with another normal distribution

$$\rho/N = e^{-(r/R-m_{Ma})^2/(2\sigma_{Ma}^2)} / (\sqrt{2\pi}\sigma_{Ma}), \quad (3)$$

where  $m_{Ma}$  is the position of the centre of this outer peak and  $\sigma_{Ma}$  is its standard deviation.

The final density profile can then be modelled as

$$\begin{aligned} \frac{\rho}{N} = & CK \frac{1 - e^{K(r/R-1)}}{-1 + e^{-K}} \\ & + \frac{Co}{\sqrt{2\pi\sigma_{Co}}} e^{-(r/R-m_{Co})^2/(2\sigma_{Co}^2)} \\ & + \frac{Ma}{\sqrt{2\pi\sigma_{Ma}}} e^{-(r/R-m_{Ma})^2/(2\sigma_{Ma}^2)}, \end{aligned} \quad (4)$$

where  $C, Co, Ma \in [0, 1]$ , (with  $C + Co + Ma = 1$  to respect the normalization of  $\rho/N$ ) are parameters describing the relative importance of each feature. Resulting fits and evolution of the fitted amplitude parameters  $C, Co, Ma$  are shown in the Fig.3 The trends of these curves are discussed in the Section IV D, on the basis of the competition between Marangoni instability, coffee-ring effect and sedimentation.

### C. Morphological properties

In our experiment, the magnetic field also change morphological properties of the deposit. More accurately, the chains formed by the particles during the evaporation process remain partly in the deposit. This morphological change can be assessed by the computing the local major-axis length  $L$  of the disjoint parts of final deposits. Those measurements are represented in Fig. 4. The main peak near the edge of the drop is actually caused by the coffee ring, which is locally seen as a very long agglomerate of particles. However, for low PBS concentrations ( $6 \cdot 10^{-3}$  and  $10 \cdot 10^{-3}$  volume fraction), chains can also appear in a region close to this edge. The length of those chains becomes longer as the magnetic field increases. However, the width of the region where they are observed does not depend on this magnetic field. For the highest PBS concentration,  $50 \cdot 10^{-3}$  volume fraction, the chains are observed everywhere in the final deposit. The mean length of the chains increases with the amplitude of the magnetic field.

## IV. DISCUSSION

To understand the evolution of the different parameters from Eq. (4), it is useful to compare the characteristic speed of each mechanism occurring in our system. In the magnitude order considerations which follow, we take all the values in SI units and therefore do not always recall the units, in order to avoid overloading the equations.

### A. Mass conservation flow

Typical speed of the coffee-ring effect  $v_{CR}$ , induced by the flow of mass conservation, solely depends on the

geometry of the droplet and scales as

$$v_{CR} \sim \frac{2 h_0 R}{h t_f}, \quad (5)$$

where  $h$  is the height of the droplet,  $h_0$  is the initial height,  $R$  is the radius droplet and  $t_f$  is the time required to completely evaporate the drop [15, 16]. It is then time dependant and diverge near the end of the evaporation, but it is worthwhile to notice that it does not depend on the varied parameters of our experiments,  $B$  and  $\kappa_0$ . The characteristic value of this speed at the beginning of the evaporation (for a droplet of height  $h_0 \sim 10^{-3}$  m, radius  $R \sim 10^{-3}$  m and an evaporation time of  $10^3$  s) has a magnitude scaling as  $v_{CR} \sim 10^{-6}$  m/s.

### B. Marangoni recirculation speed

Typical speed of Marangoni recirculation  $v_{Ma}$  scales as

$$v_{Mg} \sim \frac{Mg h h_0}{R t_f} \quad (6)$$

where  $Mg$  is the Marangoni number

$$Mg = \left( \frac{\partial \gamma}{\partial \kappa} \kappa_0 t_f \right) / (\eta R), \quad (7)$$

where  $\gamma$  is the surface tension, and  $\eta$  the viscosity of the liquid [15, 16]. We can then write

$$v_{Mg} \sim \frac{\partial \gamma}{\partial \kappa} \frac{\Delta \kappa t_f h_0^2}{\eta R^2 t_f} \sim 10^{-1} \kappa_0 \text{ m/s} \quad (8)$$

as the characteristic value of the Marangoni recirculation speed, since  $\eta \sim 10^{-3}$  Pa s and  $\frac{\partial \gamma}{\partial \kappa} \sim 10^{-4}$  N/m<sup>2</sup> [20].

### C. Sedimentation speed

Since we can consider we are in a viscous regime, the characteristic speed of sedimentation  $v_S$  depends on DLVO forces  $F_{DLVO}$ , the effective weight of the agglomerates  $W$  (taking into account both gravity and buoyancy) and the drag coefficient of the agglomerates  $D \propto \eta a$ , where  $\eta$  is the viscosity of the fluid and  $a$  the typical size of the agglomerates (we define here the drag coefficient as the ratio between the drag force and the relative speed of the object in the fluid). We then have  $v_c \propto (F_{DLVO} + W)/D$ .

#### 1. DLVO forces

The DLVO forces are the sum of electrostatic repulsion  $F_e$  and van der Waals attraction  $F_{VdW}$ :  $F_{DLVO} = F_e + F_{VdW}$ . If we note  $\lambda$  the Debye screening length, the electrostatic repulsion  $F_e$  between particles and the

substrate, taking into account the double layer of ions, scales as

$$F_e \sim -64\pi d n k_B T \lambda \exp(z/\lambda) \quad (9)$$

where  $n$  is the number of counterions per unit volume (molecules by  $\text{m}^3$ ),  $z$  is the interdistance between the substrate and the particle,  $k_B$  is the Boltzmann constant,  $T$  the temperature and  $d$  is the particle's diameter. In order to assess a typical magnitude for this force, let us first estimate the Debye length  $\lambda$

$$\lambda \sim \sqrt{\frac{\epsilon_r \epsilon_0 k_B T}{2N_A e^2 I}} \sim \frac{\lambda_{PBS}}{\sqrt{\kappa_0}} \sim \frac{10^{-9}}{\sqrt{\kappa_0}} \text{ m}, \quad (10)$$

where  $\epsilon_r \epsilon_0$  is the effective electric permittivity of water,  $N_A$  is the Avogadro number,  $e$  the fundamental charge of the electron and  $I = \kappa_0 I(PBS)$  the ionic strength of the dispersant ( $I(PBS)$  is the ionic strength of pure PBS) [51, 55]. All of those constant can be expressed in terms of the Debye length of pure PBS,  $\lambda_{PBS} \sim 10^{-9} \text{ m}$  [55], and the dilution of PBS,  $\kappa_0$ . We can also assess the number of counterions  $n$

$$n \sim N_A 10^3 \kappa_0 C_{PBS} \sim 10^{25} \kappa_0 \text{ m}^{-3}, \quad (11)$$

since the concentration  $C_{PBS}$  of ions in PBS is dominated by the concentration of NaCl and then  $C_{PBS} \approx 137 \text{ mmol/L} \sim 0.1 \text{ M}$ . Taking into account those two estimations, we eventually obtain that the electrostatic repulsion, assessed at the Debye length, goes like  $F_e \sim 10^{-9} \sqrt{\kappa_0} \text{ N}$ . All in all, we obtain a characteristic value for the electrostatic force  $F_e \sim 10^{-9} \sqrt{\kappa_0} \sim 10^{-10} \text{ N}$ , given the range of  $\kappa_0 \in [6 \cdot 10^{-3}, 5 \cdot 10^{-2}]$  we explored. The van der Waals interaction forces, estimated at the Debye length, scales as

$$F_{VdW} \sim \frac{A d}{\lambda^2} \sim 10^{-8} \kappa_0 \text{ N}, \quad (12)$$

where  $A$  is the Hamaker constant,  $A = 2.43 \cdot 10^{-20} \text{ J}$  for water. In our case, the van der Waals interaction goes from  $10^{-11} \text{ N}$  to  $10^{-10} \text{ N}$ . We can already conclude that we will have a transition in our system. Indeed, for low PBS concentration  $\kappa_0 = 6 \cdot 10^{-3}$  we have  $F_{VdW} < F_e$  while, for high concentration  $\kappa_0 = 50 \cdot 10^{-3}$ , we have  $F_{VdW} \approx F_e$ . In the former case, the complete sedimentation will be at least slowed down thanks to electrostatic repulsion, while for the latter van der Waals interactions are likely to create a faster sedimentation. We will show here that this can explain the behavior of the curves in Fig. 3.

## 2. Agglomerates properties

Before discussing the curves in Fig. 3, we still have to assess the weight  $W$  of each agglomerates and their drag

coefficient  $D$ . First of all, let us notice that the typical length of those agglomerates grows like

$$\langle L \rangle \sim d \left( 1 + \frac{\phi \chi^2 t_f B^2}{\eta \mu_0} \right)^{0.65} \sim 10^{-6} + 0.1 B^{1.3} \text{ m}, \quad (13)$$

where  $\phi \sim 10^{-3}$  is the volume fraction of the colloidal particles,  $\chi \sim 0.1$  is their magnetic susceptibility and  $\mu_0 \approx 4\pi \cdot 10^{-7}$  is the magnetic permeability of water[20]. Given the magnetic field  $B$  goes from 0 to  $10^{-3}$  in our experiments, this length ranges from  $10^{-6}$  to  $10^{-5}$ . From this we can compute the drag coefficient [25]

$$D \approx \frac{\eta \langle L \rangle}{\ln \frac{\langle L \rangle}{d} - 0.5} \sim \eta \langle L \rangle \sim 10^{-9} + 10^{-4} B^{1.3} \text{ kg/s}, \quad (14)$$

from which we can infer that the drag coefficient  $D$  goes from  $10^{-9} \text{ kg/s}$  to  $10^{-8} \text{ kg/s}$ . The effective weight of each agglomerate can be assessed as

$$W \sim \delta g \langle L \rangle d^2 \sim 10^{-14} + 10^{-9} B^{1.3} \text{ N}, \quad (15)$$

where  $\delta \sim 10^3 \text{ kg/m}^3$  is the difference in the volume density between the particles and the water and  $g \sim 10 \text{ m/s}^2$  is the gravitational acceleration. From previous range for  $B$ , we then infer that this force is comprised between  $10^{-14} \text{ N}$  and  $10^{-13} \text{ N}$ .

## 3. Global sedimentation speed

We can then distinguish two regimes regarding the sedimentation speed, depending on the concentration of PBS in the droplet. If the PBS concentration is small enough  $\kappa_0 \sim 10^{-3}$ , then the DLVO forces repel the particles from the substrate when they are close enough (typically at the Debye length). The only characteristic sedimentation speed is then the one obtained in the bulk of the droplet and determined by the effective weight of the particles :  $v_S = W/D \sim 10^{-5} \text{ m/s}$ . In this case, we then have  $v_{CR} \sim 10^{-6} \text{ m/s} \ll v_S \sim 10^{-5} \text{ m/s} \ll v_{Mg} \sim 10^{-4} \text{ m/s}$ . If the concentration of PBS is high enough, the DLVO forces between the particles and the substrate become attractive and the sedimentation is also characterized by the force which makes the particles sticking to the substrate. The speed associated to this motion can be assessed as  $v_S \approx F_{DLVO}/D$ . In this case, since we are close the transition, we can estimate that the DLVO forces are at least of the order of 10% of the electrostatic and van der Waals forces :  $F_{DLVO} \sim 10^{-11} \text{ N}$ . In this case, the sedimentation speed ranges is  $v_S \sim 10^{-2} \text{ m/s}$  for each individual particles. We then have  $v_{CR} \sim 10^{-6} \text{ m/s} \ll v_{Mg} \sim 10^{-3} \text{ m/s} \ll v_S \sim 10^{-2} \text{ m/s}$ .

#### D. Evolution of the density profile parameters

If we assume

$$Co \propto (v_{CR} - v_S)/(Co + C + Ma), \quad (16)$$

$$C \propto (v_S + v_{Mg})/(Co + C + Ma) \quad (17)$$

$$\text{and } Ma \propto (v_{Mg} - v_S)/(Co + C + Ma), \quad (18)$$

the different behaviours in our system can be understood by comparing the sedimentation speed with the two other speeds. These hypotheses comes from the fact that if the sedimentation makes the particles stick to the substrate, the fluid will not be able to move it at its own velocity, but will have to act against the sedimentation forces through a drag force. Then the effective speed for Coffee-ring construction  $v_{eff,Co}$  verifies  $D v_{eff,Co} = D v_{CR} - D v_S \Leftrightarrow v_{eff,Co} = v_{CR} - v_S$ . The same reasoning holds for the Marangoni eddy construction  $v_{eff,Ma} = v_{Mg} - v_S$ .

In the case of low initial PBS concentration  $\kappa_0$ , we established that we have  $v_{CR} \sim 10^{-6}$  m/s  $\ll v_S \sim 10^{-5}$  m/s  $\ll v_{Mg} \sim 10^{-4}$  m/s. Particles can then not completely sediment on the substrate and only the Marangoni speed  $v_{Mg}$  is relevant in this case. It is worthwhile to notice that the bulk sedimentation speed  $v_S$  still increase with  $B$  since  $W/D \propto \ln(\langle L \rangle/d) - 0.5$ . In this case, while  $Co \propto v_{CR} - v_S$  will decrease with  $B$ , while  $C$  and  $Ma$  can stay more or less constant. Indeed, given  $Co \ll Ma, C$  and  $v_S \ll v_{Mg}$ , we have  $C \propto v_{Mg}/(C + Ma)$  and  $Ma \propto v_{Mg}/(C + Ma)$ .  $Ma$  and  $C$  can still have different values because their proportionality coefficient can be different. This explains the curves in Fig.3 for  $\kappa_0 = 6 \cdot 10^{-3}$ . Indeed, for this initial concentration, the values of  $Ma$  and  $C$  remains more or less constant, while  $Co$  decreases when  $B$  increases.

For higher values of  $\kappa_0$ , for a given magnetic field  $B$ ,  $v_S$  and  $v_{Mg}$  will increase while  $v_{CR}$  will remain constant. This explains the vertical shifts of the curves in Fig.3 for increasing values of  $\kappa_0$ . Moreover, we obtained in those case  $v_{CR} \sim 10^{-6}$  m/s  $\ll v_{Mg} \sim 10^{-3}$  m/s  $\ll v_S \sim 10^{-2}$  m/s for particles close to the substrate. The coefficients  $Ma$  and  $Co$  will then be fixed by the sedimentation speed  $v_S$ . However, the order of magnitude of the various speeds is only true when particles are close to the substrate. One can understand that bulk sedimentation speed still determine the number of particles reaching the substrate and then  $Ma$ ,  $Co$  and  $C$  still depend on the magnetic field through the bulk sedimentation speed  $v_S \propto \ln(\langle L \rangle/d) - 0.5$ . Then, the coefficient  $C \propto (v_S + v_{Mg})/(Co + C + Ma)$  will grow with  $B$  while  $Co$  and  $Ma$  will substantially decrease. When  $C \gg Co, Ma$ , given the normalization of those parameters, all parameters should saturate when  $C$  approaches 1. This explains the behavior of the curves in Fig. 3 for  $\kappa_0 = 10 \cdot 10^{-3}$  and  $\kappa_0 = 50 \cdot 10^{-3}$ .

#### E. Evolution of the morphological details

As we described elsewhere, for high volume PBS concentration  $\kappa_0 = 50 \cdot 10^{-3}$ , the mean length of the chains varies as if the chains were self-organized as in an airtight chamber of liquid and then abruptly stopped after a constant time  $t_e$  which can be assimilated to the evaporation time of the droplet [20]. In other words, for this parameter, everything happens on average as if magnetic interaction dominated their assembly. This is explained by the fact that, for this value of  $\kappa_0$ , the sedimentation, which depends on the magnetic self-assembly through its bulk speed, dominates the whole process for depositde particles ( $v_{CR} \sim 10^{-6}$  m/s  $\ll v_{Mg} \sim 10^{-3}$  m/s  $\ll v_S \sim 10^{-2}$  m/s).

For low value of PBS  $\kappa_0 = 6 \cdot 10^{-3}$ , the mean length of agglomerates in the deposit is mainly constant for every value of the magnetic field  $B$ . Actually, the only actual aggregates which remain in the eventual deposit are the ones created by the coffee ring and the Marangoni eddy. This is due to the fact that the coffee-ring speed diverges near the end of the evaporation process and is able to break all the chains, which are not sticking to the substrate, as we demonstrated earlier (electrostatic repulsion counters the van der Waals attraction for  $\kappa_0 = 6 \cdot 10^{-3}$ ).

The case of intermediate concentration  $\kappa_0 = 10 \cdot 10^{-3}$  shows a mixed behaviour : for low magnetic fields, the mean length of agglomerates scales as for  $\kappa_0 = 50 \cdot 10^{-3}$ , indicating that the magnetic assembly dominates for those short chains. However, for higher magnetic field, the mean length of agglomerates seem to saturate, as it does for  $\kappa_0 = 6 \cdot 10^{-3}$ , but with a higher length. Having an intermediate behaviour might seem intuitive since we have a transition from chains broken by the coffee-ring flow to chains firmly sticking to the substrate. Moreover, the reason why short chains are able to stick on the substrate while long chains does not is probably related to the fact that long chains are easier to deform and break into smaller ones [56, 57].

## V. CONCLUSION

From the previous observations, one might conclude that the amount of PBS, through both the strength of the Marangoni recirculation [15] and the sedimentation of the particles on the substrate, is mainly responsible for the global distribution profile of the particles. Moreover, this paper shows the magnetic field mainly changes the details morphological properties of the dried deposit with a lesser influence on the density profile. Previous experiments showed that the right strength of solutal-Marangoni instabilities allows the self-organized colloids to be deposited as is after evaporation [20]. This paper demonstrates that the influence of this instability is even richer, since it also determines where the chains will be deposited and show their length can also be limited by flow-driven phenomena.

### A. Data availability

The datasets generated during and/or analyzed during the current study are available from the corresponding author on reasonable request.

### ACKNOWLEDGEMENT

A.D. is financially supported by FNRS as research fellow. This work was financially supported by the FNRS (Grant PDR T.0043.14) and by the University of Liège (Starting Grant C-13/88).

### AUTHOR CONTRIBUTION

G.L. and A.D. designed the experiments. A.D. performed the experiments, analyzed the results and wrote the initial draft of the paper. N.V. and G.L. supervised the project, and all authors discussed the results and contributed to the final manuscript preparation.

### ADDITIONAL INFORMATION

**Competing interests :** The authors declare no competing interests.

- 
- [1] Brutin, D., Sobac, B., Loquet, B. & Sampaol, J. Pattern formation in drying drops of blood. *Journal of Fluid Mechanics* **667**, 85–95 (2011).
- [2] Yakhno, T. A. *et al.* The informative-capacity phenomenon of drying drops. *IEEE engineering in medicine and biology magazine* **24**, 96–104 (2005).
- [3] Sefiane, K. Patterns from drying drops. *Advances in colloid and interface science* **206**, 372–381 (2014).
- [4] Erbil, H. Y. Evaporation of pure liquid sessile and spherical suspended drops: A review. *Advances in colloid and interface science* **170**, 67–86 (2012).
- [5] Deegan, R. D., Bakajin, O., Dupont, T. F., Huber, G. *et al.* Capillary flow as the cause of ring stains from dried liquid drops. *Nature* **389**, 827 (1997).
- [6] Deegan, R. D. *et al.* Contact line deposits in an evaporating drop. *Physical review E* **62**, 756 (2000).
- [7] Marín, A. G., Gelderblom, H., Lohse, D. & Snoeijer, J. H. Order-to-disorder transition in ring-shaped colloidal stains. *Phys. Rev. Lett.* **107**, 085502 (2011). URL <https://link.aps.org/doi/10.1103/PhysRevLett.107.085502>.
- [8] Marín, Á. G., Gelderblom, H., Lohse, D. & Snoeijer, J. H. Rush-hour in evaporating coffee drops. *Physics of fluids* **23**, 091111 (2011).
- [9] Yunker, P. J., Still, T., Lohr, M. A. & Yodh, A. Suppression of the coffee-ring effect by shape-dependent capillary interactions. *Nature* **476**, 308–311 (2011).
- [10] Yunker, P. J. *et al.* Effects of particle shape on growth dynamics at edges of evaporating drops of colloidal suspensions. *Physical review letters* **110**, 035501 (2013).
- [11] Kim, H. *et al.* Controlled uniform coating from the interplay of marangoni flows and surface-adsorbed macromolecules. *Physical review letters* **116**, 124501 (2016).
- [12] Hu, H. & Larson, R. G. Analysis of the effects of marangoni stresses on the microflow in an evaporating sessile droplet. *Langmuir* **21**, 3972–3980 (2005).
- [13] Bennacer, R. & Sefiane, K. Vortices, dissipation and flow transition in volatile binary drops. *Journal of Fluid Mechanics* **749**, 649–665 (2014).
- [14] Christy, J. R., Hamamoto, Y. & Sefiane, K. Flow transition within an evaporating binary mixture sessile drop. *Physical review letters* **106**, 205701 (2011).
- [15] Darras, A., Vandewalle, N. & Lumay, G. Transitional bulk-solutal marangoni instabilities in sessile drops. *Phys. Rev. E*. accepted for publication (2018).
- [16] Hu, H. & Larson, R. G. Marangoni effect reverses coffee-ring depositions. *The Journal of Physical Chemistry B* **110**, 7090–7094 (2006).
- [17] Nguyen, V. X. & Stebe, K. J. Patterning of small particles by a surfactant-enhanced marangoni-bénard instability. *Physical Review Letters* **88**, 164501 (2002).
- [18] Still, T., Yunker, P. J. & Yodh, A. G. Surfactant-induced marangoni eddies alter the coffee-rings of evaporating colloidal drops. *Langmuir* **28**, 4984–4988 (2012).
- [19] Davidson, Z. S. *et al.* Deposition and drying dynamics of liquid crystal droplets. *Nature Communications* **8**, 15642 (2017).
- [20] Darras, A., Migolet, F., Vandewalle, N. & Lumay, G. Remote-controlled deposit of superparamagnetic colloidal droplets. *Submitted for publication* (2018).
- [21] Farauto, J., Andreu, J. S. & Camacho, J. Understanding diluted dispersions of superparamagnetic particles under strong magnetic fields: a review of concepts, theory and simulations. *Soft Matter* **9**, 6654–6664 (2013).
- [22] Farauto, J. & Camacho, J. Cooperative magnetophoresis of superparamagnetic colloids: theoretical aspects. *Colloid Polym. Sci.* **288**, 207–215 (2010).
- [23] Tavacoli, J. W. *et al.* The fabrication and directed self-assembly of micron-sized superparamagnetic non-spherical particles. *Soft Matter* **9**, 9103–9110 (2013).
- [24] Andreu, J. S., Camacho, J. & Farauto, J. Aggregation of superparamagnetic colloids in magnetic fields: the quest for the equilibrium state. *Soft Matter* **7**, 2336–2339 (2011).
- [25] Promislow, J. H., Gast, A. P. & Fermigier, M. Aggregation kinetics of paramagnetic colloidal particles. *J. Chem. Phys.* **102**, 5492–5498 (1995).
- [26] Domínguez-García, P., Pastor, J. & Rubio, M. Aggregation and disaggregation dynamics of sedimented and charged superparamagnetic micro-particles in water suspension. *Eur. Phys. J. E* **34**, 1–7 (2011).
- [27] Domínguez-García, P., Melle, S., Pastor, J. & Rubio, M. Scaling in the aggregation dynamics of a magnetorheological fluid. *Phys. Rev. E* **76**, 051403 (2007).
- [28] Fermigier, M. & Gast, A. P. Structure evolution in a paramagnetic latex suspension. *Journal of colloid and interface science* **154**, 522–539 (1992).
- [29] Darras, A., Fiscina, J., Pakpour, M., Vandewalle, N. & Lumay, G. Ribbons of superparamagnetic colloids in magnetic field. *The European Physical Journal E* **39**,

- 1–6 (2016).
- [30] Rojas, N., Darras, A. & Lumay, G. Self-assembly processes of superparamagnetic colloids in a quasi-two-dimensional system. *Physical Review E* **96**, 012608 (2017).
- [31] Darras, A., Fiscina, J., Vandewalle, N. & Lumay, G. Relating brownian motion to diffusion with superparamagnetic colloids. *American Journal of Physics* **85**, 265–270 (2017).
- [32] Yavuz, C. T. *et al.* Low-field magnetic separation of monodisperse fe<sub>3</sub>o<sub>4</sub> nanocrystals. *Science* **314**, 964–967 (2006).
- [33] Krishnan, K. M. Biomedical nanomagnetism: a spin through possibilities in imaging, diagnostics, and therapy. *IEEE Trans. Magn.* **46**, 2523–2558 (2010).
- [34] Corchero, J. L. & Villaverde, A. Biomedical applications of distally controlled magnetic nanoparticles. *Trends Biotechnol.* **27**, 468–476 (2009).
- [35] Jeong, U., Teng, X., Wang, Y., Yang, H. & Xia, Y. Superparamagnetic colloids: controlled synthesis and niche applications. *Adv. Mater.* **19**, 33 (2007).
- [36] Gajula, G. P., Neves-Petersen, M. T. & Petersen, S. B. Visualization and quantification of four steps in magnetic field induced two-dimensional ordering of superparamagnetic submicron particles. *Appl. Phys. Lett.* **97**, 103103 (2010).
- [37] Khalil, K. S. *et al.* Binary colloidal structures assembled through ising interactions. *Nat. Commun.* **3**, 794 (2012).
- [38] Gurevich, Y., Mankov, Y. & Khlebopros, R. Self-assembly of superparamagnetic ferrihydrite nanoparticles. *Dokl. Phys.* **11**, 478–481 (2013).
- [39] Martinez-Pedrero, F. & Tierno, P. Magnetic propulsion of self-assembled colloidal carpets: Efficient cargo transport via a conveyor-belt effect. *Phys. Rev. Applied* **3**, 051003 (2015). URL <http://link.aps.org/doi/10.1103/PhysRevApplied.3.051003>.
- [40] Carstensen, H., Kapaklis, V. & Wolff, M. Phase formation in colloidal systems with tunable interaction. *Phys. Rev. E* **92**, 012303 (2015). URL <http://link.aps.org/doi/10.1103/PhysRevE.92.012303>.
- [41] Müller, K. *et al.* Pattern formation and coarse-graining in two-dimensional colloids driven by multiaxial magnetic fields. *Langmuir* **30**, 5088–5096 (2014).
- [42] Llera, M., Codnia, J. & Jorge, G. A. Aggregation dynamics and magnetic properties of magnetic micrometer-sized particles dispersed in a fluid under the action of rotating magnetic fields. *J. Magn. Magn. Matter* **384**, 93–100 (2015).
- [43] Erb, R. M., Son, H. S., Samanta, B., Rotello, V. M. & Yellen, B. B. Magnetic assembly of colloidal superstructures with multipole symmetry. *Nature* **457**, 999–1002 (2009).
- [44] Martinez-Pedrero, F. & Tierno, P. Magnetic propulsion of self-assembled colloidal carpets: Efficient cargo transport via a conveyor-belt effect. *Phys. Rev. Applied* **3**, 051003 (2015).
- [45] Martinez-Pedrero, F., Ortiz-Ambriz, A., Pagonabarraga, I. & Tierno, P. Colloidal microworms propelling via a cooperative hydrodynamic conveyor belt. *Phys. Rev. Lett.* **115**, 138301 (2015).
- [46] Carstensen, H., Kapaklis, V. & Wolff, M. Phase formation in colloidal systems with tunable interaction. *Phys. Rev. E* **92**, 012303 (2015).
- [47] Liu, P., De Folter, J. W., Petukhov, A. V. & Philipse, A. P. Reconfigurable assembly of superparamagnetic colloids confined in thermo-reversible microtubes. *Soft Matter* **11**, 6201–6211 (2015).
- [48] Edmond, K. V. *et al.* Tracking the brownian diffusion of a colloidal tetrahedral cluster. *Chaos-Woodbury* **21**, 041103 (2011).
- [49] Dreyfus, R. *et al.* Microscopic artificial swimmers. *Nature* **437**, 862–865 (2005).
- [50] Yu, J., Wang, B., Du, X., Wang, Q. & Zhang, L. Ultra-extensible ribbon-like magnetic microswarm. *Nature communications* **9**, 3260 (2018).
- [51] Bhardwaj, R., Fang, X., Somasundaran, P. & Attinger, D. Self-assembly of colloidal particles from evaporating droplets: role of dlvo interactions and proposition of a phase diagram. *Langmuir* **26**, 7833–7842 (2010).
- [52] Darras, A., Opsomer, E., Vandewalle, N. & Lumay, G. Superparamagnetic colloids in viscous fluids. *Scientific Reports* **7** (2017).
- [53] Cosgrove, T. *Colloid science: principles, methods and applications* (John Wiley & Sons, 2010).
- [54] Xie, Q. & Harting, J. From dot to ring: The role of friction in the deposition pattern of a drying colloidal suspension droplet. *Langmuir* **34**, 5303–5311 (2018).
- [55] Sultan, S., de Planque, M., Ashburn, P. & Chong, H. Effect of phosphate buffered saline solutions on top-down fabricated zno nanowire field effect transistor. *Journal of Nanomaterials* **2017** (2017).
- [56] Li, D., Banon, S. & Biswal, S. L. Bending dynamics of dna-linked colloidal particle chains. *Soft Matter* **6**, 4197–4204 (2010).
- [57] Hall, C. L., Vella, D. & Goriely, A. The mechanics of a chain or ring of spherical magnets. *SIAM Journal on Applied Mathematics* **73**, 2029–2054 (2013).

## Part IV

# Conclusion and perspectives





# Chapter 10

## Conclusion and perspectives

### 10.1 Conclusion

In this work, we studied the behaviour of superparamagnetic colloids both in equilibrium's condition and far from these conditions. The systems we studied and our main results are summarized in Figure 10.1. The first part of our work offered a more complete description and an experimental characterization of colloidal chains formed under constant magnetic fields. We consolidated the knowledge about the system, and reported unexpected observations. This might be seen as a first step towards achieving a deep understanding of the more complex systems used in applications.

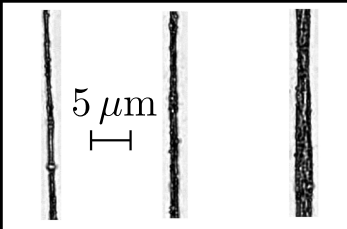
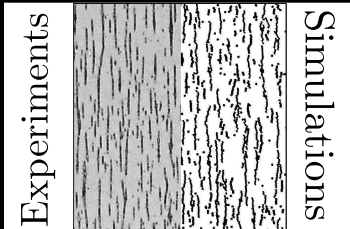
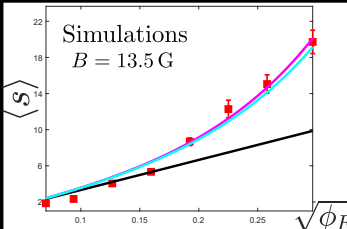
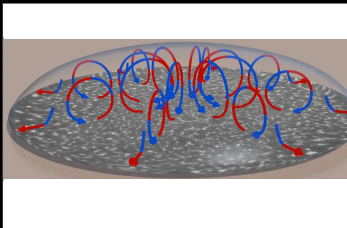
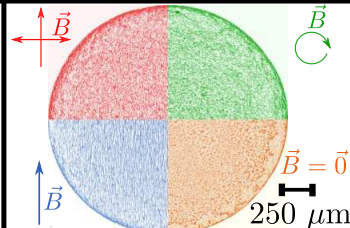
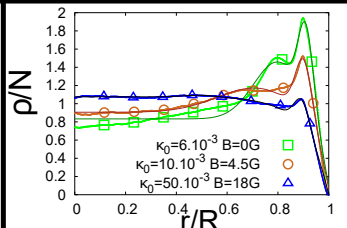
Part II		
Chapter 4	Chapter 5	Chapter 6
		
Existence of Ribbons Divergence between experiments and models	Influence of viscosity Method to fasten simulations	Effect of volume fraction New model
Part III		
Chapter 7	Chapter 8	Chapter 9
		
Temporal competition Marangoni-Coffee-Ring	Influence of $\vec{B}$ Remote control	Evidencing 3 mechanisms Density master curve

Figure 10.1: Table summarizing the various studies of this work. Main results are pictured for each chapter, and main achievements are summarized in a few words.

More accurately, our first study (Chapter 4) conducted systematic experiments in order to compare them with the existing models and simulations. We showed that the trend observed

experimentally was in agreement with the models, but only in a limited range of parameters. We provided a first explanation of this deviation by the existence of structures not taken into account by the models. The apparition of such structures, in the case of small agglomerates, is prevented by potential barriers we partially computed. However, we wanted to explore this range of parameters through numerical simulations, in order to confirm that such deviation would be observed even in ideal systems. We then observed that modifying the viscosity of the system changed the characteristic timescale of the self-assembly leading to the equilibrium (Chapter 5). We characterized this both experimentally and numerically. We found that this property could be used to fasten numerical simulations up to a given ratio depending on the magnetic field. Moreover, our results also indicate that the formation process of the agglomerates has a significant impact on the equilibrium state. This is consistent with the results of our first study, since other formation mechanisms could allow to overcome some potential barriers. We then eventually used a modification of viscosity in numerical simulations, in order to perform simulations of systems as close as possible from our initial experimental set-up, as exposed in Chapter 6. Thanks to our previous findings, we managed to perform simulations which were 40 times faster than unmodified simulations. In the unexplored set of parameters we were able to study, we evidenced that the volume fraction of the particles has further effects on the equilibrium than expected. We modified the existing model in order to take interactions between agglomerates into account. We showed that this consideration alone was sufficient to model all the available numerical data, and provided a better agreement with the experimental data. This finding highlight that mean-field theory taking into account only internal energy of aggregates may be insufficient to predict the properties of a self-assembled systems. Indeed, we clearly showed that interaction energy between aggregates had to be taken into account in order to model the behaviour of our system.

The second part of our work evidenced what influence the self-assembly of superparamagnetic colloids has on the final deposit. We demonstrated that the magnetic field could be used as a remote control of the evaporative deposit. Moreover, we used this parameter as a simple probe to characterize the influence of interactions between the particles on the substrate. We showed that self-assembly of particles mainly modifies the sedimentation of the particles and then the competition between this mechanism and coffee-ring plus Marangoni flows. We made a systematic study of the interaction of these three mechanisms and proposed a master curve to model how they shape the particles' density in the final deposit.

In more details, the first actual step of our research regarding the evaporating droplet has been to characterize the exact flows occurring in the droplet (Chapter 7), independently from any magnetic field. We showed that two mechanisms, coffee-ring effect and Marangoni instability, were competing. We also showed that the upper-hand in competition was going back and forth from one to the other on determined timescales. We gave an explanation for these timescales. We then focused on the eventual deposits left by the particles when the droplets were completely evaporated. Our first observations were performed when Marangoni instability and attraction with the substrate homogenizes the deposit, as exposed in Chapter 8. We showed that the magnetic field could be used as a remote control for those deposits. Indeed, the self-assembled agglomerates are then deposited almost as is on the substrate. However, the limiting factor for the chains length, in our setup, is the evaporation time. Indeed, this evaporation time is about a few tens of minutes, while the time required to reach the equilibrium is about a few hours, i.e. one order of magnitude higher. We then completed the picture by describing the deposits obtained with various concentrations of ions in the suspension in Chapter 9. We introduced a master curve which can reproduce all our data. We used it to show that a triple competition occurs, since sedimentation also competes with Marangoni instability and coffee-ring flow. We demonstrated that the influence of the magnetic field on the substrate is mainly

due to its influence on the sedimentation of the particles. Then, this influence also strongly depends of the interactions of the particles with the substrate. We evidenced that a transition occurred when the DLVO interaction with this substrate becomes attractive.

## 10.2 Perspectives

Beyond all these observations, several questions and challenges are still open. Regarding the size of the chains at equilibrium, simulations giving average size of chains higher than 100 particles are still required in order to compare experimental data with ideal systems. Analytical models predicting the apparition of ribbons and their influence on the mean properties of the agglomerates is still lacking. Regarding the evaporative droplets, the question of location of the chains in the deposit for low ionic concentration is still open. The way a flow of liquid interacts with a chain of colloid has been neglected in our approaches, but these flows seem able to break the chains in some conditions... Determining these conditions and how this effect influences the deposits would be an interesting advance, probably leading to further understanding of even more complex systems, such as polymers or crystals deposits. Moreover, since the sedimentation plays a key role in the eventual deposits' structure, one can wonder what would be the properties of suspended droplets, hanging below the substrate instead of lying on top of it. As preliminary results suggest, a tilt angle of the substrate might also have a deep influence on the substrate. Moreover, one can wonder how the size or the concentration of the particles influence the deposit, or how exactly dynamic aggregates (such as obtained with oscillating magnetic fields) would influence the substrate... Our current work provides several experimental set-ups, analysis tools, concepts and hypotheses which are probably going to be part of the building blocks of the answers to those questions.

More practically, during the next few months, we plan to develop several microfluidic chips in order to assess the interaction between liquid flows and magnetic colloidal assemblies. This should help to understand how chains are broken in evaporating droplets with low ions (i.e. PBS) concentration. We expect that this will be helpful to describe the variations of mean size of agglomerates along the radial coordinate of the deposits. Such a result will offer further justifications for the empirical master curves we provided for the density profiles of the deposits. It will also give more insight on the dynamics of the formation of this deposit.



# Appendix A

## Self-assembly equilibrium : detailed calculations

In the case of colloids made of incompressible materials, at constant temperature and particles number, the thermodynamic equilibrium is described by a minimum of the free energy  $F = U - TS$ , where  $U$  is the internal energy of the system,  $T$  the temperature and  $S$  the entropy. In the case of chains of superparamagnetic colloids, we have to consider the magnetic interaction energy of the particles. A common hypothesis is that the energy of a chain with  $s$  particles is  $-(s-1)\epsilon_m$ . [25] This hypothesis is equivalent to say that particles in a chain only interact with their first neighbour, and have a binding energy  $-\epsilon_m$ . Moreover in the case of a mixture of chains with various lengths, one has to take into account the mixing entropy

$$S_M = -k_B A \sum_{s=1}^{+\infty} a_s \ln(a_s), \quad (\text{A.1})$$

assumed  $a_s \ln(a_s) = 0$  if  $a_s = 0$  and where  $a_s$  is the fraction of chains with length  $s$  (i.e. containing  $s$  particles), and  $A$  is the total number of chains. We then have  $A_s = a_s A$  the number of chains with length  $s$ . We then have the relation  $A = \sum_{s=1}^{\infty} A_s$ . One can also define  $N_s = s A_s$ , the number of particles in one of the  $s$ -length chains. Moreover, if  $V$  is the volume of the suspension and  $V_{part}$  the volume of one colloidal particle,  $\phi_s = N_s \frac{V_{part}}{V}$  is the volume fraction of chains of length  $s$ . Then, if we consider that other contribution to the energy and/or the entropy of the system does not depend on the fact that a particle is comprised in a chain of length  $s$ , the Gibbs free energy of the suspension is

$$F = U - TS = \sum_{s=1}^{\infty} -A_s (s-1) \epsilon_m + k_B T A_s \ln\left(\frac{A_s}{A}\right) + F_0 \quad (\text{A.2a})$$

$$= \sum_{s'=1}^{\infty} -\frac{N_{s'}}{s'} (s'-1) \epsilon_m + k_B T \frac{N_{s'}}{s'} \ln\left(\frac{N_{s'}}{s' A}\right) + F_0 \quad (\text{A.2b})$$

where  $F_0$  contain all the other contributions to the free energy. The chemical potential of a particle contained in a chain of length  $s$  is then defined as  $\mu_s = \left. \frac{\partial F}{\partial N_s} \right|_{N_{s' \neq s}, T, V}$ . If one takes

into account the fact that  $A = \sum_{s'=1}^{\infty} \frac{N_{s'}}{s'}$  and then  $\frac{\partial A}{\partial N_s} = \frac{1}{s}$ , we get

$$\mu_s = \frac{-(s-1)\epsilon_m}{s} + \frac{k_B T}{s} \ln\left(\frac{N_s}{sA}\right) + k_B T \sum_{s'=1}^{\infty} \frac{N_{s'}}{s'} \frac{s' A}{N_{s'}} \left( \frac{\delta_{ss'}}{s' A} - \frac{N_{s'}}{s' s A^2} \right) + \mu_0 \quad (\text{A.3a})$$

$$= \frac{-(s-1)\epsilon_m}{s} + \frac{k_B T}{s} \ln\left(\frac{N_s}{sA}\right) + \frac{k_B T}{s} - \frac{k_B T}{sA} \sum_{s'=1}^{\infty} \frac{N_{s'}}{s'} + \mu_0 \quad (\text{A.3b})$$

$$= \frac{1}{s} \left[ k_B T \ln\left(\frac{N_s}{sA}\right) - (s-1)\epsilon_m \right] + \mu_0 \quad (\text{A.3c})$$

$$= \frac{1}{s} \left[ k_B T \ln\left(\frac{\phi_s}{s}\right) - (s-1)\epsilon_m \right] + \mu_s^0, \quad (\text{A.3d})$$

where  $\delta_{ss'}$  is the Kronecker symbol,  $\mu_0 = \frac{\partial F_0}{\partial N_s}$  and  $\mu_s^0 = \mu_0 + \ln\left(\frac{V}{AV_{part}}\right) \frac{k_B T}{s}$ . It is often considered that  $\mu_s^0$  is a constant, not depending on the cluster or size  $s$ . [9, 25] This is an approximation justified by the hypothesis of ideal mixing, claiming that the association rate  $k_1\phi_1^s$  is equal to the dissociation rate  $k_s\phi_s/s$ , where  $k_1$  and  $k_s$  are constants called reaction rates (see chapter 19 of [9] for more details).

The thermodynamic equilibrium being reached when all particles have the same chemical potential, we obtain from previous equations

$$\mu_s = \mu_1 \tag{A.4a}$$

$$\Leftrightarrow \frac{1}{s} \left[ k_B T \ln\left(\frac{\phi_s}{s}\right) - (s-1)\epsilon_m \right] + \mu_s^0 = k_B T \ln(\phi_1) + \mu_1^0 \tag{A.4b}$$

$$\Leftrightarrow s \ln(\phi_1) + \frac{(s-1)}{k_B T} \epsilon_m + s \frac{(\mu_1^0 - \mu_s^0)}{k_B T} = \ln\left(\frac{\phi_s}{s}\right) \tag{A.4c}$$

$$\Leftrightarrow \phi_s = s \left[ \phi_1 \exp\left(\frac{\epsilon_m(s-1)/s + (\mu_1^0 - \mu_s^0)}{k_B T}\right) \right]^s \tag{A.4d}$$

$$\Leftrightarrow \phi_s \approx s \left[ \phi_1 \exp\left(\frac{\epsilon_m(s-1)/s}{k_B T}\right) \right]^s \tag{A.4e}$$

$$= s \left[ \phi_1 \exp\left(\frac{\epsilon_m}{k_B T}\right) \right]^s \exp\left(\frac{-\epsilon_m}{k_B T}\right). \tag{A.4f}$$

The approximation A.4e has been obtained by assuming that  $\mu_s^0$  does not depend on  $s$  and is a constant  $\mu^0$ . In the case of superparamagnetic colloids, this can also be justified if

$$|\mu_1^0 - \mu_s^0| \ll \frac{(s-1)}{s} |\epsilon_m| \tag{A.5a}$$

$$\Leftrightarrow \ln\left(\frac{V}{AV_{part}}\right) \frac{k_B T}{s} (s-1) \ll \frac{(s-1)}{s} |\epsilon_m| \tag{A.5b}$$

$$\Leftrightarrow \ln\left(\frac{V}{AV_{part}}\right) k_B T \ll |\epsilon_m|, \tag{A.5c}$$

which is the case when volume fraction is of the order of at least a percent  $\phi_0 \geq 0.01$  (since  $AV_{part}/V \lesssim \phi_0$ , where  $\phi_0$  is the total volume fraction, denoted  $\phi$  elsewhere, and is the sum of all the  $\phi_s$ ), and if the magnetic energy is much higher than the Brownian energy  $k_B T \ll \epsilon_m$ , i.e. for  $\Gamma \gg 1$ . This last hypothesis is assumed in most developments, since in other conditions the self-assembly of particles usually does not occur [25, 33].

Furthermore, since the volume occupied by all the particles is a constant, we have the constraint  $\phi_0 = \sum_{s=1}^{\infty} \phi_s$ , where  $\phi_0$  is the total volume fraction of the particles, or also the value

of  $\phi_1$  without aggregation. We can then write

$$\phi_0 = \sum_{s=1}^{\infty} \phi_s \quad (\text{A.6a})$$

$$= \sum_{s=1}^{\infty} s \left[ \phi_1 \exp\left(\frac{\epsilon_m}{k_B T}\right) \right]^s \exp\left(\frac{-\epsilon_m}{k_B T}\right) \quad (\text{A.6b})$$

$$= \frac{\phi_1}{x} \sum_{s=1}^{\infty} s x^s \quad (\text{A.6c})$$

$$= \frac{\phi_1}{x} \frac{x}{(1-x)^2} \quad (\text{A.6d})$$

$$\Leftrightarrow \phi_0 \exp(\beta \epsilon_m) = \frac{x}{(1-x)^2}, \quad (\text{A.6e})$$

where we defined  $x = \phi_1 \exp(\beta \epsilon_m)$  with  $\beta = \frac{1}{k_B T}$ . In order for  $\sum_{s=1}^{\infty} s x^s$  to converge to  $\frac{x}{(1-x)^2}$ , we also assumed  $x < 1$ . From the last equality, we see that  $x$ , and then  $\phi_1$ , are determined by the values of  $\phi_0$ ,  $k_B T$  and  $\epsilon_m$ . Then, the distribution of chains length at thermodynamic equilibrium depends not only on the competition between magnetic interaction energy and thermal energy, but also relies on the volume fraction of colloidal particles. In the case where  $\phi_0 \exp(\beta \epsilon_m) \ll 1$ , and then  $x/(1-x)^2 \approx x$ , the last equality can be written, at first order,  $x = \phi_0 \exp(\beta \epsilon_m)$ , leading to  $\phi_1 = \phi_0$  meaning there is no formation of chains. On the contrary, if  $\phi_0 \exp(\beta \epsilon_m) \gg 1$ , or  $x \rightarrow 1 \Rightarrow x/(1-x)^2 \approx 1/(1-x)^2$ , then  $x = 1 - \frac{1}{\sqrt{\phi_0 \exp(\beta \epsilon_m)}}$  at first order in  $\frac{1}{\sqrt{\phi_0 \exp(\beta \epsilon_m)}}$ . In this case, we have

$$A_s = \frac{\phi_s V}{s V_{part}} \quad (\text{A.7a})$$

$$\propto x^s \quad (\text{A.7b})$$

$$\approx \left[ 1 - \frac{1}{\sqrt{\phi_0 \exp(\beta \epsilon_m)}} \right]^s \quad (\text{A.7c})$$

$$\approx \exp\left(\frac{-s}{\sqrt{\phi_0 \exp(\beta \epsilon_m)}}\right). \quad (\text{A.7d})$$

Such an expression of  $A_s$  implies that the mean length of the chains is written

$$\langle s \rangle \equiv \frac{\sum_{s=1}^{\infty} s A_s}{\sum_{s'=1}^{\infty} A_{s'}} \quad (\text{A.8a})$$

$$\approx \left[ 1 - \exp\left(-\frac{1}{\sqrt{\phi_0 \exp(\beta \epsilon_m)}}\right) \right]^{-1} \quad (\text{A.8b})$$

$$\approx \sqrt{\phi_0 \exp(\beta \epsilon_m)}. \quad (\text{A.8c})$$

It is worthwhile to notice that those mathematical approximations are even more pertinent when  $\sqrt{\phi_0 \exp(\beta \epsilon_m)}$  is large.

In order to relate this mean length to the experimental parameters, one has still to determine the value of  $\epsilon_m$ . This parameter is the absolute value of magnetic binding between two

neighbours in a chain. It can then be estimated as the opposite of the mean value of magnetic interaction energy of two agglomerated dipoles  $\langle U \rangle$ . Using the expression of Eq. (1.14), this is written  $\langle U \rangle = -\frac{\Gamma}{\beta}[1 - \frac{3}{2}\langle \sin^2 \theta \rangle]$  where  $\langle \sin^2 \theta \rangle$  is the average value of  $\sin^2 \theta$ , weighted by their probability determined in the canonical ensemble. We then have :

$$\langle \sin^2 \theta \rangle = \frac{\int_0^{2\pi} d\phi \int_0^{\theta_0} \sin^3 \theta \exp(\Gamma[1 - \frac{3}{2} \sin^2 \theta]) d\theta}{\int_0^{2\pi} d\phi \int_0^{\theta_0} \sin \theta \exp(\Gamma[1 - \frac{3}{2} \sin^2 \theta]) d\theta} \quad (\text{A.9a})$$

$$= \frac{\int_0^{\theta_0} \sin^3 \theta \exp(\Gamma[1 - \frac{3}{2} \sin^2 \theta]) d\theta}{\int_0^{\theta_0} \sin \theta \exp(\Gamma[1 - \frac{3}{2} \sin^2 \theta]) d\theta} \quad (\text{A.9b})$$

if we assume that no other constraint than magnetic interaction restricts the accessible states. The integration stops at  $\theta = \theta_0$ , because the magnetic interaction is repulsive beyond this value and the particles can never be agglomerated with greater angles. The additional factor  $\sin \theta$  comes from the Jacobian for spherical coordinates. By using the stationary phase approximation, [25] one can find an approximation of this integral

$$\langle \sin^2 \theta \rangle = \frac{\int_0^{\theta_0} \sin^3 \theta \exp(\Gamma[1 - \frac{3}{2} \sin^2 \theta]) d\theta}{\int_0^{\theta_0} \sin \theta \exp(\Gamma[1 - \frac{3}{2} \sin^2 \theta]) d\theta} \quad (\text{A.10a})$$

$$\approx \frac{\exp(\Gamma) \int_0^{\theta_0} \theta^3 \exp(-\Gamma \frac{3}{2} \theta^2) d\theta}{\exp(\Gamma) \int_0^{\theta_0} \theta \exp(-\Gamma \frac{3}{2} \theta^2) d\theta} \quad (\text{A.10b})$$

$$\approx \frac{\int_0^{\infty} \theta^3 \exp(-\Gamma \frac{3}{2} \theta^2) d\theta}{\int_0^{\infty} \theta \exp(-\Gamma \frac{3}{2} \theta^2) d\theta} \quad (\text{A.10c})$$

$$= \frac{2}{3\Gamma} \quad (\text{A.10d})$$

where the last equality directly comes from the relation  $\frac{I_{n+2}}{I_n} = \frac{n+1}{2a}$  where  $I_n = \int_0^{\infty} x^n \exp(-ax^2) dx$ , obtained by integrating by parts once  $I_{n+2}$ .

Eventually, one then obtains  $\beta \epsilon_m \equiv -\beta \langle U \rangle = \Gamma[1 - \frac{3}{2} \langle \sin^2 \theta \rangle] \approx \Gamma - 1$ . This approximation is even better when  $\Gamma \gg 1$  is large. However, even if  $\Gamma = 3$ , a numerical estimation of the initial integral gives  $\beta \langle U \rangle = 2.07$ , which is different from less than 5% from  $\Gamma - 1 = 2$ . This model then implies that the mean length of the chains is  $\langle s \rangle = \sqrt{\phi_0 \exp(\Gamma - 1)}$  when  $\Gamma \gg 1$ . Of course, when this model predicts  $\langle s \rangle < 1$ , it simply means there is no aggregation of the colloidal particles and the real value of  $\langle s \rangle$  will be 1.



# Bibliography

- [1] D. H. Everett *et al.*, *Basic principles of colloid science* (Royal society of chemistry, 2007).
- [2] P. C. Hiemenz and R. Rajagopalan, *Principles of Colloid and Surface Chemistry, revised and expanded* (CRC press, 1997).
- [3] T. Cosgrove, *Colloid science: principles, methods and applications* (John Wiley & Sons, 2010).
- [4] D. J. Shaw, *Introduction to colloid and surface chemistry* (Butterworth, 1966).
- [5] N. Pottier, *Physique statistique hors d'équilibre: processus irréversibles linéaires* (EDP Sciences, 2007).
- [6] R. Pashley and M. Karaman, *Applied colloid and surface chemistry* (John Wiley & Sons, 2005).
- [7] B. Cabane and S. Hénon, *Liquides: solutions, dispersions, émulsions, gels* (Belin, 2007).
- [8] M. Reichert, *Hydrodynamic Interactions in Colloidal and Biological Systems*, PhD thesis, Universität Konstanz, 2006.
- [9] J. N. Israelachvili, *Intermolecular and surface forces: revised third edition* (Academic press, 2011).
- [10] M. Elimelech, J. Gregory, and X. Jia, *Particle deposition and aggregation: measurement, modelling and simulation* (Butterworth-Heinemann, 2013).
- [11] R. Bhardwaj, X. Fang, P. Somasundaran, and D. Attinger, *Langmuir* **26**, 7833 (2010).
- [12] J. Mahanty and B. W. Ninham, *Dispersion forces, Vol. V* (Academic Press London, 1976).
- [13] T. F. Tadros, *Colloid Stability, Vol I* (Wiley-VCH, 2007).
- [14] D. H. Everett, *Basic principles of colloid science* (Royal Society of Chemistry, 1988).
- [15] W. C. Elmore, *Phys. Rev.* **54**, 1092 (1938).
- [16] R. Haghgooeie, C. Li, and P. S. Doyle, *Langmuir* **22**, 3601 (2006).
- [17] A. F. Demirörs, P. P. Pillai, B. Kowalczyk, and B. A. Grzybowski, *Nature* **503**, 99 (2013).
- [18] U. Jeong, X. Teng, Y. Wang, H. Yang, and Y. Xia, *Adv. Mater.* **19**, 33 (2007).
- [19] J. Faraudo, J. S. Andreu, and J. Camacho, *Soft Matter* **9**, 6654 (2013).
- [20] J. Faraudo and J. Camacho, *Colloid Polym. Sci.* **288**, 207 (2010).
- [21] J. W. Tavaoli *et al.*, *Soft Matter* **9**, 9103 (2013).
- [22] C. T. Yavuz *et al.*, *Science* **314**, 964 (2006).
- [23] K. M. Krishnan, *IEEE Trans. Magn.* **46**, 2523 (2010).
- [24] J. L. Corchero and A. Villaverde, *Trends Biotechnol.* **27**, 468 (2009).

- [25] J. S. Andreu, J. Camacho, and J. Faraudo, *Soft Matter* **7**, 2336 (2011).
- [26] G. P. Gajula, M. T. Neves-Petersen, and S. B. Petersen, *Appl. Phys. Lett.* **97**, 103103 (2010).
- [27] K. S. Khalil *et al.*, *Nat. Commun.* **3**, 794 (2012).
- [28] Y. Gurevich, Y. Mankov, and R. Khlebopros, *Dokl. Phys.* **11**, 478 (2013).
- [29] F. Martinez-Pedrero and P. Tierno, *Phys. Rev. Applied* **3**, 051003 (2015).
- [30] H. Carstensen, V. Kapaklis, and M. Wolff, *Phys. Rev. E* **92**, 012303 (2015).
- [31] Merckmillipore website, <http://www.merckmillipore.com/BE/fr/products/ivd-oem-materials-reagents/polymeric-microspheres-and-magnetic-beads/magprep-magnetic-particles/noSb.qB.SwYAAAFArcZkiQpx,nav>, Accessed: 2019-01-23.
- [32] J. H. Promislow, A. P. Gast, and M. Fermigier, *J. Chem. Phys.* **102**, 5492 (1995).
- [33] J. Faraudo, J. S. Andreu, C. Calero, and J. Camacho, *Advanced Functional Materials* **26**, 3837 (2016).
- [34] S. Fraden, A. J. Hurd, and R. B. Meyer, *Phys. Rev. Lett.* **63**, 2373 (1989).
- [35] M. Kolb, *Phys. Rev. Lett.* **53**, 1653 (1984).
- [36] F. Martínez-Pedrero, M. Tirado-Miranda, A. Schmitt, and J. Callejas-Fernández, *Phys. Rev. E* **76**, 011405 (2007).
- [37] S. Miyazima, P. Meakin, and F. Family, *Phys. Rev. A* **36**, 1421 (1987).
- [38] F. Martinez-Pedrero and P. Tierno, *Phys. Rev. Applied* **3**, 051003 (2015).
- [39] K. H. Taylor, *The influence of magnetic cohesion on the stability of granular slopes*, PhD thesis, University of Nottingham, 2009.
- [40] J. Yu, B. Wang, X. Du, Q. Wang, and L. Zhang, *Nature communications* **9**, 3260 (2018).
- [41] N. Vandewalle and S. Dorbolo, *New Journal of Physics* **16**, 013050 (2014).
- [42] R. Messina and I. Stanković, *Physica A: Statistical Mechanics and its Applications* **466**, 10 (2017).
- [43] R. Messina and I. Stanković, *EPL (Europhysics Letters)* **110**, 46003 (2015).
- [44] R. Messina, L. A. Khalil, and I. Stanković, *Physical Review E* **89**, 011202 (2014).
- [45] R. Messina and L. Spiteri, *The European Physical Journal E* **39**, 81 (2016).
- [46] C. L. Hall, D. Vella, and A. Goriely, *SIAM Journal on Applied Mathematics* **73**, 2029 (2013).
- [47] J. Hernández-Rojas, D. Chakrabarti, and D. Wales, *Physical Chemistry Chemical Physics* **18**, 26579 (2016).
- [48] K. Müller *et al.*, *Langmuir* **30**, 5088 (2014).
- [49] M. Llera, J. Codnia, and G. A. Jorge, *J. Magn. Magn. Matter* **384**, 93 (2015).

- 
- [50] R. M. Erb, H. S. Son, B. Samanta, V. M. Rotello, and B. B. Yellen, *Nature* **457**, 999 (2009).
- [51] F. Martinez-Pedrero, A. Ortiz-Ambriz, I. Pagonabarraga, and P. Tierno, *Phys. Rev. Lett.* **115**, 138301 (2015).
- [52] H. Carstensen, V. Kapaklis, and M. Wolff, *Phys. Rev. E* **92**, 012303 (2015).
- [53] P. Liu, J. W. De Folter, A. V. Petukhov, and A. P. Philipse, *Soft Matter* **11**, 6201 (2015).
- [54] P. Domínguez-García, J. Pastor, and M. Rubio, *Eur. Phys. J. E* **34**, 1 (2011).
- [55] P. Domínguez-García, S. Melle, J. Pastor, and M. Rubio, *Phys. Rev. E* **76**, 051403 (2007).
- [56] K. V. Edmond *et al.*, *Chaos-Woodbury* **21**, 041103 (2011).
- [57] R. Dreyfus *et al.*, *Nature* **437**, 862 (2005).
- [58] A. Darras, J. Fiscina, N. Vandewalle, and G. Lumay, *American Journal of Physics* **85**, 265 (2017).
- [59] A. Darras, J. Fiscina, M. Pakpour, N. Vandewalle, and G. Lumay, *The European Physical Journal E* **39**, 1 (2016).
- [60] A. Darras, E. Opsomer, N. Vandewalle, and G. Lumay, *Scientific Reports* **7** (2017).
- [61] A. Darras, N. Vandewalle, and G. Lumay, *Effect of volume fraction on chains of superparamagnetic colloids at equilibrium* (The European Physical Journal E, submitted, 2019).
- [62] F. Burmeister *et al.*, *Langmuir* **13**, 2983 (1997).
- [63] M. Wood, *Journal of the Royal Society Interface* **4**, 1 (2006).
- [64] G. Edelman, T. G. van Leeuwen, and M. C. Aalders, *Forensic science international* **223**, 72 (2012).
- [65] M. Raymond, E. Smith, and J. Liesegang, *Science and justice* **36**, 161 (1996).
- [66] K. Sefiane, *Journal of Bionic Engineering* **7**, S82 (2010).
- [67] T. A. Yakhno *et al.*, *IEEE engineering in medicine and biology magazine* **24**, 96 (2005).
- [68] D. Brutin and V. Starov, *Chemical Society Reviews* **47**, 558 (2018).
- [69] S.-a. Ryu, J. Y. Kim, S. Y. Kim, and B. M. Weon, *Scientific Reports* **7**, 1079 (2017).
- [70] V. Vysotskii, V. Roldughin, O. Y. Uryupina, I. Senchikhin, and A. Zaitseva, *Colloid Journal* **79**, 190 (2017).
- [71] D. Brutin, B. Sobac, and C. Nicloux, *J. Heat Transfer* **134**, 061101 (2012).
- [72] H. Y. Erbil, *Advances in colloid and interface science* **170**, 67 (2012).
- [73] T. Kajiya, D. Kaneko, and M. Doi, *Langmuir* **24**, 12369 (2008).
- [74] Á. G. Marín, H. Gelderblom, D. Lohse, and J. H. Snoeijer, *Phys. Fluids* **23**, 1111 (2011).

- [75] Á. G. Marín *et al.*, Proc. Nat. Acad. Sci. U.S.A. **109**, 16455 (2012).
- [76] D. Mampallil and H. B. Eral, Advances in colloid and interface science **252**, 38 (2018).
- [77] R. D. Deegan *et al.*, Nature **389**, 827 (1997).
- [78] R. D. Deegan *et al.*, Physical review E **62**, 756 (2000).
- [79] P. J. Yunker, T. Still, M. A. Lohr, and A. Yodh, Nature **476**, 308 (2011).
- [80] H. Hu and R. G. Larson, Langmuir **21**, 3963 (2005).
- [81] H. Hu and R. G. Larson, Langmuir **21**, 3972 (2005).
- [82] H. Hu and R. G. Larson, The Journal of Physical Chemistry B **110**, 7090 (2006).
- [83] V. X. Nguyen and K. J. Stebe, Physical Review Letters **88**, 164501 (2002).
- [84] T. Still, P. J. Yunker, and A. G. Yodh, Langmuir **28**, 4984 (2012).
- [85] R. Bennacer and K. Sefiane, Journal of Fluid Mechanics **749**, 649 (2014).
- [86] H. Kim *et al.*, Physical review letters **116**, 124501 (2016).
- [87] M. Anyfantakis, Z. Geng, M. Morel, S. Rudiuk, and D. Baigl, Langmuir **31**, 4113 (2015).
- [88] K. Joshi, T. Muangnapoh, M. D. Stever, and J. F. Gilchrist, Langmuir **31**, 12348 (2015).
- [89] A. Darras, N. Vandewalle, and G. Lumay, Physical Review E **98**, 062609 (2018).
- [90] A. Darras, F. Mignolet, N. Vandewalle, and G. Lumay, Physical Review E **98**, 062608 (2018).
- [91] A. Darras, N. Vandewalle, and G. Lumay, *Effect of volume fraction on chains of superparamagnetic colloids at equilibrium* (submitted, 2019).
- [92] T. Pöschel and T. Schwager, *Computational granular dynamics: models and algorithms* (Springer Science & Business Media, 2005).
- [93] F. Radjaï and F. Dubois, *Discrete-element modeling of granular materials* (Wiley-Iste, 2011).
- [94] J. Y. Ooi, V. Magnanimo, J. Sun, and S. Luding, Powder technology **293**, 1 (2016).